Femtosecond Laser Interactions In The Condensed Phase: Application To Transient Absorption And Materials Processing

by

Simon Morris Ameer-Beg

Being A Thesis Submitted To The University Of Central Lancashire In Partial Fulfilment Of The Requirements For The Degree Of

Doctor Of Philosophy

In Collaboration With British Nuclear Fuels Plc

10th April 1999

“And the end of all our exploring

Will be to arrive where we started

And know the place for the first time”

T.S.Elliot

Abstract

Solid State laser systems are now capable of generating temporal pulses of sub-10 fs duration and facilitate the study of ultrafast phenomena in chemical, biological and physical systems. The high field intensities inherent in these pulses, means that highly non-linear processes may be observed. Studies of solution phase transient absorption and femtosecond pulse laser ablation have been undertaken and in each case an experimental apparatus has been developed.

Ultrafast pump-probe studies of room temperature solutions of 3-hydroxyflavone and a number of its derivatives have been undertaken. Measurement of transient absorption spectra attributable to the excited tautomer arising from ESIPT was observed throughout the visible wavelength range (400 - 700 nm). In cyclohexane and acetonitrile solutions, ESIPT was found to be so rapid that it was only possible to assign a time constant ≤ 35 fs to the process. In ethanol, however, a time constant of 60 fs was determined. The slower ESIPT in this solvent is attributed to the greater strength of the solute-solvent interactions. The influence of substituents in the 4' position of the phenyl ring of 3-hydroxyflavone has also been investigated and we observe unusual behaviour for a cyano substituent in polar solvents and for dimethylamino and aza-Crown substituents. We attribute this behaviour to charge transfer followed by rapid solvent re-organisation. The possibility of the formation of TICT states is also discussed.

Ultrafast laser ablation has been studied for a variety of dielectric, semiconducting and metallic substrates with emphasis on the development of the technique for rapid prototyping of micro-fluidic devices. Some fundamental observations of the ablation mechanisms and residual structures is presented along with results for prototyped devices for molecular diffusion and macro-filter applications.

Acknowledgements

I'd like to thank the following people for their valuable contributions to the undertaking of this research and the preparation of this thesis. Particular thanks go to Walter Perrie and Bob Brown for their support as my supervisory team at BNFL and UCLAN respectively. For technical and moral support on our various scientific and extra-curricular excursions I'd like to thank Xavier Poteau who was there "when it all happened" for the ultrafast chemistry at LENS and MBI. For a valuable couple of months training and support at the very beginning, I thank Penny Weavers (formally of Leeds university). For technical assistance at RAL, LENS and MBI, I thank Mike Towrie, Pavel Matousek, Paolo Foggi, Frederic Newhaas, Erik Nibbering and Oliver Duhr. For assistance with the various microscopies at BNFL, thanks to Sharon Rathbone, Walter Weaver, Dave Goddard and Andy May. For his continued persistence and enthusiasm for our micro-machined membranes, I thank Andy Alderson.

And last, but by no means least, I thank my family and, in particular, my wife for their support and patience throughout.

Index

Chapter 1 **Introduction**

- 1.1 Thesis Overview
- 1.2 Ultrashort Pulse Generation And Amplification
    - 1.2.1 Modelocking
    - 1.2.2 Solid State Femtosecond laser Sources
    - 1.2.3 Chirped Pulse Amplification
- 1.3 Femtosecond Laser Techniques
    - 1.3.1 Pulse Measurement And Characterisation
    - 1.3.2 Pulse Broadening In Optical Elements & Pulse Compression
    - 1.3.3 Non-Linear Wavelength Conversion
        - 1.3.3.1 Second Harmonic Generation
        - 1.3.3.2 White Light Continuum
- 1.4 Transient Spectroscopy In The Condensed Phase
    - 1.4.1 Experimental Techniques
    - 1.4.2 Excited State Intramolecular Proton Transfer
- 1.5 Femtosecond Laser Ablation
    - 1.5.1 Principles
    - 1.5.2 Current Literature
        - 1.5.2.1 Metals
        - 1.5.2.2 Semiconductors
        - 1.5.2.3 Dielectrics

Chapter 2 **Experimental**

2.1 The BNFL Laser System

2.2 Femtosecond Pump-Probe Spectroscopy

2.2.1 Experimental System For Dual Wavelength Kinetics

2.2.2 Experimental Observation Of White Light Continuum

2.2.3 European User Facilities

2.2.4 Data Analysis

2.3 Femtosecond Laser Ablation

2.3.1 Experimental System For Ultrashort Laser Ablation

2.3.2 Sample Preparation And Analysis

Chapter 3: **Pump-Probe Spectroscopy:**

ESIPT To Oxygen (3-Hydroxyflavone and Derivatives)

3.1 3-Hydroxyflavone

3.2 4'-Chloro-3-Hydroxyflavone

3.3 4'-Methyl-3-Hydroxyflavone

3.4 4'-Methoxy-3-Hydroxyflavone

3.5 4'-Cyano-3-Hydroxyflavone

3.6 4'-*N*, *N*-Dimethylamino-3-methoxyflavone

3.7 4'-*N*, *N*-Dimethylamino-3-hydroxyflavone

3.8 4'-(1"-Aza-4",7",10",13"-Tetraoxacyclopentadecyl)-3-Hydroxyflavone

3.9 Conclusions

Chapter 4: **Ultrashort Pulse Laser Ablation.**

4.1 Fundamental Parameters

4.1.1 Glasses

4.1.2 Semiconductors

4.1.3 Metals

4.2 Prototype Micro-mechanical Devices

4.2.1 Microchemical Contactor For Metal Ion Extraction

4.2.2 Microchemical Contactor For The Nitration Of Benzene

4.2.3 Auxetic Macro-filter

4.3 Conclusions

Appendix: Publications

1. "Femtosecond Laser Microstructuring Of Materials",

   Appl. Surf. Sci. Vol: 127-129, pp875-880 (1998).

2. "An Auxetic Filter: A Tuneable Filter Displaying Enhanced Size Selectivity Or Defouling Properties"

   Accepted *Ind. Eng. Chem. Res.* (1999).

3. "Ultrafast Measurements Of Excited State Intramolecular Proton Transfer (ESIPT) In Room Temperature Solutions Of 3-Hydroxyflavone"

   Accepted *Chem. Phys. Lett* (1999).

Chapter 1: INTRODUCTION

1.1 Thesis Overview

The last decade has witnessed significant advances in the ability to generate short pulses of radiation throughout the optical (and indeed) vuv and x-ray regions of the electromagnetic spectrum. These developments have had (and continue to have) a tremendous impact on the field of chemical dynamics[1] and high intensity light-matter interactions[2]. Fundamental questions concerning chemical reactions are now routinely studied in real-time experiments (see for example the review by Zewail[3]). Fig. 1.1.1 shows the typical timescales of some elementary physical, chemical and biological processes in the condensed phase.

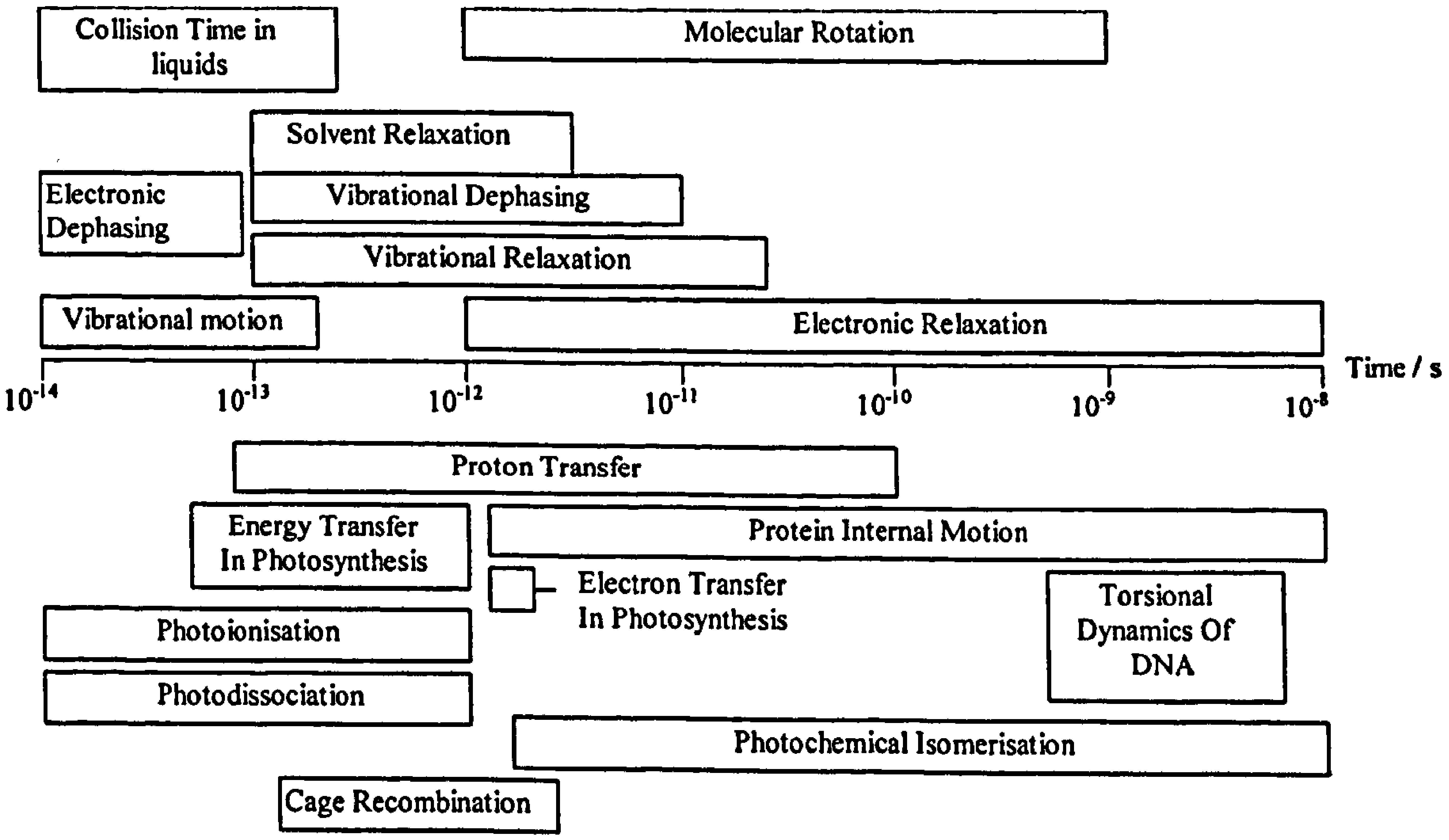

Fig. 1.1.1 Approximate time scales of elementary molecular relaxation phenomena and some chemical and biological manifestations of these phenomena[4].

The majority of chemical reactions occur in the condensed phase. This has driven a theoretical and experimental effort towards the understanding of chemical reactivity in the condensed phase at the molecular level. While the half-life of a unimolecular reaction may span from picoseconds to years, the actual time that a molecule spends traversing the potential surface from reactant to product is very short. In understanding rate processes, the most important stage of a reaction is the 'transition state,' representing the structure of the reactants [and solvent] at the point where the reaction crosses from the reactant surface to that of the product. With the emergence of laser sources in the picosecond and femtosecond range, direct "real time" studies of ultrafast dynamic processes and coherent control of reactions in the condensed and gas phases become possible.

The development of stable ultra-intense sources of sub-picosecond pulses has enabled researchers to examine the interaction of laser fields with matter for such diverse purposes as x-ray generation[5], mass spectrometry[6] and multiphoton imaging[7]. This thesis reports the development of two such femtosecond laser applications of interest to BNFL and the research interests of the Centre for Photochemistry at the University of Central Lancashire. Studies of Excited State Intramolecular Proton Transfer (ESIPT) in 3-hydroxyflavone derivatives have been undertaken at a variety of European centres as well as in house at BNFL for which a transient absorption spectrometer was developed. In addition to this, an investigation of the interaction of ultra-intense laser pulses with a variety of target materials has led to the development of a laser ablation workstation for the micro-machining of micro-fluidic devices of interest to BNFL.

The structure of the thesis has been ostensibly dictated by the nature of the research undertaken. Chapter 1 consists of this overview and a number of sections which outline relevant background information with regard to ultrashort pulse generation and amplification (Section 1.2), pulse characterisation and manipulation (Section 1.3) and sections devoted to each of the subject areas; transient spectroscopy of ESIPT (Section 1.4) and femtosecond laser ablation (Section 1.5). Chapter 2 is a discussion of the experimental conditions and techniques employed in the collection of data and is divided into three sections. Section 2.1 provides details regarding the BNFL femtosecond laser system (BMI Alpha 1000) previously installed at the Company Research Laboratories (CRL) at BNFL Springfields. Section 2.2 discusses the development at CRL of a two colour pump-probe absorption experiment and outlines the facilities used at other sites as part of the European transport and mobility for researchers (TMR) large scale facilities program. Section 2.3 discusses the development of a laser ablation workstation for rapid prototype production of micro-fluidic devices. The experimental results and discussion are presented as two separate chapters due to the disparate nature of the subject matter. Chapter 3 is concerned with the experimental results for pump-probe spectroscopy on compounds which undergo ESIPT and some other charge transfer processes. Chapter 4 presents results of femtosecond ablation experiments on a variety of substrate materials. In both cases, discussion is undertaken alongside the results and conclusions are presented at the end of the chapter in order to simplify the thesis structure. Finally, publications from the research are presented as an appendix. In all cases, references highlighted in the text are given at the end of the chapter concerned.

1.2 Ultrafast Pulse Generation And Amplification.

In this section the theory of mode-locked pulse generation is given, followed by a practical discussion of solid state ultrafast lasers and the method of chirped pulse amplification as applied to ultrashort pulses.

1.2.1 Modelocking[8,9]

The majority of devices used to generate ultrashort laser pulses rely on the technique of modelocking. In principle, modelocking entails modulation of the loss [or gain] in a laser at a frequency equal to the inverse of the time required for a pulse to travel one round trip inside the cavity. In order to generate short pulses using modelocking, the laser resonator must support a large number of longitudinal modes. Under these conditions, modulation results in the locking together of the phases of the oscillating longitudinal modes, generating a series of discrete laser pulses that are separated by the cavity round trip time.

In order to have a stable standing wave within a laser cavity it is clear that we must fulfil the condition whereby the change in phase between reflectors must be an integral multiple, n of π [i.e. the cavity length l, is an integral number of half wavelengths, λ]

$$l = \frac{n\lambda}{2} \qquad 1.2.1$$

In a free running system, these longitudinal modes will have random phases and the laser intensity will vary with time depending on the number of modes in phase at any particular time; the output is CW.

A particular mode with angular frequency $\omega_0=2\pi\nu$ (where ν is the laser frequency) will have a time variation of the electric field, E(t) at a particular position (say the output mirror), given by

$$E(t)=E_0\exp(i\omega_0 t) \qquad 1.2.2$$

Other modes will have slightly different temporal variations of the electric field. The nth mode of frequency $(\omega_0+n\Delta\omega)$ will have

$$E_n(t)=E_n\exp(i(\omega_0+n\Delta\omega)t+\phi_n) \qquad 1.2.4$$

where $\Delta\omega$ is the angular frequency separation ($\Delta\omega = 2\pi\Delta\nu = \pi c/l$) and ϕ_n is the difference in phase between the nth mode and ω_0.

The total electric field is the sum of all the $E_n(t)$ fields, so

$$E(t)=\sum_{n=0}^{N-1}E_n\exp(i(\omega_0+n\Delta\omega)t+\phi_n) \qquad 1.2.5$$

where N is the number of modes present in the laser cavity.

If we make the phase difference between the modes $\phi_n=0$ and assume that the electric field amplitudes are equal, the total electric field becomes;

$$E(t)=E_0\exp(i\omega_0 t)\begin{bmatrix}1+\exp(i\Delta\omega t)+\exp(i\Delta\omega t)^2+\ldots\\ \ldots+\exp(i\Delta\omega t)^n+\ldots\ldots+\exp(i\Delta\omega t)^{N-1}\end{bmatrix}$$

hence $$E(t)=E_0\exp(i\omega_0 t)\times\exp\left(\frac{i(N-1)\Delta\omega t}{2}\right)\left[\frac{\sin\left(\frac{N\Delta\omega t}{2}\right)}{\sin\left(\frac{\Delta\omega t}{2}\right)}\right] \qquad 1.2.6$$

The intensity of the radiation at the output mirror is of interest and is given by the product of E(t) with its complex conjugate E^*,

$$I(t)=E(t)E^*(t)=\frac{E_0^2\sin^2\left(\frac{N\Delta\omega t}{2}\right)}{\sin^2\left(\frac{\Delta\omega t}{2}\right)} \qquad 1.2.7$$

This temporal variation of intensity represents a train of modelocked pulses, emitted at a period $t_{roundtrip}=2l/c$ and of pulselength $t_0= t_{roundtrip}/N$. This is demonstrated in fig. 1.2.1.

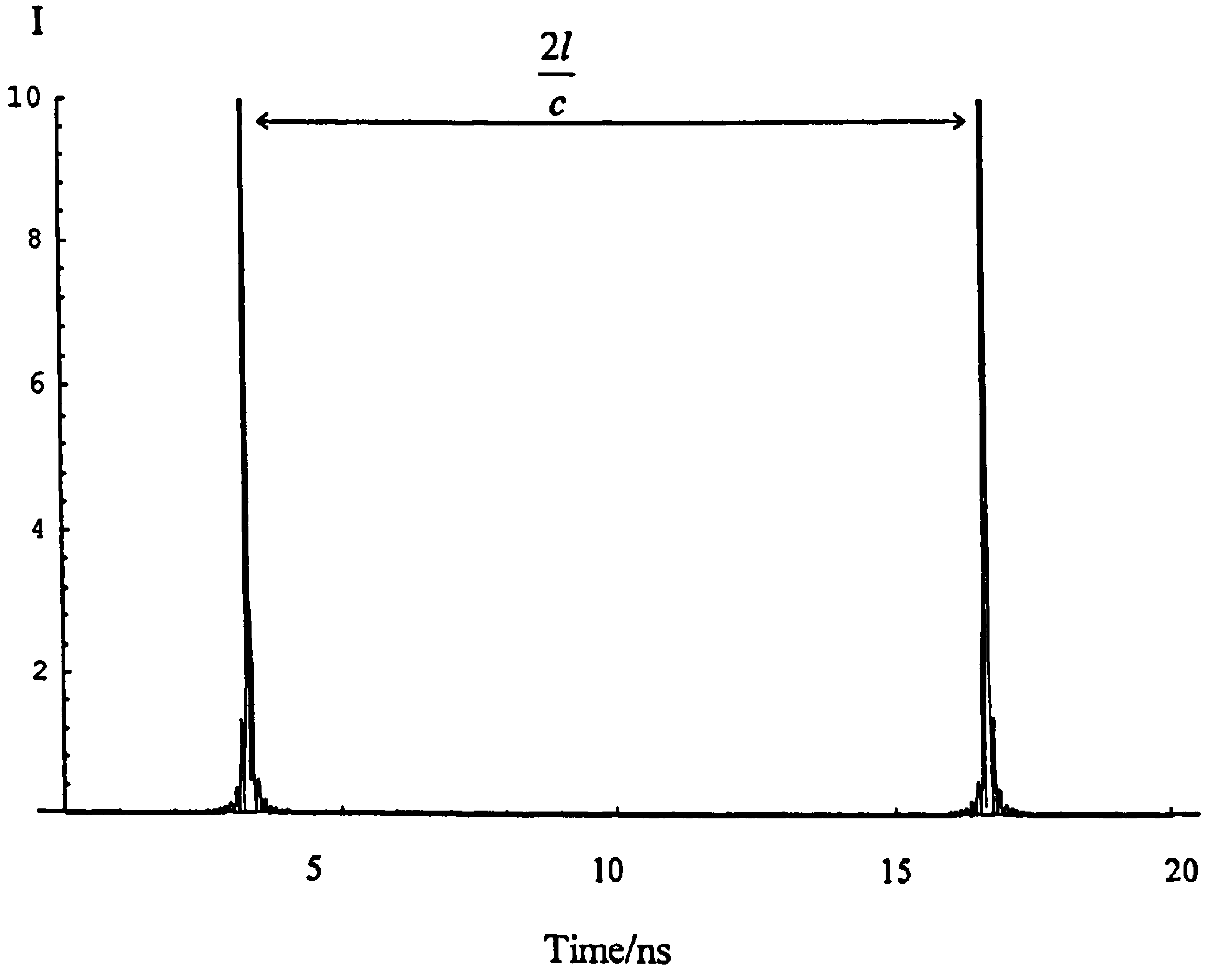

Fig.1.2.1 76MHz, 100 fs Modelocked laser pulses modelled using Eqn. 1.2.7 [corresponding to 1.3×10^5 phase locked modes and a bandwidth of $\approx$10 nm]

Clearly for ultra-short pulses it is desirable to have a large number of propagating modes in the laser cavity due to the uncertainty relation, $\Delta\nu\Delta t \approx 1$, where the number of modes is proportional to $\Delta\nu$.

Many techniques for the 'phase locking of modes' have been developed, all of which act upon the laser in basically the same manner. In order to initiate the pulse some sort of switch is modulated at precisely the rate at which the pulse oscillates between the high reflector and the output coupler of the laser cavity. Only light which passes through the switch can be amplified and since the switch is closed at all other times only one pulse circulates around the cavity. Therefore the modulation frequency must be precisely matched to the repetition rate $1/t_{roundtrip}$. An active system imposes a modulation frequency on the circulating pulse via some external reference and it is clear that timing and cavity thermal stability in such systems is critical. Passively modelocked systems, however, determine their timing from the pulse itself, automatically opening on arrival of the pulse, so that timing jitter due to, for example, a change in cavity length, is automatically compensated for by the switching mechanism [typically a saturable absorber].

A self-modelocking Ti:Sapphire laser relies on a passive mechanism to create an ultrashort pulse[10]. Intense pulses propagating through dispersive media can create perturbations in the refractive index of the medium, so called intensity dependent refractive index phenomena[11]. A Gaussian shaped pulse will undergo a lensing effect due to the difference in refractive index between the edges and the centre of the beam [Kerr lensing]. In a Ti:Sapphire laser the Kerr lens can be formed in the crystal gain medium. Normally, the laser will operate exclusively in CW mode, however by perturbing a cavity mirror, a sufficiently high intensity fluctuation can occur to produce a Kerr lens in the crystal. If the cavity is well designed an intracavity slit can then be introduced into the beam which creates higher losses for the CW beam and the modelocked beam alone propagates in the cavity. The mechanism is described in the following section.

1.2.2 Solid State Femtosecond laser Sources[12]

The last few years have brought about significant advances in ultrashort pulse laser physics[3,13,14]. The development of novel all-optical modulation techniques along with the appearance of ultra-broadbandwidth gain media [e.g. Titanium doped Sapphire] has opened a new era for femtosecond technology. Within a period of as little as five years we have witnessed the emergence and evolution of a new generation of ultrashort pulsed lasers based exclusively on solid state components. In this section I hope to provide a brief synopsis of the basic operating principles and the major performance limitations of solid state femtosecond lasers and summarise recent technological advances allowing the generation of near transform limited sub-10 fs optical pulses direct from laser oscillators.

Although picosecond optical pulses were first generated in a solid state medium [Nd:Glass] in the mid-60's, progress in ultrashort solid state pulse generation halted soon after the first pioneering experiments. The picosecond relaxation time of the saturable absorbers used for passive modelocking prevented researchers from pushing the pulse generation below the picosecond limit. Hence, attention shifted to organic dye lasers, which, as a result of their nanosecond upper-state lifetimes, were capable of actively participating in short pulse formation [gain saturation], allowing intracavity pulse shortening down to the femtosecond regime by using "slow" (picosecond)-relaxation time absorbers. Operation of femtosecond dye lasers continues to be a highly sophisticated art up to the present, mainly because of the large number of inaccessible system parameters. The demand for consistent reproducibility in laser performance could not be met until the recent development of solid state systems.

The development of all solid state laser technology has been possible by the use of the intensity induced change in the refractive index. This ultrafast "Kerr effect" can be transformed into an almost instantaneous saturable absorber effect by introducing appropriate linear optical components into the cavity. The two most successful embodiments of this general concept have been additive pulse modelocking and self [or Kerr-lens] modelocking. The effect of these passive Kerr modulators on the envelope of an electric field E(t) can [to a first approximation] be written as[12]

$$\Delta E(t)=\left(\frac{\kappa}{2}+i\phi\right)|E(t)|^2 \qquad 1.2.7$$

where, κ and ϕ measure the strengths of self-amplitude and self-phase modulation [SAM and SPM] respectively. Apart from SAM and SPM, intracavity group velocity dispersion [GVD] is a major pulse shaping effect, which is characterised by the parameter[13]

$$D=\frac{\lambda^3}{2\pi c^2}\frac{d^2n}{d\lambda^2}L.\Delta\lambda \propto \frac{d^2T_r(\lambda)}{d\lambda^2} \qquad 1.2.8$$

i.e. by the second derivative of the refractive index with respect to the wavelength [the peak of the laser wavelength spectrum]. L is the pathlength in the medium. In order to avoid a strong pulse broadening due to the interaction of a pulse carrying a positive chirp [as a consequence of ϕ>0] with normal dispersion [D>0] the intracavity GVD must be negative. GVD and SPM are discussed in detail in Sections 1.32 and 1.33 respectively.

Both additive-pulse and Kerr-lens modulators exhibit SPM coefficients that are much larger than the corresponding SAM parameters. ϕ>>κ implies that steady-state pulse formation is dominated by a soliton-like interplay between SPM and negative GVD. Hence, assuming; i) a linear variation of $T_r(\lambda)$ as a function of λ, i.e. $D(\lambda)=D(\lambda_0)$;

ii) evenly distributed SPM and GVD in the cavity; and iii) a sufficiently broadband gain medium; the pulse duration τ is expected to obey the soliton formula[12]

$$\tau \approx \tau_s = \frac{3.53|D|}{\phi W} \qquad 1.2.9$$

where W is the intracavity pulse energy. The soliton like behaviour of the steady state pulse has been verified in a self-modelocked fused silica prism controlled Ti:Sapphire laser down to the 10 fs regime[15]. Although κ does not significantly effect τ, optimised SAM is essential for stabilising the pulse against noise and perturbations as well as preventing the emergence of a narrow-band CW background, which tends to co-exist with the modelocked pulse in soliton-like systems which have not been optimised.

In femtosecond solid state lasers the pulse duration can be reduced by decreasing the magnitude of intracavity GVD until one of the assumptions or approximations [i-iii] leading to equation 1.2.9 fails. The most severe limitation in practical broadband lasers originates from the increasing deviation of $T_r(\lambda)$ from a linear function as the oscillation spectrum broadens. The lowest order contribution to this deviation is referred to as third order dispersion [TOD]. As the pulse duration decreases and/or the pulse energy increases the separate action of GVD and SPM increasingly modulates the pulse parameters [duration, bandwidth] as the pulse circulates in the cavity. This modulation can be regarded as a periodic perturbation of the ideal soliton-like pulse and manifests itself in an additional term $\Delta\tau=\alpha(z)\phi W$, where α depends on the position of the pulse in the cavity. Other potential limitations to pulse shortening are the gain and resonator bandwidths.

Until recently broadband negative GVD has been introduced in short pulse oscillators almost exclusively by a pair of Brewster-angled prisms. The layout of a prism controlled Ti:Sapphire laser [similar to the Mira 900F] is shown in fig. 1.2.2. To obtain the shortest pulse duration, the circulating pulse is coupled out of the cavity after traversing the dispersive delay line (double pass through P_1 and P_2) and an extracavity prism pair allows control of GVD outside the laser cavity. Since the prism pair also introduces a high order dispersion, careful selection of prism material is required if the pulse duration is to be minimised. For Ti:Sapphire, the optimum prism material is fused silica, which by minimising TOD in the cavity allows generation of near transform limited pulses of 11-12 fs in duration around 800 nm. Recent investigations[16] predicted a vanishing of the TOD component in Ti:Sapphire/Fused Silica system at 850 nm. In fact, tuning to this wavelength, extremely broad, symmetric bandwidth mode-locked spectra can be generated [symmetry is lost as a result of residual TOD].

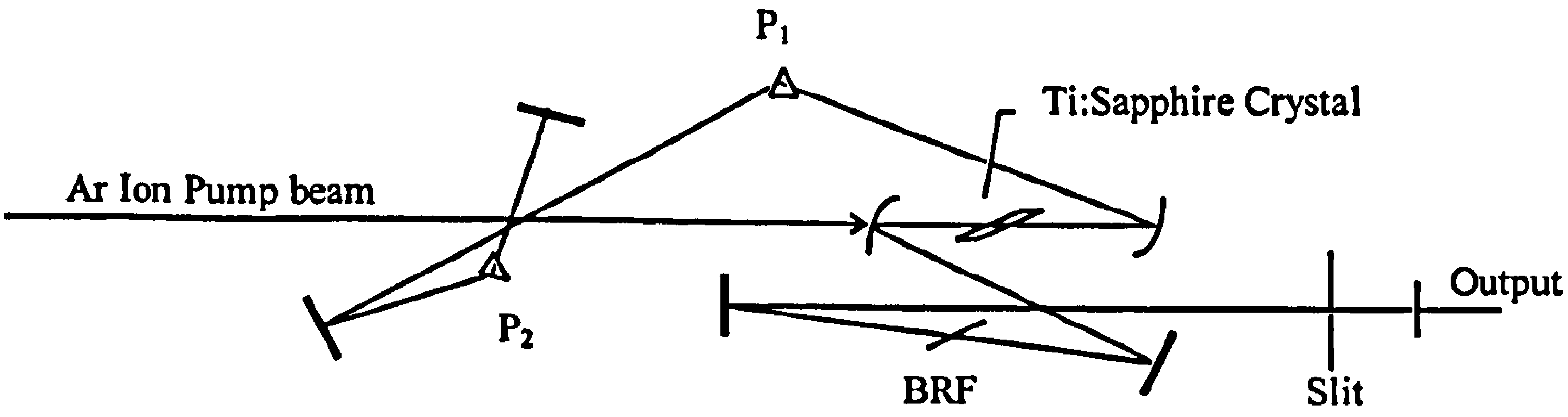

Fig. 1.2.2 Schematic showing the Ti:Sapphire Laser; P_1 and P_2 are the prisms. BRF; Birefringent filter, for frequency tuneability.

Recently a novel technique has been proposed and demonstrated for intracavity dispersion control[17]. Broadband, high-reflectivity multilayer dielectric mirrors have been developed with their multi-layer period modulated during the evaporation process. This modulation not only broadens the high-reflectivity band-width but, more importantly, offers the possibility of engineering the dispersion properties of the mirrors. As a first embodiment of this general concept, chirped dielectric mirrors exhibiting a nearly the shortest pulse duration, the circulating pulse is coupled out of the cavity after traversing the dispersive delay line (double pass through P_1 and P_2) and an extracavity prism pair allows control of GVD outside the laser cavity. Since the prism pair also introduces a high order dispersion, careful selection of prism material is required if the pulse duration is to be minimised. For Ti:Sapphire, the optimum prism material is fused silica, which by minimising TOD in the cavity allows generation of near transform limited pulses of 11-12 fs in duration around 800 nm. Recent investigations[16] predicted a vanishing of the TOD component in Ti:Sapphire/Fused Silica system at 850 nm. In fact, tuning to this wavelength, extremely broad, symmetric bandwidth mode-locked spectra can be generated [symmetry is lost as a result of residual TOD].

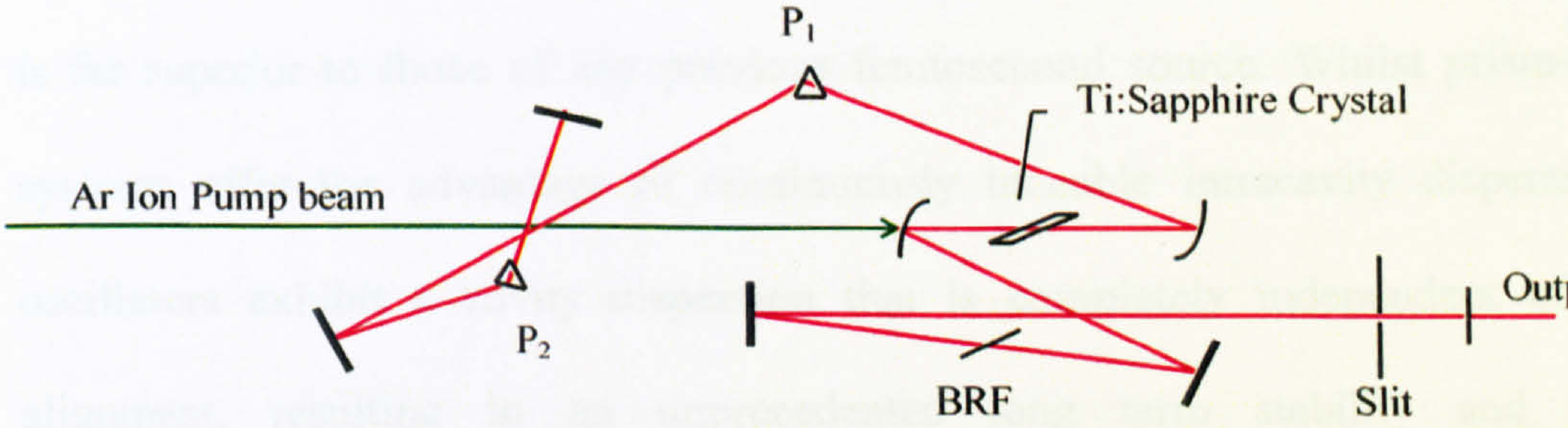

Fig. 1.2.2 Schematic showing the Ti:Sapphire Laser; P_1 and P_2 are the prisms. BRF; Birefringent filter, for frequency tuneability.

Recently a novel technique has been proposed and demonstrated for intracavity dispersion control[17]. Broadband, high-reflectivity multilayer dielectric mirrors have been developed with their multi-layer period modulated during the evaporation process. This modulation not only broadens the high-reflectivity band-width but, more importantly, offers the possibility of engineering the dispersion properties of the mirrors. As a first embodiment of this general concept, chirped dielectric mirrors exhibiting a nearly constant [high order dispersion free] GVD over the wavelength range 720-890 nm have been fabricated, where the wavelength range can be easily shifted to match the emission spectra of other lasers by simply rescaling the layer thicknesses. Using these mirrors, compact mirror dispersion controlled [MDC] self-mode-locked oscillators can be constructed. TOD is significantly reduced in this system as compared to its prism controlled counterpart. It is possible to generate highly stable near transform limited sub-10 fs $Sech^2$-shaped pulses.

In strong contrast to dye lasers, ultra-short pulse formation in solid state lasers using Kerr-modulators can be described and controlled in terms of a few uniquely defined and experimentally accessible parameters [κ, ϕ, D and W]. As a result, the reliability of femtosecond solid-state lasers and the reproducibility of their performance is far superior to those of any previous femtosecond source. Whilst prism-controlled systems offer the advantage of continuously tuneable intracavity dispersion, MDC oscillators exhibit a cavity dispersion that is completely independent of resonator alignment, resulting in an unprecedented long term stability and day-to-day reproducibility of femtosecond pulse parameters. These advances are expected to give rise to further expansion of ultrafast techniques into new areas of science and technology[18].

1.2.3 Chirped Pulse Regenerative Amplification

The continued development of tuneable, solid-state laser materials has resulted in the production of ever more powerful and efficient ultrashort pulse laser sources. Titanium-doped sapphire [Ti:Al_2O_3] is an excellent example; tuneable from 680 to 1100nm, it has a much broader range than that of traditional organic dyes previously used in femtosecond oscillators and amplifiers. In addition to this unprecedented tuneability, the energy storage characteristics of these materials make it possible to produce compact, high peak power lasers. The challenge in solid-state laser design comes in extracting this energy in an ultrashort pulse. For a 100 fs pulse, the peak power exceeds Gigawatts for energies as low as a few millijoules. Consequently the intensity that can develop in a amplifier chain can quickly lead to self-focusing and catastrophic damage to optical components. This limitation can be overcome by temporally stretching the pulse prior to amplification, for example a 100 fs pulse can be stretched by a factor of 10000 to around 1 ns, with standard size optical components. The stretched pulse can then be safely amplified. Because the peak power has been reduced [by the same factor as above], the pulse can extract significant energy from the amplifiers without risk of catastrophic damage from self focusing. After amplification, the pulse is recompressed back to its Fourier transform limit. This technique is known as chirped pulse amplification and recompression [CPA][19,20,21,22].

The basic scheme for CPA is given in fig 1.2.3. Initially, a short pulse is generated in, for example, a self-modelocked Ti:Sapphire laser. The pulse is then temporally stretched [chirped] using a grating arrangement to introduce positive group velocity dispersion [GVD] (GVD and Pulse re-compression are discussed in Section 1.3.2). The amount of stretch introduced depends on the level of amplification that is required. If the final pulse energy is in the 100 mJ range, a stretched pulse-width of 1 ns is desirable. For a few millijoules, the pulse needs only be stretched to a few hundred picoseconds. Below a millijoule, 10's of picoseconds is sufficient.

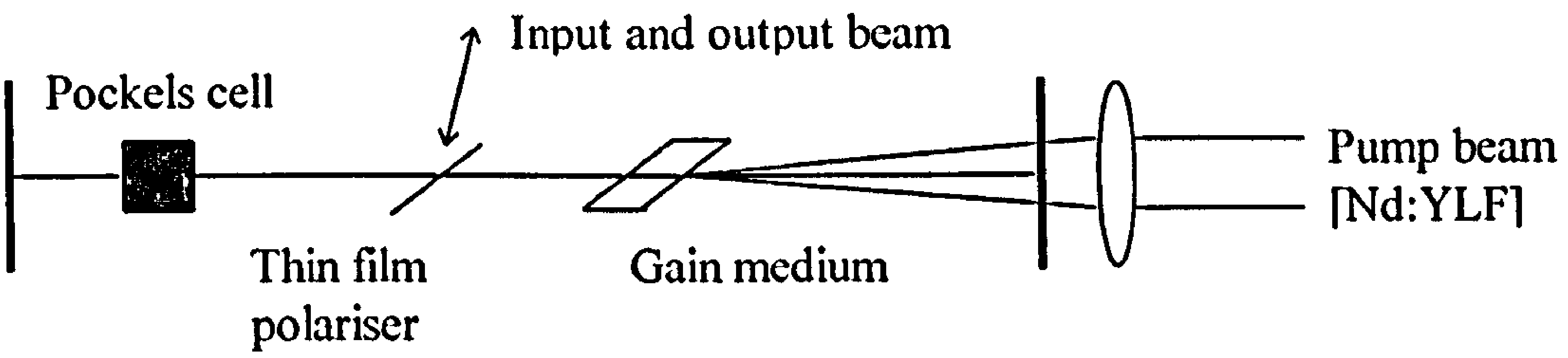

Fig. 1.2.3 Schematic of regenerative amplifier cavity.

After stretching any number of amplification stages can be introduced providing the damage threshold is not exceeded in the chain. For millijoule systems a regenerative amplifier scheme is typically employed. This configuration consists of a high quality [high Q] optical resonator that contains the gain medium, a Pockels cell and a thin film polariser [Fig. 1.2.3]. The Pockels cell is oriented to give a static quarter wave birefringence that allows an incident pulse to make one pass in the cavity before exiting. With a pulse inside the cavity, a quarter wave voltage is applied to the cell and the net birefringence is now a half wave per pass and the pulse is trapped in the cavity. The pulse is allowed to make as many round trips as necessary to fully deplete the gain. At this point, a further quarter wave voltage is applied to the Pockels cell and the pulse is forced to exit the cavity (cavity dumped).

Clearly, one of the advantages of this type of configuration is that any arbitrary number of passes is possible in the cavity, thereby only small single pass gains are required. This means that for laser pumped gain media, the pump fluence can be kept relatively low, and the crystal can therefore tolerate an imperfect pump beam profile much more readily. Extraction efficiencies can be very high [20-30% have been demonstrated][21]. Also the configuration is easy to align. Because an optical cavity is used, the amplified beam has the spatial mode of the resonator, acting as a built in spatial filter ensuring high beam quality.

The limiting factor for regenerative amplification is that broadband intracavity elements are required. In general, the more passes that are made in the cavity the broader the bandwidth requirement, so that spectral narrowing is minimised. After amplification the pulse is recompressed using an arrangement similar to that of the stretcher, this time introducing negative dispersion.

In conclusion, chirped pulse regenerative amplification and recompression allows the efficient amplification of ultrashort pulses to peak powers far in excess of those available in conventional laser systems.

1.3 Femtosecond Laser Techniques

This section aims to present various techniques which are core to the development of ultrafast spectroscopic methods at BNFL. Initially correlation techniques for pulse measurement will be described, subsequently the factors affecting pulse length in optical elements are considered and methods for frequency conversion are discussed.

1.3.1 Measurement Of Ultrashort Pulses

The problem of measuring the duration of modelocked ultrashort pulses is of great practical and theoretical interest[23]. Since the fastest conventional photodiodes have response times of $\sim 1\times 10^{-11}$ s, it is impossible to use these optical detectors to measure 100 fs (1×10^{-13} s) pulses. A number of techniques developed for this purpose all take advantage of some non-linear process to obtain a spatial autocorrelation trace of the optical pulse intensity. The measurement of a pulse of 100 fs is thus replaced with measuring the spatial extent of an autocorrelation trace of length ~30 μm, which is a relatively simple task.

The most commonly used autocorrelators consist of a Michelson interferometer [see fig. 1.3.1] with its output focused into a second harmonic generation [SHG] crystal[24]. The resulting second harmonic signal is measured by a 'slow' photodiode. Given that a second harmonic signal will only be generated if two photons arrive simultaneously in the non-linear crystal, as one pulse is scanned through a replica of itself [in space] the signal measured by the photodiode will vary due to the amount of pulse overlap 'seen' by the SHG crystal.

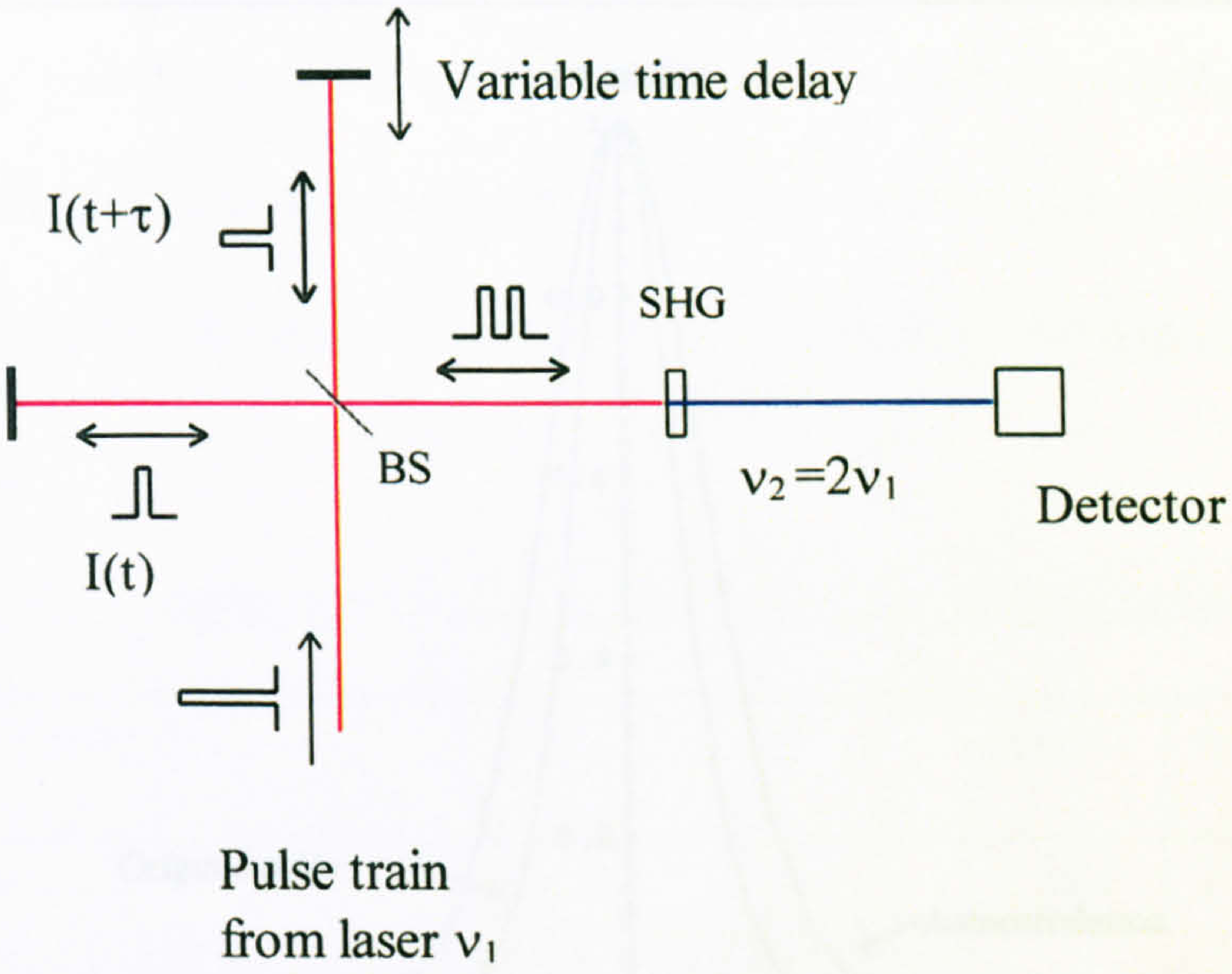

Fig 1.3.1 Schematic for autocorrelation measurement; SHG, second harmonic crystal.

The autocorrelation function can be expressed, both with and without background [with and without SHG components arising from a single pulse replica] and as fast [interferometric] or slow depending on the accuracy of measuring the spatial increment on the delay line.

Mathematically the 2nd order background free slow autocorrelation is given as[24]

$$g_0^2(\tau)=\frac{\int_{-\infty}^{\infty} I(t)I(t+\tau)dt}{\int_{-\infty}^{\infty} I(t)dt} \tag{1.3.1}$$

where I(t) is the pulse intensity and τ is the time delay between pulse duplicates.

In this case the uncertainty in the measurement of τ is such that certain oscillatory terms containing information about time dependent phase shifts [chirping] average to zero. A $\mathrm{Sech}^2(t/\Delta t)$ pulse profile is shown with its associated autocorrelation function in fig. 1.3.2

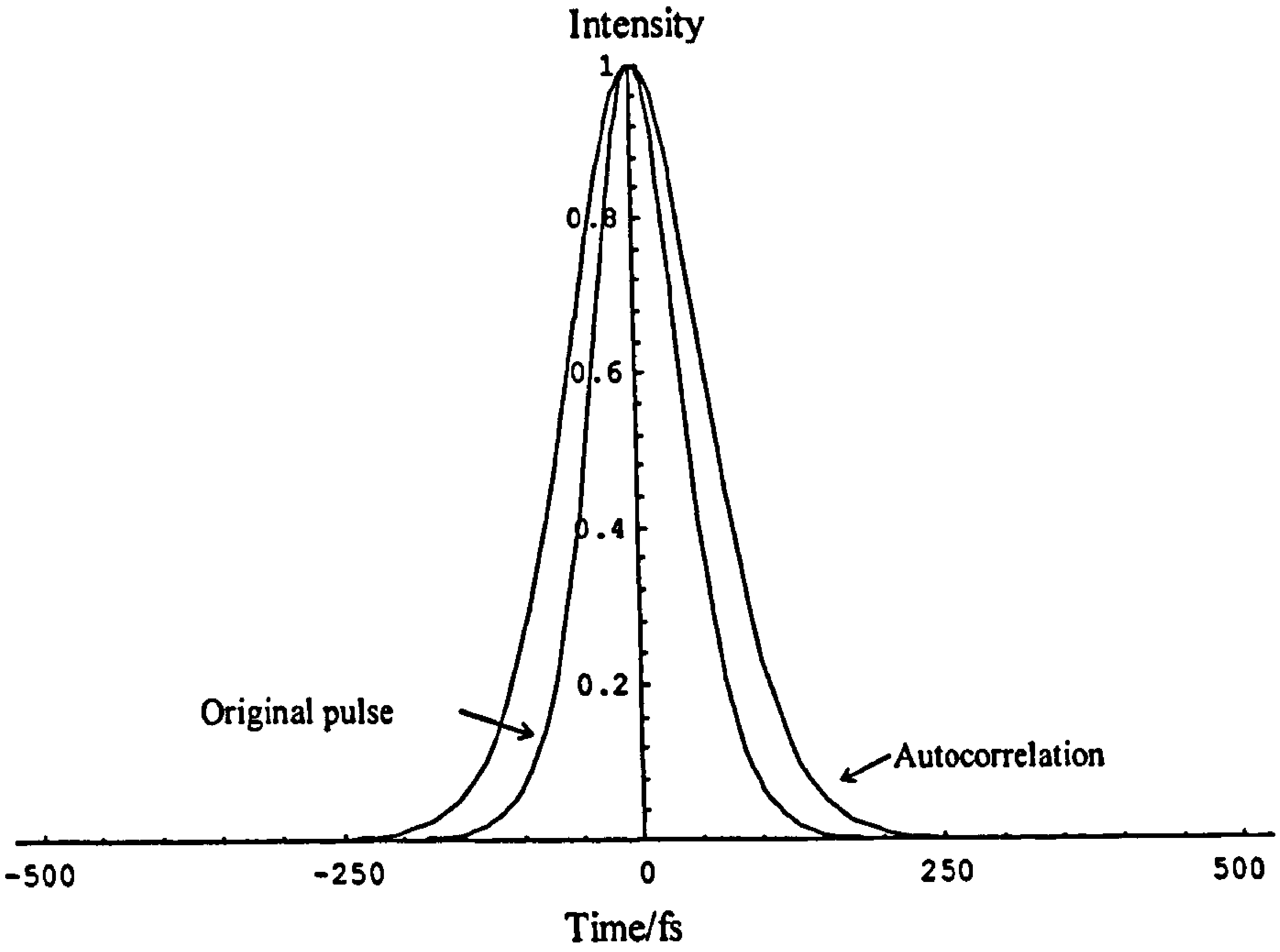

Fig.1.3.2 Sech^2(t/Δt) pulse with its associated autocorrelation function (Δt=100 fs).

The interferometric autocorrelation is given as[24]

$$g_B^2 = 1 + \frac{2\int_{-\infty}^{\infty} E^3(t)E(t+\tau)dt + 2\int_{-\infty}^{\infty} E(t)E^3(t+\tau) + 3\int_{-\infty}^{\infty} E^2(t)E^2(t+\tau)dt}{\int_{-\infty}^{\infty} E^4(t)dt} \qquad 1.3.2$$

where E(t) is the electric field envelope. Note that in this case the measurement is not background free, and information is gained at the expense of signal to noise ratio.

It is clear that the second order autocorrelation function is intrinsically symmetrical and cannot be used to obtain the pulse shape unless the pulse is known from other information to be symmetric itself. Higher order correlation functions can give definite information on pulse shape and have been used to characterise pulses for various laser types. The vast majority of work, however, uses the autocorrelation function to provide an estimate of the pulse duration based on a number of assumptions. If the pulse is transform limited, the FWHM of I(t), Δt, is directly related to the FWHM of $g^2{}_0(\tau)$, Δτ, through a numerical factor dependent on the shape of I(t) (estimated by taking the Fourier transform of the spectrum). Table 1.3.1collects together the numerical factors along with the time bandwidth products for transform-limited pulses of some given shapes. It is common practice to obtain Δt by selecting the appropriate factor and dividing Δτ by it.

Table 1.3.1 Autocorrelation correction factors for various pulse shapes

Pulse Shape	I(t)	ΔνΔt	Δτ/Δt
Square	$\left(\frac{-\Delta t}{2} \le t \le \frac{\Delta t}{2}\right)$	0.886	1
Gaussian	$\exp\left\{-\frac{t^2}{\Delta t^2}\right\}$	0.441	1.414
Sech^2	$\mathrm{sech}^2\left\{\frac{t}{\Delta t}\right\}$	0.315	1.5427
Lorentzian	$\frac{1}{\left\{1+ t^2/\Delta t^2\right\}}$	0.221	2
Single Sided Exponential	$\exp\left\{-\frac{1}{\Delta t}t\right\}(t>0)$	0.11	2

At CRL, we have two autocorrelation methods available to measure the pulse width characteristics of both the seed laser oscillator [Mira 900] and the regenerative amplifier [Alpha 1000]. The experimental methods differ due to the difference in the frequency of pulse generation in each system; the Mira operates at 76 MHz and the regenerative amplifier at 1 kHz. For the Mira, a CW autocorrelator [Femtoscope] has been used to measure the pulse width. This consists of a Michelson interferometer as described above with the addition of a shaker assembly to continuously scan the time delay. The frequency of the shaker is chosen (~30 Hz) so that the laser frequency appears essentially CW to it. The Femtoscope is useful for pulses in the frequency range 10 kHz - 100 MHz. Below this frequency minimum the autocorrelation is no longer 'real-time' [the autocorrelation will no longer be produced from a single scan by the shaker].

For measurement of pulses from the regenerative amplifier, a single shot autocorrelator is used [BMI, AM-100][25]. The AM-100 relies on transforming the temporal profile of the pulse duplicates into spatial data, which can be imaged on a CCD camera. A diagram of the AM-100 is given below [fig. 1.3.4].

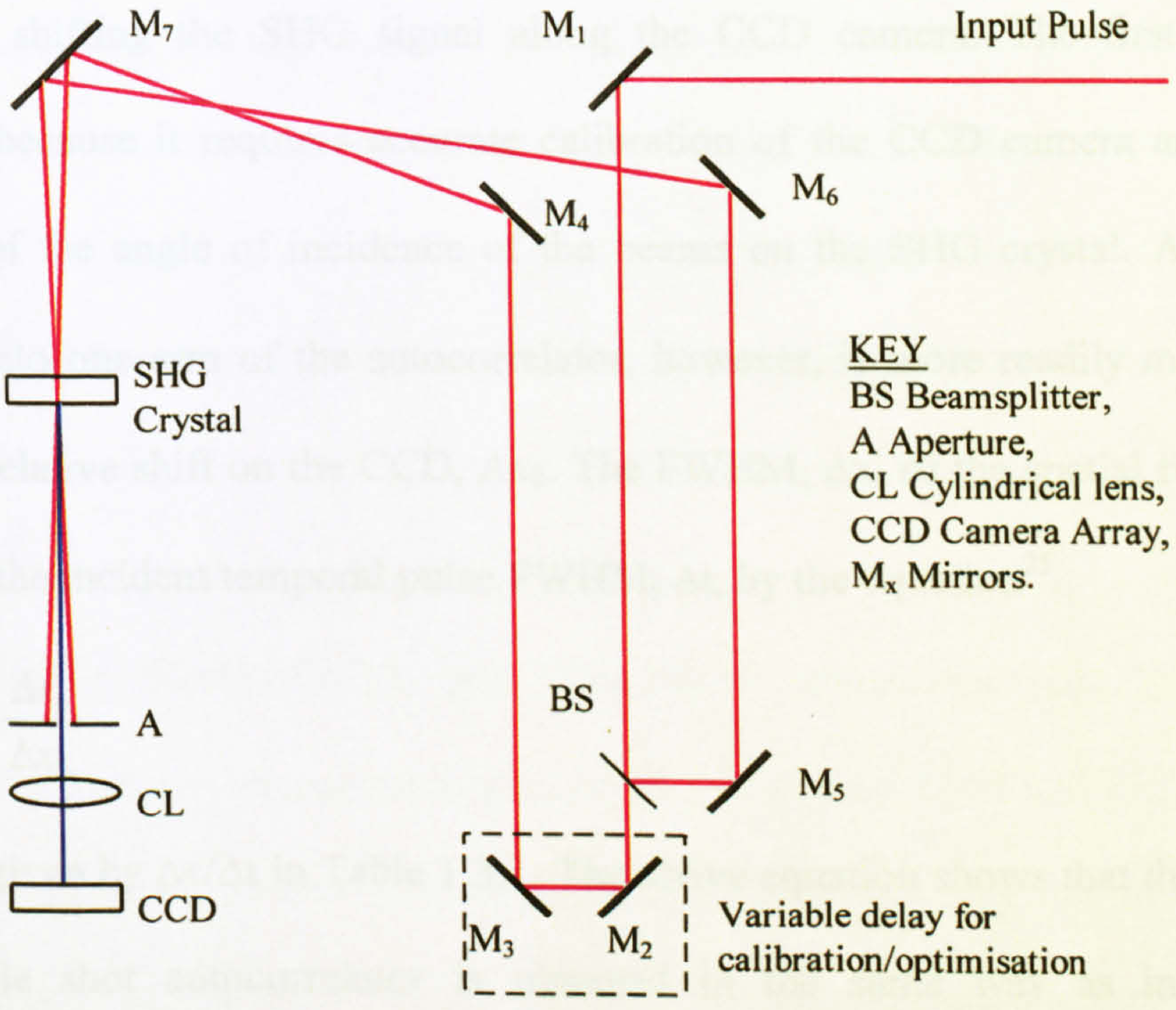

Fig. 1.3.4. Single shot autocorrelator.

The laser output is directed onto M_1 and split into two replica pulses at the beamsplitter, BS. The two arms are directed via $M_{2\text{-}4}$ and $M_{5\text{-}6}$, respectively onto M_7 and in turn onto the SHG crystal, where a second harmonic signal is generated and focused using the cylindrical lens onto the CCD camera. The resulting signal is processed and viewed on an oscilloscope. The two pulses incident on the SHG crystal are not collinear so the second harmonic signal is only produced when the pulses overlap both temporally and spatially. The spatial intensity distribution of the second harmonic signal is related to the incident radiation intensity such that[25]

$$S(x) \propto \int I(t+\tau) I(t-\tau) dt \qquad 1.3.3$$

therefore, one may obtain the same information as with a classical autocorrelator in a single pulse. The absolute measurement of the pulse width can be obtained either by measuring the exact spatial width of the pulse or by introducing a delay into one beam and thereby shifting the SHG signal along the CCD camera. The first method is undesirable because it requires accurate calibration of the CCD camera and an exact knowledge of the angle of incidence of the beams on the SHG crystal. A delay, Δt_0, introduced into one arm of the autocorrelator, however, is more readily measured and relates to a relative shift on the CCD, Δx_0. The FWHM, Δx, of the spatial function S(x) is related to the incident temporal pulse FWHM, Δt, by the equation[25]

$$\Delta t = K^{-1} . \Delta x \frac{\Delta t_0}{\Delta x_0} \qquad 1.3.4$$

where K is given by $\Delta\tau/\Delta t$ in Table 1.3.1. The above equation shows that the calibration of the single shot autocorrelator is obtained in the same way as in a classical autocorrelator leading to a simple measurement method.

We have found that to obtain reliable results, uniform illumination of the SHG crystal is essential and great care must be taken when setting up the apparatus, as misalignment or spatial inhomogenieties can effect the measurement.

1.3.2 Pulse Broadening In Optical Elements And Pulse Compression

For pulses propagating in optical materials, significant pulse broadening can occur due to dispersion in optical materials, thereby reducing the temporal resolution of ultrafast instruments. Such broadening is well studied for prisms, gratings and bulk media[26].

The generation and amplification of femtosecond laser pulses require that one compensate for the pulse broadening effects. In addition to the effects of optical elements in the cavity, significant pulse distortions have been observed for high-intensity pulses travelling through air. Three major broadening mechanisms have received significant attention, namely group-velocity dispersion [GVD], third-order dispersion [TOD] and self-phase modulation [SPM]. In addition to these effects, a fourth phenomenon pulse front distortion [PFD] in lenses has been shown to have a significant effect on pulse length.

Whilst the effects of GVD and TOD can be compensated for, by passing the light through a suitable arrangement of gratings and prisms, SPM and PFD can lead to irreversible temporal broadening. In considering these effects, one can treat the optical pulse as a wave packet with central frequency ω_0 propagating through a dispersive medium. A useful way to discuss this is in terms of the Taylor series expansion of the phase[13]

$$\phi(\omega) \approx \phi(\omega_0) + \left(\frac{\partial\phi}{\partial\omega}\right)_{\omega_0}(\omega-\omega_0) + \tfrac{1}{2}\left(\frac{\partial^2\phi}{\partial\omega^2}\right)_{\omega_0}(\omega-\omega_0)^2 + \tfrac{1}{6}\left(\frac{\partial^3\phi}{\partial\omega^3}\right)_{\omega_0}(\omega-\omega_0)^3 + \ldots.. \qquad 1.3.5$$

The first term in this Taylor-series expansion represents the propagation of the central frequency of the pulse. The linear term is related to the inverse of the group velocity of the pulse and is responsible for PFD[27]. The quadratic term refers to the change in shape of the pulse as it travels through the medium and gives rise to GVD. The phase term of an input pulse in the transform limit, due to GVD in dispersive media is given by[13]

$$\frac{d^2\phi_m}{d\omega^2} = \frac{\lambda^3}{2\pi c^2}\frac{d^2 n}{d\lambda^2}x \qquad 1.3.6$$

where c is the speed of light in vacuum and x is the distance propagated in the medium.

Thus GVD induced by propagation through a dispersive medium results in a time-dependent frequency sweep or 'chirp' in the laser pulse. In most materials, the lower-frequency components travel faster than the higher-frequency components, resulting in increased pulse length. This means that the broadening due to GVD depends upon the initial laser pulse width. For example, if a 75 fs pulse is passed through a 25 cm cell of water, the output pulse is broadened to 410 fs. However, a 1 ps pulse would exhibit essentially no distortion passing through the same cell.

The cubic term in Equation 1.3.5 causes complex pulse broadening and reshaping and is referred to as third-order dispersion [TOD]. TOD only becomes significant at large bandwidths and intensities and so must be considered in ultrashort regimes. The phase term for TOD in bulk media is given by[28]

$$\frac{d^3\phi_m}{d\omega^3} = -\frac{\lambda^4}{2\pi^2 c^3}\left(\frac{3d^2 n}{d\lambda^2} + \frac{\lambda d^3 n}{d\lambda^3}\right)x \qquad 1.3.7$$

Two schemes are commonly used to compensate for GVD; a four prism arrangement proposed by Fork et al[28], and a grating pair proposed by Treacy[29]. Both schemes introduce a negative GVD thereby slowing the red pulse components and allowing the blue pulse components to 'catch-up'. The phase terms for GVD and TOD for a double prism pair [Eqn. 1.3.8 and 1.3.9] and a double grating pair [Eqn. 1.3.10 and 1.3.11] are given below[28,30];

$$\frac{d^2\phi_p}{d\omega^2}=\frac{\lambda^3}{2\pi^2c^2}\frac{d^2P}{d\lambda^2} \qquad \text{GVD} \quad 1.3.8$$

$$\frac{d^3\phi_p}{d\omega^3}=\frac{-\lambda^4}{4\pi^2c^3}\left(3\frac{d^2P}{d\lambda^2}+\lambda\frac{d^3P}{d\lambda^3}\right) \qquad \text{TOD} \quad 1.3.9$$

$$\frac{d^2\phi_g}{d\omega^2}=\frac{\lambda^3 l_g}{\pi c^2 d^2}\left[1+\left(\frac{\lambda}{d}-\sin\gamma\right)^2\right]^{-3/2} \qquad \text{GVD} \quad 1.3.10$$

$$\frac{d^3\phi_g}{d\omega^3}=\frac{-d^2\phi_g}{d\omega^2}\frac{6\pi\lambda}{c}\frac{\left(1+\frac{\lambda}{d}\sin\gamma-\sin^2\gamma\right)}{\left[1-\left(\frac{\lambda}{d}-\sin\gamma\right)^2\right]} \qquad \text{TOD} \quad 1.3.11$$

Lenses present a special case for analysis; not only are GVD, TOD and SPM factors in determining the pulse width but the linear term in equation 1.3.5 also becomes significant. For simplicity we will assume that TOD and SPM are insignificant in this case (in a practical situation this is probably true for pulses >100 fs). The most significant effect (especially in the UV and for large aperture lenses) is pulse front distortion [PFD]. In this case, the pulse front [defined as the surface coinciding with the peak of the pulse] moves with group velocity through a lens and is delayed with respect to the phase front. This is peculiar to the lens case as the path length in the media of the lens is dependent on radius. A parabolic delay is therefore seen across the diameter of the lens. It is clear that GVD is also radially dependent, however, as we will see, the effect on pulse width is relatively insignificant. It is interesting to note that PFD has been, for the most part, ignored as a source of pulse distortion in experiments. This is for the most part because autocorrelation techniques are not capable of detecting spatial beam distortions (the autocorrelation for two interacting parabolic wave fronts is the same as that for a plane wave front).

Following the proof of Bor[31]; to calculate the propagation time we begin with Fermat's principle. Stating;

$$L_1 + nL_2 + L_3 + L_4 = nD_0 + f \qquad 1.3.12$$

Where, f = Focal length of the lens.

$L_{1,2,3,4}$=Pathlengths defined in fig.

and D_0 =The central thickness of the lens.

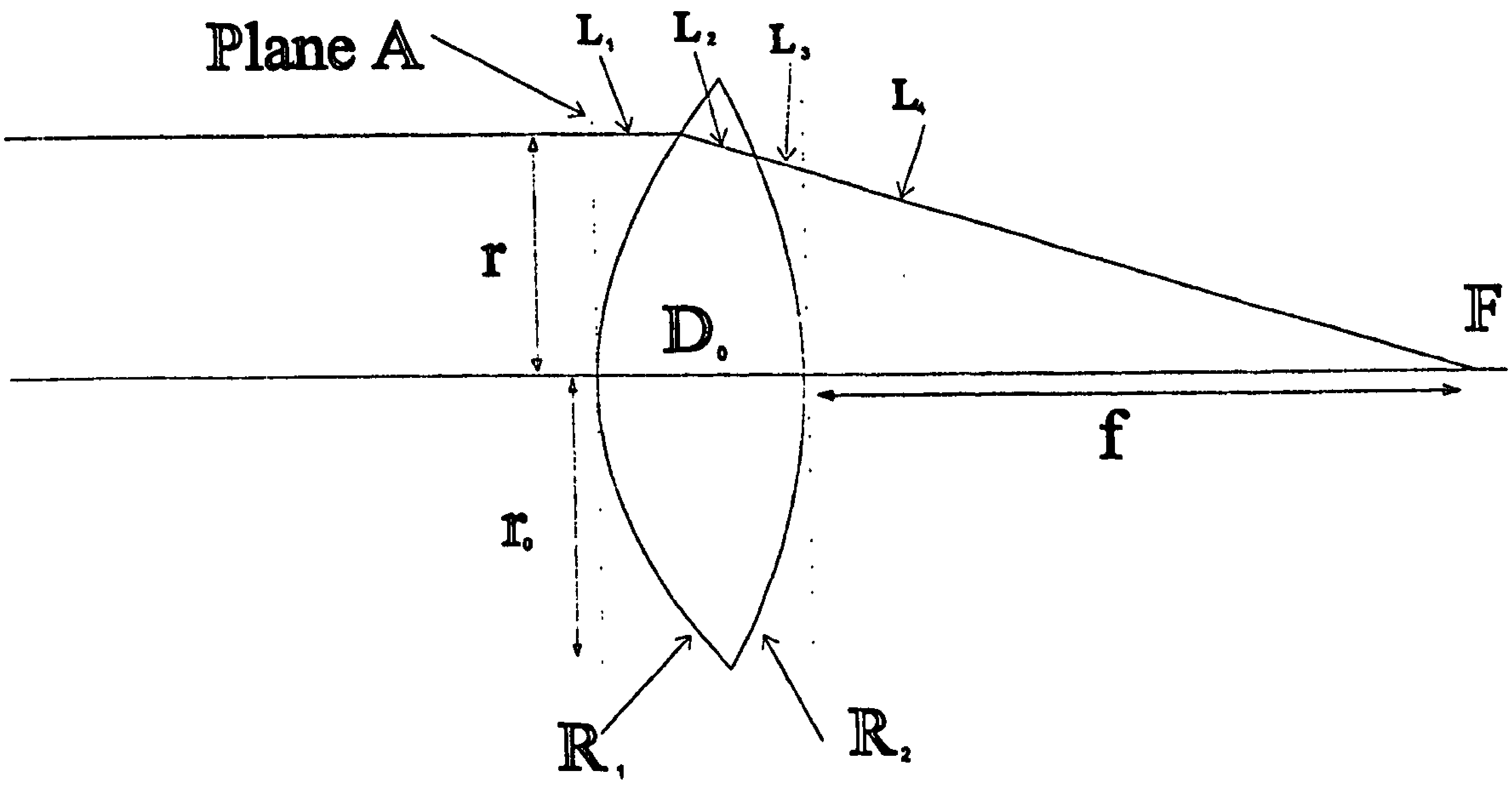

fig. 1.3.4 Basic geometry for geometrical optical derivation of PFD in simple lenses.

A pulse is propagating in a medium with group velocity given by $v_g = d\omega/dk$, where ω is the angular frequency and k is the wave-vector. In this case it is far more convenient to define group velocity in terms of wavelength in vacuum λ and refractive index, n(λ). Now the group velocity is expressed as;

$$v_g = \frac{c}{\left(n - \lambda \frac{dn}{d\lambda}\right)} \qquad 1.3.13$$

The propagation time T(r) of a plane wave from plane A to the focal point, F, can be given as;

$$T(r) = \frac{L_1 + L_3 + L_4}{c} + \frac{L_2}{c}\left(n - \lambda\frac{dn}{d\lambda}\right) \qquad 1.3.14$$

In the paraxial approximation we obtain for D_0, L_2 and f;

$$\begin{aligned} D_0 &= \frac{r_0^2}{2}\left(\frac{1}{R_1} - \frac{1}{R_2}\right) \\ L_2 &= D_0 - \frac{r^2}{2}\left(\frac{1}{R_1} - \frac{1}{R_2}\right) \\ \frac{1}{f} &= (n-1)\left(\frac{1}{R_1} - \frac{1}{R_2}\right) \end{aligned} \qquad 1.3.15$$

where r and r_0 are the input radii of an arbitrary and the marginal ray respectively and R_1 and R_2 are the radii of curvature of the lens surfaces.

Now substituting the expressions 1.3.15 into 1.3.14 and using the definition of the focal length given by Fermat's theorem we obtain the propagation time;

$$T(r) = \frac{f}{c} + \frac{D_0}{c}\left(n - \lambda\frac{dn}{d\lambda}\right) + \frac{r^2}{2c}\left(\frac{1}{R_1} - \frac{1}{R_2}\right)\lambda\frac{dn}{d\lambda} \qquad 1.3.16$$

Substituting the expression for D_0 into Eqn. 1.3.16 and taking $r = r_0$ we obtain the propagation time for the marginal ray;

$$T_m = T(r = r_0) = \frac{f}{c} + \frac{D_0 n}{c} \qquad 1.3.17$$

Since the optical pathlength from Plane A to F is nD_0+f it follows that the marginal ray propagates with the phase velocity.

The temporal delay ΔT(r) between the group and phase fronts for a ray at arbitrary radius r is therefore;

$$\Delta T(r) = T(r) - T_m = \frac{r_0^2 - r^2}{2c}\left(\frac{1}{R_1} - \frac{1}{R_2}\right)\left(-\lambda\frac{dn}{d\lambda}\right)$$
$$\Delta T(r) = \frac{r_0^2 - r^2}{2cf(n-1)}\left(-\lambda\frac{dn}{d\lambda}\right) \qquad 1.3.18$$

For materials of practical interest, λdn/dλ has a negative value in the spectral range of transparency. It is instructive to compare the relative magnitudes of PFD and GVD in lens designs. As we have already seen the magnitude of the induced GVD is given by equation 1.3.6. A more practical form of this equation is given by

$$\Delta\tau_{GVD} = \frac{\lambda}{c}\frac{d^2n}{d\lambda^2}\Delta\lambda x \qquad 1.3.19$$

where the usual symbolic conventions are observed. We can then substitute the axial thickness;

$$x = \frac{r_0^2}{2f(n-1)} \qquad 1.3.20$$

and assuming a transform limited sech^2 pulse to give;

$$\Delta\tau_{GVD} = \frac{\lambda^3}{c^2}\frac{d^2n}{d\lambda^2}\frac{r_0^2}{f(n-1)}\frac{0.16}{\Delta\tau_{pulse}} \qquad 1.3.21$$

where $\Delta\tau_{pulse}$ is the full width at half maximum [FWHM] of the pulse. Since PFD and GVD are both functions of the f number [f#] of the lens they can be plotted graphically for comparison. Fig. 1.3.5 shows PFD and GVD calculated for a single element fused silica lens at 790 nm with a pulse width chosen at 80 fs (in this case the lens diameter is fixed at 25 mm). It is clear that the pulse stretch is several orders of magnitude more significant in PFD than in GVD. This is likely to remain true even for real lenses which will be thicker in order to maintain a workable edge thickness. The comparison is all the more significant when we consider that the initial pulse duration and stretch due to GVD add in quadrature.

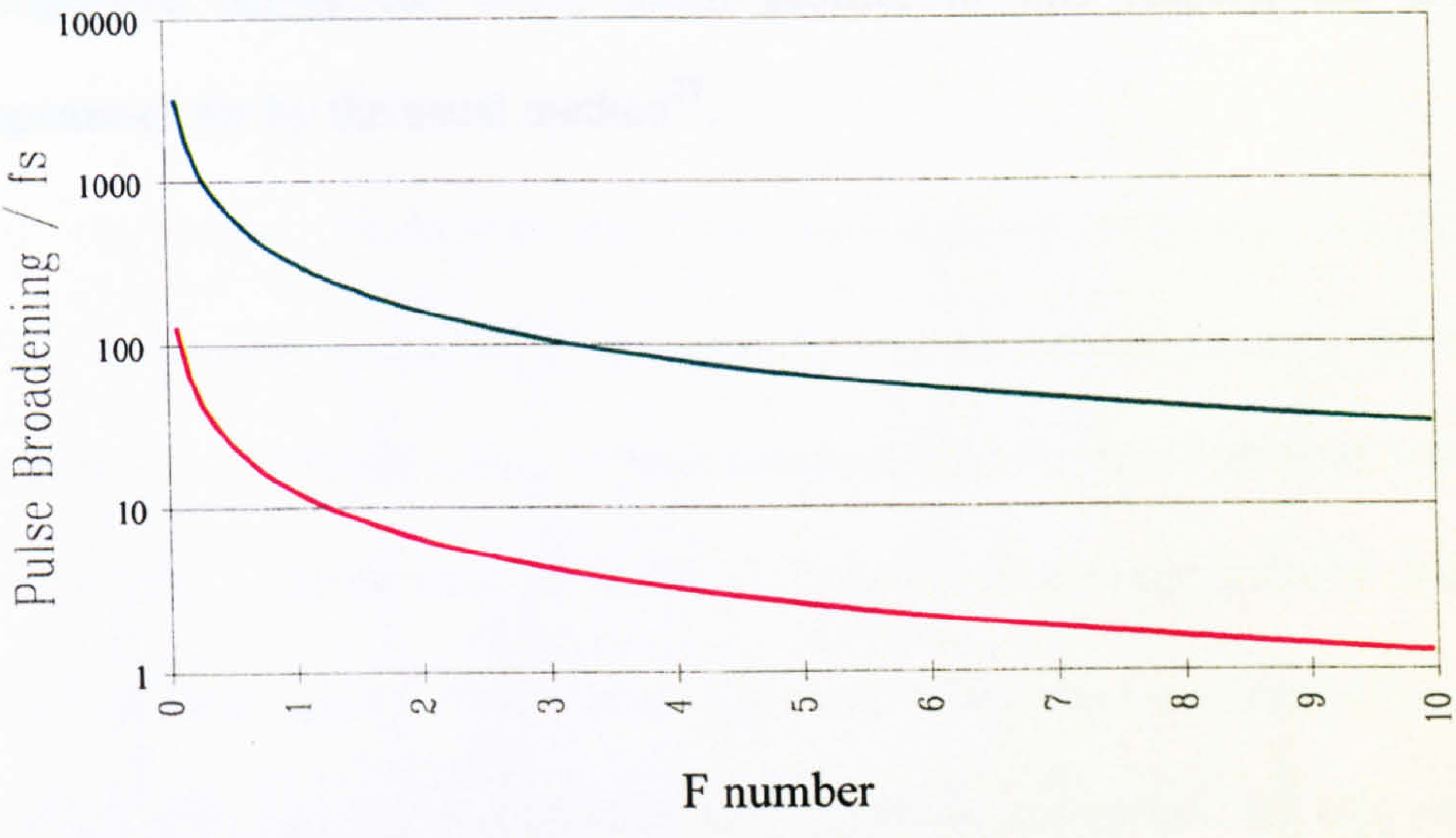

Fig. 1.3.5 Effect of F# on PFD and GVD in an arbitrarily chosen fused silica singlet lens ($\lambda = 790$ nm, $r_0 = 12.5$ mm).

The ratio of PFD to GVD is then given by

$$\xi = \frac{\sqrt{\tau^2_{pulse} + \Delta\tau_{GVD}} - \tau_{pulse}}{\Delta\tau_{PFD}} \qquad 1.3.22$$

Using the same data as before and fixing the f# = 2, the ratio of GVD to PTD is $\xi \sim 1/1015$.

As both these phenomena are radially dependent they cannot be corrected in the usual manner (as different radial components require different compensations), but they can be minimised by an astute choice of lens (using only large f#) and by taking into account the spatial profile of the beam. For example, a Gaussian intensity distribution will minimise the effect on the FWHM but will suffer a slight change to its rising edge at the focus. A "top hat" (radially homogeneous) profile, conversely, will have a FWHM equal to the sum of the original FWHM and $\Delta\tau_{PFD}$. However, it has been shown that by replacing singlet lenses with achromatic lenses PFD can be eliminated and GVD homogenised across the entire beam profile; in this respect, the GVD can be compensated for by the usual method[27].

1.3.3 Non-Linear Wavelength Conversion

Application of femtosecond laser pulses to spectroscopy in a wide range of molecules requires the ability to generate wavelength tuneable pulses to excite specific electronic or vibrational states. Whilst solid-state femtosecond sources are intrinsically tuneable over a limited bandwidth, this is typically in the near infrared. However, peak intensities generated by these sources are compatible with non-linear optical techniques by which their outputs can be frequency up/down converted. By this means broadly tuneable, coherent femtosecond sources are now available from the vacuum ultraviolet to far-infrared to address an increasing array of applications. For the purpose of this project, the most appropriate methods for wavelength conversion were Second Harmonic Generation and White Light Continuum (or Supercontinuum) generation. I cover each subject in turn.

1.3.3.1 Second Harmonic Generation

The first experiment in non-linear optics[32] consisted of generating the second harmonic (347 nm) of a ruby laser beam (694 nm) that was focused in a quartz crystal. The conversion efficiency of this first experiment (~ 10^{-8} %) has been improved to a point where ~ 30 % conversion may be observed in a single pass through a few centimetres of a non-linear crystal[8].

Second harmonic generation is a special case of sum frequency generation ($\nu_3 = \nu_1+\nu_2$) where two photons of the same frequency ($\nu_1=\nu_2$) interact to form a signal photon at twice the initial frequency ($\nu_3 = 2\nu_1$). The intensity of the generated second harmonic assuming an undepleted pump regime is given by[33]

$$I_{2\omega} = 2\omega^2 d_{ijk}^2 \left(\frac{\mu\mu_o}{\varepsilon\varepsilon_o}\right)^{3/2} I^2(\omega) \left\{\frac{2\sin\left(\Delta kL/2\right)}{\Delta kL}\right\}^2 \qquad 1.3.23$$

where ω is the angular frequency (2πν), d is the non-linear susceptibility tensor and Δk represents the relation[33]

$$\Delta k = k^{2\omega} - 2k^{\omega} = \frac{4\pi}{\lambda}\left[n^{2\omega} - n^{\omega}\right] \qquad 1.3.24$$

where n, represents the refractive index at ω and 2ω. If $\Delta k \neq 0$ then the generated second harmonic will propagate with a different phase velocity to the fundamental and destructive interference will occur between SHG light generated at different points in the crystal. The coherence length is the maximum crystal length useful for producing second harmonic power (i.e. when $\sin(\Delta k/L)=1$) and is given by[33]

$$l_c = \frac{\pi}{\Delta k} = \frac{\lambda}{4\left[n^{2\omega} - n^{\omega}\right]} \qquad 1.3.25$$

It is clear that we need to phase match co-linear beams in a non-linear crystal to maximise relation 1.3.25. Typically $n^{2\omega} > n^{\omega}$ due to normal dispersion, hence the most effective method of phase matching is to exploit the birefringence of non-linear crystals.

In anisotropic materials there are two normal modes of propagation for each frequency. These waves are orthogonally polarised and travel at different phase velocities. In uniaxial crystals, for example, one of these waves, called the ordinary wave, sees a constant index of refraction, n_o independent of its direction of propagation. The second wave, sees a refractive index $n_e(\theta)$ which is dependent on its direction of propagation. The angle θ describes the direction of propagation relative to one of the principal axes of the medium. The limits of the extraordinary index are n_o for $\theta = 0$ and n_e for $\theta = 90°$. Since the non-linear susceptibility is a tensor and can couple waves of orthogonal polarisation, it is possible to mix ordinary and extraordinary waves in an anisotropic medium and achieve the phase matching conditions given above.

There are two types of phase matching. Type I refers to the situation where the pump beams are linearly polarised (either o+o=e or e+e=o (where o and e are ordinary and extra-ordinary rays respectively) and is the preferred form for SHG). Type II corresponds to a situation where the pump is in a superposition of orthogonal polarisation's (o+e=o or e+o=e and is typically used for sum frequency generation). The phase matching angle for SHG in uniaxial crystals (single axis of symmetry which coincides with the optical axis) is given by[33],

$$\sin^2\theta_m = \frac{\left(n^e_{2\omega}\right)^2}{\left(n^o_{\omega}\right)^2}\left[\frac{\left(n^o_{2\omega}\right)^2-\left(n^o_{\omega}\right)^2}{\left(n^o_{2\omega}\right)^2-\left(n^e_{2\omega}\right)^2}\right] \quad \text{for o+o=e phase matching.} \qquad 1.3.26$$

$$\sin^2\theta_m = \frac{\left(n^e_{\omega}\right)^2}{\left(n^o_{2\omega}\right)^2}\left[\frac{\left(n^o_{2\omega}\right)^2-\left(n^o_{\omega}\right)^2}{\left(n^e_{\omega}\right)^2-\left(n^o_{\omega}\right)^2}\right] \quad \text{for e+e=o phase matching.} \qquad 1.3.27$$

Experimentally we used a crystal of beta Barium Borate (BBO, β-BaB_2O_4) to generate tuneable wavelengths in the region 425 - 375 nm. BBO is a non-linear crystal with a combination of unique features; wide transparency and phase matching angles, a large non-linear coefficient , high damage threshold and excellent optical homogeneity. The phase matching angle for type I SHG in BBO is given as a function of fundamental wavelength in fig. 1.3.6 calculated from expression 1.3.26 and the refractive indices given by[33]

$$\begin{aligned} n_o^2 &= 2.7405+\frac{.0184}{\left(\lambda^2-0.0179\right)}-0.0155\lambda^2 \\ n_e^2 &= 2.3730+\frac{.0128}{\left(\lambda^2-0.0156\right)}-0.0044\lambda^2 \end{aligned} \qquad 1.3.28$$

The calculated phase matching angle for frequency doubling the harmonic at 800 nm (the peak of the laser output in its tuning range) is 29.0713°. The BBO crystal is cut specifically for this angle and doubling for other wavelengths is then achieved by careful tuning of the laser beam incidence angle.

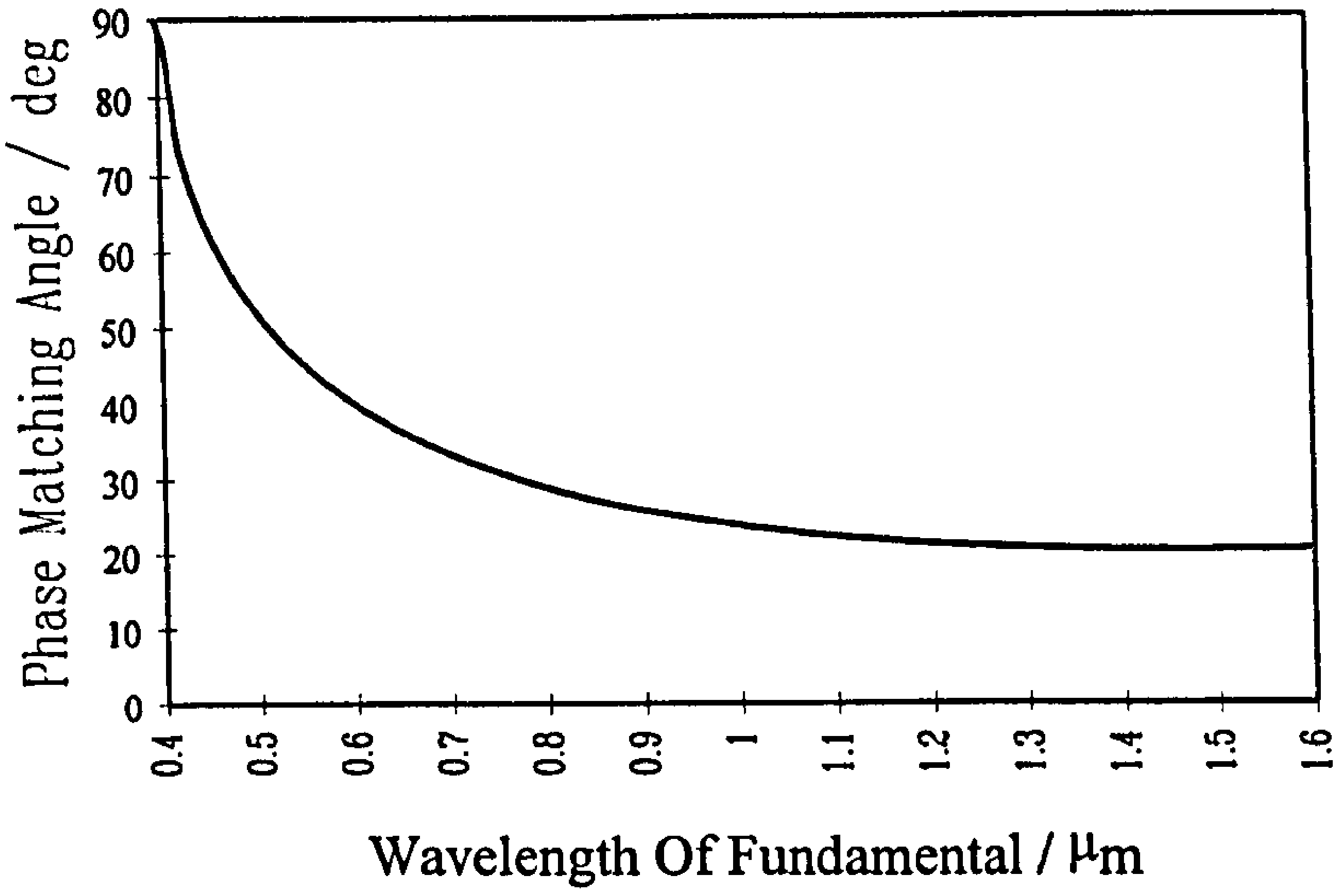

Fig.1.3.6 Phase matching angle as a function of fundamental wavelength for BBO.

For ultrashort pulses the quasi-cw approximation can no longer be applied and pulse propagation effects must be considered. In general, the interacting pulses will travel with different group velocities and over a certain distance they will no longer physically overlap reducing the conversion efficiency. The critical distance over which the interacting pulses clearly separate is given by[33]

$$L_c = \left| \frac{v_{g\omega} v_{g2\omega}}{v_{g\omega} - v_{g2\omega}} \right| \tau \qquad 1.3.29$$

where τ is the pulse width and ν denotes the group velocities given by

$$v_{ga} = c\left(n_a + \omega_a \left(\frac{\partial n}{\partial \omega} \right)_{\omega = \omega_a} \right)^{-1} \qquad 1.3.30$$

Here α denotes the appropriate field, ω or 2ω. For the situation of SHG at 800 nm with an 80 fs pulse, the critical thickness is $L_c = 259.1$ μm.

1.3.3.2 White Light Continuum Generation

Intense picosecond/femtosecond pulses propagating in non-linear media can produce frequency broadened output beams with a nearly 'white' spectrum, known as a supercontinuum (SC) or white light continuum (WLC)[34]. WLC formation has been observed in a wide variety of media; liquids [H_2O, D_2O, ethylene glycol, phosphoric acid], solids [quartz, glass, calcite, NaCl, CaF_2] and gases [Xe, Ar]. The observed WLC is correlated with self-focusing and self-trapping of filaments[35]. The threshold[36] for WLC is thought to be media independent and is of the order 10^{11} Wcm^{-2}. Various processes are believed to be responsible for continuum generation. Whenever an intense laser pulse propagates through a medium, it changes the refractive index, which in turn changes the phase, amplitude, and frequency of the incident laser pulse. A phase change can cause a frequency sweep within the pulse envelope. This process is termed Self-Phase Modulation [SPM]. Non-degenerate four wave mixing [FWM] usually occurs simultaneously with the SPM process[37]. Photons at the laser frequency parametrically generate photons to be emitted at Stokes and anti-Stokes frequencies in an angular pattern due to the required phase matching condition. When a coherent vibrational mode is excited by a laser, stimulated Raman scattering [SRS] occurs. SRS is an important process that competes and couples with SPM. The interference between SRS and SPM causes a change in the emission spectrum resulting in stimulated Raman scattering cross phase modulation [SRS-XPM]. A process similar to SRS-XPM occurs when an intense laser pulse propagates in a medium possessing a large second and third order non-linear susceptibility. Both second harmonic generation and SPM occur and can be coupled together. The interference between SHG and SPM alters the emission spectrum and is known as second harmonic generation cross-phase modulation [SHG-XPM]. A process closely related to XPM, induced phase modulation [IPM], occurs when a weak pulse at a different frequency propagates through a disrupted medium whose refractive index is changed by an intense laser pulse. The phase of the weak optical field can be modulated by the time variation of the refractive index originating from the primary, intense pulse.

All the proposed models have difficulties in explaining WLC. Moreover, none of them is universal enough to explain the common characteristics observed in such a variety of media. For example SPM as a source of WLC predicts a spectral broadening smaller than observed and fails to explain the spatial properties of WLC and accompanying ring emission. Under conditions where SPM plays a more prominent role than self-focusing and propagation effects, such as WLC generated in a short interaction length by femtosecond pulses, the observed spectrum is independent of emission angle and retains the directional properties of the pump beam. An accurate model of WLC should not depend on the spectroscopic details of the media and must fully explain the spatial properties of the phenomenon. However, a simple model for self-phase modulation should provide us with at least a feel for the phenomenon[34].

Following the arguments of Yariv[8], a sufficiently intense laser pulse can induce a significant change in refractive index of a medium. This in turn can affect beam propagation, a self action phenomenon. In this instance the refractive index is given by

$$n = n_0 + n_2 I(t) \tag{1.3.31}$$

where n_2 is the intensity dependent refractive index, which is dependent on the 3rd order non-linear susceptibility. All systems possess a non-linear refractive index. For $n_2>0$, an intense pulse with, for example, a Gaussian transverse intensity profile will produce a refractive index change, ∂n, given by

$$\partial n = n_2 E^2(t) \qquad 1.3.32$$

which is clearly a maximum at the most intense part of the pulse. This will produce a lensing effect referred to as self-focusing. Spectrally, a time varying phase shift [SPM] occurs given by

$$\Delta\phi = \frac{\partial n \omega z}{c} \qquad 1.3.33$$

As the time derivative of the phase of the wave is the angular frequency of the wave, the phase shift leads to a frequency shift with respect to the central laser frequency ω_0

$$\omega - \omega_0 = -\frac{\partial \Delta\phi}{\partial t} = -\frac{\omega}{c} z n_2 \frac{\partial I(t)}{\partial t} \qquad 1.3.34$$

If n_2 is positive the pulse sees an up chirp, a positive frequency sweep. Since the intensity varies throughout the pulse envelope, the various parts of the pulse undergo different phase shifts leading to a frequency chirp which is directly proportional to the distance travelled in the medium. This means that the pulse is spectrally broadened with a frequency sweep but its electric field envelope remains unchanged. This is shown pictorially in fig. 1.3.6.

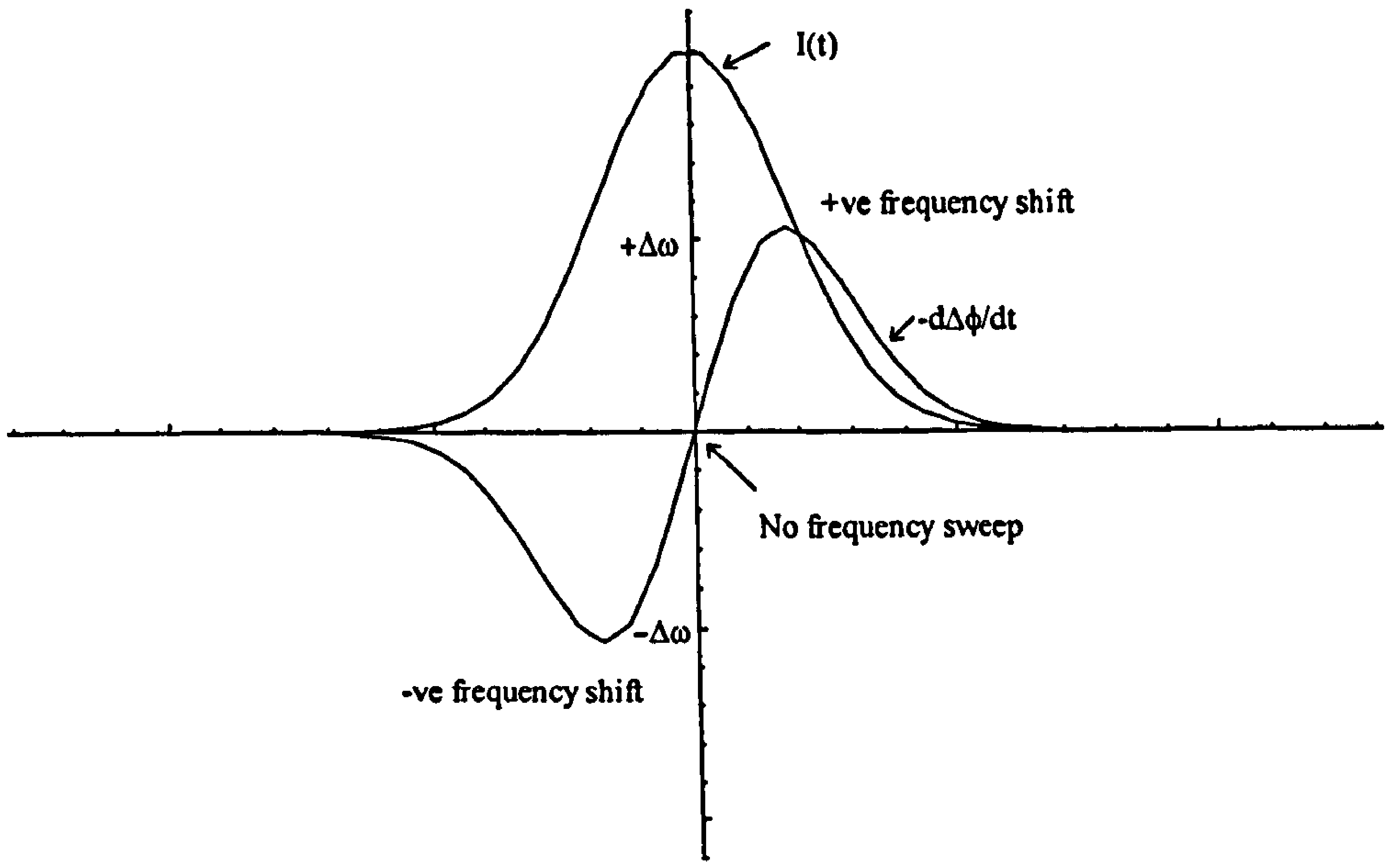

Fig.1.3.6 Gaussian pulse and its associated frequency sweep due to SPM.

To find the total frequency excursion due to SPM we assume a Gaussian pulse profile

$$I(t) = I_0 \exp-\left(\frac{t}{\Delta t}\right)^2 \qquad 1.3.35$$

where Δt is the full width at half maximum. It is clear that the maximum periods of frequency excursion occur for times ±Δt. From this we find that the total angular frequency excursion Δω is given by

$$\Delta\omega = 2(\omega - \omega_0) = \frac{4\omega_0 z n_2 I_0}{c\Delta t}\exp(-1) \qquad 1.3.36$$

and hence

$$\Delta\nu = 1.472 \ \frac{z n_2 I_0}{\lambda_0 \Delta t} \qquad 1.3.37$$

where ν is the optical frequency, λ_0 the central laser wavelength and z the pathlength in the medium. The maximum frequency shift indicates the following points;

- The frequency excursion is inversely proportional to the input pulse duration (Δt). Clearly the shorter the incoming pulse the greater the spread of generated frequencies.
- The spectral broadening is proportional to n_2. The supercontinuum generation can be enhanced by increasing the non-linear refractive index.
- The spectral broadening is linearly proportional to pulse amplitude I_0.
- Spectral broadening is proportional to λ_0 and z.

For example a pulse from a Ti:Sapphire laser [800 nm, 100 fs, 10μJ] incident on a 1 cm thick fused silica window [$n_2 = 3.2\times10^{-16}$ cm^2W^{-1}] with a spot size of 100 μm [corresponding to an area of ~3.14×10^{-4} cm^2], will generate a frequency excursion of 19000 GHz [~633cm^{-1}, ~40.5nm]. This is in agreement with experimental results published by Alfano for frequency generation due primarily to SPM in fused silica[16].

It is clear that SPM alone cannot predict the huge frequency excursion observed [300-1000 nm typically]. In most practical situations, however, the action of self focusing will significantly increase the peak intensities within the media and under the correct circumstances 'trap' the focus so that it travels through the medium [self-trapping]. A far broader spectrum can be observed due to an increased apparent interaction volume. With the additional complexity of four wave mixing, stimulated Raman Scattering and [in $\chi^{(2)}$ media] SHG, it is clear that complex and highly unstable broad spectra are obtainable as the various processes compete and interfere with one another.

For pump-probe spectroscopy it is clear that we must develop a method for continuum generation that is both highly stable and reproducible on a day-to-day basis. A large body of work has been presented in the literature on this subject but many of the experimental parameters are omitted. However, it is clear that a method of supercontinuum generation which is dominated by SPM is required. Experimental investigation of WLC generation is given in Chapter 2.

1.4 Transient Spectroscopy In The Condensed Phase

In this section I aim to describe the main experimental techniques and principles of transient spectroscopy, followed by a brief literature review of Excited State Intramolecular Proton Transfer (ESIPT) processes as studied on the ultrafast time-scale (typically < 1 ps) for some relevant molecules.

1.4.1 Experimental Techniques

Transient absorption spectroscopy is probably the simplest form of pump-probe spectroscopy, yet it is a powerful technique used by many researchers, principally due to its versatility and simplicity. It has been used to study a number of important photochemical and photo-physical processes in the condensed phase[38,1], for example photo-dissociation and recombination[39,40], optical bleaching and recovery, vibrational relaxation[41], solvation and charge transfer [i.e. electron and proton transfer][42].

In order to record the transient absorption of a spectroscopically unknown molecule it is necessary to measure the optical density change due to the pump irradiance with both time [kinetics] and wavelength [spectra]. For spectral measurements the change in optical density is recorded at fixed time delays by varying the wavelength; this may be achieved by changing the probe wavelength for each successive measurement or by probing with a spectrum of wavelengths using an optical multi-channel analyser[43].

Transient kinetic experiments involve measuring the change in optical density at fixed wavelengths while varying the probe delay[43]. For brevity I will restrict myself to a discussion of transient absorption kinetics, as many of the features of this technique are common to the measurement of transient spectra.

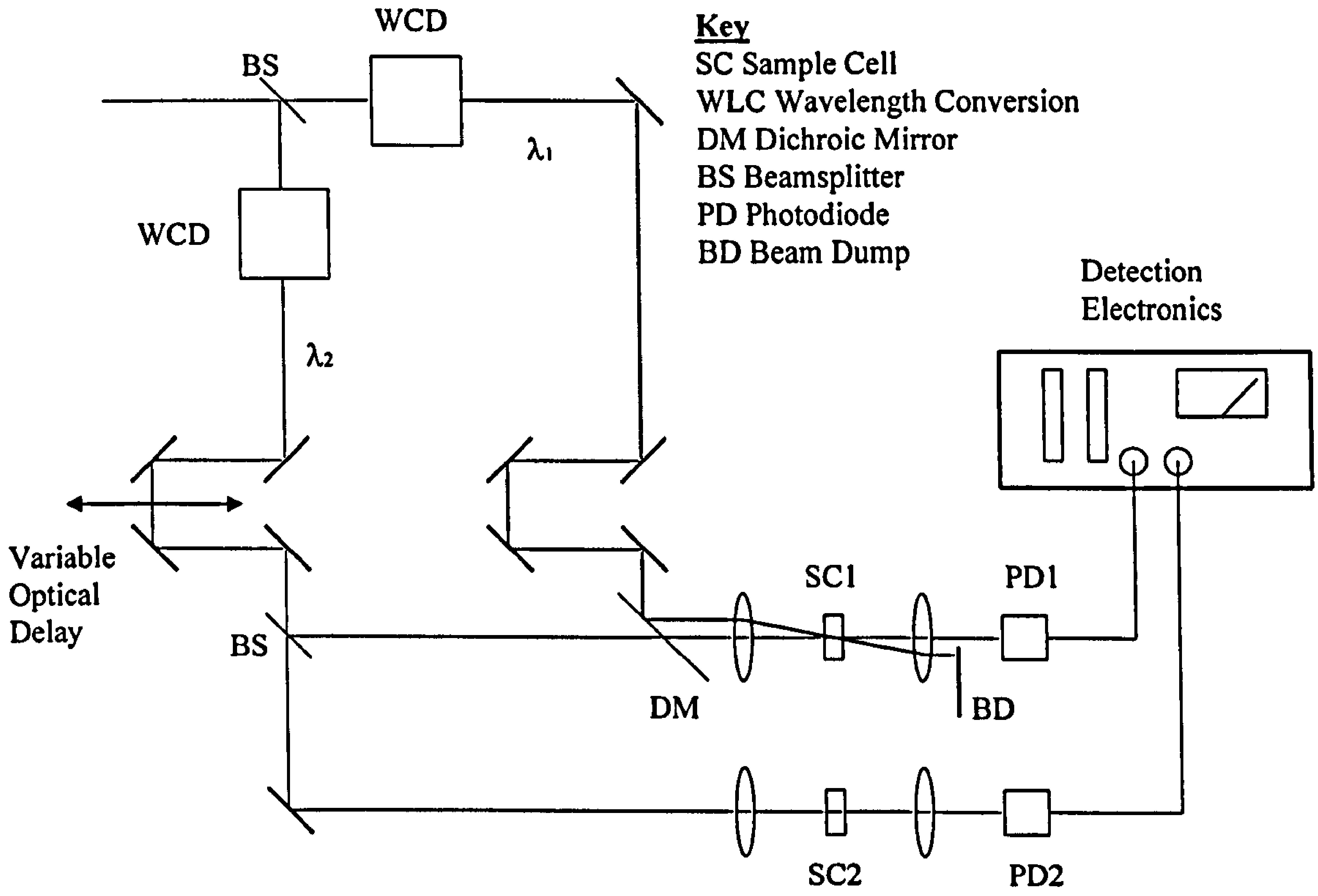

Fig1.4.1 Block diagram for a transient absorption spectrometer.

Figure 1.4.1 shows a typical arrangement for a two-pulse pump-probe transient absorption spectrometer[44]. In this Michelson interferometric set-up, the pump pulse at wavelength λ_1 excites the sample. After a variable time delay, τ, the second pulse at wavelength λ_2 is introduced to the sample to probe the change of absorbance at λ_2. The variable time delay between the pump pulse and the probe pulse is achieved by varying the difference in optical paths through a high precision mechanical translation stage typically controlled via a computer.

The detected transient absorption change may be classified into three categories: absorption, bleach and gain. If the intensity of the probe pulse decreases in the presence of the pump pulse, then there is an increase in *absorption* of the sample. If the intensity of the probe beam increases in the presence of the pump pulse, but remains less than the intensity of the probe beam before it enters the sample, then the pump has caused a *bleach* in the density of the absorbing molecules. Finally, if the intensity of the probe beam increases in the presence of the pump pulse beyond its incident intensity, the transient signal is referred to as *stimulated gain*. In this later case, the signal results from the molecules in the excited state being stimulated back to a lower level by the probe pulse.

The typical pump-pulse-induced relative absorbance change amounts to far less than a few percent of the total absorbance of the sample. Unfortunately, this is generally less than the pulse to pulse fluctuations exhibited by the lasers used in such studies. As a result, a normalisation and signal averaging scheme is of vital importance to increase the signal to noise ratio in transient absorption experiments. In the set-up shown, a reference beam is employed to reduce shot to shot noise. In this case the laser pulse is split into two beams. One beam overlaps the region of the sample excited by the pump laser beam, while the other beam traverses through the sample cell in a region that is not perturbed by the pump pulse. The ratio of the intensities of the probe and reference beam as a function of the delay time reflects the evolution of the transient absorbance of the sample. In general, multiple laser shots are averaged at a particular delay time in order to achieve an acceptable signal to noise ratio.

For laser systems with a repetition rate higher than 500 Hz it is necessary to modulate the probe radiation using a mechanical chopper to introduce an AC component in the transmitted intensity of the probe beam[41]. This AC component is then detected by a lock-in amplifier as a function of delay time. It should be noted that the selection of the modulation frequency is not random, a judicious choice will place the modulation frequency at or near the minimum of the intrinsic noise spectrum of the laser.

Many types of detectors are used in transient absorption spectrometers. Typically, however, a silicon-based diode is chosen, due to its large bandwidth response and cost-effectiveness. In cases where the transmitted signal is weak, photomultiplier tubes may be employed. For studies in the infrared, pyroelectric detectors or up-conversion techniques may be used.

Transient absorption spectroscopy can not only be used to measure population kinetics, but also orientational dynamics when polarised pump and probe light pulses are employed. The orientational anisotropy, ΔI(t), defined by equation 1.4.2, can be studied directly by making separate transient absorption measurements with pump and probe beams having parallel and perpendicular polarisations[4].

$$\Delta I(t)=\frac{I_{para}(t)-I_{perp}(t)}{I_{para}(t)+2I_{perp}(t)} \qquad 1.4.2$$

The polarisation characteristics of the laser beams are usually controlled by calcite polarisers and waveplates, and Pockels cells or photo-elastic modulators are used when periodic switching between different polarisations are needed. In cases when population information is desired, the relative polarisations of pump and probe pulses are set at 54.7°, which is the so-called 'magic angle'[45,46].

Time-resolved emission spectroscopy is an important and commonly used tool in the study of chemical reaction dynamics in the condensed phase. There are three general approaches to obtaining time resolution in emission spectroscopy: time-correlated single photon counting, direct detection by streak camera and fluorescence up-conversion. Each of these techniques has its limitations and advantages and the best approach will depend on the characteristics of the chemical system being studied. The following is limited to a brief discussion of fluorescence up-conversion.

Despite the routine generation of sub-100 fs laser pulses, it has been a challenge to obtain time resolution comparable to the laser pulse width in time resolved fluorescence spectroscopy. The best technique developed to date relies on the optical gating of the fluorescence emission by non-linear optical crystals. This technique is currently used to study a wide variety of chemical phenomena. In the following section the technique and general principles are introduced.

The basic concepts of optical gating in a non-linear optical crystal to obtain time resolution in emission experiments are outlined in fig. 1.4.2. The incoherent fluorescence photons excited by a pump laser pulse are focused into a non-linear frequency mixing crystal. Another ultrafast, appropriately delayed [probe] pulse is overlapped with the fluorescence spot in the crystal. The relative timing sequence of the pump, fluorescence and the probe pulses are illustrated in the lower portions of fig.1.4.2.

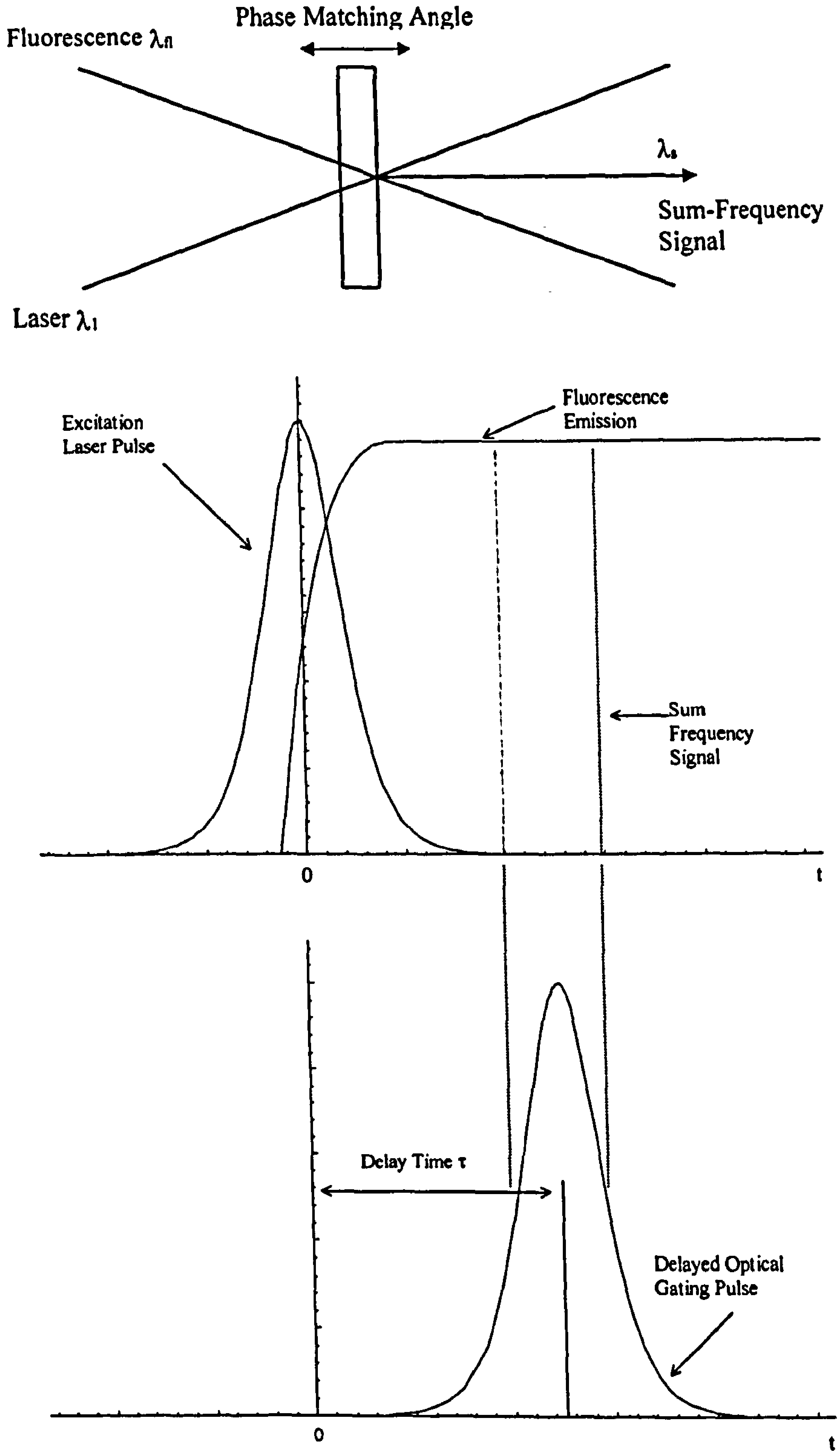

Fig. 1.4.2 Principle of fluorescence up-conversion.

The non-linear optical crystal is oriented to satisfy the phase matching conditions for the frequency mixing process. The mixing process is generally sum-frequency generation [due to the availability of sensitive detectors in the UV and visible regions, i.e. PMT's], however, these discussions also apply to difference frequency mixing, which has been used to time-resolve UV emission. The light generated at the sum frequency is then collected and sent into subsequent light detection and data acquisition devices.

The sum-frequency signal can be expressed by the following equation;

$$I_{sum}(\tau) = \int I_{fl}(\tau) I_{probe}(t-\tau)dt \qquad 1.4.3$$

where I_{sum}, I_{fl}, and I_{probe} are the intensities of the sum, fluorescence and probe beams respectively. Equation 1.4.3 clearly shows that the sum frequency signal is only present when fluorescence photons and the probe pulse are simultaneously coincident on the crystal. Since the probe is typically much shorter than the time-dependent fluorescence, it acts as an optical gate to the up conversion signal, analogous to an electronically gated boxcar integrator. In principle, this technique has a time resolution comparable to the probe pulse width. The actual time resolution of the measurement also depends on the temporal width of the pump (i.e. the accuracy in the definition of $t = 0$).

Fig. 1.4.3 shows the basic experimental arrangement for an up-conversion experiment. At time $t=0$, the sample is excited by an ultrashort laser pulse at wavelength λ_2. The resulting fluorescence, λ_{fl}, is then collected and focused on a non-linear crystal [MXC]. A second laser pulse at λ_1 overlaps the fluorescence spot on the crystal. The delay time, τ, between the arrival of the fluorescence and the second laser pulse is typically adjusted by moving a computerised translation stage. The generated sum frequency light (Where $1/\lambda_{sum} = 1/\lambda_{fl} + 1/\lambda_1$) is detected by a photomultiplier after rejection of stray and laser light by a monochromator. The signal level of this experiment is usually low due to the small conversion efficiency of the mixing process and the lack of peak intensity of the incoherent fluorescence light. This is especially true for high-repetition rate, low power laser systems. In these cases photon counting electronics are often used to improve the signal to noise ratio.

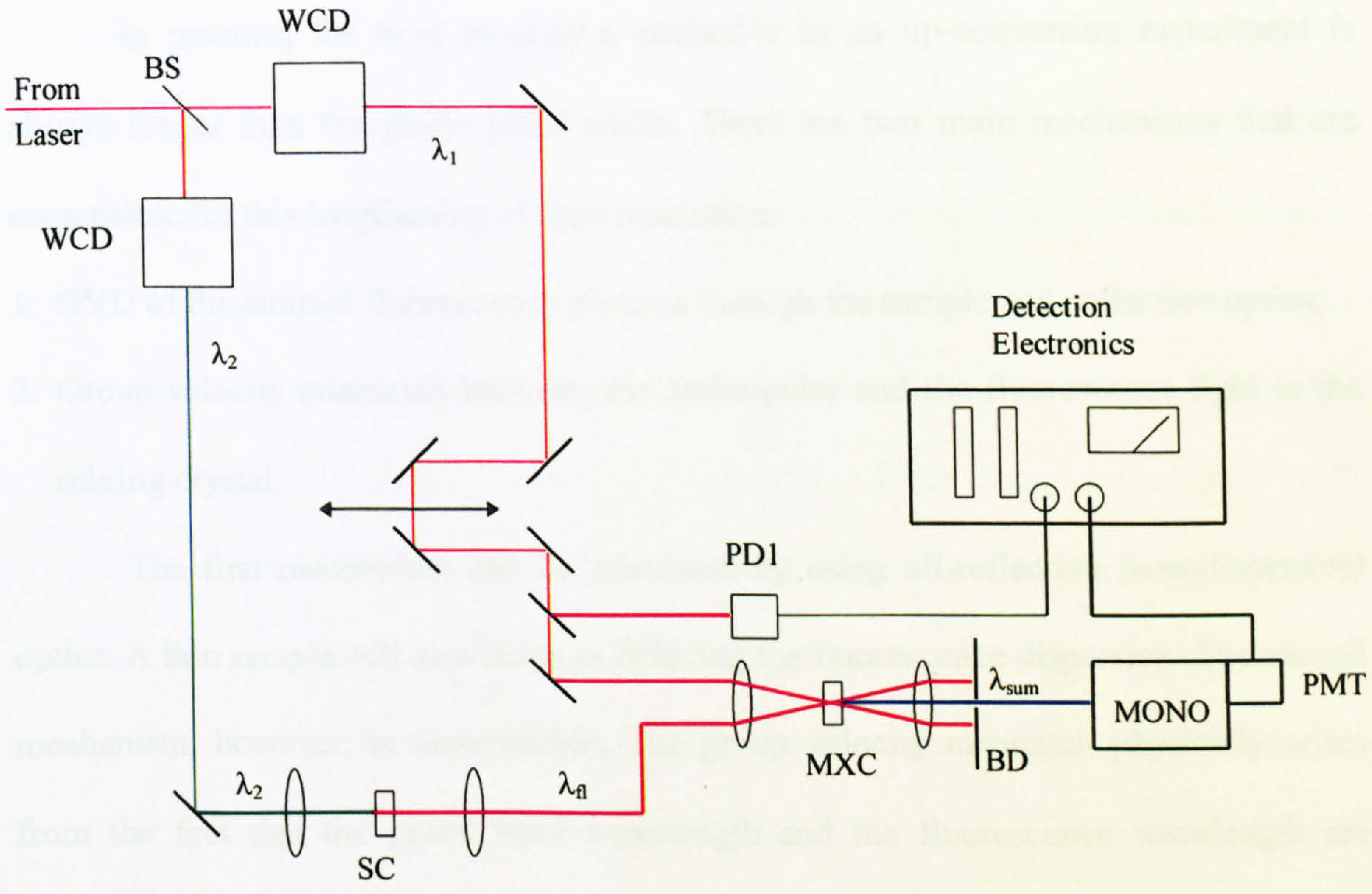

Fig. 1.4.3 Schematic for a fluorescence up-conversion instrument. In addition to the abbreviations in fig.1.5.1; MXC, mixing crystal; MONO, monochromator; PMT, photomultiplier.

The fluorescence up-conversion technique can be used to study orientation dynamics in a similar fashion to transient absorption spectroscopy. The angle between the polarisations of the detected fluorescence and the up-conversion gating pulse is determined by the type of phase matching in the sum-frequency generation crystal [0° for type I and 90° for type II (for further definition see Section 1.33)]. Therefore the fluorescence anisotropy can be measured in the same manner as described by equation 1.4.2, i.e., measuring separate up-conversion data with parallel and perpendicular polarisations between the excitation and up-conversion gating pulse. When only population information is desired the polarisation angle between pump and probe pulses should be set at 54.7^0. Care must be taken in selecting fluorescence collection optics that maintain polarisation properties.

In practice, the time resolution attainable in an up-conversion experiment is always longer than the probe pulse width. There are two main mechanisms that are responsible for this lengthening of time resolution:

1. GVD of the emitted fluorescence photons through the sample and collection optics.
2. Group velocity mismatch between the probe pulse and the fluorescence light in the mixing crystal.

The first mechanism can be alleviated by using all-reflective (non-dispersive) optics. A thin sample cell also helps in reducing the fluorescence dispersion. The second mechanism, however, is unavoidable. The group velocity mismatch physically arises from the fact that the probe laser wavelength and the fluorescence wavelength are different. In order to minimise the effect, a low dispersion, thin non-linear crystal is required. Unfortunately, a low-dispersion crystal will typically have a low non-linear susceptibility also, resulting in inefficient conversion. The non-linear mixing signal scales with the crystal thickness, so the desire to obtain the shortest time resolution needs to be balanced with the fact that a reasonable signal level is required to obtain meaningful results. Two ways to reduce the group-velocity mismatch are to keep the probe wavelength as close as possible to the fluorescence wavelength and use type I phase-matching ($e+e \rightarrow o$; or $o+o \rightarrow e$) whenever possible.

1.4.2 Excited State Intramolecular Proton Transfer

Proton or hydrogen atom transfer represents one of the most elementary reactions which can occur in chemical and biological systems[47] and these processes are often initiated by the absorption of light. Enhancement of the acidity or basicity of a molecule on absorption of a photon of light is a phenomenon which is well known and the terms photo-acid and photo-base have been used to describe molecules which experience such an enhancement in the excited state[48]. In these systems, upon absorption of a photon, the molecule either loses (photo-acid) or gains (photo-base) a proton, the other partner in the exchange usually being the solvent. In numerous heterocyclic aromatic molecules, photoexcitation results in intramolecular proton transfer where a proton, initially linked to an acidic donor atom, moves to a basic acceptor group that is part of the same molecule. This process is known as excited state intramolecular proton transfer (ESIPT)[49,50]. The geometry change is highly localised within the molecular structure, affecting mainly the proton and neighbouring groups. In a number of compounds, absorption of a photon initiates a closed reaction cycle comprising proton transfer in the excited state, radiative or radiationless deactivation of the reaction product (the photo-tautomer) and reverse proton transfer to reform the original molecular geometry. The latter reaction step occurs either via the electronic ground state or the triplet manifold.

The formation of the photo-tautomer leads to substantial changes in the vibrational spectra and the electronic absorption and emission bands of the molecule. These have been investigated by both steady state and time-resolved spectroscopic techniques as well as by theoretical methods[50]. Time-resolved methods using ultrashort laser pulses to monitor the photophysical properties give insight into the dynamics and the mechanism for this type of reaction. These measurements provide information on the relevant potential energy surfaces and the vibrational degrees of freedom involved in the structural change.

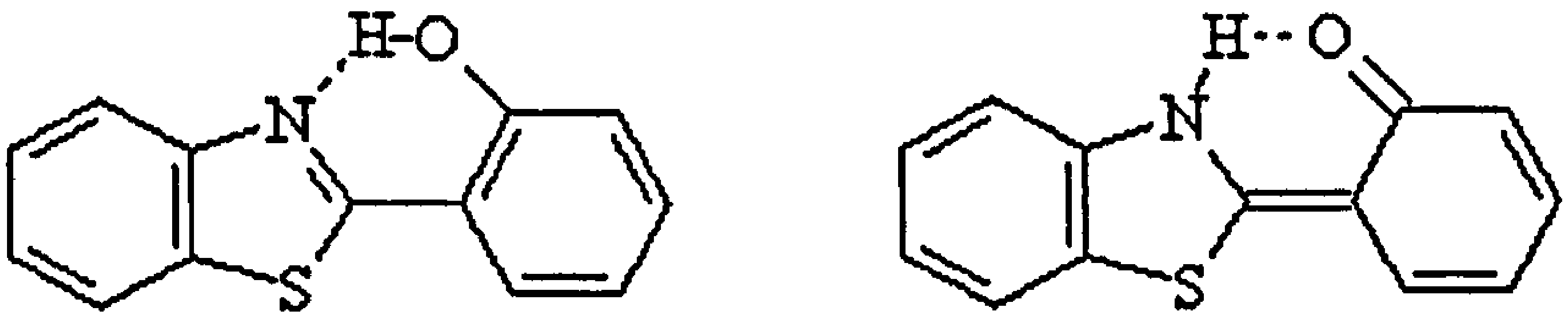

Normal

Tautomer

I

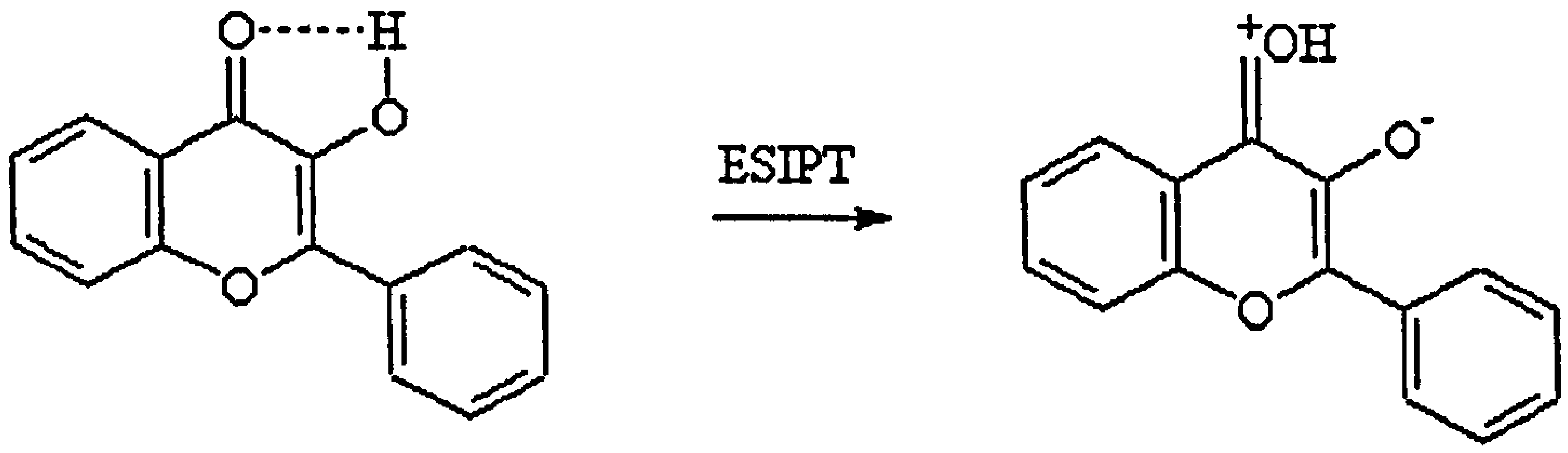

Normal

Tautomer

II

Fig. 1.4.4 Normal and tautomer structure of 2-(2'-hydroxyphenyl) benzothiazole (I) and 3-hydroxyflavone (II).

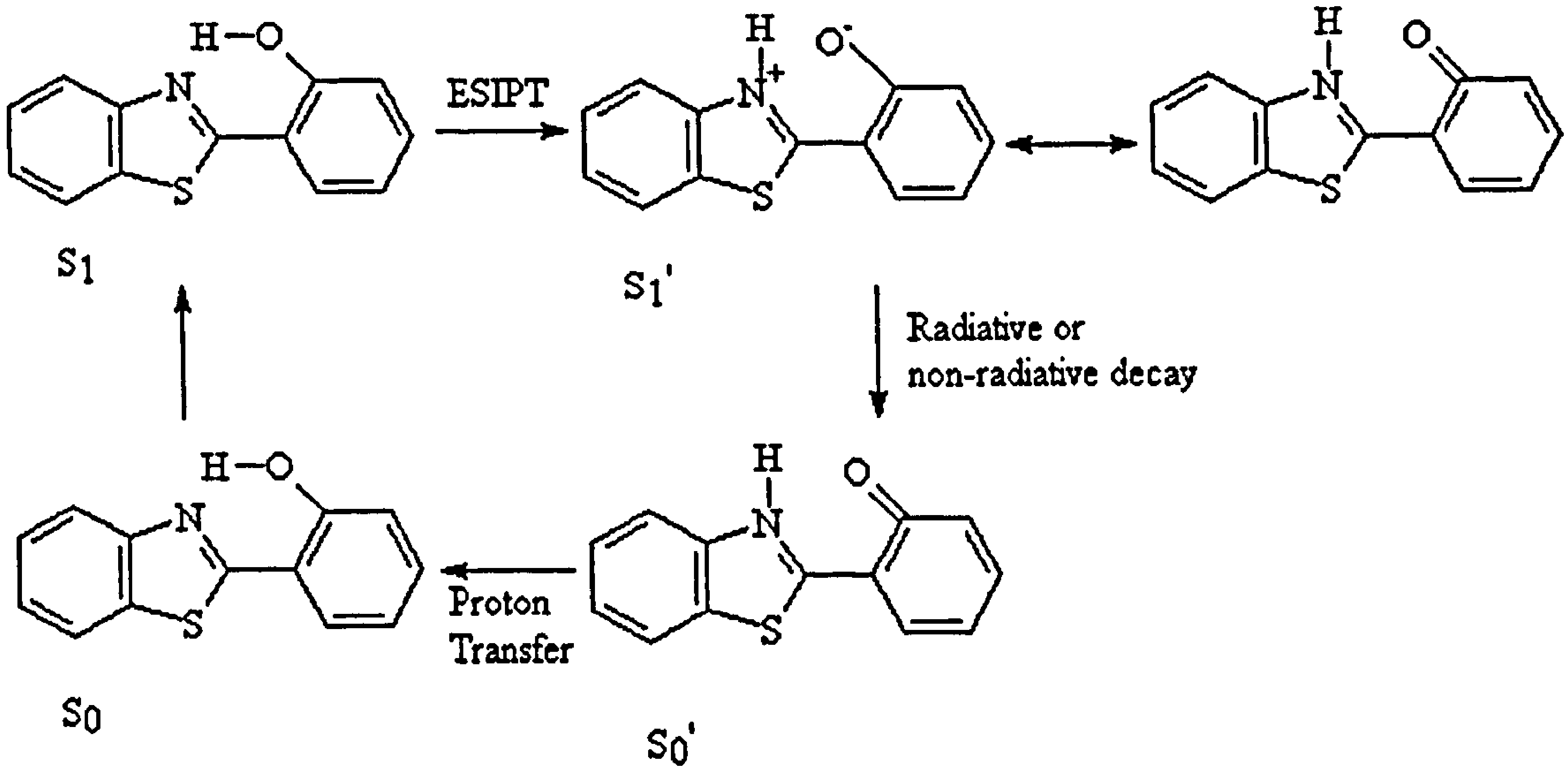

Fig. 1.4.5 ESIPT in 2-(2'-hydroxyphenyl) benzothiazole.

The structural requirements for a molecule to exhibit ESIPT are quite strict. The acidic group in the molecule is almost invariably a hydroxyl group and the basic acceptor is usually a heterocyclic nitrogen atom or the oxygen of a carbonyl function. Examples of systems containing these groups are 2-(2'-hydroxyphenyl)benzothiazole (HPBT, **I**) and 3-hydroxyflavone (3-HF, **II**) respectively. It is noticeable that the donor and acceptor sites are in close proximity in these systems and it is usual for the sites to be hydrogen bonded in the ground state. The zwitterion produced as a result of ESIPT usually has a resonance form similar to that in Fig. 1.4.5 and this has led to the adoption of the terms enol and keto to describe the species before and after the ESIPT reaction. However, there are a number of systems (including **II**) where this terminology is erroneous and it is better to describe the states as a normal or Franck-Condon excited state and the tautomer excited state produced via ESIPT. The generic description of proton transfer reaction involves reaction co-ordinates of the type

$$O_a—H——O_b \qquad \text{or } O_a—H——N \qquad 1.4.4$$

where the light hydrogen nucleus is between two heavier hetero-atoms. With H moving (or transferring) between O_a and O_b, for example, the O_a—H bond is broken and a new one (H-O_b) is formed. This elementary description, which may involve neutral H motion or zwitterion (H^+O^-) formation, is abundant in organic photochemistry and proton transfer spectroscopy[51]. However, even under collisionless conditions, the motion may not be that simple. The motion of the hydrogen on the picosecond or femtosecond time scale may be localised (as Eqn. 1.4.4), or may involve nuclear motions with a simultaneous redistribution of electrons in many bonds. The nature of the bonding and electronic charge distribution determines the reaction pathway, while intramolecular vibrational energy redistribution (IVR) may play a role if the nuclei have enough time to change their positions during the course of the reaction[1].

In general, ESIPT involving excited singlet states shows very fast reaction kinetics. Proton transfer times in the sub-picosecond regime were estimated from early picosecond measurements, which could not temporally resolve the change. A substantially higher time resolution is required in the femtosecond regime in order to probe the proton dynamics directly. In this section I describe the recent progress in the investigation of excited state intramolecular proton transfer (ESIPT) with particular attention to the ultrafast dynamics.

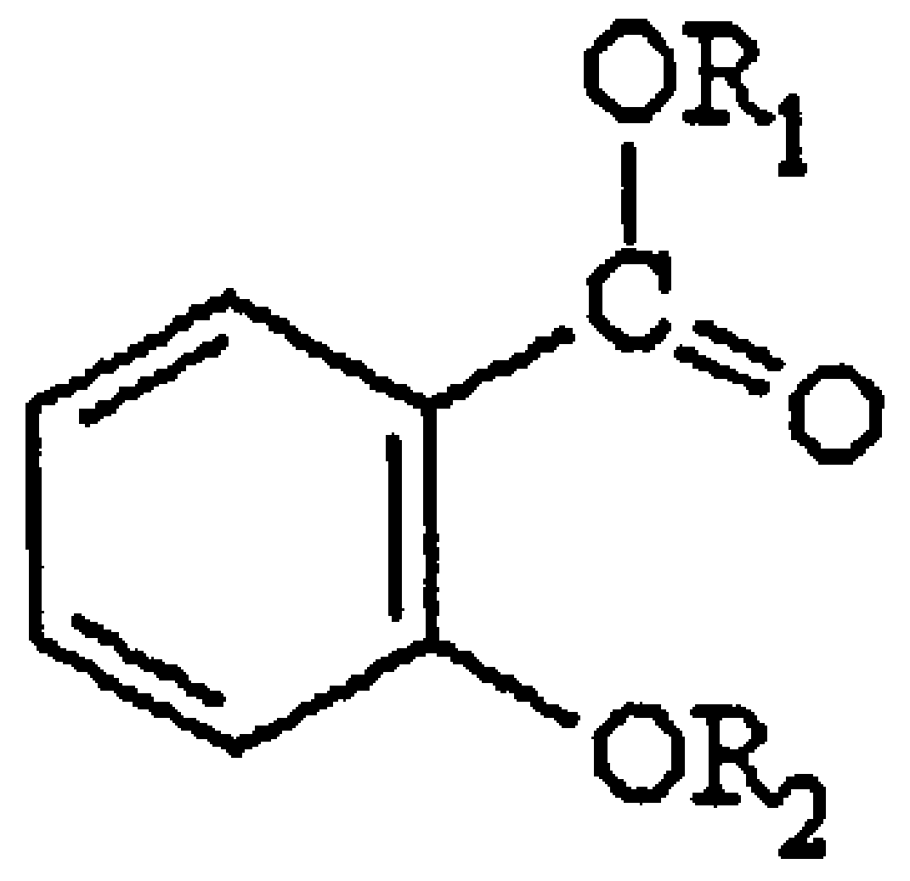

Fig. 1.4.6 Structures of salicyclic acid (III, R_1=H, R_2=H), methyl salicylate (IV, R_1=CH_3, R_2=H), methyl 2-methoxybenzoate (V, R_1=CH_3, R_2=CH_3) and 2-methoxybenzoic acid (VI, R_1=H, R_2=CH_3).

A whole host of molecular systems have been shown to undergo ESIPT, the first reported study (to the best of our knowledge) was by Weller[52], who was studying the solution phase absorption and fluorescence properties of salicyclic acid (**III**) and methyl salicylate (**IV**). The latter was found to exhibit two fluorescence bands in methylcyclohexane at room temperature compared to methyl 2-methoxybenzoate (**V**) which had only one, corresponding to the higher energy band of **IV**. **III** in methanol also exhibited only one emission band, but the size of the Stokes shift for this band (10000 cm^{-1}) compared to that for 2-methoxybenzoic acid (**VI**, 5000 cm^{-1}) implied that the fluorescence was also anomalous here.

Weller suggested that the explanation for these observations was that ESIPT occurred in both **III** and **IV** to yield a zwitterionic species (Fig. 1.4.7). He calculated that the proton transfer rate constant at 93 K was $\geq 10^8$ s^{-1} and that an activation energy of $\leq$10 kJ mol^{-1} was involved in the ESIPT step. Weller considered that the proton transferred species was the zwitterion in Fig. 1.4.7 but it is also possible to write down an uncharged resonance structure (also shown in the figure). Further studies support this picture of an excited state proton transfer although subsequent experiments have avoided molecules **III** and **VI** as prototype molecules for ESIPT due to the complication of dimerisation in the ground state.

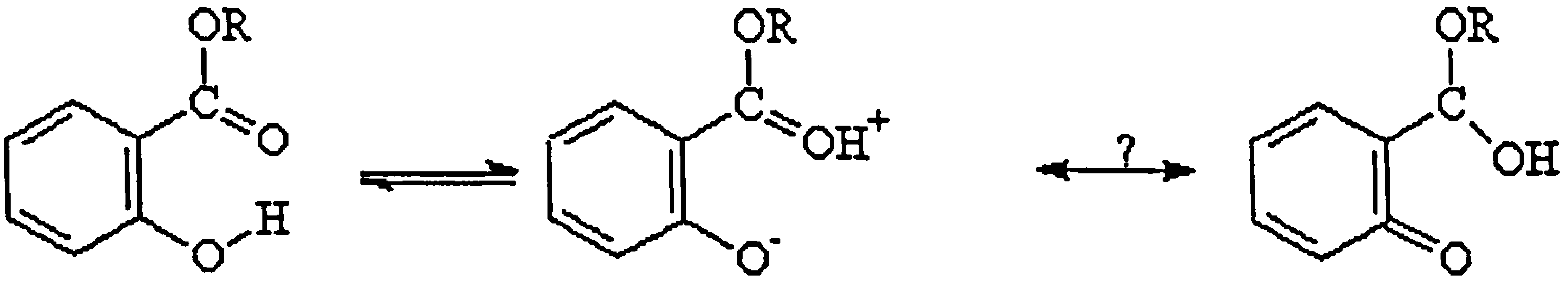

Keto

Zwitterion

Enol

Fig.1.4.7 ESIPT in esters of salicyclic acid.

Much work on these molecules has concentrated on the long time dynamics of both the keto and enol species and interested readers should consult the two reviews on the subject as it is beyond the scope of this thesis[49,50]. However, Herek et al[42], have undertaken a study of the ultrafast dynamics of **IV** and **V** (and deuterated species) in the gas phase, thereby isolating the molecule from collisional and solvent effects in order to resolve the pure proton movement in the excited state. The dynamics were probed using a femtosecond fluorescence depletion technique. Unlike the typical pump-probe experiment in which the pump excites the molecule to an intermediate state and the probe carries it to a final fluorescing state, here the emitting state is intermediate so that the probe depletes the fluorescence by absorption to some higher excited state. Both short and long (up to 120 ps) transients were obtained, depleting the fluorescence at both emission maxima: 330 and 440 nm, corresponding to the enol and keto states respectively. In the case of the 330 nm state the lifetime was long (in comparison to the transient dynamics ~1.1 ns) leaving the excited state population constant on the time-scale of interest. However, for the 440 nm state, the decay was on the picosecond time scale.

Measurement of a rise component of 60 ± 10 fs is reported for the 440 nm state indicating the rate of proton transfer along the hydrogen bond. Discussion of the relevant vibrational modes that could contribute to a transfer rate on this time-scale lead Herek et al to tentatively propose that the state is populated by low frequency modes associated with out of plane deformations of the "ring" comprising the intramolecular hydrogen bond. However, the OH stretch period is 13 fs (taking an O-H stretch frequency of 2582 cm^{-1}). They suggest that dispersion of the wavepacket in the excited state could easily be responsible for broadening to 60 fs due to the large number of vibrational modes in the excited state of the keto form. They conclude that pump-probe experiments with better time resolution (cross-correlation of pump and probe was ~ 80 fs) may yield faster kinetics information.

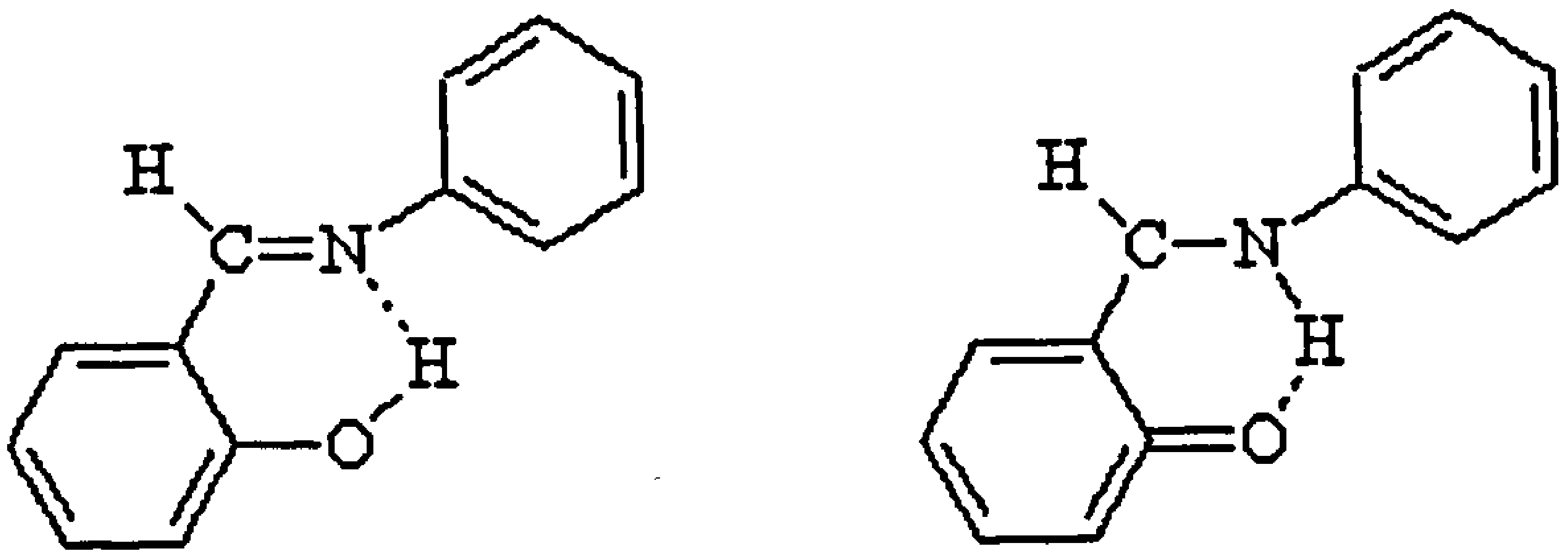

Normal Tautomer

Fig. 1.4.8 Normal and tautomer structure of saliclideneaniline (VII)

Sekikawa et al[53] reported measurement of proton transfer rates in thermochromic salicylideneaniline (SA,VII) crystals. Three SA substituent species were investigated: N-5'-chlorosalicylideneaniline (ClSA), 4-methyl-N-5'-chlorosalicylideneaniline (MClSA) and 4-methyl-N-salicylideneaniline (MSA). Comparison of these three samples was expected to reveal substitutional effects on the dynamics of the proton transfer. They measured the decay rate of the S_1 normal excited state fluorescence by femtosecond fluorescence up-conversion and attribute this to the rate of ESIPT to form the keto species (direct measurement of the rise time of the keto fluorescence would be ambiguous due to thermal population of the keto ground state at time zero). The lifetime of the excited enol was found to be less than a few picoseconds (as we expect from previous studies). The rate of S_1 state decay was shown to be dependent on both the nature of the substituent and the probe energy, suggesting the existence of a potential barrier to proton transfer in the excited state. The results of their experiments are summarised in Table 1.4.1. The difference in the dynamics of the proton transfer among ClSA, MClSA and MSA can be explained in terms of the change in the barrier height of the potential-energy surface in the excited state. The energy separation (E_g) between the excited enol (S_1) and keto (S_1') forms is obtained from stationary fluorescence and excitation spectra. If it is assumed that the hydrogen bond lengths are the same for all the molecules, both the height and the width of the potential barrier increase with decreasing E_g. They suggest that the presence of two decay rates at lower fluorescence energies also suggests the existence of the potential barrier between the two forms: if there were no barriers, the fluorescence would decay exponentially with the continuous elongation of the decay time towards the lower energy fluorescence. In addition, the rate of proton transfer should be faster in the barrier-less potential (as observed in Tinuvin and 3-hydroxyflavone (see later)).

Table 1.4.1 Time constants for saliclideneaniline derivatives

Molecule	$E_g = E(S_1) - E(S_1') / eV$	$E_g / kJ\ mol^{-1}$	S_1 Decay Rate / $\times 10^{12}\ s^{-1}$
ClSA	0.044	4.24	1.28 ± 0.04
MClSA	0.030	2.89	0.36 ± 0.04
MSA	0.023	2.292	0.28 ± 0.06

In a low temperature experiment at 77 K, Sekikawa et al show that the rate of transfer is not significantly different to that at 293 K. Since the rate of proton transfer by thermal activation is expected to become exponentially lower with temperature, it is concluded that quantum-mechanical proton tunnelling through the barrier is taking place. The existence of a potential barrier is supported by the deuteration effect on the dynamics of the proton transfer; the rate of proton transfer in ClSA becomes smaller on deuteration from 1.28 to 1.00 ps^{-1}. For a model such that the two energy surfaces (normal and tautomer state) cross to form a potential barrier, the rate of proton transfer correlates with the frequency of the O - H stretching mode, so that the reduction of the rate by deuteration indicates the existence of the barrier. This result contrasts markedly with previous studies of proton transfer in the femtosecond regime (notably Herek et al[52]). This may be due to the difference in the phase of the investigated system. In the liquid and gas phases, a molecule has more degrees of freedom in order to shorten the hydrogen bond length, resulting in a barrier-less potential. Sekikawa et al conclude that further investigation of the potential energy surfaces involved in proton transfer is necessary. Kobayashi et al[54] confirmed these conclusions showing a deuterium effect was observed in another salicylideneaniline derivative; N, N'-bis(salicylidene)-p-phenylenediamine, where the S_1 lifetime increased from 1.0 to 1.3 ps on deuteration.

In a recent paper by Mitra and Tamai[55] the solution phase dynamics of **VII** were reported in cyclohexane and ethanol. Transient absorption spectra for **VII** in cyclohexane show the presence of an absorption band in the region 400-500 nm and corresponding emission centred around 620 nm. Mitra and Tamai suggest that evolution of the absorption band around 420 nm and the emission at 620 nm occur at the same time and indicate the presence of the keto species, although the dynamics may be complicated by uncorrected dispersion in the white light continuum. A time dependent spectral shift in the 420 nm band towards the blue is observed which, they suggest, corresponds to the relaxation of vibrationally hot molecules, leading to the formation of photochromic products from the proton transferred tautomer (again we suggest caution in the assignment of processes which occur on a time-scale comparable with the dispersion of the continuum). They find the rise time of the 420 nm band to be 210 fs in cyclohexane and 380 fs in ethanol. It is interesting to note that the experimental error quoted later in the paper is 400-600 fs indicating that any proton transfer on the time scale indicated would not be sufficiently resolved! Certainly it would appear that the dynamics of the proton transfer are significantly different in the solid and liquid phases and that the dynamics of the proton transfer are solvent dependent. The rate of proton transfer in solution appears to be instrument limited in this case, indicating a barrier-less potential to the proton transfer.

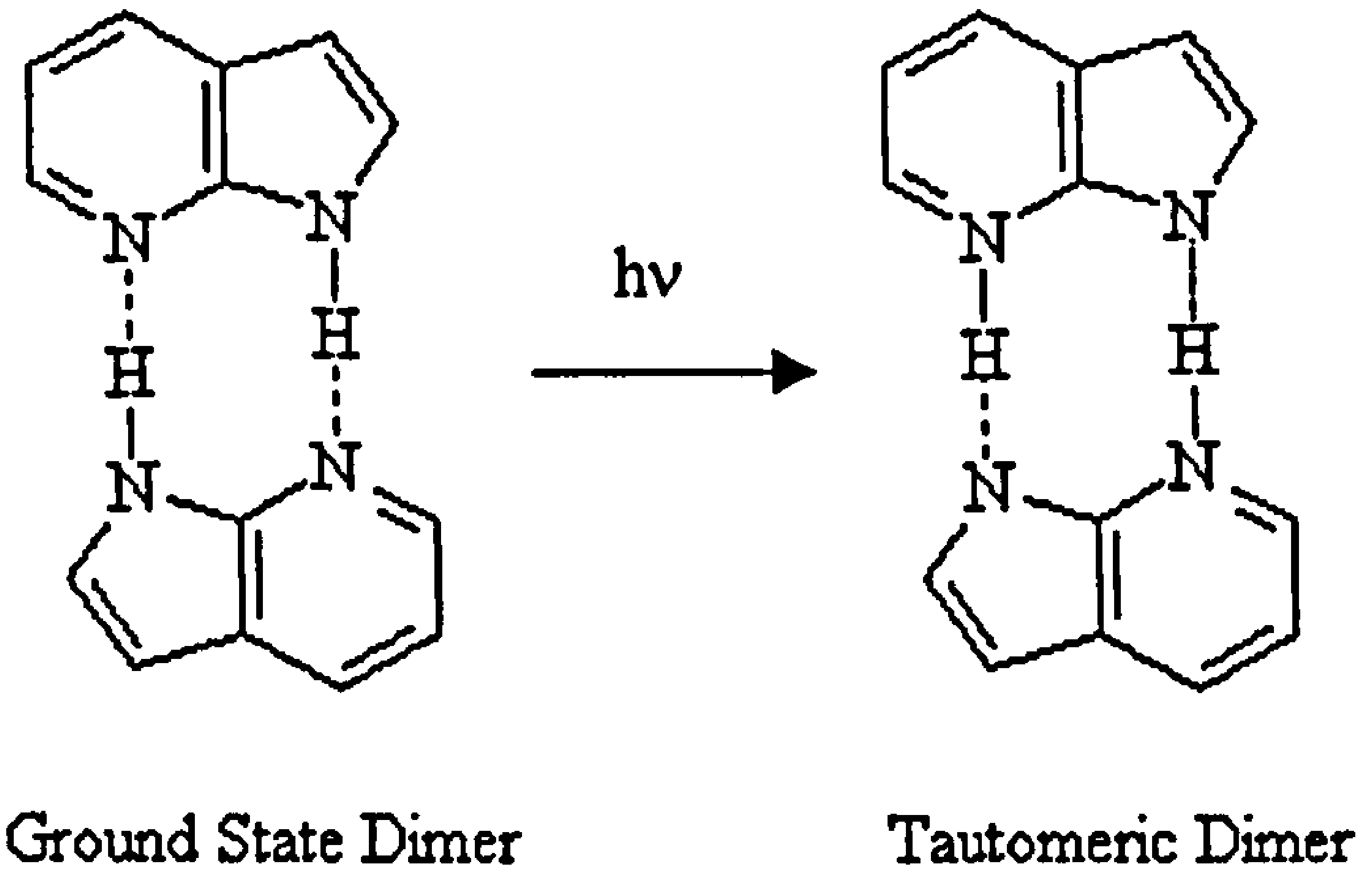

Fig. 1.4.9 Normal and tautomer structure of 7-azaindole (VIII).

Dimers of 7-azaindole (VIII) in non polar solvents have been proposed as a model for DNA base pairs for many years[56].VIII dimers are thought to undergo double-proton transfer in the excited state as shown in Fig. 1.4.9. The case of intermolecular double proton transfer reactions in dimers differs from the more typical case of an acid in a base solvent or cluster, in that a sterically specific geometry is required for the double proton exchange. The reaction is then less dependent on the solvent and can represent a model for proton transfer in the gas phase. Lopez-Martins et al[57] undertook a study of the picosecond time-resolved photoelectron spectroscopy of VIII. Dimers were prepared by pulsed supersonic helium expansion (1.2 atm) and both the fluorescence and photoelectron spectra (PES) were recorded. Fluorescence excitation spectra recorded over the absorption range of the dimer show a progression of bands with a fundamental frequency of ~ 117 cm^{-1} corresponding to the symmetric stretching motions of the N-H$_{\Lambda}$ N. To probe the time dependence of the tautomerisation reaction, the authors recorded photoelectron spectra using 2 pulse durations of 0.8 and 5 ps of equal energy. A dramatic drop in the collected PES was reported for the longer pulse duration. The authors suggest that this indicates that the excited state lifetime of the dimer is significantly less than 5 ps and that the ionisation cross-section is significantly less for the reactant excited state.

Douhal et al[58] investigated the dual proton transfer of prepared dimers of **VIII** in a molecular beam. Transient signals were obtained by time resolved ionisation spectroscopy, with the ion signal being measured as a function of probe delay by time-of-flight mass spectrometry. They studied the dynamics (with an instrumental function of ~ 150 fs) on both **VIII** and its deuterated analogue to investigate possible quantum tunnelling effects. Excitation with excess vibrational energy (E) is shown to change the time constant for the proton transfer from 650 fs (E = 0) to 200 fs (E = 1.5 kcal mol^{-1}) indicating that although the vibrational excess energy plays a part in proton transfer a direct reaction pathway exists. On deuteration and excitation with 1.0 kcal mol^{-1} excess energy, the time constant is shown to increase from 360 fs to 3 ps (or 1.5 ps for deuteration of a single moiety in the dimer). These results are known to be consistent with a model involving quantum mechanical tunnelling. The authors obtain a barrier height of ~ 2.6 kcal mol^{-1} for the second proton transfer step and suggest that this is reflected in the ps timescale for the transfer.

Takeuchi and Tahara[59] also investigated the excited state dynamics of the proton transfer reaction of **VIII**, using the femtosecond fluorescence up-conversion technique with a time resolution of ~280 fs. Solutions of 10^{-2} mol dm^{-3} concentration in hexane were used to prepare an estimated 87 % of the **VIII** molecules as dimers. They measured fluorescence kinetics from both emission bands and observed tri-exponential dynamics corresponding to τ_1 = 200 ± 100 fs, τ_2 = 1100 ± 100 fs and a “slow” component with τ=3.2 ns. The long lifetime is assigned to the decay of the proton transferred tautomer and the two fast lifetimes to ultrafast relaxation from the primary excited state (τ_1) to another excited state of the dimer followed by double proton transfer to the tautomer excited state (τ_2). However it is interesting to note that the ultrafast decay (present as a rise component for fluorescence measured at long wavelengths) is of the order of the ESIPT rate as measured in a variety of systems. The authors note that previous measurements in the gas phase revealed similar time constants which had been attributed to the transfer of a single (short time dynamics) and both protons (long time dynamics) respectively.

A model of an intermediate single proton transfer prior to double proton transfer is further supported by the work of Folmer et al[60] using the phenomenon of coulomb explosion to arrest and directly interrogate the reaction. A beam of 7-azaindole dimers was prepared in a pulsed beam in vacuum. The desired tautomerisation was initiated with a low intensity ultrashort pulse at 312 nm and at subsequent times the reaction was probed using a high intensity 120 fs pulse (624 nm, 2 mJ) to accomplish intense field ionisation and subsequent coulomb explosion. The ions produced were analysed by time-of-flight mass spectrometry. The authors report the detection of mass units of 119 amu and 118 amu as well as a large number of smaller fragments and the dimer mass (~236 amu). They associate the 118 amu fragment to one half of a dimer molecule and the 119 amu fragment to the intermediate state where only one proton has been transferred. A fragment at 117 amu was not detected, indicating that this part of the intermediate forms the observed smaller fragments. A plot of the ratio of 119 to 118 amu mass fragments gives the temporal evolution of the intermediate state, a rise of ~

660 fs is observed corresponding to the first proton transfer and a value of ~ 5 ps is given for the decay corresponding to the second proton transfer.

Of particular interest to the research reported here is the work on 3-hydroxyflavone (II), the excited state dynamics of which has received significant interest in the literature on longer time scales (ps and ns). The anomalous fluorescence behaviour of 3-hydroxyflavone was first reported in detail by Sengupta and Kasha[61] although they noted that Frolov et al[62] had earlier reported on the luminescence of **II** and related molecules in 77 K ethanol glasses. The emission spectrum was found to exhibit two emission bands, the presence and intensity of which were very sensitive to solvent and temperature. Excitation spectra for the two emission bands were identical and closely matched the absorption spectrum indicating that this behaviour was due to some excited state process. It was proposed that the two emission bands corresponded to fluorescence from the Franck-Condon excited state S_1 (emission around 400 nm) and the tautomer S_1' produced by ESIPT (emission around 500 nm) as shown in Fig. 1.4.10.

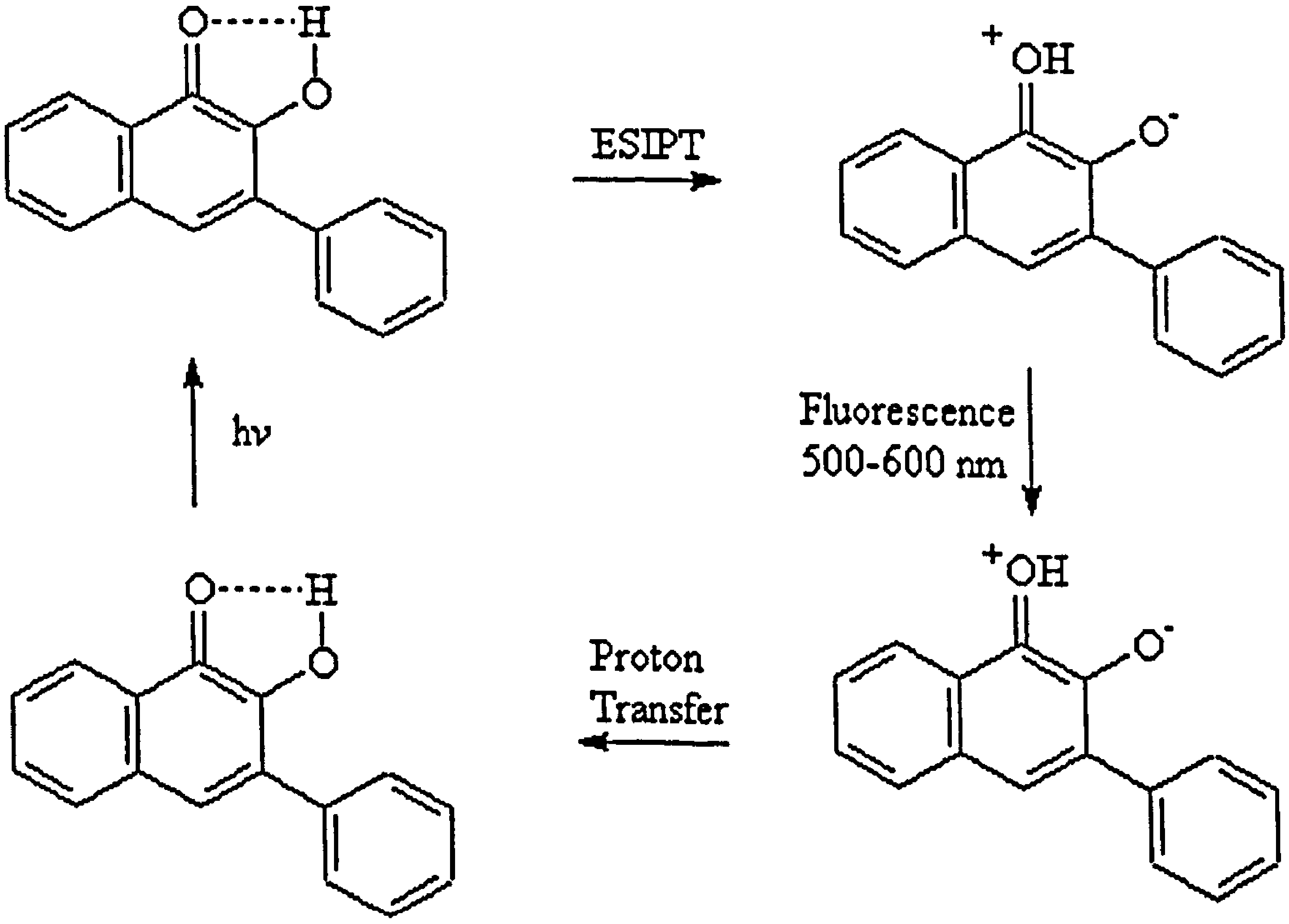

Fig. 1.4.10 ESIPT in 3-hydroxyflavone

It was suggested that the ESIPT step could be prevented by external hydrogen bonding (i.e. to the solvent) and that it was necessary for the 2-phenyl ring to be co-planar for the full basicity of the carbonyl oxygen to be developed. It is noteworthy that this explanation still holds essentially true.

Following the initial report, the photophysics of **II** has been studied by a number of research groups. There are several early papers which report on the solution fluorescence kinetics of both the normal (from S_1) and tautomer (from S_1') fluorescence. All of these found that the tautomer exhibited multi-exponential kinetics including a rise time which matched the decay of S_1. However, there was some disagreement as to whether the fluorescence decay of S_1 and the rise of S_1' was single or double exponential. In all cases this process was found to be rapid with values quoted by Wolfe and Thistlethwaite[63] of 69 ± 8 ps for the decay of the S_1 fluorescence and 65 ± 10 ps for the rise of the S_1' fluorescence in deuterated methanol giving an indication of the speed of the process. The lifetime of the S_1' state was found to vary considerably with the solvent environment from a few hundred picoseconds to several nanoseconds and some representative data is given in Table 1.4.2.

The amount of fluorescence from the two species was found to vary with temperature such that the ratio of the quantum yields of fluorescence for S_1 and S_1' increased with decreasing temperature[63,64]. It was found that the lifetimes of both the species also increased with decreasing temperature. The lifetime of the S_1 fluorescence in methyltetrahydrofuran was found to increase up to a maximum value of 1.8 ns at 150 K and below[64] which allowed the authors to calculate an activation barrier for ESIPT of approximately 12 kJ mol^{-1}. Similar measurements in deuterated methanol and methylcyclohexane gave activation energies of 7.6 and 22 kJ mol^{-1} respectively[63]. In the light of later findings, interpretation of these values as being the activation energies for ESIPT is dubious.

Table 1.4.2 Solvent effect on the tautomer fluorescence of 3-hydroxyflavone[50]

Solvent	Lifetime (ns)
Methylcyclohexane[63]	4.58 ± 0.03
Methylpentane[64]	~ 4.00
Polymethylmethacrylate[63]	6.09 ± 0.06
Methyltetrahydrofuran[64]	~ 1.00
Deuterated Methanol[63]	0.37 ± 0.025
Benzonitrile[65]	2.00
Acetonitrile[65]	0.85
Triton X-100 micelles[66]	< 0.80/1.90

The S_1' state exhibits similar temperature dependent behaviour. In all the solvent systems which have been studied, the lifetime increases as the temperature is decreased until a maximum value is obtained and further reduction in temperature elicits no further increase in S_1' lifetime. Once again it is possible to calculate activation energies for this process in S_1' and values between 11.8 kJ mol^{-1} (polymethylmethacrylate) and 29.8 kJ mol^{-1} (methylcyclohexane) have been obtained[63,64]. These values are believed to relate to the torsional motion of the S_1' state, probably involving the bond between the pyrone and phenyl rings.

Some of the above work and its interpretation was thrown into question when McMorrow and Kasha[67,68]revealed that they had found the behaviour of **II** to be extremely sensitive to the presence of hydrogen bonding impurities in non-hydrogen bonding solvents. In rigorously purified hydrocarbon solvents ground state molecules of

II are intramolecularly hydrogen bonded and there appears to be little or no intrinsic potential energy barrier to ESIPT following excitation, only tautomer fluorescence is observed. However, in alcohol or aqueous solvents it was proposed that a range of mono- and poly-solvated species were present (including the anion of **II** in water[68]) whose ground state distribution is temperature dependent. The addition of traces of water to a hydrocarbon solution of **II** at 77 K leads very clearly to emission, not only from S_1' but also S_1 and the 3-hydroxyflavone anion.

The tautomer rise-time was found to be < 8 ps in pure hydrocarbon solvents at ambient temperature and 37 ± 6 ps at 77 K[69]. Most subsequent attempts to measure ESIPT in non-interacting solvents have proved to be instrument limited, including measurements on **II** in solid argon at 10-15 K and on 3-hydroxychromone (where the 2-phenyl group is absent) and two substituted 3-hydroxyflavones in hydrocarbon solvents at room temperature[70] although Ernsting and Dick[71] were able to calculate the ESIPT rate constant as 7.4×10^{11} s^{-1} on the basis of line shapes in the jet-cooled emission of **II**. Peluso et al[72] have calculated the potential energy surfaces for the ground and excited states of **II** using MINDO/AM1 and attribute the rapidity of the proton motion to the promoting effect of a low-frequency bending vibration which shortens the distance between donor and acceptor sites (much as Herek et al[42] and Elsaesser and coworkers[75] predicted from experimental observations for **IV** and Tinuvin P respectively).

Relatively little work has been published in the literature with regard to the experimental measurement of ESIPT in **II** at femtosecond time-scales. Recent work by Schwartz et al[73] reported the first observation of the ESIPT process on an ultrafast time scale. Measurements of the transient absorption with a resolution of 125 fs, were undertaken for absorption at 620 nm after excitation with a 310 nm UV pump pulse. The results of their experiments are summarised in table 1.4.3. The fast transient absorption changes of **II** in dry methylcyclohexane (MCH) showed a resolved sub-picosecond component of 210 fs convoluted with the 125 fs time integrated Gaussian instrumental function. In methanol the ultrafast rise component was shown to fit to the instrument function convoluted with an 80 fs exponential rise component. They showed that the addition of hydrogen bonding impurities significantly increased the rate of ESIPT and they suggested that the time scale for the proton transfer in MCH (210 fs) indicates that no part is played by twisting of the phenyl group. Discussion of the effect of hydrogen bonding impurities leads the authors to suggest that a different mechanism is responsible for ESIPT in polar solvents. They suggest that the formation of hydrogen bonded complexes creates *inter*-molecular motions which may play an important role in the tautomerisation process. If the new intermolecular modes are also displaced, the resulting wavepacket could follow a trajectory in the excited state which is altered from the unsolvated species leading to a different measured proton transfer time. They propose that a cyclically hydrogen bonded monosolvate (Fig. 1.4.11) would lead to dual proton transfer moderated by the stretching of the two intermolecular hydrogen bonds alone (i.e. without coupling into low frequency in plane vibrations in order to modulate the intramolecular hydrogen bond). In contrast disolvated complexes (Fig. 1.4.12) would not undergo proton transfer and may explain the presence of the slower rise component. The authors propose that this slow rise component is the time for desolvation of 3-HF$(ROH)_2$ to become either the monosolvated or the free 3-HF species. A note added in proof reports no significant isotope effect for the deuterated 3-hydroxyflavone in methylcyclohexane or for deuterated methanol in agreement with the previous work of Elsaesser and co-workers on HPBT[83].

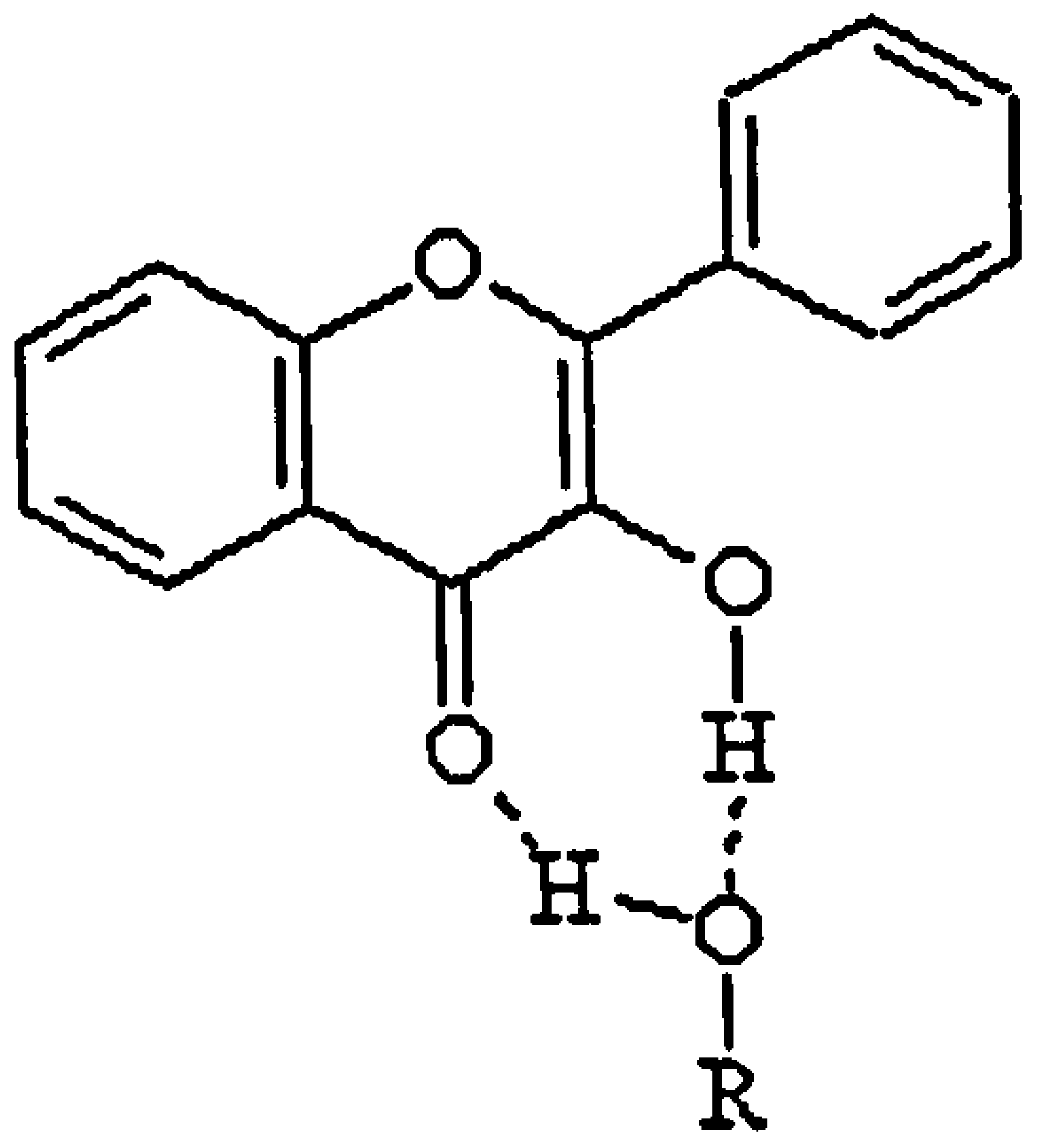

Fig. 1.4.11 Proposed structure for cyclically hydrogen bonded 3-hydroxyflavone methanol monosolvate.

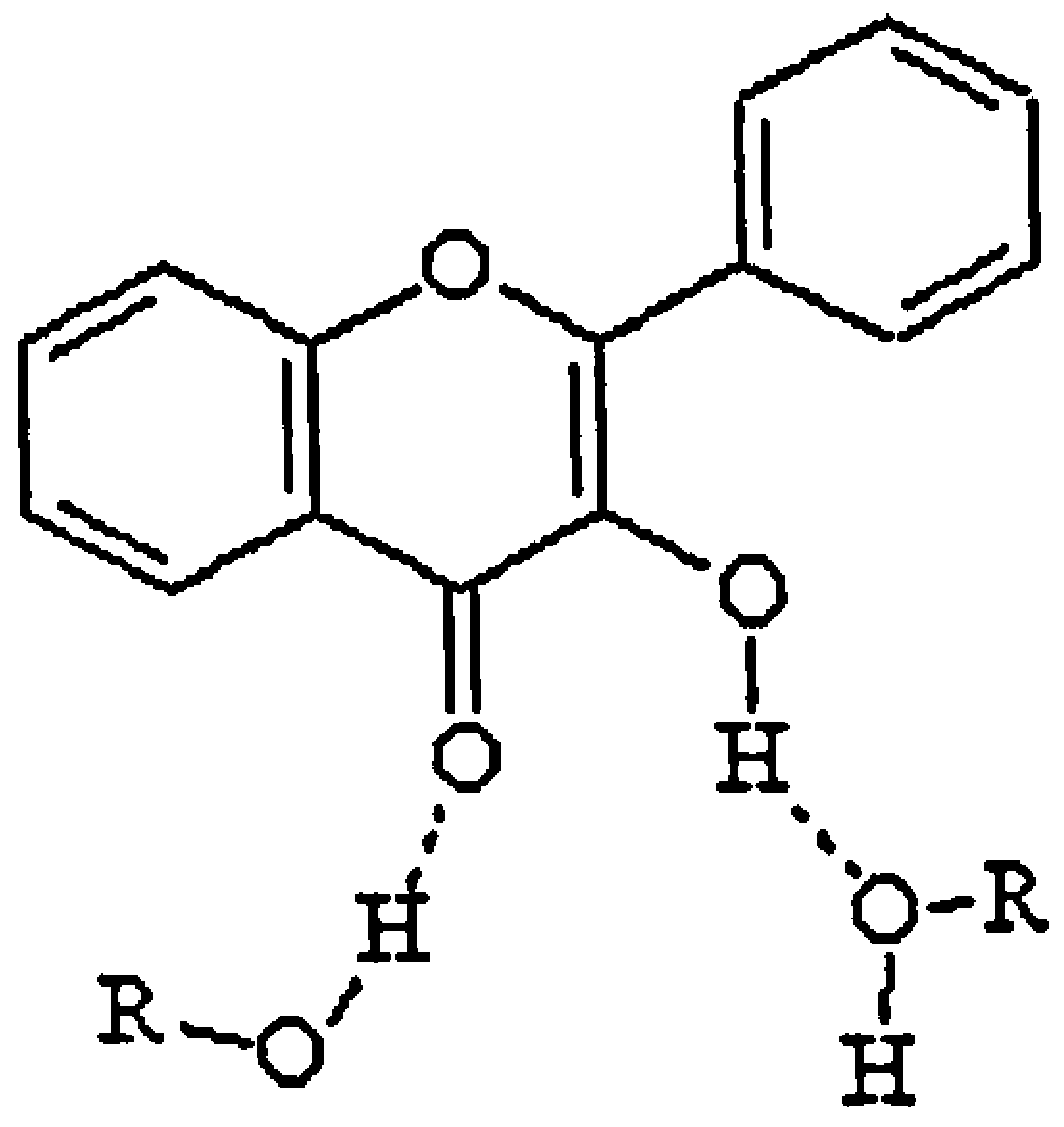

Fig. 1.4.12 Proposed structure for disolvated 3-hydroxyflavone methanol complex.

Table 1.4.3 Effect of solvent on ESIPT dynamics of 3-hydroxyflavone[73]

Solvent	τ_1, fs	τ_2, ps	τ_1 / τ_2
Dry MCH	210 ± 30	9.3 ± 0.5	1.34 ± 0.2
MCH+MeOH (drop)	160 ± 30	9.7 ± 0.5	0.69 ± 0.2
MCH sat. by MeOH	110	10.2 ± 0.5	0.49 ± 0.15
MeOH	80	10 ± 0.3	0.42 ± 0.1

Ormson et al[74] report the excited state transient spectra for **II** in methylcyclohexane with a resolution of ~ 200 fs after excitation at 295 nm. Two distinct absorption bands are present, centred around 460 (blue) and 575 nm (green). Evolution of both of these bands is clearly resolved, showing the blue band shifting from approximately 430 nm to 460 nm in approximately 10 ps. After this point the transient absorption spectrum remains approximately constant and simply decays with a lifetime of the order of 5 ns (the lifetime of the tautomer species). The shape of the green band also changes in time but the evolution is somewhat contaminated by the laser fundamental at ~590 nm. It is possible that the blue edge of the 410 - 500 nm absorption band is due to the S_1' state of **II** which then evolves into a lower energy configuration on a time-scale comparable with solvent relaxation. A study of the kinetics of this absorption band should elucidate this assignment.

A molecule which has received significant attention in the literature as an analogue for ESIPT is Tinuvin P (2-(2'-hydroxy-5'-methylphenyl)benzotriazole, **IX**). Along with the *ortho*-hydroxybenzophenones, benzotriazoles such as **IX** have been used for more than thirty years as ultraviolet photostablisers in polymer systems. Upon excitation with UV light, ESIPT can take place and the rapid cycle $S_0 \rightarrow S_1 \rightarrow S_1' \rightarrow S_0' \rightarrow S_0$ can occur to dissipate the absorbed energy.

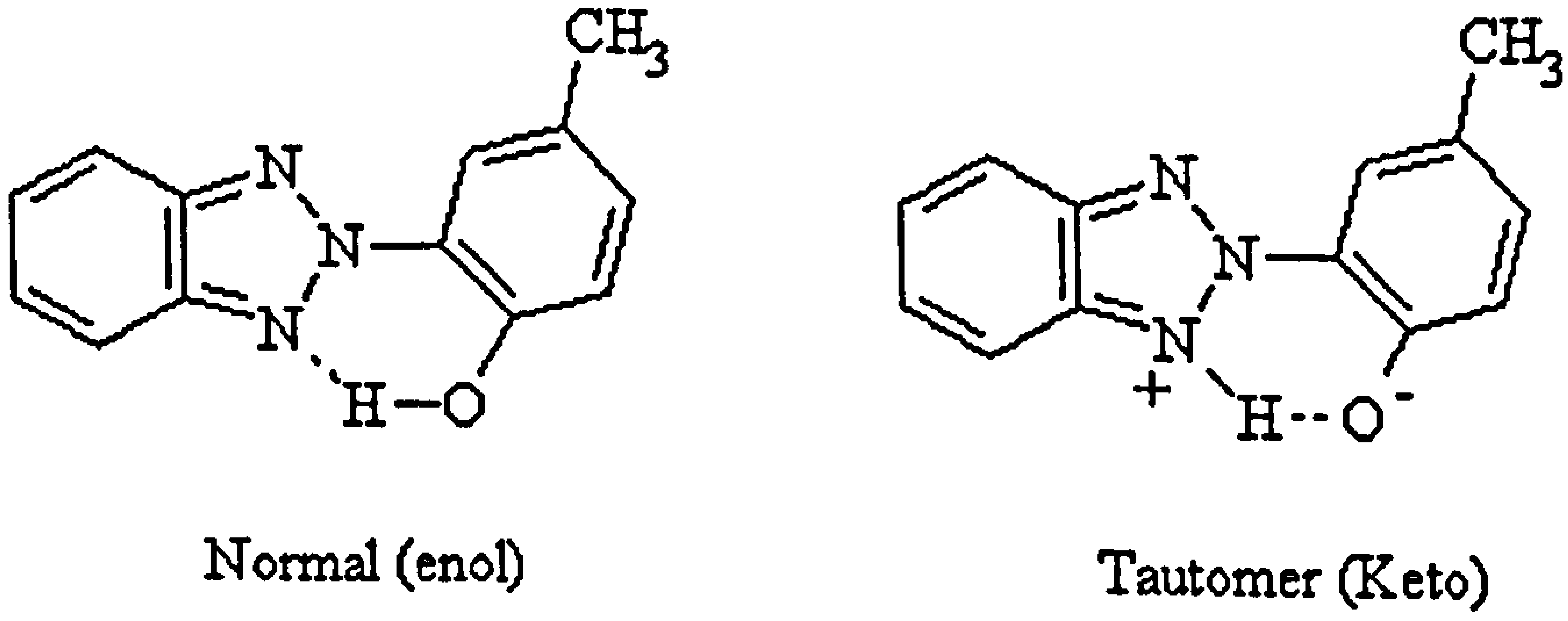

Fig. 1.4.13 Normal and tautomer structures of Tinuvin P (IX).

The enol form of **IX**, which represents the main ground state species, shows a $S_0 \rightarrow S_1$ absorption band around 350 nm and emission from the tautomer structure is located in the wavelength range between 600 and 800 nm with an extremely low fluorescence quantum yield of ~ 10^{-5}. Wiechmann et al[75] investigated the ultrafast dynamics of **IX** in non-polar solvents. Femtosecond pump-probe measurements were undertaken at a number of probe wavelengths in cyclohexane with a resolution of ~ 70 fs. The transient gain of the S_1' state in C_2Cl_4 is shown to possess a rise component of about 100 fs that is attributed to the proton transfer reaction. This is followed by ultrafast decay to the S_0' state with a time constant of ~150 fs and transformation back to the enol form within 600 fs. The rapid depopulation of the S_1' state is attributed to rapid internal conversion by vibrational redistribution, corresponding to large-amplitude motions in the low frequency range (80 to 200 cm^{-1}). Vibrationally hot molecules in the ground state are cooled on a time-scale of several tens of picoseconds by interaction with the solvent. The authors conclude that the rapid proton transfer and subsequent back transfer to the ground state enol suggest a potential energy surface with negligible potential barrier to proton transfer (as depicted in Fig.1.4.14).

In a further paper Wiechman et al[76] reported ultrafast time-resolved measurements of **IX** in a number of solvent and polymer environments. Their results on a picosecond time-scale suggest that the solvent environment strongly affects the quantum yield of the keto tautomer and the kinetics of the S_1 state. Analysis of data from **IX** with a methoxy substituent in place of the OH (so that proton transfer cannot occur) suggests that the S_1 emission is from a twisted conformer of **IX** without an intramolecular hydrogen bond (indicating that the proton transfer only occurs for the planar conformer). This is in contrast with previous explanations which suggest coupling between solvent molecules and the hydroxylic group of **IX**. DMSO was shown to exhibit by far the strongest solvent effect with significant broadening and red shifting of the enol excited state emission. The emission lifetime of the state is very short (170 ps) and the fraction of the enol species emitting is very high (60 %). Wiechmann et al conclude that the high polarity of DMSO could not be the only reason for this behaviour when compared to acetonitrile which has nearly the same polarity. However, DMSO is a hydrogen bonding solvent and they suggest that this might have some bearing upon the twisting of the enol form prior to ESIPT. Coupling to the solvent then accounts for the short fluorescence lifetime of the S_1 twisted conformer. Femtosecond spectroscopy of the tautomer species compared well with previous measurements by the same team and the authors observe that the proton transfer rate remains essentially unchanged in the different solvent environments. For **IX** in a polystyrene film, slower proton transfer was observed (approximately 200 fs) with an S_1' state lifetime of 350 fs and a back transfer (S_0'-S_0) rate of the order 1.2 ps. This result, when compared with the previously discussed paper on crystalline salicylideneanilines, suggest that although the molecule is sterically hindered in the polymer matrix, it is not sufficiently confined to restrict the low frequency modes thought to facilitate proton transfer.

Frey and Elsaesser[77] investigated the process of back proton transfer using 70 fs UV pulses to probe the absorption of **IX** in the region 310-400 nm. The data shows a decrease in absorption (compared to the steady state) and a broadening of the absorption followed by complete recovery of the ground state population within 30 ps. They conclude that the ultrafast back transfer of the proton (700 ± 100 fs) creates vibrationally hot molecules at approximately 1200 K (as estimated from the temperature dependent specific heat of the compound). Intramolecular randomisation of energy then occurs (facilitated by the large number of anharmonically coupled low frequency modes of **IX**) on a time scale comparable with the proton transfer (50 - 500 fs) followed by solvent relaxation in 30 ps.

Lenz et al[78] measured resonant and non-resonant Raman spectra for **IX** to facilitate quantitative calculation of the equilibrium vibrational temperature after excitation at 310 nm in non-polar solvents. Raman spectra were measured in the frequency range 850 and 1650 cm^{-1}. The intensity of a mode at 1552 cm^{-1} showed a pronounced solvent dependence and the authors suggest (based on normal mode analysis) that this mode contains essential contributions of the C-O stretching and O-H bending co-ordinates, which should be intimately involved in the enol-keto transformation. It is interesting to note that the O-H stretching mode at around 3200 cm^{-1} has a Franck-Condon factor which is too small to be observed in their spectra. Calculations based on the Raman data adequately reproduce the absorption spectra for the S_0-S_1 transition at times > 10 ps with a maximum vibrational temperature of 1200 K (estimated from intramolecular randomisation of 32260 cm^{-1} photon energy in all 78 vibrational modes of **IX**). On ultrafast time-scales the measured spectra show significantly broader absorption than calculated. Lenz et al conclude that this is due to a non-equilibrium thermal population distribution, i.e. a finite picosecond time interval is required prior to randomisation of the vibrational energy.

Chudoba et al[79] measured the femtosecond transient absorption of **IX** in cyclohexane for various excitation energies above and below the absorption band of the purely electronic transition. The authors found that there was no measurable difference in the kinetics of the proton transfer measured across the excited state abscrption spectrum, suggesting that there is no significant potential barrier to proton transfer under these conditions. They also observed that the absorption and emission bands overlap significantly (~2000 cm^{-1}) which they suggest is evidence of strong vibrational excitation of the keto species, since large Stokes shifts between the enol absorption and tautomer emission are usually observed. Substantial populations of molecules in high lying vibrational states may couple to the electronic transitions. Transitions from high lying vibronic states in S_1' lead to an enhancement of the emission at short wavelengths, whereas population of vibrational levels in the ground state result in an enhancement of the low-frequency absorption edge.

A recent paper by Chudoba et al[80] claims to have detected vibrational coherence in spectrally resolved transients (corrected for solvent response) observed from **IX** with a time resolution of approximately 20 fs. Experimental measurement of the S_1' rise component with improved resolution gives a proton transfer time constant of between 60-80 fs and spectrally integrated data (measured with a 10 nm band-pass filter) shows the characteristic behaviour as described above in other experiments. However, for a detection window of approximately 4 nm around 726 nm, pronounced oscillatory transmission changes persisting up to ~700 fs are observed. It was observed from systematic variation of the detection window from 716 - 784 nm that the oscillatory changes are most pronounced on the short wavelength tail of the spectrum. After subtraction of the known dynamics (rise and decay, as fitted by a four state model), Fourier analysis of the remaining oscillatory signal shows strong contributions around the frequencies of 250 and 470 cm^{-1}. The authors conclude that this is direct evidence for the importance of low-frequency modes in the proton transfer reaction. They also note that the vibrational coherence in these modes persists much longer than the formation time of the keto-state of 60 - 80 fs, suggesting that the potential energy surface along these reaction co-ordinates does not change significantly due to the proton transfer reaction. The frequency spectrum of the vibrations and the proposed potential surface of the excited state are given in Fig. 1.4.18.

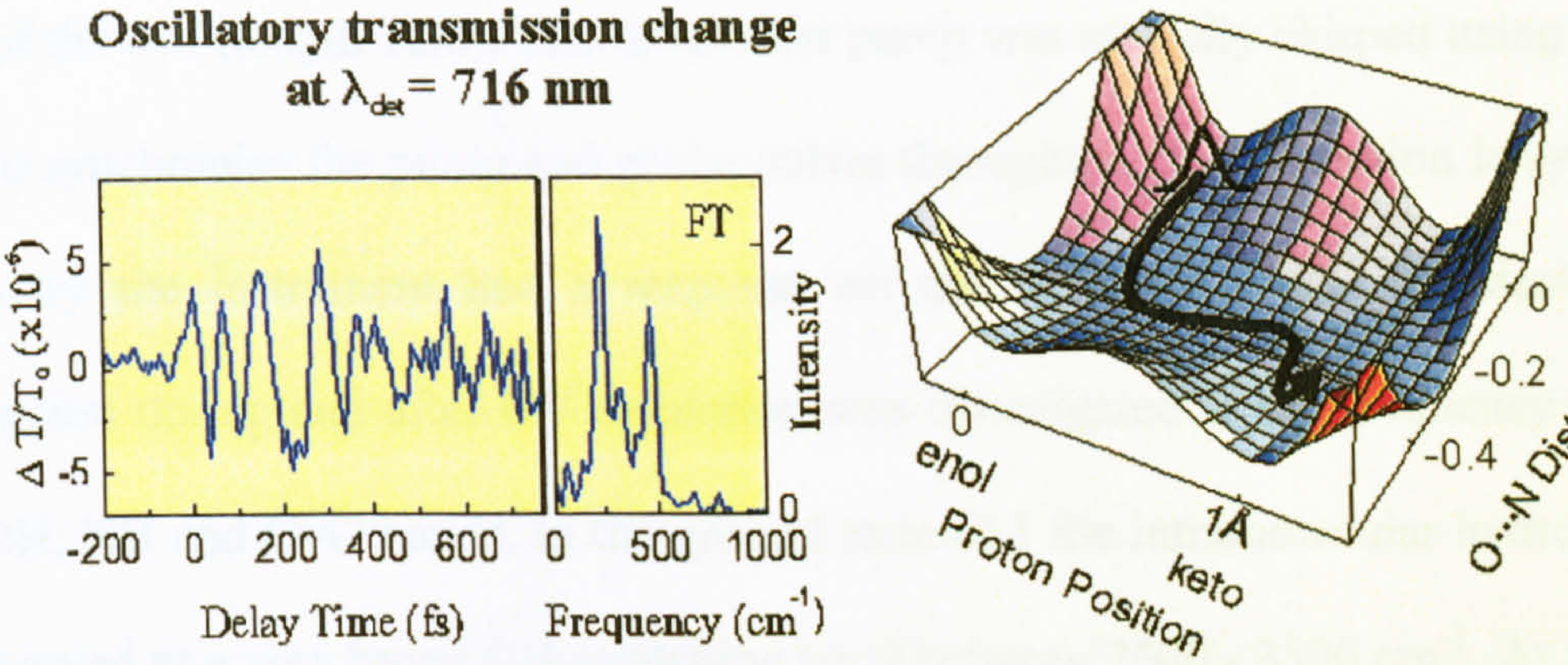

Fig. 1.4.18 Oscillatory transmission changes measured in Tinuvin P and a proposed excited state potential energy surface showing the possiblity of proton motion mediated by low frequency twisting vibrations[80]

(Reproduced from http://www.mbi-berlin.de/en/research/projects/IIe/IIe6/pot.gif).

Elsaesser and Kaiser[81] investigated the visible and infrared spectroscopy of **I** (HPBT), a structurally similar molecule to **IX**, on a picosecond time-scale. Although, strictly speaking, not an ultrafast study, transient spectra in the infrared (3 to 10 μm) for these types of molecules have not been measured on time-scales less than picoseconds due to instrumental limitations. Infrared spectroscopy specifically probes the local binding geometry of the hydroxylic proton which is transferred after electronic excitation. The changes in vibrational absorption due to an ultraviolet pump pulse are monitored by infrared probe pulses tuneable in the wavelength range from 2 to 10 μm. The absorption cross-sections of vibrational transitions in **I** are much smaller than those of the electronic S_0 - S_1 transition, i.e., the penetration depths of the ultraviolet and infrared pulses are drastically different. In order to compensate for this a pump-probe geometry was adopted in which the sample cell was transversely pumped by the ultraviolet pulses (cell thickness 0.1 cm) and the infrared beam intersected along the axis of the cell (length 1cm). The ultraviolet pump was spatially chirped using a grating pair to synchronise the pump and probe pulses throughout the interaction length. In this geometry the instrument had a response on the order of 4 ps. Transient infrared absorption during and after UV excitation was investigated in the frequency ranges of the OH, NH and C=O bands. In the ground state of I the intramolecular hydrogen bond is observed as a very broad OH-stretching band between 2600 - 3500 cm^{-1}. At 3070 cm^{-1} the CH-stretching band is superimposed on the OH band leading to a sharp peak in the spectrum. Transient spectra at 50 ps after excitation show a decrease in absorption in the wings of the OH-band, whereas the oscillator strength increases considerably between 2800 and 3100 cm^{-1}. The kinetics of the transient are shown to recreate those of transient gain measurements on this time-scale (in the same report) and the authors tentatively assign this transient band to an NH-stretching mode. They also find that the ground state infrared spectrum of **I** shows no evidence of a C=O stretching band, demonstrating that in non-polar solvents the proton is predominantly present as an OH bond (no presence of ground state keto species at time zero). Transient spectra at 50 ps show the presence of an intense band centred around 1540 cm^{-1} (in the frequency range for C=O stretching vibrations) indicating the presence of an excited state keto species. The authors conclude that these results are conclusive proof of a structural change in the molecule i.e. proton transfer, in the excited state.

Laermer et al[82] measured the rise time of the transient gain of the keto tautomer of **I** using femtosecond pump-probe spectroscopy in non-polar solvents at 630 nm. With an instrumental function determined by measurement of the ground state bleaching of Oxazine-1 dye dissolved in ethanol, deconvolution of the instrumental function from the transient signal of **I** gives a rise time of 170 ± 20 fs relating to the formation of the keto tautomer. The time-scale of this transfer once more suggests the influence on proton transfer of low frequency bending modes in the vibrational relaxation of the molecule to the keto S_1' state.

Elsaesser et al[83] measured the transient gain at 540 nm for **I** and its deuterated analogue 2-(2'-deuteroxyphenyl) benzothiazole (DBP) in non-polar C_2Cl_4. In contrast to the work on crystalline salicylideneanilines discussed earlier, no pronounced deuterium effect was observed. The time delayed formation of both keto-HBP and DBP were temporally resolved and have time constants of 160 ± 20 fs (in agreement with Laermer et al[82]) and 140 ± 20 fs respectively. The gain decays with a fluorescence lifetime of 300 ps. They conclude that this result suggests that O-H and O-D stretching vibrations are of minor importance for the transfer reaction. They suggest that, as for **IX**, the redistribution of electronic charge immediately after excitation of the enol tautomer establishes a virtually barrier-less excited state potential with a broad minimum for the keto configuration.

In conclusion, we have a picture of ultrafast proton transfer characterised by a schematic of the potential energy surface in Fig. 1.4.18. A wavepacket, created in the excited state by an ultrashort pump pulse, propagates along a reaction co-ordinate due to an origin shift of a low frequency mode. Subsequent motion along this co-ordinate leads to a change of the potential energy surface along another vibrational co-ordinate of higher frequency, opening an essentially barrier-less channel for the transfer reaction in the gas and liquid phases.

1.5 Femtosecond Laser Ablation

In this section I aim to describe the main experimental techniques and principles of laser ablation, followed by a brief literature review of laser ablation using ultrafast laser pulses (typically < 1 ps) for materials of relevance to the experimental sections of this thesis.

1.5.1 Principles

The ability to machine sub micron features in a wide variety of materials has a number of technological applications in industry and medicine. One machining method which shows promise is that of pulsed laser ablation[84,85]. Currently CO_2, nanosecond Nd: YAG and excimer laser systems are the most commonly used for machining. However, it is believed that the limiting factor for the spatial resolution of laser ablation (at a particular wavelength) is the diffusion of heat outward from the irradiated area. This diffusion length is proportional to the square root of the pulsewidth, therefore diffusion length will decrease by shortening the pulse width. Further, a nanosecond pulse will generate a plasma at a surface within its temporal pulse width. The plasma will thereby decouple the radiation from the surface and the remaining pulse energy will serve only to heat the plasma. In contrast, femtosecond pulses will effectively be absorbed by the surface before generation of a plasma plume.

Laser micromachining, specifically drilling, marking and cutting, involves the removal of material from a target substrate. Material removal takes place throughout the ablation process, where a target under laser irradiation absorbs energy and undergoes a phase transformation to liquid or vapour. The melted liquid is expelled from the interaction region (laser focus) by the recoil from the expulsion of vaporised material at the liquid/vapour phase boundary. Other processes associated with the laser matter interaction include heat conduction, radiation and plasma expansion.

The primary interaction mechanism is electronic excitation by the absorption of photons, which may be accomplished by both linear and non-linear means, depending on the properties of the material, laser wavelength and intensity. In metals, the band structure allows absorption of most moderate to low energy photons because the Fermi level is in the middle of the conduction band. For semiconductors and insulators, the Fermi energy is between the valence and conduction bands and so an absorption cut-off for photons with energy less than the bandgap is present. Absorption of energy can hence be accomplished by one of two processes; electron avalanche and multiphoton absorption.

In transparent dielectric materials, the bound valence electrons have an ionisation potential or bandgap greater than the laser photon energy. The bound electrons do not absorb the laser light at low intensities. However, in any real material there are always some conduction electrons present due to the presence of metallic impurities. Thermal or linear optical ionisation's of shallow energy levels of such impurities seed electrons for the avalanche process. A free electron, when simply oscillating in an electric field, does not gain energy when averaged over an optical cycle. However, a free electron may gain energy through collisions with bound electrons and the lattice through dephasing. This process is termed Joule heating (or inverse Bremstrahlung). The electron can be accelerated such that its kinetic energy exceeds the ionisation potential of a bound electron, therefore further collisions with bound electrons may result in an ionisation event. The free electron transfers most of its energy to the bound electron resulting in two low kinetic energy free electrons. The process may then continue leading to an avalanche where free electron density grows exponentially from the low seed electron density. When enough bound electrons are ionised by this process, a plasma with "critical density" is created and the transparent material is broken down and becomes absorbing (absorption of the initial seed electrons is negligible). For nanosecond and longer pulses the critical density is customarily taken to be ~ 10^{18} cm^{-3} since this is the density at which significant absorption for irreversible damage is considered to occur.

When the laser field strength is very high, as is the case for ultrashort pulse laser irradiation, bound electrons of the transparent material may be directly ionised through multiphoton absorption. A bound electron can be excited from the valence band to the free energy or conduction band by the simultaneous absorption of m photons in the laser pulse, such that $mh\nu \geq E_i$, where $h\nu$ is the photon energy and E_i is the ionisation potential or bandgap. This process is important in the case of high intensity fields, as the absorption of the material will deviate considerably from Beer-Lambert behaviour. The absorption becomes proportional to a power of the intensity given by the number of photons required to reach the conduction band. The equation describing multiphoton absorption is as follows;

$$\frac{dn}{dt} = N\sigma^{(m)}F^{m} \qquad 1.5.1$$

This states that the rate of change of valence electrons to conduction electrons is dictated by N, the active ion density; $\sigma^{(m)}$, the m-photon absorption cross-section and F the incident photon flux density. Electrons excited by this process may subsequently become seed electrons for the avalanche process. In certain cases, intense pulses may create enough multiphoton absorption to eliminate the need for further impact ionisations to exceed the critical electron density. In general, once a material has a critical density of electrons, it starts absorbing sufficient photon energy to undergo ablation. The absorbed energy in the electron plasma is transferred, in part, to the motion of atoms or ions in the lattice by electron-phonon coupling. Typical transfer times between hot electons and the lattice are on the order of a picosecond.

For "long" pulsed lasers (> 1 ps), ablation of material occurs through melt expulsion driven by the vapour pressure. This is an unstable process in which the dynamics of the liquid phase and the driving vapour conditions are complex. The melt layer is re-solidified, resulting in geometric changes to the ablated regions. With ultrashort, ultra-intense pulses (<<1ps) the deposited energy is limited to a shallower depth and the absorbed energy heats the material rapidly to the vapour phase, with high kinetic energy. The material is removed by direct vaporisation away from the surface without formation of a significant recast (solidified melt) layer. Most of this will be accomplished after the laser irradiation has occurred. The material is still heated by the thermal diffusion over a longer time scale. However, the resulting melt layer thickness will be small because most of the heated material reaches the vaporisation temperature and there is rapid cooling due to the steep temperature gradient. The heating of the material by heat diffusion is further reduced by the fact that a large amount of the absorbed energy is carried away by the direct vaporisation. Because little liquid is involved, ablation and material removal become highly precise.

The thermal diffusion length is approximately obtained from the expression;

$$L = \sqrt{D.t} \qquad 1.5.2$$

where L is the diffusion length, D is the ratio of thermal conductivity to the volume heat capacity and t is the pulse width. It can be seen that for sufficiently short t, L can become almost insignificant in comparison to the linear absorption depth and the focal spot size of the laser. For example, the thermal diffusion length for silicon and gallium arsenide are given in Table 1.5.1 with comparison for femtosecond, picosecond and nanosecond pulses at 395 and 790 nm and the corresponding linear absorption.

Table 1.5.1 Calculated heat affected zones for silicon and GaAs

Material	Thermal Diffusivity (cm^2s^{-1})	Absorption Depth (nm)		HAZ For Pulse Width (nm)		
		790 nm	395 nm	170 fs	300 ps	30 ns
Silicon	0.9	2500	12.5	4	164	1640
GaAs	0.24	250	20	2	85	850

Many models use this fact in asserting that thermal diffusion is negligible. However, this is not the case, for example for pulses with $t < e_t$ (the electron-phonon relaxation time) the electron plasma can still deliver significant energy to the surrounding material. In the case of ultrashort pulses the heated volume is governed by the absorption depth and therefore the threshold for ablation becomes independent of the pulse width (as long as $t << t_e$) and critically dependent on the laser intensity, due to the non-linear absorption mechanism.

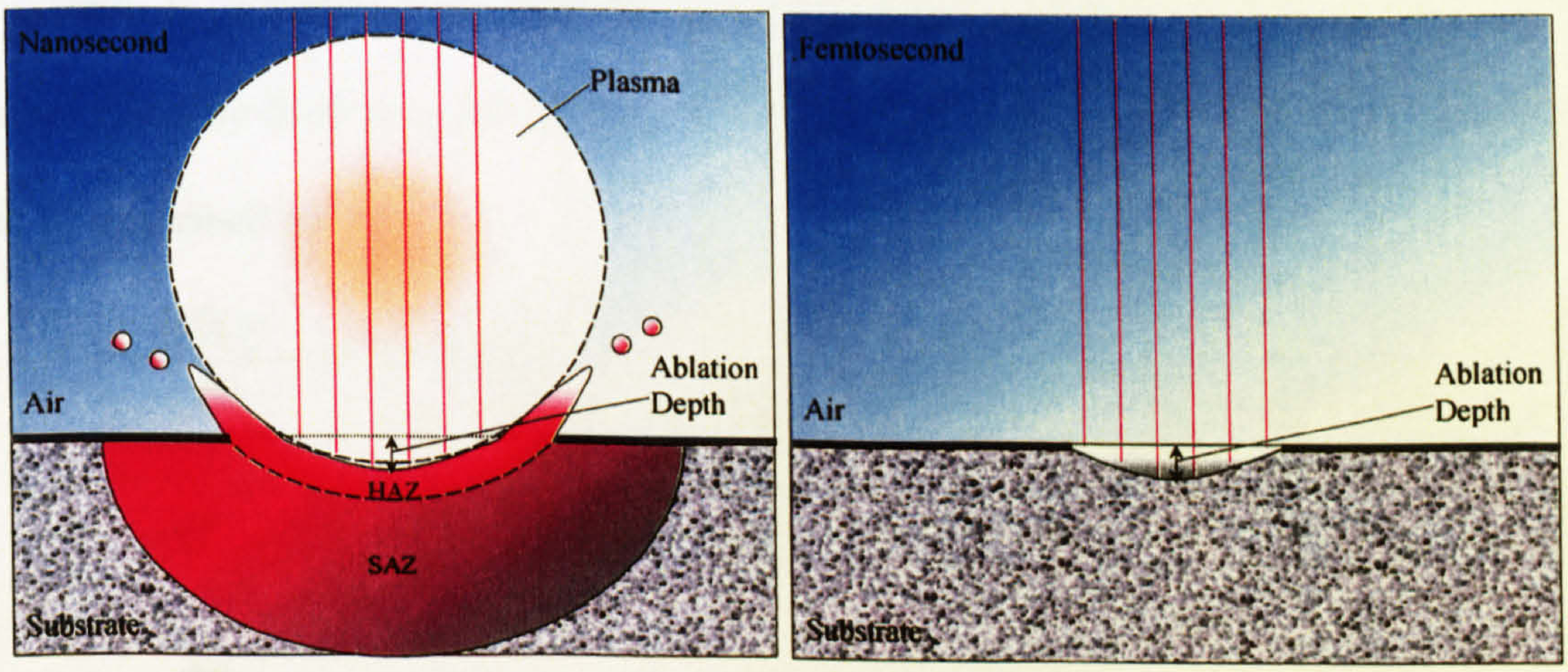

Fig. 1.5.1 Schematic model of nanosecond and femtosecond laser ablation.

The main features of nanosecond and femtosecond laser ablation are given in Fig. 1.5.1. In the nanosecond case, an absorbing plasma is formed within the pulselength, which both serves to "shield" the surface from the incoming radiation and in part transfers heat back to the substrate. A heat effected zone (HAZ) is evident due to the thermal conductivity of the material (Eqn. 1.5.2) and there is also a region which is effected by the recoil shock of the vapour, liquid and plasma phases which penetrates deep into the bulk of the material. In the femtosecond case, however, the ultrashort pulse is absorbed prior to the equilibration of electron and lattice temperatures (and certainly prior to plasma formation) and the ablation depth is approximately equal to the absorption depth. HAZ is virtually eliminated due to Eqn. 1.5.2 and shock effected zone (SAZ) is minimised due to the reduced plasma-substrate interaction.

In order to fully appreciate the advantage of ultrashort pulses in precise micromachining applications, I describe a one dimensional, two temperature diffusion model, following the arguments of Chichkov et al[86].

The evolution of absorbed laser energy involves thermalisation within the electron subsystem, energy transfer to the lattice and energy losses due to the electron heat transport into the target. We may assume that the thermalisation of the electron subsystem is ultrafast and that the electron and the lattice sub-systems can be characterised by their temperatures (T_e and T_l). The energy transport into the metal can then be described by

$$C_e \frac{\partial T_e}{\partial t} = -\frac{\partial Q(z)}{\partial z} - \gamma(T_e - T_l) + S \qquad 1.5.3$$

$$C_l \frac{\partial T_l}{\partial t} = -\gamma(T_e - T_l) \qquad 1.5.4$$

$$Q(z) = -k_e \frac{\partial T_e}{\partial z} \qquad 1.5.5$$

$$S = I(t) A \alpha \exp(-\alpha z) \qquad 1.5.6$$

where z is the direction perpendicular to the target surface, Q(z) is the heat flux, S is the laser heating source tem, I(t) is the laser intensity, A=1-R and α are the surface transmissivity and the material absorption coefficient, C_e and C_l are the heat capacities (per unit volume) of the electron and lattice subsystems, γ is the parameter characterising the electron-lattice coupling and k_e is the electron thermal conductivity. We neglect the thermal conductivity in the lattice subsystem (phonon component). The electronic heat capacity is much less than that of the lattice, therefore electrons can be heated to very high transient temperatures. When the electron temperature (in units of energy) remains smaller than the Fermi energy, the electron heat capacity and the non-equilibrium electron thermal conductivity are given by $C_e=C_e'T_e$ (where C_e' is a constant) and $k_e=k_0(T_i)\cdot T_e/T_i$ (where $k_0(T_i)$ is the conventional equilibrium thermal conductivity).

Equations 1.5.3 to 1.5.6 have three characteristic timescales τ_e, τ_i and τ_L, where $\tau_e=C_e/\gamma$ is the electron cooling time, $\tau_i=C_i/\gamma$ is the lattice heating time ($\tau_e<<\tau_i$) and τ_L is the duration of the laser pulse. These parameters define three different regimes of the laser-substrate interaction, which we term femtosecond, picosecond and nanosecond regimes.

Femtosecond Pulses

First we consider the case when $\tau_L<<\tau_e$. For $t<<\tau_e$, which is equivalent to $C_eT_e/t>>\gamma T_e$, the lattice coupling can be neglected. In this case the solution of 1.5.3 is given as (neglecting the electron heat conduction term)

$$C_e\frac{\partial T_e}{\partial t}=2I_a\alpha\exp(-\alpha z) \qquad 1.5.7$$

and gives

$$T_e(t)=\left(T_0^2+\frac{2I_a\alpha}{C_e'}t\exp(-\alpha z)\right)^{\frac{1}{2}} \qquad 1.5.8$$

where $I(t)=I_0$ is assumed constant, $I_a=I_0A$, and $T_0=T_e(0)$ is the initial temperature. At the end of the laser pulse the electron temperature is given by

$$T_e(\tau_L)=\left(\frac{2F_a\alpha}{C_e'}\right)^{\frac{1}{2}}\exp(-\alpha z) \tag{1.5.9}$$

where $T_e(\tau_L)>>T_0$ is assumed and $F_a=I_a\tau_L$ is the absorbed laser fluence.

The evolution of the electron and lattice temperatures after the laser pulse are described by 1.5.3-6 with S=0. Initial conditions for the electron and lattice temperatures are given by 1.5.9 and $T_i=T_0$. After the laser pulse the electrons cool rapidly due to energy transfer to the lattice and heat conduction to the bulk. Since the electron cooling time is very short, 1.5.4 can be written as $T_i\approx T_e(\tau_L)\ t/\tau_i$ (neglecting the initial lattice temperature). The attainable lattice temperature is determined by the average cooling time of the electrons and is given by

$$T_i\cong T_e^2(\tau_L)\frac{C_e'}{2C_i}\cong\frac{F_a\alpha}{C_i}\exp(-\alpha z) \tag{1.5.10}$$

Significant evaporation of the target occurs when C_iT_l becomes larger than $\rho\Omega$, where ρ is the density and Ω is the specific heat of evaporation. Using 1.5.10 we can write the condition for evaporation in the form

$$F_a\geq F_{th}\exp(\alpha z) \tag{1.5.11}$$

where $F_{th}\sim\rho\Omega/\alpha$ is the threshold laser fluence for evaporation with femtosecond pulses. Then the ablation depth per pulse, L is given by

$$L\approx\alpha^{-1}\ln\left(\frac{F_a}{F_{th}}\right) \tag{1.5.12}$$

This logarithmic dependence of the ablation depth on the laser fluence is well known and has been demonstrated experimentally in many instances (see for example the reviewby Shirk and Molian[87]).

Due to the very short timescales involved in the ablation with femtosecond pulses the ablation process can be considered as a direct solid-vapour (or solid-plasma) transition. In this case the lattice is heated on a picosecond time scale which results in the creation of vapour and plasma phases followed by a rapid expansion. During all these processes thermal conduction into the target can be neglected in a first approximation. These advantages of femtosecond laser ablation allow very precise and pure laser processing of materials.

Picosecond Pulses

Now we turn to the discussion of ablation with picosecond pulses when the following condition is fulfilled $\tau_e << \tau_L << \tau_i$.

At a time $t >> \tau_e$, which is equivalent to $C_e T_e / t << \gamma T_e$, equation 1.5.3 for the electron temperature, becomes quasi-stationary and 1.5.3-6 reduce to

$$\frac{\partial}{\partial z}\left(k_e \frac{\partial T_e}{\partial z}\right) - \gamma (T_e - T_i) + I_a \alpha \exp(-\alpha z) = 0 \qquad 1.5.13$$

$$T_i = \frac{1}{\tau_i} \int_0^t \exp\left(-\frac{t-\theta}{\tau_i}\right) T_e(\theta) d\theta + T_0 \qquad 1.5.14$$

Here 1.5.14 is written in the integral form. These equations describe the heating of targets with laser pulses such that $\tau_L >> \tau_e$. When the condition $t << \tau_i$ is fulfilled, 1.5.14 can be simplified due to the quasi-stationary character of the electron temperature. Neglecting T_0, we get

$$T_i \approx T_e\left(1 - \exp\left(-\frac{t}{\tau_i}\right)\right) \approx \frac{t}{\tau_i} T_e \qquad 1.5.15$$

As can be seen from this expression, in the picosecond regime the lattice temperature remains much less than the electron temperature. This allows us to neglect the lattice temperature in 1.5.13. The analysis of 1.5.13 and 15 is especially simple when the condition $k_eT_e\alpha^2 \ll \gamma T_e$ is fulfilled. In this case the electron cooling is due to the energy exchange with the lattice. The electron and lattice temperature at the end of the laser pulse are given by

$$T_e \approx \frac{I_a\alpha}{\gamma}\exp(-\alpha z), \quad T_i \approx \frac{F_a\alpha}{C_i}\exp(-\alpha z) \qquad 1.5.16$$

Note that once more the attainable lattice temperature after the laser pulse is again determined by the electron cooling time. Since $\tau_L \gg \tau_e$, the attainable lattice temperature and the lattice temperature at the end of the laser pulse are approximately equal. In femtosecond and picosecond regimes 1.5.10 and 1.5.16 give the same expressions for the lattice temperature. Therefore the expressions derived for threshold fluence and ablation depth remain unchanged.

Thus a logarithmic dependence of the ablation rate on fluence is also possible in the picosecond domain. However, in this case we have neglected the electron heat conduction to the target, and this would be critical in the formation of a melted zone within the target. In spite of this one can consider the evaporation as a direct solid-vapour (or solid-plasma) transition, although the presence of a liquid phase within the target significantly reduces the precision of laser processing in this regime.

Nanosecond Pulses

In now turn to a comparison with nanosecond laser ablation in the regime where the condition $\tau_L \gg \tau_i$ is fulfilled. In this case the electron and lattice temperatures are equal $T_e=T_i=T$ and 1.5.3 - 5 reduce to

$$C_i\frac{\partial T}{\partial t} = \frac{\partial}{\partial z}\left(k_0\frac{\partial T}{\partial z}\right) + I_a\alpha\exp(-\alpha z) \qquad 1.5.17$$

In this regime, the absorbed laser energy first heats the target surface to melting point and then to the vaporisation temperature. During the interaction the main source of energy losses is the heat conduction into the bulk of the target. The heat penetration is given by 1.5.2. The energy deposited inside the target mass is given by $E_m \sim I_a t/\rho L$. When at $t = t_{th}$ this energy becomes larger than the specific heat of evaporation Ω, significant evaporation occurs. The condition for strong evaporation can be written as

$$I > I_{th} \sim \frac{\rho\Omega D^{1/2}}{\tau_L^{1/2}}, \quad F > F_{th} \approx \rho\Omega D^{1/2} \times \tau_L^{1/2} \qquad 1.5.18$$

for laser intensity and fluence respectively. The threshold of ablation with nanosecond pulses grows as $\tau_L^{1/2}$.

In the case of ablation with long pulses there is enough time for the thermal wave to propagate into the target and to create a relatively thick layer of melted material. In this case the evaporation occurs from the liquid metal, which makes precise materials processing with nanosecond pulses very complicated.

1.5.2 Current Literature

In recent years a considerable body of work has appeared in the literature to address the effects of ultrashort pulse ablation and has been the subject of a short review[87]. Most of this work deals with experimental observations and there has been little effort invested in the explanation of the fundamental phenomena associated with such short pulses. The experimentally observed effects are detailed below for each type of material.

1.5.2.1 Metals

Initial experiments in femtosecond pulse laser ablation or, at least, surface modification studies were reported as long ago as 1985 by Downer et al[88] at the prolific AT&T Bell labs. However, for the most part these studies were concerned with the onset of surface melting and damage of semiconductor surfaces at low fluence. The first publication of femtosecond laser ablation of metals was in a paper by Krüger and Kautek in 1994[89]. Since that point various groups have published a plethora of data on the fundamental aspects of ablation, but notably few groups have shown the application of the phenomena[90,91,92,93,94].

A summary of a selection of laser ablation experiments is given in Table 1.5.2. It should be noted that the determination of the threshold laser fluence, F_{th}, for ablation is by no means trivial. For the most part, F_{th} is determined by the onset of macroscopic material removal and a fit to the two-temperature model of ablation (Eqn. 1.5.12). However, actual material removal by desorption (especially for metals under vacuum) may occur for much more modest fluence.

Table 1.5.2 Summary of femtosecond laser ablation of metal substrates.

Substrate	**Δt / fs**	**λ / nm**	**F_{th} / Jcm^{-2}**	**F / Jcm^{-2}**	**d / nm**	**Pressure**
Gold[89]	300	612	0.25	0.3	20	1 bar
Gold[95]	150	800	~0.3			1 bar
Gold[96]	500	248	0.21	0.3	17	10^{-8} bar
Nickel[96]	500	248	0.1	0.3	15	10^{-8} bar
Indium[96]	500	248	0.125	0.3	90	10^{-8} bar
Molybdenum[96]	500	248	0.15	0.3	6	10^{-8} bar
Tungsten[96]	500	248	0.4	0.6	10	10^{-8} bar
Copper[96]	500	248	0.175	0.3	8	10^{-8} bar
Platinum[89]	300	612	0.1	0.3	25	1 bar
Copper[93]	150	780	0.14			

For example, the experimental measurement by macroscopic damage for the ablation threshold of gold shows good agreement between experiments by Krüger and Kautek[89] and Preuss et al[96] (despite differences in the experimental parameters). However, the determination of fluence by optical emission from a laser produced plasma by Pronko et al[95] is slightly higher at 0.3 (± 0.1) Jcm^{-2} at 800 nm. In contrast, experiments by time-of-flight mass spectrometry give threshold fluences of ~20 mJcm^{-2}, due possibly to thermal desorption effects at high repetition rate. For the purpose of consistency we take the threshold fluence to mean the time at which significant macroscopic damage occurs.

The optical emission studies conducted by Pronko et al[95] measured the threshold fluence for pulsewidths ranging from 100 fs to 7 ns. Their results suggest that the threshold is exponentially dependent ($F_{th} \propto e^{\tau_p}$) for pulsewidths above ~5 ps and relatively independent of pulsewidth below this point. They conclude that the transition from a weak to strong pulselength dependence is due to the role of thermal diffusion vs absorption.

Taking advantage of both the more precise ablation threshold and the reduced role of thermal diffusion, Pronko et al[95] showed that features smaller than the 1/e spot size at the focus (and indeed the theoretical limit) may be ablated. A pulse from a Ti:Sapphire regenerative amplifier (150 fs, 800 nm) was prepared such that only the centre of the Gaussian spatial profile was just at the ablation threshold for a silver substrate when focused by a microscope objective. The spot size had a minimum theoretical diameter of 6 μm, whereas the diameter of the ablated region was of the order of 300 nm. The pit depth was only 52 nm, indicating that the effects of thermal diffusion had been eliminated. A comparison with a 7 ns pulsed laser showed that the minimum ablation area for the ultrashort pulse was approximately 60 % of the theoretical spot size. The morphology of the ablated region (analysed by atomic force microscopy) indicated the presence of a molten phase which had been expelled from the ablated region to form an annulus above the surface, to a height comparable to the ablation depth (~500 nm). In contrast the ultrashort pulse shows little evidence of melting, although significant redeposition of expelled material had occurred (experiments were performed in ambient atmosphere).

Chichov et al[97] investigated hole drilling of materials using a commercial Ti:Sapphire laser system. The image projection method was used to obtain a spot size of 170 μm. Laser hole drilling experiments were carried out in vacuo (~10^{-4} mbar) on 100 μm thick steel and copper foils at fluences ranging from 0.1 to 5 $\mathrm{Jcm^{-2}}$. For steel, holes drilled with 10^4 pulses in the femtosecond regime (150 fs, 0.5 $\mathrm{Jcm^{-2}}$, 780 nm) show no trace of molten material, only a vapour dust ring around the ablation site. Comparisons with both nanosecond and picosecond pulse ablation at this wavelength show that the instability introduced by the formation of a molten phase is virtually eliminated for pulses in the femtosecond region.

In a further experiment, the second harmonic at 390 nm was used to drill holes in 500 μm thick steel and copper. The ablated structures showed the existence of characteristic microstructure which they attribute to an instability of the plane evaporation front due to diffraction effects and pulse to pulse fluctuations. These microstructures had previously been observed on gold by Krüger and Kautek[89] but on a much reduced scale (close to threshold) and attributed to interference between incident and surface reflected beams. Examination of the micrographs of Chichkov et al reveals an increase in scale of the microstructure from sub-micron to ~10 microns for holes drilled with 10 to 100 pulses respectively, possibly indicating amplification and randomisation of the microstructure for repeated pulse exposure.

Preuss et al[96] reported a comprehensive study of laser ablation of metals in the ultraviolet at 248 nm and with pulses of 500 fs. The details are summarised in Table 1.5.1 with ablation depth per pulse at 0.3 Jcm^{-2} given for direct comparison. Ablation rates were also studied for both nickel and indium in air and vacuum. In each case the threshold for ablation was not significantly affected by environment. However, the ablation rate was seen to increase by a factor of 2-3 as the pressure was reduced from atmospheric to 10^{-5} mbar. They conclude that the increase in ablation rate was due to vapour pressure exceeding the ambient and minimising re-deposition.

The ablation data was compared to the model given above (Eqn 1.5.4) and shown to be in good agreement for most of the investigated materials, with the exception of indium, possibly because only unpolished samples of indium were used (thereby reducing the initial reflectance).

Simon and Ihlemann[98] reported the ablation of copper (chosen for its high thermal diffusivity) for various pulse widths from 0.16 to 50 ps at 248 nm. Holes were drilled using a Schwartzchild (all reflective) objective in order to minimise PFD and maximise energy transmission in the UV. The spot size at the focus was approximately 400 nm. For ablation at 1.2 Jcm^{-2}, melt expulsion is clearly evident at all pulse widths. However, it would appear to be reduced in scale with pulsewidth as we expect. The authors comment that 50 ps pulses produce smoother variations in structure (a uniformly expelled ring around the ablated region) as opposed to irregular ejection and resolidification of droplets. In contrast to previously published material Simon and Ihlemann maintain that the environment does not significantly affect the residual morphology.

Further experiments on copper, produced periodic (period 364 nm) imaged structures. Ablation at 500 fs and 0.6 Jcm^{-2} shows good feature definition, in contrast to ablation at 50 ps implying that edge definition is heat diffusion dependent. The quality of the edge definition for 0.6 Jcm^{-2} in comparison to that produced at 1.2 Jcm^{-2} seems also to suggest a dependence on laser fluence.

The recent work of Nolte et al[93] supports the hypothesis of a fluence dependent regime for copper. A 1 mm thick polycrystalline Cu foil was ablated using 150 fs pulses at various fluences and two logarithmic dependences were identified between ablation depth and laser fluence. For fluences < 0.5 Jcm^{-2}, a fit to the data using Eqn 1.5.4 gives F_{th} = 0.14 Jcm^{-2} and α^{-1} ~ 10 nm (the value for α^{-1} is in agreement with previously measured value of 13 nm for 780 nm). At fluences > 0.7 Jcm^{-2} the second logarithmic dependence is evident. This is characterised by a higher energy penetration depth and threshold fluence given as 80 nm and 0.46 Jcm^{-2} respectively. Analysis at various pulsewidths revealed that the first regime is only present for ultrashort pulses (where the penetration depth is greater than the thermal diffusion depth given by 1.5.2).

A qualitative difference is also observed for the two regimes. For ablation governed by the absorption depth, no trace of molten material is observed (vacuum ~ 10^{-4} mbar). At higher fluences, a thin layer of material appears. The sub-micron features (which are characteristic of the first regime) on the ablated surface melt away in the high fluence regime indicating a larger heat penetration depth.

A theoretical treatment using a two-temperature model, concluded that for fluences below 0.5 Jcm^{-2} the hot electron density is low and energy transfer out of the skin depth becomes negligible. For higher pulse energies the influence of electronic heat conduction becomes important and the second ablation regime appears.

In summary, ultrashort pulses for metal ablation offer benefit in terms of increased resolution due to minimisation of heat diffusion in the low fluence regime.

1.5.2.2 Semiconductors

The ablation of metals has always been noted to be different from the ablation of semiconductors and insulators at modest fluences. This difference is due to the transition from linear to non-linear processes, including multiphoton absorption.

The initial study of semiconductor microstructuring by femtosecond ablation was undertaken by Downer et al[88]. They describe a method using a pump-probe technique to image excited surfaces as a function of time. Laser induced reflectivity changes of the surface due to a 620 nm pump pulse are observed to occur on a timescale comparable with the pulsewidth (~80 fs). However, the reflectivity has a rise time corresponding to the electron-phonon relaxation time of 1 ps. For fluences below approximately 2.5 times the melting threshold, the reflectivity then remains relatively constant until later than 1 ns, when resolidification begins. At higher fluence levels ablation of the central region occurs, indicated by a darkening of the image due to scattering of the probe by hot silicon clusters ejected from the melt pool.

Tom et al[99] reported further evidence of laser induced disorder using time resolved surface second harmonic generation on a silicon substrate. They found that the SH reflection changed abruptly in a way which is consistent with the top 75-130 Å of the silicon surface losing cubic symmetry in <150 fs. Because this timescale is less than twice the electron-phonon relaxation time the result suggests that the laser induces disorder before the phonons equilibrate above the melting temperature. At the laser intensities used, 5 % of the valence band is photoexcited if we assume linear absorption and even more if non-linear absorption is considered. At 10 % promotion from the valence band, there is already the equivalent to a charged defect at next-nearest-neighbour sites which could force the atoms to conform to a random configuration. At

40 % the bonding is sufficiently weakened that the lattice is predicted to be unstable due to shear stress. At greater than 40 % it is suggested that the lattice is unstable to the small amount of vibrational energy transferred to the lattice in the first 100 fs. In any case, if the atoms disorder this quickly, they are probably cold, compared to the equilibrium melt. A previous experiment by Kanemitsu et al[100] using 400 fs pulses also (in retrospect) seems to support this conclusion i.e. that liquid silicon is formed during the pulse duration but superheated on a timescale comparable with electron-phonon equilibration. They also analyse the anomalous surface transformations near threshold which clearly indicate that the silicon has melted and formed a raised amorphous ring of material at the extremity of the melted region. They conclude that these multi-annular surface transformations are consistent with a thermal shock wave due to the expansion and subsequent contraction of the surface on cooling.

In a number of recent papers, gallium arsenide has also been shown to undergo similar surface transformations[101,102,103]. Glezer et al[104] suggested that ultrafast transitions occur when high intensity femtosecond pulses are incident on GaAs surfaces. They suggest that the excited valence electrons destabilise the covalent bonds within the material thereby causing a phase transition (as proposed for Si). This transition subsequently eliminates the band gap and the affected volume subsequently behaves like a metal. Multi-angle pump probe measurements were undertaken on GaAs and dielectric constants obtained from the data. It was found that for fluences above 0.05 Jcm^{-2} the Drude model was no longer accurate in predicting the dielectric constant. From this they conclude that initial increases in reflectivity are caused not by changes in dielectric constant but by significant changes in the electronic structure of the semiconductor.

Krüger and Kautek[105] compared ablation of n-type silicon <111> surfaces with femtosecond and nanosecond pulses at ~600nm. They show that although phase transformations occur on a timescale comparable or less than the pulse length (300fs), ultrashort pulse ablation eliminates melt splashing and irregular morphologies due to negligible light-plasma interaction. Although surface microstructure is not eliminated the scale of corrugation features is much reduced. They show that the threshold fluence for ultrashort pulsed ablation is dominated at low fluence by non-linear absorption leading to a well-defined penetration depth significantly less than the linear absorption. Ablation threshold is given as < 0.2 Jcm^{-2} (in agreement with Downer et al[88] for the threshold for particle emission at approximately twice the melting threshold of 0.1 Jcm^{-2}). This may indicate that a two-regime process may occur (as for Cu) with the linear absorption regime playing a role at higher fluences.

Pronko et al[106] used a two-temperature finite difference model to describe the response of semiconductors under ultrashort pulse irradiation in the energy regime where vaporisation and melting can occur. Comparison of their results was made with analysis of damage and plasma optical emission threshold fluences. They find that the threshold fluence for optical damage is of the order of 0.13 Jcm^{-2} for an 80 fs laser pulse at 800 nm. They conclude that the absorption depth is laser field strength dependent (pulselength dependent) and that the mechanism for energy absorption is avalanche electron ionisation. Absorption depth was measured at threshold fluence to be of the order of 100 nm; significantly less than the linear absorption coefficient at 800 nm (6.6 μm).

Hebst et al[107] reported use of an excimer laser to ablate both Si and Ge, using pulses of 15 mJ at 400 fs and 7.5 mJ at 100 fs. The maximum intensity achieved was 3×10^{13} Wcm^{-2}. Samples were ablated using a 1 mm aperture, imaged at 55:1 onto the sample. During the drilling process they found that vertical cones and pillars were formed as seen previously for 612 nm and 800 nm ablation. They claim that no evidence of a liquid phase was observed on any of the samples indicating that melt ejection was not the mechanism for ablation. This may be due to the decreased linear absorption depth at UV wavelengths. They observe the presence of horizontal steps of approximately $\lambda/2$ dimensions on the sides of the ablated regions. The morphology of these steps resembled threshold ablation patterns. The most probable ablation mechanism, they conclude, would appear to be a direct transition to either a vapour or plasma phase. Evidence of some minor chipping around the ablated holes was proposed to be due to sonic shock in the material, however abrasion by the rapidly expanding plasma/vapour plume is an equally valid explanation. SEM studies comparing both grounded and ungrounded samples provided evidence of permanent structural changes caused by multi-photon emission of electrons. This emission caused a negative charge distribution in the material, which in turn created defects and amorphous regions. It was found that 100 fs pulses showed better edge definition at ablated sites than the 400 fs pulses, probably an effect of reduced thermal diffusion.

It is clear that the ablation of semiconductors is non-trivial even for ultrashort pulses, although the effects of thermal diffusion and plasma-light interaction are negligible. Surface second harmonic studies seem to indicate the formation of a disordered state within the pulsewidth, which undergoes a transition to a plasma/vapour phase on a picosecond timescale.

1.5.2.3 Dielectrics

As the bandgap becomes larger than the single photon energy, non-linear processes such as multi-photon absorption and impact ionisation become more important. Investigations of the ablation behaviour of insulating ceramics, which have significantly higher bandgap compared to semiconductors, have also been investigated.

Ilhemann et al[108], in the first reported study of femtosecond laser ablation of dielectric materials, compared nanosecond and femtosecond laser ablation of fused silica. They used 193, 248 and 308 nm wavelengths with 20 - 30 ns pulses and compared results with 248 nm for 500 fs pulses. Experiments were undertaken at 1 bar for the ns pulses and at 10^{-2} mbar for femtosecond pulses, to prevent air breakdown in front of the sample. As the bandgap for fused silica is ~ 8 eV, the photon energies used were not sufficient for single photon excitation to occur in the bulk.

The effects of ablation at 248 nm, 8.2 Jcm^{-2} and 500 fs showed a two-stage ablation process on the front surface of thin samples. The femtosecond and nanosecond ablation processes differed significantly. The incubation period is only one or two pulses (as opposed to ten or more for nanosecond pulses) and the material removal rate remains constant after incubation (as opposed to increasing for larger numbers of pulses). The surface of the hole switches from a smooth, reflecting surface to a rippled, absorbing surface with a few drops of melted and recooled glass attached.

Comparison of femtosecond and nanosecond data shows that femtosecond pulses exhibit a reduced thermal diffusion effect. Large scale cracks were observed for the nanosecond samples, but not for the femtosecond case. This indicates that thermal diffusion and material heating (HAZ) cause thermo-mechanical stresses that lead to cracking. For the femtosecond pulse ablated sample, the strongest evidence for thermal damage is the presence of small droplets of material, which have melted and undergone rapid cooling. Ablation at 193 nm gave the best results for all conditions, probably due to increased linear absorption at surface impurities and therefore a reduced absorption depth. The threshold for femtosecond laser ablation at 248 nm was measured to be around 1 Jcm^{-2}.

Du et al[109] studied the breakdown of fused silica induced by near infrared photons at 780 nm, for pulse widths from 150 fs to 7 ns. The energy threshold for ablation varied with the square root of the pulse width only if the pulse width was longer than 10 ps. They also observed an increase in ablation threshold for single laser shots below approximately 1 ps, which they attribute to a saturation of the ionisation rate per unit length for fields on the order of a few $MVcm^{-1}$. They suggest that the breakdown mechanism was multi-photon ionisation for the generation of initial free electrons, followed by electron avalanche ionisation.

Barium borosilicate glass was investigated as a substrate for silicon thin films by Krüger and Kautek[110]. Femtosecond laser ablation at 612 nm (300 fs) gave an ablation threshold of 1.2 Jcm^{-2}, sharply contrasting with a linear threshold of approximately 25 Jcm^{-2} at 308 nm for 50 ns pulses where the absorption coefficient is 4400 cm^{-1} (barium borosilicate glass is practically transparent at 612 nm). They observe that it takes several pulses above threshold to generate melt ripples and first ablation features, supporting the hypothesis of an incubation effect. They suggest that inhomogenieties in the material removal indicates the necessity of defects to efficiently couple laser radiation into the surface. Massive ablation results in cavity surfaces which provide a sufficient number of defect sites allowing for homogeneous ablation. Micrographs of ablated glass reveal that the material has been mechanically broken away from the bulk, resulting in a sharp edged morphology of approximately 1 μm dimensions. They note that the expanding glass vapour abrades the brittle walls and edges and results in some micro-cracking.

In a further paper, Kautek and co-workers[111] investigated the ablation characteristics of a range of glasses for an increasing number of pulses at a fixed fluence (2.8 Jcm^{-2}, 612 nm and 300 fs). Similar morphologies are observed for all glasses investigated. Fused silica shows a more pronounced incubation effect than the other investigated glasses, in all probability due to an greater bandgap in comparison with borosilicate and lime glasses. Once ablation takes place, unique ripple structures are observed. They suggest that these structures are not generated by coherent light interference patterns because their size does not correlate with the wavelength. They associate these structures with surface plastification and melting followed by relaxation of internal mechanical stresses.

Table 1.5.3 Summary of femtosecond laser ablation of dielectric substrates.

Substrate	**λ / nm**	**Δt / fs**	**F_{th} / Jcm^{-2}**
Fused Silica	825	120	1.2
Sapphire	825	120	1.6
BaF_2	1053	400	1.6
CaF_2	1053	400	2
MgF_2	1053	400	2.1
LiF_2	1053	400	2.6

Von der Linde[112] and co-workers determined the laser induced optical breakdown thresholds in optically transparent solids using pump-probe techniques. The threshold for plasma formation in fused silica for a pulse length of approximately 120 fs was found to be in agreement with that determined previously by Du et al[109] and Krüger and Kautek[111]. Further, they showed that a significant reflectivity change occurs with a rise time of ~ 200 fs (50 % reflectivity at 10 Jcm^{-2}) indicating that an overdense electron plasma is formed on this time-scale. They also concluded that there is no systematic variation of the threshold among three different materials (MgF_2, sapphire, fused silica), indicating that the phenomena responsible for surface breakdown is extrinsic, in contrast to results already published for bulk breakdown thresholds (on picosecond and nanosecond scales).

Stuart et al[113] also studied the damage thresholds for fused silica and fluoride glasses. Damage was measured using a Normanski microscope with an ultimate resolution of approximately 0.5 μm. In contrast with the results of Von der Linde[112] they suggest that the threshold damage fluence scales with the bandgap energy, indicating that the mechanism for damage is multiphoton initiated avalanche ionisation. The damage thresholds for fluoride glasses and fused silica are given in Table 1.5.3.

The measurements of both Stuart et al[113] and Von der Linde et al[112] seem to suggest that there is no rise in ablation threshold for pulse lengths less than 1 ps in contrast with the results of Du et al[109]. This discrepancy may be attributed to the difference in measuring technique or to the effect of incubation on the substrate (Du et al measured single pulse thresholds). In a paper by Varel and co-workers[114], both single shot and 5 pulse thresholds were obtained. Thresholds determined for plasma emission showed no rise in ablation rate below 1 ps duration for either experimental condition. Thresholds determined by damage measurement show a rise in ablation rate for single shot measurements, although these are in agreement, within experimental error, with those determined from the multiple exposure measurement. They conclude that the plasma studies (which directly compare with the measurements of Du et al) confirm the findings of both Stuart et al[113] and Von der Linde[112]. Measurements by Kautek and co-workers[115] on borosilicate glass also confirm this result for pulse durations down to 20 fs.

Significant interest has been shown in polymeric materials due to their importance as photomasks in lithography. Polymers are very different from metallic and indeed oxide ceramic materials such as glass, in that they are bound together by weak bonds, van de Waals, dipole-dipole and hydrogen bonds.

The first experiments on femtosecond laser ablation of polymer substrates were by Küper and Stuke[116]. They ablated PMMA (polymethylmethacrylate) with 300 fs pulses at 248 nm and compared results with ablation for 16 ns pulses. They observe a reduced threshold for femtosecond ablation and an etch rate per pulse which does not follow the linear model of Beer-Lambert. They suggest that this is due to an incubation effect. They observe that surface roughness is also reduced for femtosecond pulses.

Küper and Stuke[117] also investigated the femtosecond laser ablation of both polytetrafluoroethylene (Teflon^{TM}, PTFE) with 248 nm laser pulses. Attempts to ablate Teflon with a nanosecond pulsed excimer laser (248 nm, 16 ns, 2Jcm^{-2}), led to a chemically degraded and disrupted surface after 50 pulses. In contrast 300 fs, 1 Jcm^{-2} pulses smoothly ablated the substrate and the edges of the ablated region showed little or no thermal damage.

The experiment used 4 mm thick commercial Teflon sheets ($\alpha_{248\ nm}$= 158 cm^{-1}, density = 2.15 g cm^{-3}) that had been polished and cleaned with methanol. Multiple holes were drilled at a range of fluences and pulse numbers at 248 nm and 300 fs. Possible residual thermal effects were eliminated by using 1 Hz repetition rate. In contrast to ablation of PMMA, the Teflon showed no measurable incubation effect. As fluence was increased, the etch rate deviated from the linear Beer-Lambert behaviour, indicating the presence of non-linear absorption. Threshold fluence for Teflon was determined to be of the order of 0.5 Jcm^{-2} for 300 fs pulses. The ablation rate per pulse increased approximately linearly between 0.5 and 1 Jcm^{-2} (from 0.4 to 0.75 μm / pulse) after which the rate of increase slowed dramatically, with a value of 1.3 μm per pulse at 4 J cm^{-2}. This is large compared to the disrupted surface that was formed by 2 Jcm^{-2} for 16 ns pulses, which has not removed a significant amount of material even after 50 pulses.

Kumagai et al[118] used ~200 fs pulses at 798 nm to ablate a variety of polymer substrates in vacuum (~10^{-5} Torr). Ablation depths for 200 pulse irradiation were measured by a stylus profile monitor. The photon energy in the IR is not sufficient to directly break the chemical bonds of the polymer (the absorption coefficient at 798 nm is 300 times less than at 248 nm) so the authors propose that a multiphoton mechanism is responsible for the observed ablation at this wavelength. Interestingly, the observed ablation rates are comparable to that of KrF laser ablation at 248 nm and 300 fs. However, the observed threshold fluence of 0.29 Jcm^{-2} significantly higher than shown for excimer pulses ~ 0.07 Jcm^{-2} for ArF ablation at 248 nm (for PTFE). Comparison of the experimental results with a multiphoton model show good agreement between experiment and 3 photon absorption for polyamide (Kapton) and 5 photon absorption for tetrafluoroethylene-hexafluoropropylene co-polymer (FEP). They conclude that solid-state high intensity femtosecond laser ablation in the infrared is a viable alternative to UV excimer laser ablation.

Bor et al[119] determined the time dependent reflectivity of PMMA, Teflon, Mylar and Kapton that had been exposed to 7 mJ (5 Jcm^{-2}), 0.5 ps pulses at 248 nm. Reflectivity was probed using 496 nm light on a picosecond timescale. The rise time of the reflectance was measured to be instrument limited, suggesting that a solid-state plasma is formed within the pulse width and decays with a time constant of the order 10 - 20 ps, giving an indication of the electron-phonon relaxation time. After 20 ps, the reflectance has dropped below that of the original unablated surface, indicating the presence of an absorbing plasma on the surface. The authors propose that this "transient mirror" could be used as a high contrast saturable absorber for UV excimer laser pulses.

A number of recent papers have reported the application of femtosecond pulsed laser microstructuring on dielectric materials. In particular Chen and co-workers[92] reported the fabrication of Bragg reflector grating structures with a period of 360 nm and a modulation depth of 80 nm in lithium niobate for DBR (distributed Bragg reflector) lasers. Davis and coworkers[91] used 120 fs laser pulses at 810 nm to write waveguide structures inside a range of glasses (silica and ZBLAN) with application to the telecommunications industry. They show that high intensity irradiation of the material produces an increase in silicon colour centres, non-bridging oxygen hole centres and peroxy radicals. In a similar application in bulk materials, Glezer et al[90] reported the application of short pulses to optical data storage. The decreased feature size of femtosecond produced damage allowed them to write binary data patterns in three dimensions with a density of $\sim 10^{13}$ bits cm^{-3} with a 0.65 Numerical Aperture objective. Comparison with 200 ps pulses shows the advantage of ultrashort pulses in reducing damage volume (feature diameters of 200 nm for 100 fs at 780 nm, compared to ~ 5 μm for 200 ps pulses) and eliminating cracking due to thermal shock.

Sub-picosecond lasers have been shown to create more precise, lower threshold ablation fluences for insulating materials[115]. Theoretical arguments point towards an increase in non-linear absorption compared to the nanosecond case. It is also evident that femtosecond pulses at fluences far above the ablation threshold cause unwanted thermal effects within the materials. In conclusion, for maximum precision in femtosecond ablation, fluences should be kept close to the ablation threshold.

---

[1] J. Manz and L. Wöste (Eds), *Femtosecond Chemistry*, VCH (1995).

---

[2] T. Baumert and G. Gerber, *Physica Scripta* T72: pp 53-68 (1997).

[3] A. H. Zewail, *J. Phys. Chem.* 100: pp12701-12724 (1996).

[4] G. Flemming, *Chemical Applications Of Ultrafast Spectroscopy*, Oxford University Press (1986).

[5] J. Cao and K. Wilson, *SPIE*, 3273, pp 219-224 (1998).

[6] K. Ledingham and P. Singhal, *In. J. Mass Spectro .& Ion Processes*, 163 (3), pp149-169 (1997).

[7] S. Potter, *Current Biology*, 6(12) pp1595-1598 (1996).

[8] A. Yariv, *Quantum Electronics*, Saunders College Publishing (1991).

[9] B. Couillaud and V. Fossati-Bellami, *Lasers & Applications*, Jan & Feb: pp 79 - 83; pp 91 - 94 (1995).

[10] W. Sibbett, R. S. Grant, D. E. Spence, *Appl. Phys. B.*, 58: p171 (1994).

[11] R. L. Sutherland, *Handbook Of Nonlinear Optics*, Marcel Dekker (1996).

[12] J. L. Martin, A. Migus, G. A. Mourou and A. H. Zewail (Eds.), *Ultrafast Phenomena VIII*, Springer-Verlag (1992).

[13] J. D. Simon, *Rev. Sci. Instru.m.* 60: p3597 (1989).

[14] A. Miller and W. Sibbett, *J. Mod. Opt.* 35, p1871 (1988).

[15] M. Asaki, C. Huang, D. Garvey, J. Zhou, H. Kapteyn, M. Murnane, *Opt. Lett.* 18 pp977-979 (1993).

[16] P. F. Curley, Ch. Spielmann, T. Brabec, F. Krausz, E. Wintner and A. J. Schmidt, *Opt. Lett.* 18: p54 (1993).

[17] A. Stingl, M. Lenzner, Ch. Spielmann, F. Krausz and R. Szipäcs, *Opt. Lett.* 20: p602 (1995).

[18] M. Reed (Ed.), *Commercial Applications Of Ultrafast Lasers* , SPIE vol. 3269, (1998).

[19] F. Salin, J. Squier, G. Mourou and G. Vaillancourt, *Opt. Lett.* 16: p1964 (1991).

[20] K. Wynne, G. D. Reid and R. M. Hochstrasser, *Opt. Lett.* 19: p895 (1994).

[21] J. Squier, F. Salin, G. Mourou and D. Harter, *Opt. Lett.* 16: p324 (1991).

[22] M. K. Reed, M. K. Steirner-Shepard and D. K. Negus, *IEEE J. Quant. Electron.* 31: p1615 (1995).

[23] A. Yariv, *Quantum Electronics*, Saunders Publishing (1991).

[24] K. L. Sala, G. A. Kenney-Wallace and G. E. Hall, *IEEE J. Quant. Electron.* QE-16: p990 (1980).

[25] F. Salin, P. Georges, G. Roger and A. Brun, *Appl. Opt.* 26: p4528 (1987).

[26] Z. L. Horvath, Z. Benko, A. P. Kovacs, H. A. Hazim and Z. Bor, *Opt. Engin.* 32: p2491 (1993).

[27] S. Ameer-Beg, A. J. Langley, I. N. Ross, W. Shaikh and P. F. Taday, *Opt. Commun.* 122: p99 (1996).

[28] R. Fork, C. Brito-Cruz, P. C. Becker and C. V. Shank, *Opt. Lett.* 12: p483 (1987).

[29] E. B. Treacy, IEEE J. Quant. Electron. QE-5, pp 454-459 (1969).

[30] A. J. Langley, W. J. Woad, I. N. Ross and W. Shaikh, *Appl. Opt.* 33: p3875 (1994).

[31] Z. Bor, *J. Mod. Opt.* 35: pp1907 - 1918 (1988).

[32] J. A. Armstrong, N. Bloembergen, J. Ducuing and P.S. Pershan, *Phys. Rev.* 127: p1918 (1962).

[33] R. L. Sutherland, *Handbook Of Nonlinear Optics (Optical Engineering: 52)*, Marcel Dekker (1996).

[34] R. Alfano, *The Supercontinuum Laser Source*, Springer-Verlag (1989).

[35] I. Golub, *Opt. Lett.* 15: p305 (1990).

[36] R. Fork, C. V. Shank, C. Hirlimann, R. Yen and W. J. Tomlinson, *Opt. Lett.* 8: p1 (1983).

[37] R. R. Alfano and S. L. Shapiro, *Phys. Rev. Lett.* 24: p584 (1970).

[38] G. Flemming, *Chemical Applications Of Ultrafast Spectroscopy*, Oxford University Press (1986).

[39] M. J. Rosker, T. S. Ross and A. H. Zewail, *Chem Phys. Lett.* **146**: pp175 - 179 (1988).

[40] U. Banin and S. Ruhman, *J. Chem. Phys.*, **98**: pp4391 - 4403 (1993).

[41] T. Hasche, S. H. Ashworth, E. Riedle, M. Woerner and T. Elsaesser, *Chem. Phys. Lett.* **244**: p164 (1995).

[42] J. L. Herek, S. Pedersen, L. Bañares and A. H. Zewail, *J. Chem. Phys.* **97**: pp 9046 - 9061 (1992).

[43] P. Foggi, L. Pettini, I. Sànta, R. Righini and S. Califano, *J. Phys. Chem.*, **99**: p7439 (1995).

[44] T. P. Dougherty and E. J. Heilweil, *Opt. Lett.* **19**: p129 (1994).

[45] N. P. Ernsting and M. Kasche, *Rev. Sci. Instrum.* **62**: p600 (1991).

[46] B. I. Green, R. M. Hochstrasser and R. B. Weisman, *J. Chem. Phys.* **70**: p1247 (1979).

[47] E. Caldin and V. Gold (Eds), *Proton Transfer Reactions*, Chapman and Hall (1975).

[48] E. L. Wehry, *Modern Fluorescence Spectroscopy(Vol: 2), Plenum Press (1976)).*

[49] S. M. Ormson and R. G. Brown, *Prog. React. Kinetics.* **19**: pp 45 - 91 (1994).

[50] D. Le Gourrierec, S. M. Ormson and R.G. Brown, *Prog. React. Kinetics.* **19**: pp 211 - 275 (1994).

[51] M. Kasha, *J. Chem. Soc., Faraday Trans.* **82(2)**: p2379 (1986).

[52] A.Weller, *Electrochem.* **60**: pp 1144 - 1147 (1956).

[53] T. Sekikawa, T. Kobayashi and T. Inabe, *J. Phys. Chem. A.* **101**: pp 644 - 649 (1997).

[54] T. Kobayashi, T. Sekikawa, T. Inabe, *J.Lumin.* **72-74**: pp 508 - 510 (1997).

[55] S. Mitra, N. Tamai, *Chem. Phys. Lett.* **282**: pp 391 - 397 (1998).

[56] C. A. Taylor, M. A. El-Bayoumi, M. Kasha, *Proc.Natl. Acad. Sci. U.S.A.* **63**: p253 (1969).

[57] R. Lopez, P. Long, D. Solgadi, B. Soep, J. Syage and Ph. Millie, *Chem. Phys. Lett.* **273**: pp219 - 226 (1997).

[58] A. Douhal, S. K. Kim and A. Zewail, Nature, **378**: pp 260 - 263 (1995).

[59] S. Takeuchi and T. Tahara, *Chem. Phys. Lett.* **277**: pp 340 - 346 (1997).

[60] D. E. Folmer, L. Poth, E. S. Wisniewski and A. W. Castleman Jr. *Chem. Phys. Lett.* **287**: pp 1 - 7 (1998).

[61] P. K. Sengupta and M. Kasha, *Chem.Phys.Lett.* **68**: pp382 - 385 (1979).

[62]Yu. L. Frovlov, Yu. M. Sapozhnikov, S. S. Barer, N. N. Pagodaeva and N. A. Tyukavkina, *Izv. Akad. Nauk. USSR. Ser. Khim.* **10**: pp2364 - 2367 (1974).

[63]G. J. Wolfe and P. J. Thistlethwaite, *J.Am.Chem.Soc.* **103**:pp 6916 - 6923 (1981).

[64] M. Itoh, K. Tokumura, Y. Tanimoto, Y. Okada, H. Takeuchi, K. Obi and I. Tanaka, *J. Am. Chem. Soc.* **104**: pp4146 - 4150 (1982).

[65] G. A. Brucker, D. F. Kelley and T. C. Swinney, *J. Phys. Chem.* **95**: pp3190 - 3195 (1991).

[66] M. Sarker and P. K. Sengupta, *Chem. Phys. Lett.* **179**: pp68 - 72 (1991).

[67] D. McMorrow and M. Kasha, *J.Am.Chem.Soc.* **105**: pp5133 - 5134 (1983). J.Phys.Chem. 88:2235-2243, (1984)

[68] D. McMorrow and M. Kasha, *J.Phys.Chem.* **88**: pp2235 - 2243 (1984)

[69] D. McMorrow, T. P. Dzugan and T. J. Aartsma, *Chem. Phys. Lett.* **103**: pp492 - 496 (1984)

[70] G. A. Brucker and D. F. Kelley, *J.Phys.Chem.* **92**: pp3805 - 3809 (1988).

[71] N. P. Ernsting and B. Dick, *J.Chem.Phys.* **136**: pp181 - 186 (1989).

---

[72] A. Peluso, C. Adamo and G. Del Re, *J. Math. Chem.* 89: pp249 - 274 (1992).

[73] B. J. Schwartz, L. A. Peteanu and C. B. Harris, *J. Phys. Chem.* 96: pp 3591 - 3598 (1992).

[74] S. M. Ormson, D. Le Gourrierec, R. G. Brown an P. Foggi, J. Chem. Soc., Chem. Commun. pp2133 - 2134 (1995).

[75] M. Wiechmann, H. Port, F. Laermer, W. Frey and T. Elsaesser, *Chem. Phys. Lett.* 165: pp 28 - 34 (1990).

[76] M. Wiechmann, H. Port, W. Frey, F. Lärmer and T. Elsaesser, *J. Phys. Chem.* 95: pp 1918 - 1923 (1991).

[77]W. Frey and T. Elsaesser, *Chem. Phys. Lett.* 189: pp 565 - 570 (1992).

[78] K. Lenz, M. Pfeiffer, A. Lau, T. Elsaesser, *Chem. Phys. Lett.* 229: pp 340 - 346 (1994).

[79] C. Chudoba, S. Lutgen, T. Jentzsch, E. Riedle, M. Woerner and T. Elsaesser, *Chem. Phys. Lett.* 240: pp 35 - 41 (1995).

[80] C. Chudoba, E. Riedle, M. Pfeiffer and T. Elsaesser, *Chem. Phys. Lett.* 263: pp 622 - 628 (1996).

[81] T. Elsaesser and W. Kaiser, *Chem. Phys. Lett.* 128: pp 231 - 237 (1986).

[82] F. Laermer, T. Elsaesser and W. Kaiser, *Chem. Phys. Lett.* 148: pp 119 - 124 (1988).

[83] T. Elsaesser, F. Laermer and W. Frey, *Inst. Phys. Conf. Ser.* 126: pp 543 - 548 (1991).

[84] J. R. Hobbs, *Laser Focus World*, 30: pp 69-72 (March, 1994).

[85] D. Stern, R. W. Schoenlien, C. A. Puliafito, E. T. Dobi, R. Birngruber and J. G. Fujimoto, *Arch. Opthalmol.* 107: pp587 - 592 (1989).

[86] B. N. Chichkov, C. Momma, S. Nolte, F. von Alvensleben and A. Tünnermann, *Appl. Phys. A.*, 63: pp 109 - 115 (1996).

[87] M. D. Shirk and P. A. Molian, *J. Laser. Appl.* 10: pp 18 - 28 (1997).

[88] M. C. Downer, R. L. Fork and C. V. Shank, *J. Opt. Soc. Am. B.* 2: pp595 - 599 (1985).

[89] W. Kautek and J. Krüger, *Proc. SPIE*, 2207: pp 600 - 611 (1994).

[90] E. N. Glezer, M. Milosavljevic, L. Huang, R. J. Finlay, T.-H. Her, J. P. Callan and E. Mazur, *Opt. Lett.* 21: pp 2023 - 2025 (1996).

[91] K. M. Davis, K. Miura, N. Sugimoto and K. Hirao, *Opt. Lett.* 21: pp 1729 - 1731 (1996).

[92] K. Chen, J. Ihlemann, P. Simon, I. Baumann and W. Sohler, *Appl. Phys. A.* 65: pp 517 - 518 (1997).

[93] S. Nolte, C. Momma, H. Jacobs, A. Tünnermann, B. N. Chichkov, B. Wellegehausen and H. Welling, *J. Opt. Soc. Am. B.*, 10: pp 2716 - 2722 (1997).

[94] T. Von Woedtke, P. Abel, J. Krüger and W. Kautek, *Sensors and Actuators B*, 42: pp 151 - 156 (1997)

[95] P. P. Pronko, S. K. Dutta, J. Squier, J. V. Rudd, D. Du and G. Mourou, *Opt. Commun.*, 114: pp 106 - 110 (1995)

[96] S. Preuss, A. Demchuk and M. Stuke, *Appl. Phys. A*, 61: pp 33 -37 (1995).

[97] B. N. Chichkov, C. Momma, S. Nolte, F. von Alvensleben and A. Tünnermann, *Appl. Phys. A.*, 63: pp 109 - 115 (1996).

[98] P. Simon and J. Ihlemann, *Appl. Surf. Sci.* 109: pp 25 - 29 (1997).

[99] H. W. K. Tom, G. D. Aumiller and C. H. Brito-Cruz, *Phys. Rev. Lett.* 60: pp 1438 - 1441 (1988).

[100] Y. Kanemitsu, Y. Ishida, I. Nakada and H. Kuroda, *Appl. Phys. Lett.* 48: pp 209 - 211 (1986).

---

[101] T. Schroder, W. Rudolf, S. V. Gororkov and I. L. Shumay, *Appl. Phys. A.*, **51**: pp 49 - 51 (1990).

[102] P. Saeta, J.-K. Wang, Y. Siegal, N. Bloembergen and E. Mazur, *Phys. Rev. Lett.* **67**: pp 1023 - 1026 (1991).

[103] S. V. Govorkov, I. L. Shumay, W. Rudolph and T. Schroder, *Opt. Lett.* **16**: pp 1013 - 1015 (1991).

[104] Y. Siegal, E. N. Glezer and E. Mazur, *Femtosecond Chemisty (Ed. J. Manz and L. Wöste)*, Chapt. **19**: VCH (1995).

[105] W. Kautek and J. Krüger, *Mat. Sci. Forum.* **173-174**: pp 17 - 22 (1995).

[106] P. P. Pronko, P. A. Van Rompay, R. K. Singh, F. Qian, D. Du and X. Liu, *Mat. Res. Soc. Symp. Proc.* **397**: pp 45 - 51 (1996).

[107] G. Herbst, M. Steiner, G. Marowasky and E. Matthias, *Mat. Res. Soc. Symp. Proc.* **397**: pp 69 - 74 (1996).

[108] J. Ihlemann, B. Wolff, P. Simon, *Appl. Phys.A.*, **54**: pp 363 - 368 (1992).

[109] D. Du, X. Liu, G. Korn, J. Squier and G. Mourou, *Appl. Phys. Lett.* **64**: pp 3071 - 3073 (1994).

[110] J. Krüger and W. Kautek, *Proc. SPIE.*, **2403**: pp 436 - 447

[111] J. Krüger and W. Kautek, *Appl. Surf. Sci.*, **96 - 98**: pp 430 - 438 (1996).

[112] D. von der Linde and H. Schüler, *Opt. Soc. Am. B.*, **13**: pp 216 - 222 (1996).

[113] B. C. Stuart, M. D. Feit, S. Herman, A. M. Rubenchik, B. W. Shore and M. D. Perry, *Phys. Rev. B.*, **53**: pp 1759 - 1761 (1996)

[114] H. Varel, D. Ashkenasi, A. Rosenfeld, R. Herrmann, F. Noack and E. Campbell, *Appl. Phys. A*, **62**, pp293 - 294 (1996).

[115] W. Kautek, J. Krüger, M. Lenzner, S. Sartania, C. Spielmann and F. Krausz, *Appl. Phys. Lett.*, **69**: pp 3146 - 3148 (1996).

[116] S. Küper and M. Stuke, *Appl. Phys. B*, **44**: pp 199 - 204 (1987).

[117] S. Küper and M. Stuke, *Appl. Phys. Lett.*, **54**: pp 4 - 6 (1989).

[118] H. Kumagai, K. Midorikawa, K. Toyoda, S. Nakamura, T. Okamoto and M. Obara, *Appl. Phys. Lett.*, **65**: pp 1850 - 1852 (1994).

[119] Z. Bor, B. Racz, G. Szabo, D. Xenakis, C. Kalpouzos and C. Fotakis, *Appl. Phys. A.*, **60**: pp 365 - 368 (1995).

Chapter 2: Experimental

This chapter details the systems developed for the experimental programs of femtosecond photochemistry and laser ablation. Section 2.1 provides details regarding the BNFL femtosecond laser system including system characterisation and typical operating parameters and procedures. Sections 2.2 and 2.3 give an account of the apparatus developed for the photochemical and ablation studies respectively.

2.1 The BNFL Ti:Sapphire Laser System

A schematic of the CRL laser system is given in Fig. 2.1.1 An argon ion laser [Coherent Innova 310] operating in multi-line visible mode [approximately 8 W] is used to optically pump a self-modelocked Titanium Sapphire laser [Coherent Mira 900F] to produce 10 nJ pulses of ~100 fs duration. The output of the Ti:Sapphire passes through an optical isolator and is positively chirped to produce 300 ps pulses for amplification in the regenerative cavity. Pulses are injected into the regenerative cavity [BMI Alpha 1000S][1], amplified and then ejected using a Pockels cell. The output from the regenerative amplifier is then temporally re-compressed to approximately 80 fs with energy of the order of 800 μJ. The regenerative amplifier is pumped using 9 W from a frequency doubled Q-switched Nd:YLF laser [BMI 621-D, 1 kHz, 200 ns].

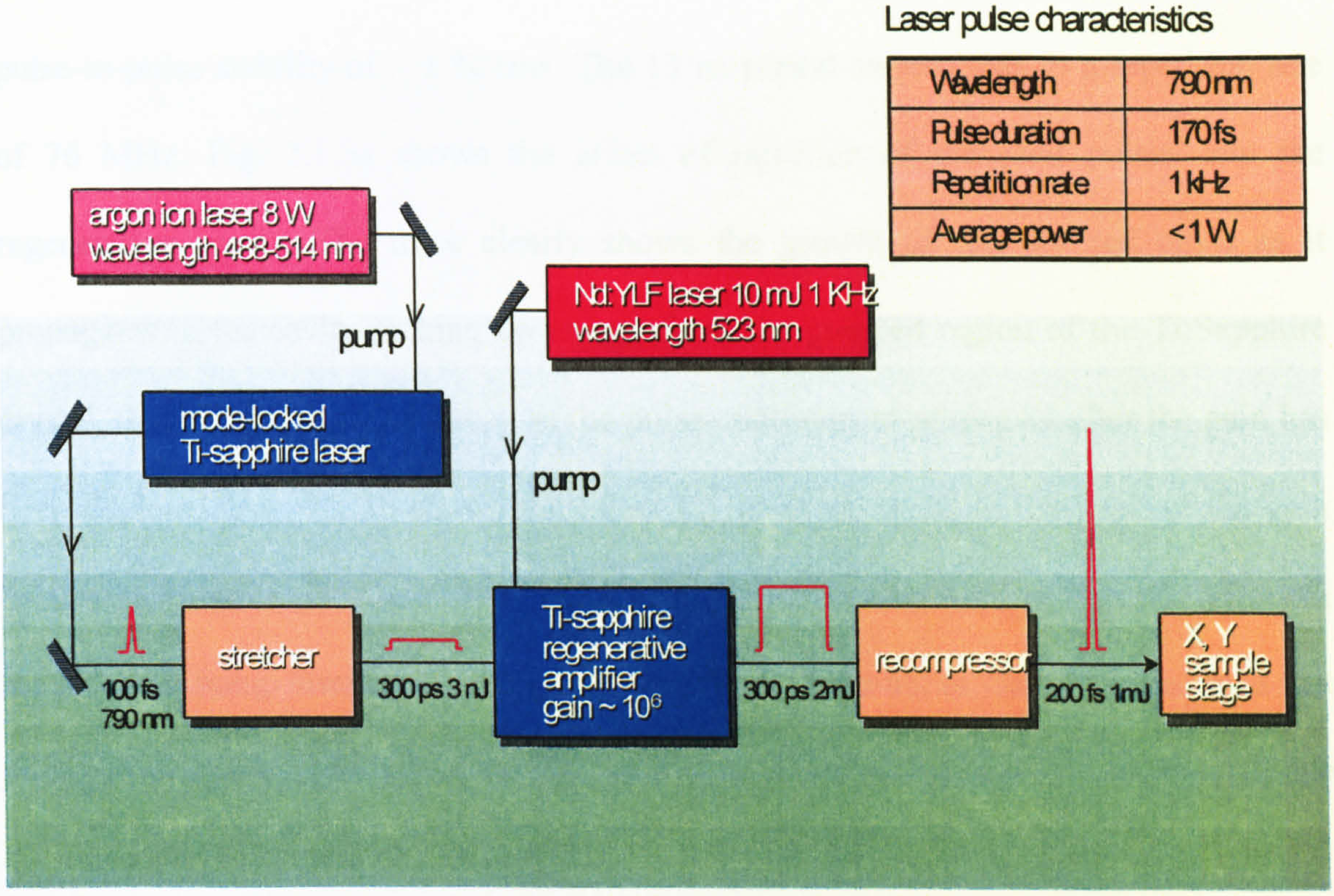

Laser pulse characteristics

Wavelength	790nm
Pulseduration	170fs
Repetitionrate	1kHz
Averagepower	<1W

Fig. 2.1.1 Schematic of BNFL femtosecond laser system.

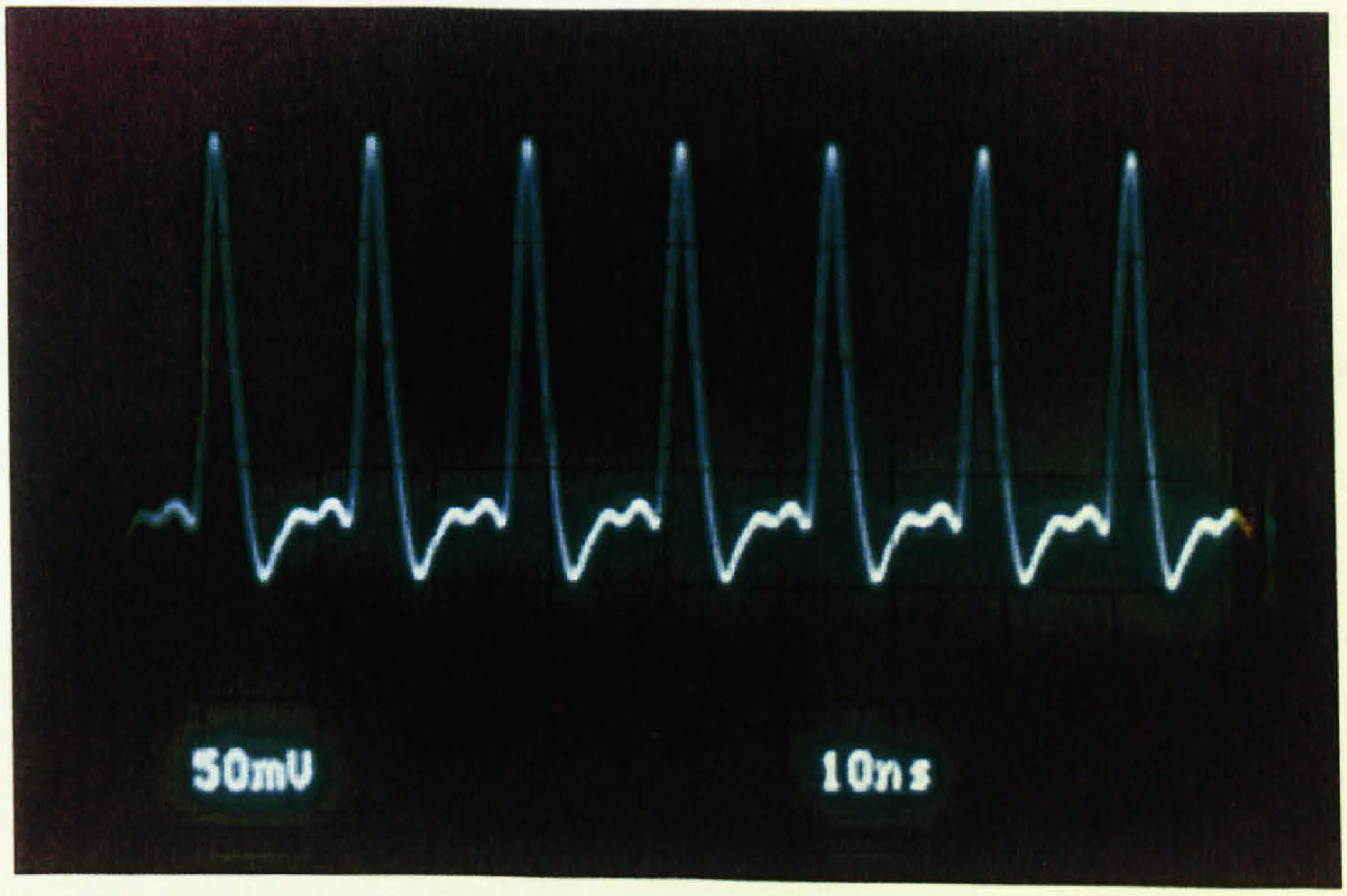

Fig. 2.1.1 Modelocked output of Mira 900F.

Solid State lasers exhibit excellent pulse to pulse stability[2]. Fig. 2.1.2 shows the modelocked output of the seed laser observed with a fast photo-diode and demonstrates pulse-to-pulse stability of ~ 1 % rms. The 13 ns period corresponds to a repetition rate of 76 MHz. Fig. 2.1.3a shows the effect of injection of the seed pulses into the regenerative cavity. The trace clearly shows the growth of the injected pulse as it propagates in the cavity picking up energy from the pumped region of the Ti:Sapphire crystal, then the exponential decay as the pulse continues to propagate after the gain has been depleted. Fig. 2.1.3b shows the effect of cavity dumping at the peak of the gain using synchronous ejection by the Pockels cell. The Pockels cell is synchronised to both the Nd:YLF pump laser and Ti:Sapphire oscillator. These traces were obtained by a fast photo-diode placed behind the cavity end mirror and coupled to a 400 MHz analogue oscilloscope [Tektronix 2465B].

The spectrum of the amplified laser pulse after recompression is routinely measured using a spectrometer [Jarrel-Ash Monospec 18 spectrograph (f/3.8), with an Alton LS-2000 diode array and 100 μm slit]. The measured bandwidth is typically of the order of 13 nm. Fig 2.1.4 shows an autocorrelation of the amplified pulses corresponding to a pulse width of ~ 80 fs. The time bandwidth product $\Delta t\Delta\nu \cong 0.500$ shows the pulse to be 1.59 times the transform limit if we assume a Sech^2 pulse profile [$\Delta t\Delta\nu = 0.315$].

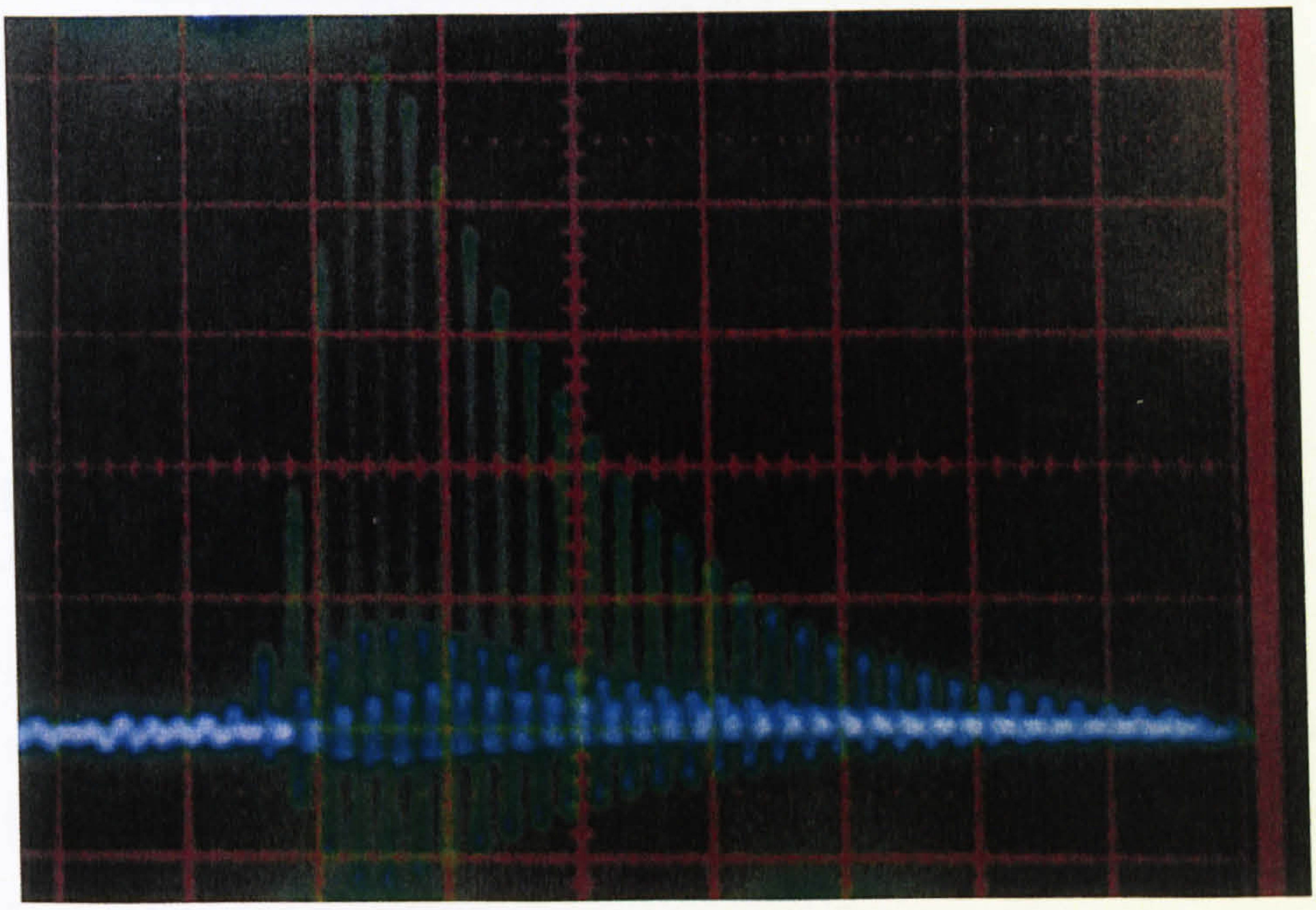

Fig. 2.1.3a Injection seeding in the regenerative amplifier cavity.

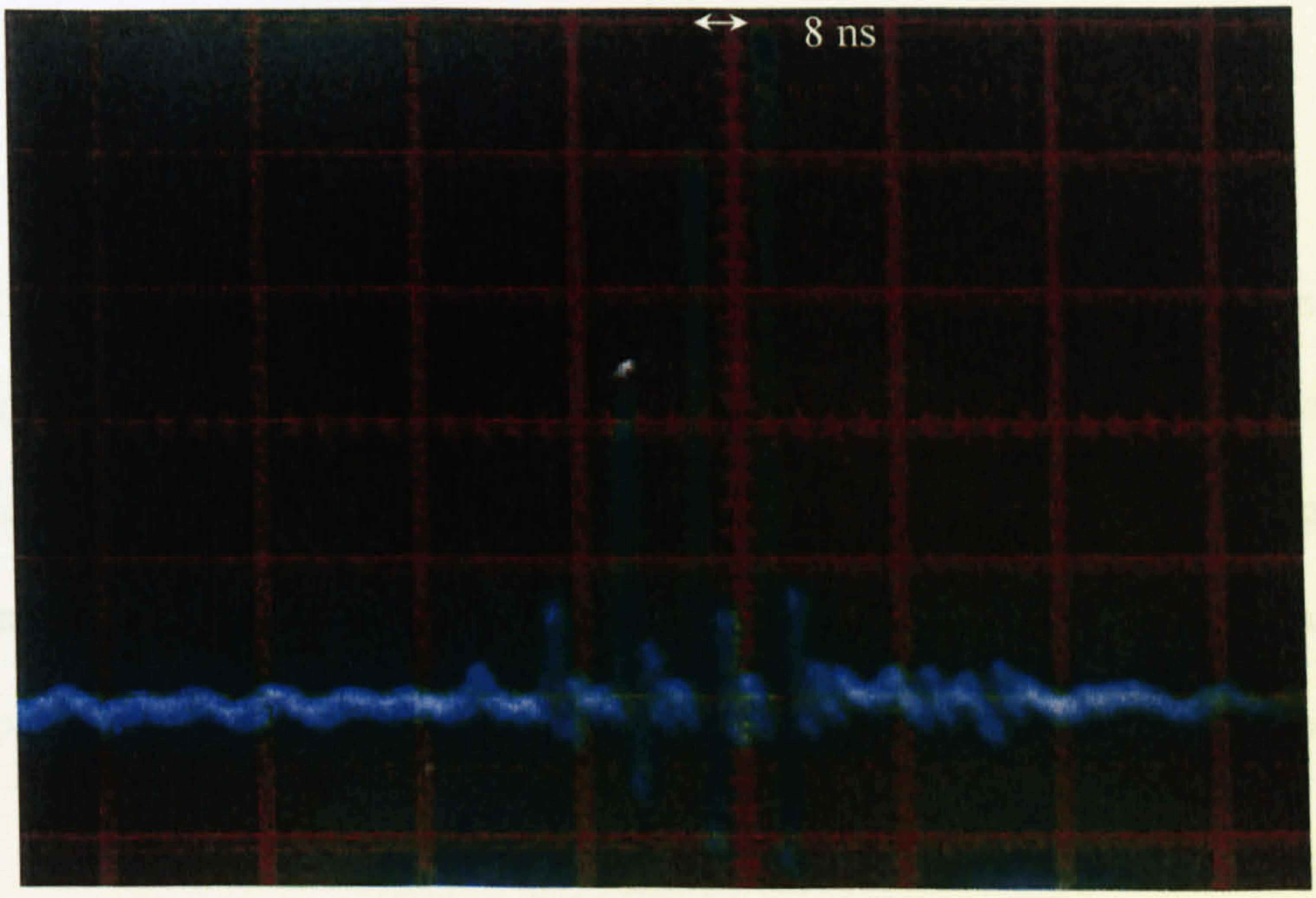

Fig. 2.1.3b Cavity dumping of the regenerative amplifier cavity.

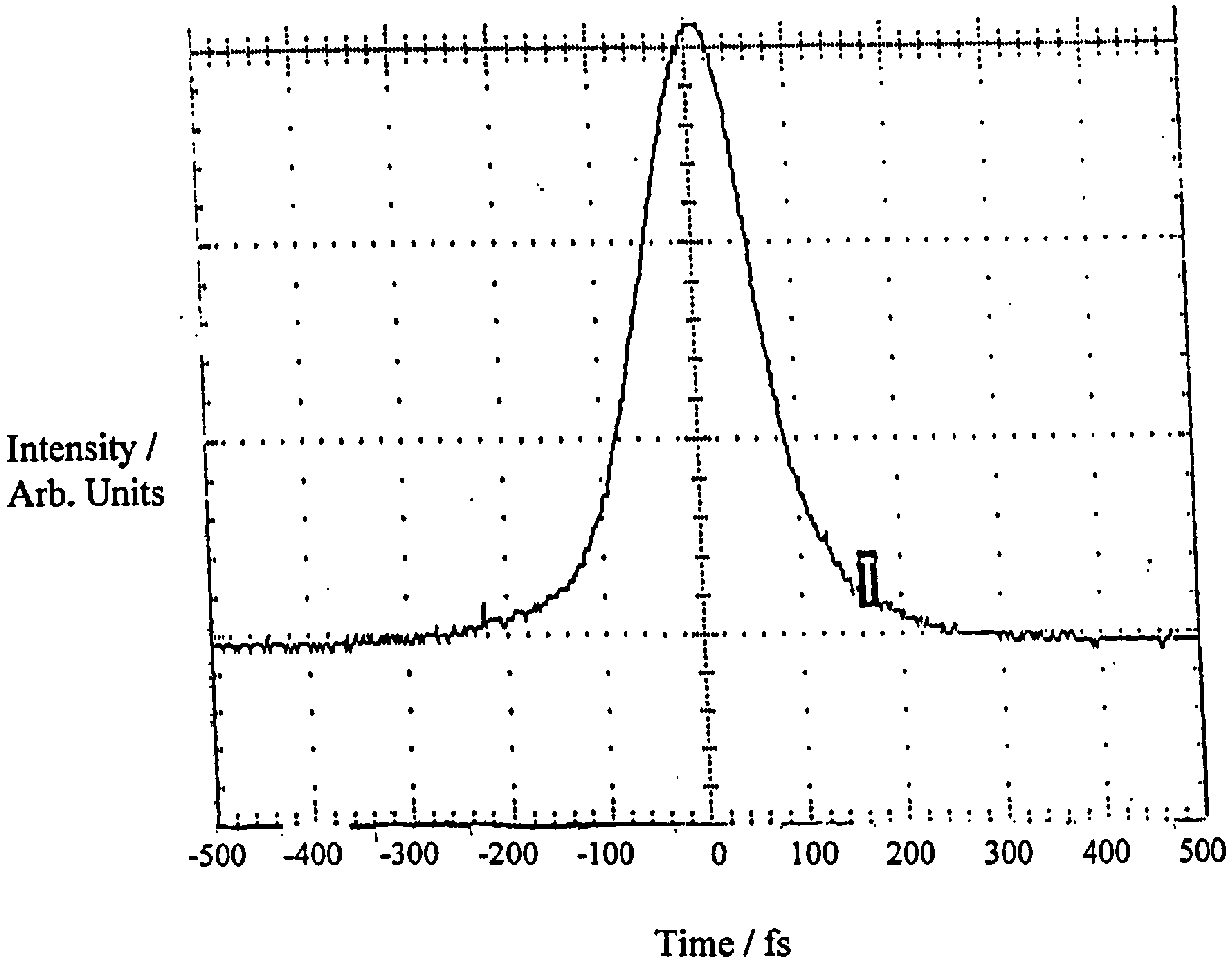

FWHM: 128fs Autocorrelation
80 fs "Real" assuming Sech^2 pulse profile

Fig. 2.1.4 Autocorrelation of amplified laser pulse after recompression.

Observation of the continuum generated by optical breakdown of the air, by focusing the compressed output of the regenerative amplifier with a 50 mm focal length lens, was found to be an excellent method for optimising the pulse length after compression. Fig. 2.1.5 shows a photograph of the continuum projected onto a card. A small spark is observed in the region of the focus indicating the breakdown of the air.

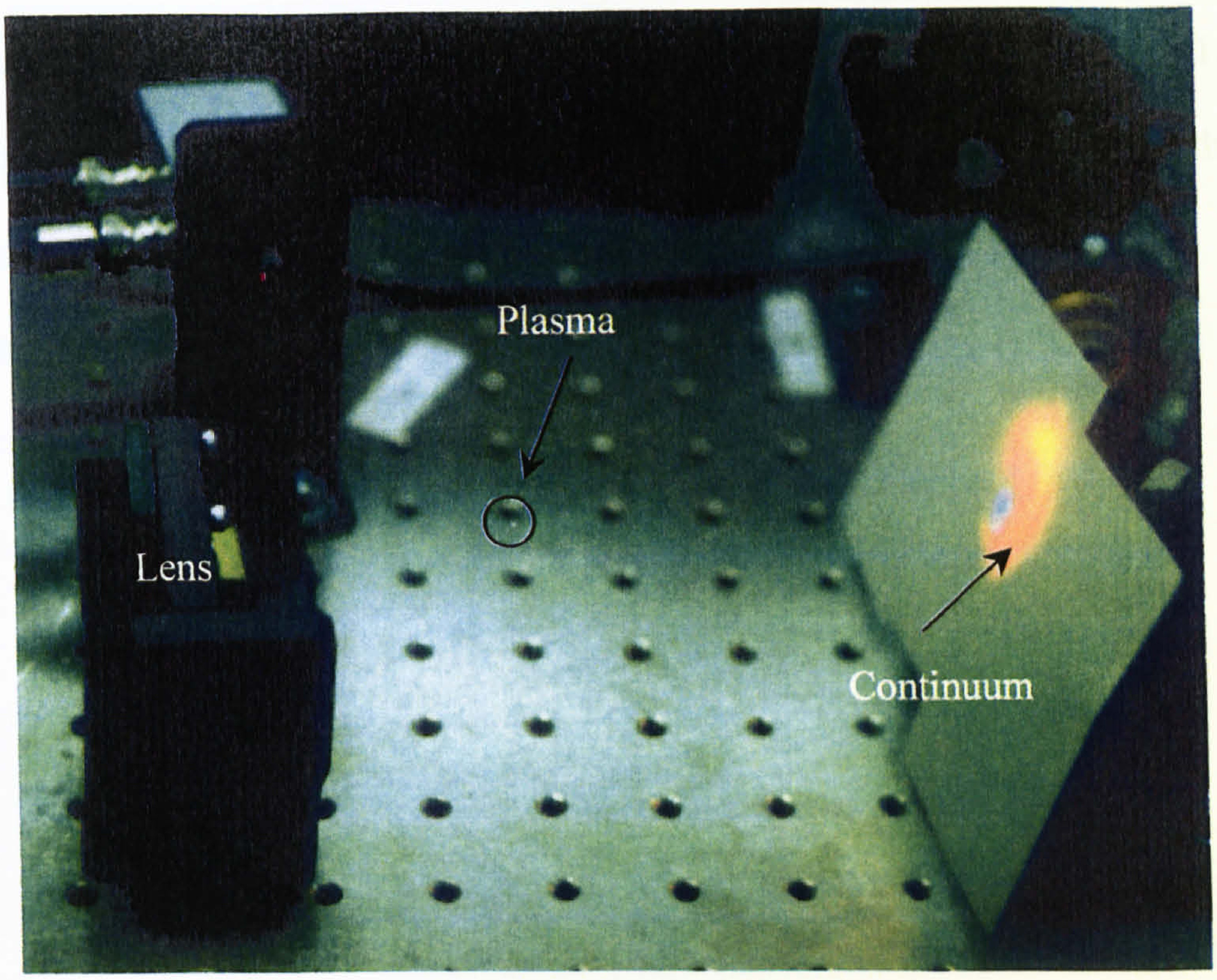

Fig. 2.1.5 Optical breakdown of the air in the vicinity of the focus of a 50 mm focal length lens.

A significant factor in the quality and reproducibility of ablated structures is the spatial profile of the laser beam as quantified by the M^2 value. Measurement of the M^2 (which should be ~1 for pure Gaussian beams) is typically by measurement of the laser divergence from[3];

$$M^2 = \frac{\theta \pi d}{\lambda} \qquad 2.1.1$$

where θ is the half angle of divergence of the laser beam and d is the diameter of the beam waste at the focus of a lens. Undertaking a measurement of θ and d for a specific lens provides us with enough information to estimate the M^2 value. For this purpose the output from the regenerative amplifier was attenuated to approximately 0.01% of the beam energy and focused using a lens with f = 1 m. The spot size was measured using a CCD beam profiler (Spirocon). Simple trigonometry gives us a value of the half angle divergence as 1.786 mrad and a corresponding M^2 of 2.13 and 1.77 for the x and y dimensions respectively. The slight ellipticity of the beam may be due to a minor misalignment of the stretcher/compressor, or more likely, an error in the measurement due to beam distortions in optical elements.

2.2 Femtosecond Pump-Probe Spectroscopy

In the following section I describe the system designed and built for dual wavelength transient kinetics at BNFL's femtosecond applications laboratory together with experimental observations of white light continuum and outline the principal features of the European user facilities to which I had access.

2.2.1 Experimental System For Dual Wavelength Transient Kinetics

For experimental measurement of two colour transient absorption kinetics an apparatus has been developed to provide pump pulses in a number of spectral ranges [given in table 2.2.1] and probe pulses with wavelength range of approximately 350 to 1000 nm from a continuum source. The system has been demonstrated using the 4'-*N*, *N*-dimethylamino-3-hydroxyflavone molecule and is shown to have an instrumental function of ~ 230 fs (as measured by the stimulated Raman emission at 450 nm in cyclohexane).

Table 2.2.1 Wavelength ranges available for excitation pulse by non-linear frequency mixing in BBO.

	Wavelength Range	Energy / μJ
Fundamental	850 - 750 nm	500 - 800
OPG	420 - 1000 nm	40 - 60
Second Harmonic	425 - 375 nm	100 - 300
Third Harmonic	280 - 250 nm	50 - 75

A complete scheme for a pump delayed two colour pump-probe apparatus is given in fig. 2.2.1 and a photograph of the actual arrangement is shown in fig. 2.2.2. Near transform limited 80 fs pulses at 790 nm [as described previously] are split into two arms using an 80:20 ultrafast beamsplitter [BS_1]. The pump beam, provided by the more intense transmitted beam, is then incident upon a gold-coated cube retroreflector [RR] mounted on a motorised translation stage [Photon Control] to provide the time delay between pump and probe. The appropriate frequency conversion is by type I SHG in BBO [0.3 mm thick], after reducing the beam radius in a 3:1 telescope formed by L_3 and L_4 (f = 300 mm and f = -100mm respectively). The second harmonic beam was then reflected by a dichroic mirror (M_{10}) to remove the fundamental and focused onto the sample by L_5 [f = 300 mm], to give an estimated spot size of 124 μm (in the diffraction limit).

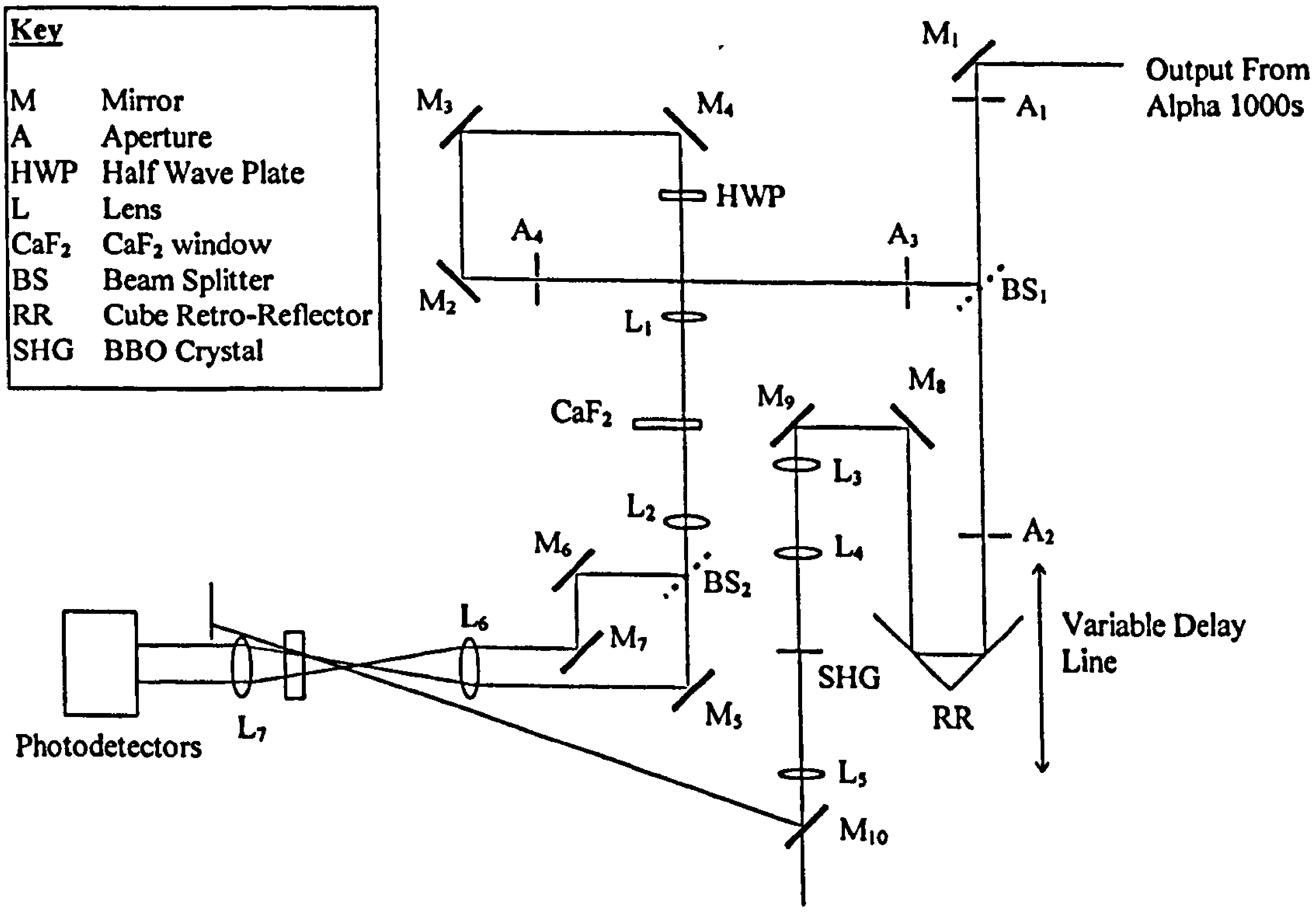

Fig. 2.2.1 Schematic of transient absorption spectrometer.

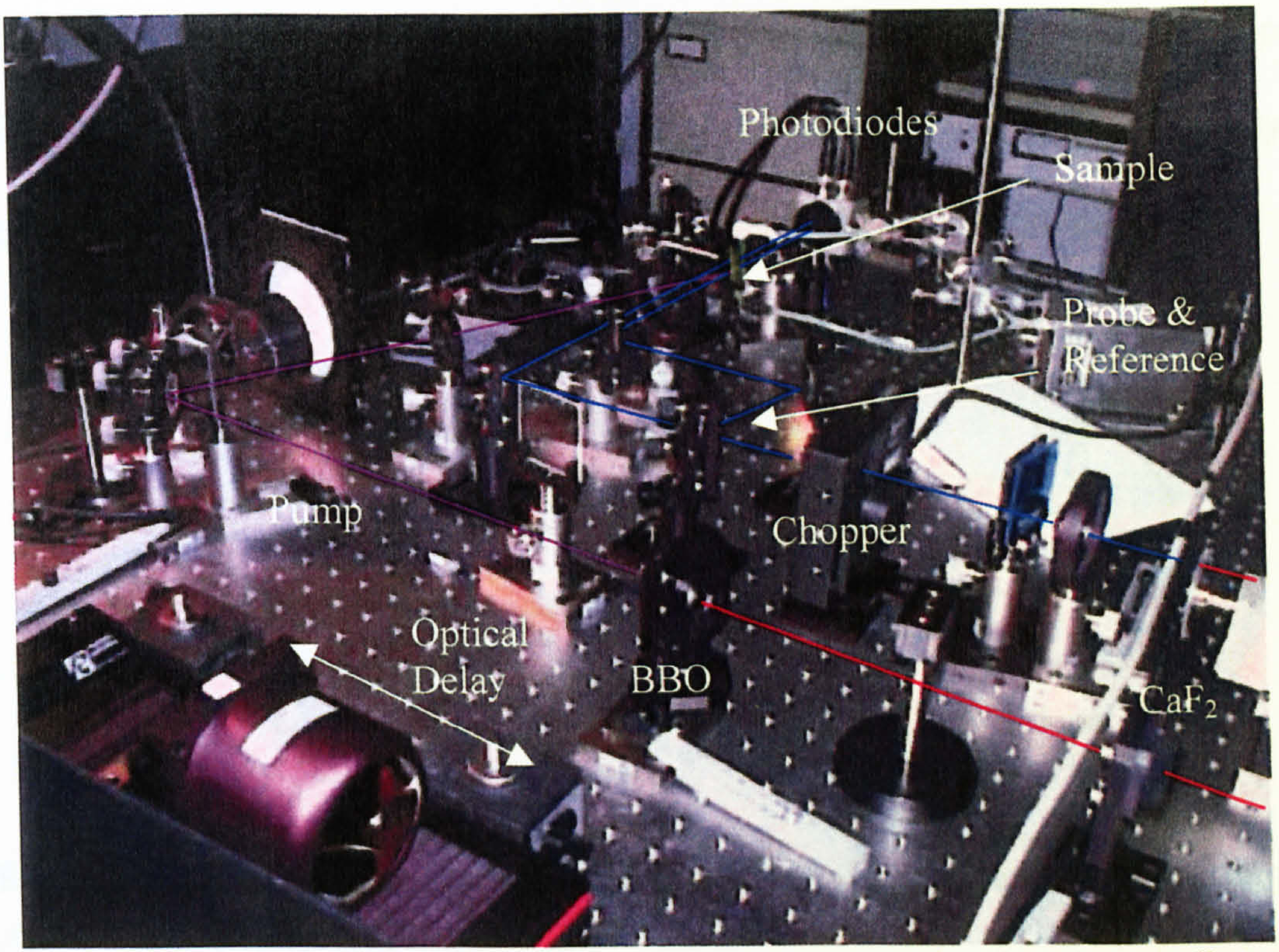

Fig. 2.2.2 Photograph of the experimental arrangement, showing the non-linear frequency conversion (CaF_2 and BBO for probe and pump respectively), optical delay, sample cell and detection electronics.

The probe beam reflected from BS_1 is reflected by M_2, M_3 and M_4 to provide a static delay and is then incident on a half wave plate [HWP] in order to bring the polarisation to the "magic angle" with respect to the pump. The probe is further attenuated using neutral density filters to approximately 10 μJ. The probe continuum is generated by focusing the beam onto a 2 mm thick CaF_2 disk rotating at approximately 2 Hz. The quality of the continuum is controlled by an iterative process of moving the position of the CaF_2 disk with respect to the focal point of the lens, the angle of the window [pathlength] and pulse energy. A brief discussion of the properties of the continuum is given in Section 2.2.2. The continuum is approximately collimated by L_2 [f = 75 mm] and split by a 50:50 aluminium beamsplitter [BS_2] to provide signal and reference beams. Both signal and reference are then focused by L_6 [f = 150 mm] into the sample cell in the fashion illustrated in Fig. 2.2.3. The diffraction limited spot size of the probe beams was of the order of 14.6 μm so that the probe volume is approximately one tenth of the pump volume ensuring uniform absorption changes across the beam.

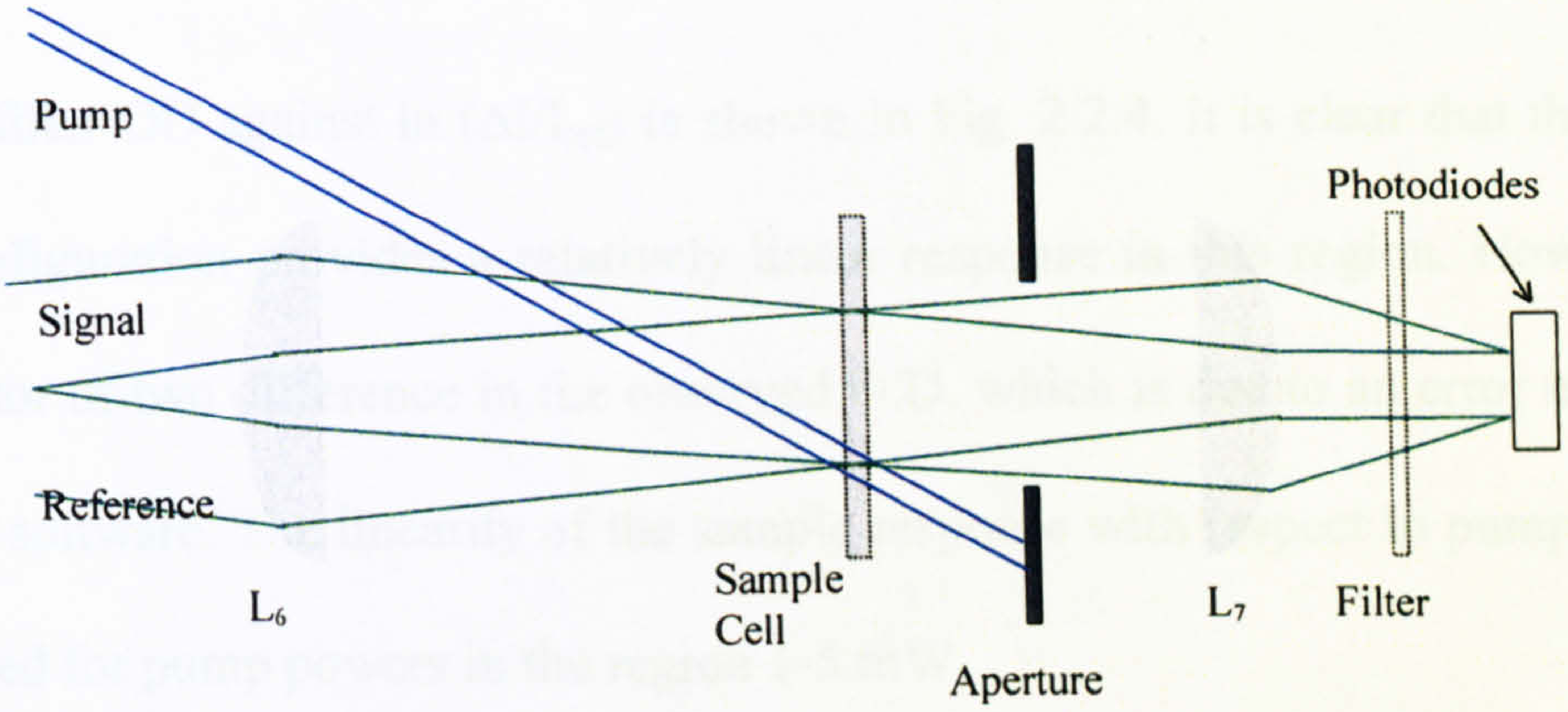

Fig. 2.2.3 Schematic of the detection geometry for referenced transient absorption.

The sample cell was made from Spectrosil Q to provide maximum transmission throughout the ultraviolet and visible wavelength range. To minimise heat conduction effects the sample solution must be flowed, so a simple 1 mm pathlength spectroscopic flow cell [Lightpath Optical Ltd] was employed. The cell was sealed to PTFE tubing using VITON high performance heat shrinkable tubing [Majortek Components]. An air tight seal was obtained by using tubing with a shrink bore of less than the cell inlet/outlet tubing without applying external stress to the cell. A small all-Teflon diaphragm pump [Whatman mini] was used to circulate the sample [flow rate ~ 0.3 lt/min] using a reservoir of approximately 100 ml.

Signal and probe beams were detected after appropriate wavelength filtering for probe (with 10 nm bandpass filters) using a dual element pin photodiode [EG&G Optoelectronics UV100BQ] with a quartz window for enhanced response in the ultraviolet. The output of each photodiode was measured using a lock-in amplifier [EG&G] synchronised to a mechanical chopper [EG&G Electro-optics].

The linearity of the detection system at 450 nm was checked by placing neutral density filters in the signal arm of the probe and measuring[4];

$$\frac{I_{reference}-I_{probe}}{I_{reference}} = \exp\left(-\Delta OD\right) \approx -\Delta OD \text{ (for small signals)} \tag{2.2.1}$$

A plot of filter OD against ln ($\Delta I/I_{ref}$) is shown in Fig. 2.2.4. It is clear that the reverse biased configuration provides a relatively linear response in this region. However, we note a factor of two difference in the observed O.D. which is due to an error in the data collection software. The linearity of the sample response with respect to pump intensity was verified for pump powers in the region 1-5 mW.

Both the lock-in amplifiers and the motorised delay stage are controlled via the GPIB interface of an IBM personal computer. Software was developed using LabView (National Instruments) providing simple integration of data collection, instrument control and data presentation by the use of virtual instruments. Data was collected at approximately twice the time constant of the Lock-in amplifier with a user selectable number of acquisitions per time delay [typically 10]. It is clear that for long acquisition times the long-term stability of the laser becomes an issue. For this reason the number of acquisitions per time delay was minimised and a number of runs [in both directions] are averaged.

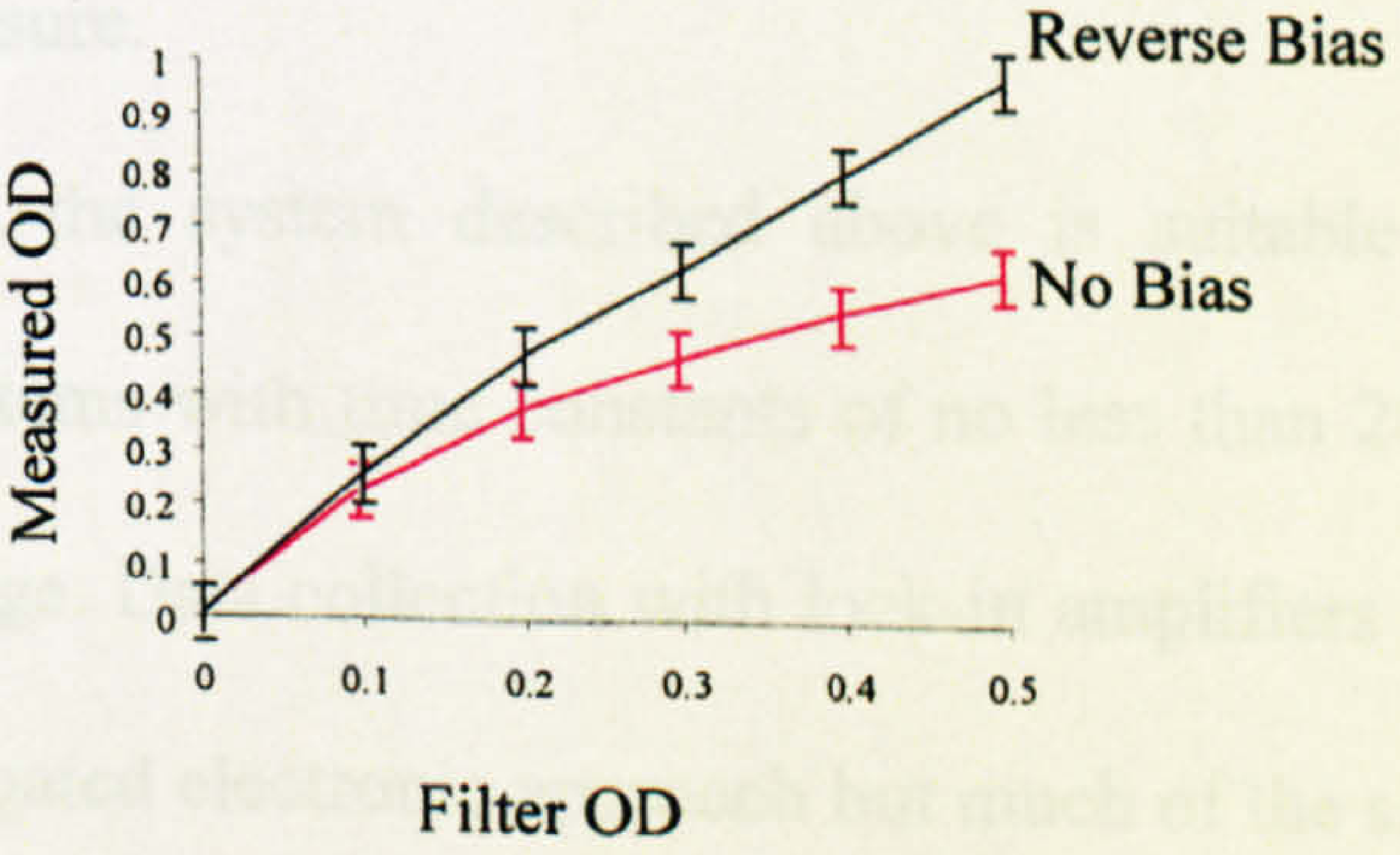

Fig. 2.2.4 Plot of filter OD with Ln ($\Delta I/I_{ref}$)

The instrumental response of the experiment may be determined by measurement of the FWHM of the stimulated Raman emission generated in the solvent at ~ 450 nm in cyclohexane. The Raman signal is shown in fig. 2.2.5 with a Gaussian pulse of FWHM 280 fs, approximately corresponding to the cross-correlation of pump and probe.

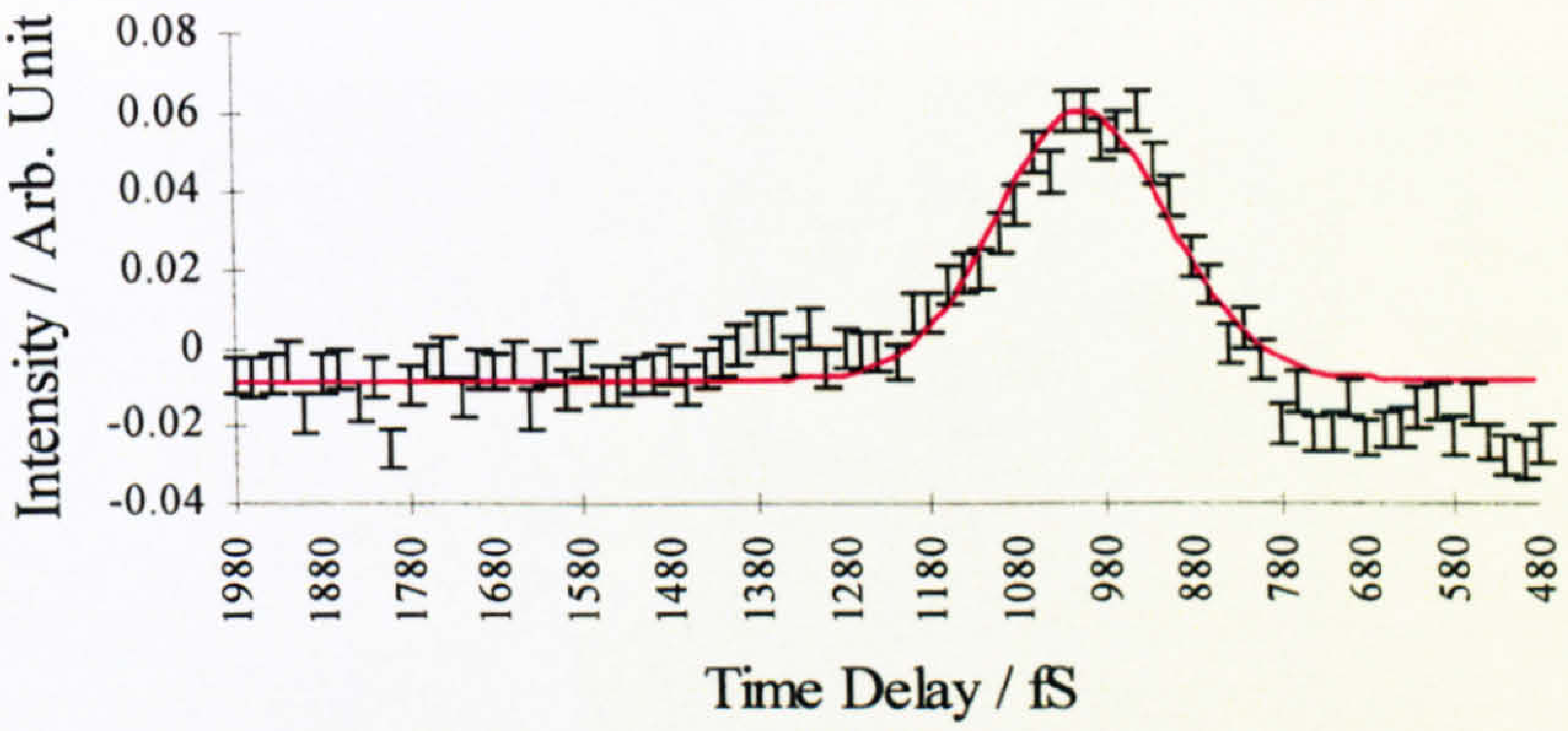

Fig. 2.2.5 Plot of stimulated Raman spike instrumental function (error bars with ±0.005) with Gaussian fit (solid red line).

Samples for analysis were prepared in solution to give an OD ~ 1.0 for a 1 mm pathlength (corresponding to cell width) at the pump wavelength. All solvents used were HPLC or spectroscopic grade to minimise possible sources of error. Samples were checked spectroscopically before and after the experiments to ensure that they had not degraded during exposure.

In conclusion the system described above is suitable for obtaining kinetic measurements on systems with time constants of no less than 280 fs with transients in the UV or visible range. Data collection with lock-in amplifiers is relatively slow when compared to an time gated electronic approach but much of the signal averaging is taken care of prior to data storage, so that approximately the same time is spent on an experimental cycle. Signal to noise is good and transients of the order of 1 % absorption can be measured with a minimum of signal averaging (10-20 acquisitions per channel).

2.2.2 Experimental Observations Of White Light Continuum

Experiments to demonstrate a stable and reproducible white light continuum were undertaken at BNFL in conjunction with the pump-probe experiments. The experimental arrangement is as in fig. 2.2.1 with the media for the generation of the continuum in the place of CaF_2.

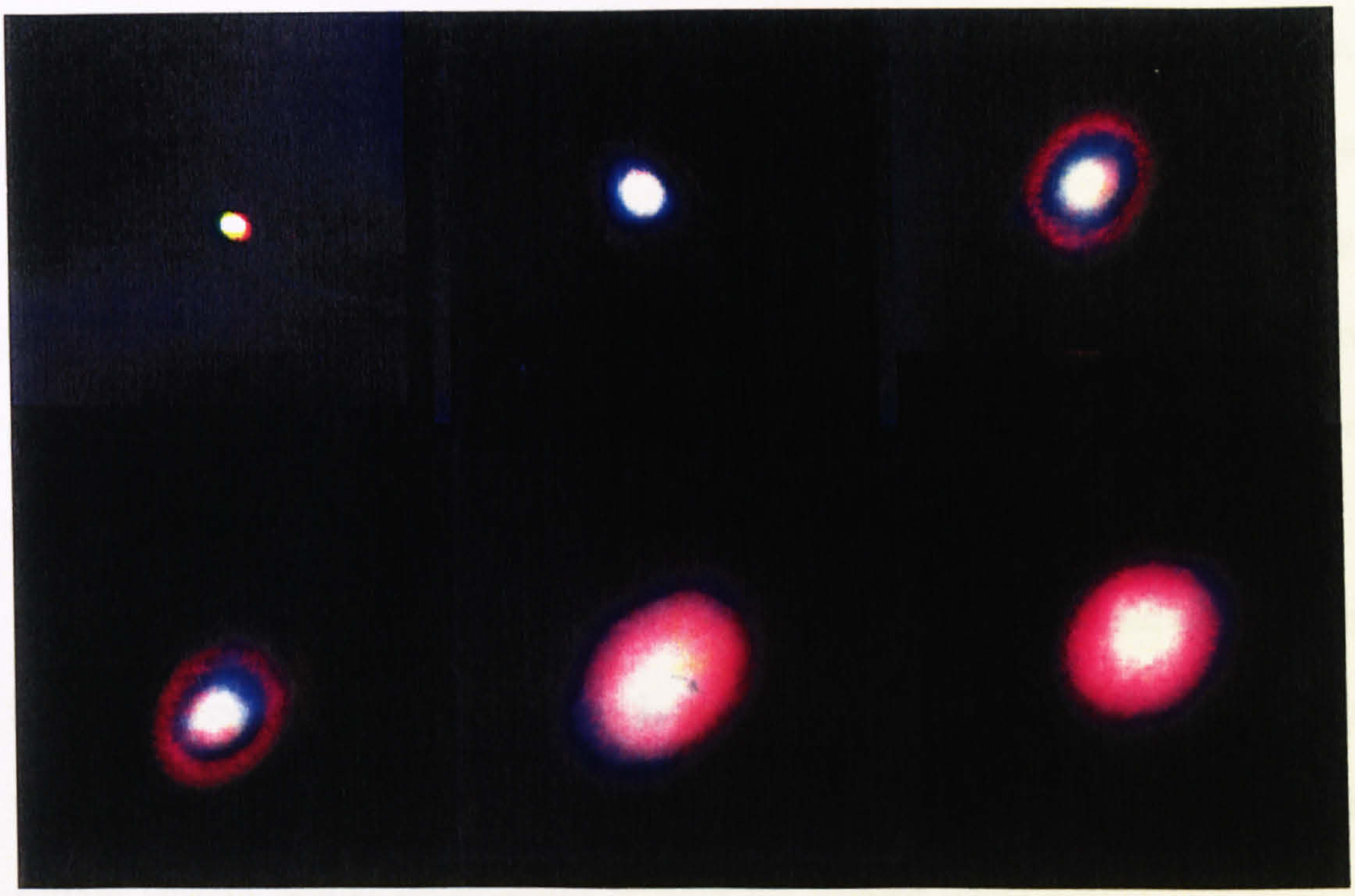

Fig. 2.2.6 Experimental observation of white light continuum generated in a 1 mm pathlength water cell with varying laser intensity (Images scanned from 35 mm film).

Preliminary work was undertaken using a cell containing H_2O, a well documented medium for white light generation[5,6]. The output of the regenerative amplifier was attenuated to approximately 25 μJ and focused through a 40 cm focal length lens onto a 1cm quartz cell containing de-ionised water. The cell was oriented close to Brewster's angle to reduce reflections from the cell walls. By moving the cell with respect to the focal point of the lens continua were generated (Fig. 2.2.6). Far from the focal point [low intensity beams] the generated spectra appear unstable and yellow indicating only a small frequency excursion due to SPM. As the intensity is increased the frequency spread clearly increases until a relatively low intensity white beam is evident. After the cell, the radiation appears to diverge with similar characteristics to the incident beam. For observation times of <15 s the continuum remains relatively stable. However, for longer observation times it is clear that the quality is deteriorating as the spectrum becomes increasingly red [decreasing frequency excursion] and unstable. This is also evident from observing the cell itself. At low intensities a weak unstable filament is evident [due to self-focusing] and the filament appears to fluctuate in intensity with time. As the intensity is further increased, coloured rings become evident around the central white region, with redder components towards the centre and blue towards the edge [due to the optical path difference in the medium].

Observing the cell itself, a strongly white, trapped filament can be seen. There is still some evidence of fluctuation, however, and this is probably due to bubble formation along the filament. Further increasing the intensity we observe an interference pattern [strong spatial modulation] in both the central white region and rings, which appear perpendicular to each other. Higher intensities reveal yet more interference, with further patterns introduced, until a strong, apparently uniform white light continuum is produced. However, the produced continuum is both spatially and temporally unstable and follows the divergence characteristics of the rings, which appear to be independent of the incident beam.

It is our belief that the interference patterns produced at the higher intensities are due to interaction between self focused filaments, a single pattern being due to a pair of filaments and further patterns due to an increasing number of filaments. It is believed that the instability of the continuum at intensities just above threshold is due to heating of the water in the cell causing fluctuations in the refractive index, which clearly reduces the effectiveness of the SPM. To eliminate the heating effects a longer focal length lens [50cm] to reduce the power density, was applied. However, noise reduction was traded for signal intensity.

In order to reduce the cumulative heating effect evident in the static cell, a flowing cell was used. The water was pumped through the cell with a micro-pump gear pump (pump series 180) at a flow rate which afforded a clearance ratio of approximately one [i.e. the surface area exposed to the pulse was renewed between consecutive pulses]. The white light generated appears the same as for the static cell, however the stability is greatly improved. Repeated experiments using the same pump and probe wavelengths as above showed a remarkable difference in the stability of the continuum. However, for measurements of kinetics in 4'-*N*, *N*-dimethylamino-3-hydroxyflavone probe beams of ~ 450 nm were required at sufficiently high intensity and stability to detect a relatively weak transient. At this wavelength the signal to noise was unsatisfactory. Although the water was clearing between each pulse, noise was generated due to ablation of the cell walls from the high intensity at the beam waist.

Clearly a further method of generation was required. The flow cell was replaced with a jet formed using a nozzle created by removing the sealed base of a 1mm thick sample cell. Due to the nature of the continuum generation it is necessary to control the pathlength in the medium, z, and this clearly requires a highly stable jet. Glycol forms a more stable jet than water due to its higher viscosity, however the intensity dependent refractive index for glycol is very low. A compromise of a 50:50 mix was used. In agreement with Fork *et al*[5], the most stable continuum was generated using a 5 cm focal length lens and attenuating the incident light energy to ~10 μJ per pulse. The generated continua showed similar behaviour to the flowing cell but there was a marked improvement in stability. It became clear that a far more stable and intense continuum source was required for repeatable transient absorption experiments in all regions of the UV-Visible spectrum.

Glasses have been given considerable attention in the literature and the use of short optical fibres in pulse compression is well documented[7]. A low n_2 in fused silica means that high intensities must be incident on samples to produce a sufficient frequency excursion. Preliminary experiments show that even at low intensities, local heating effects can cause microscopic damage to the sample surface. Despite this, however, the continuum generated in fused silica shows little difference to that of water. To avoid optical damage we used a 2 mm thick CaF_2 window mounted on the rotating shaft of a high stability motor at approximately 2 Hz. Continua generated in this manner, with careful control of incident energy and the position of the plate in the focus, can be highly stable and intense [to the point that attenuation is required to avoid saturation of the photodetectors]. Although a chirp will occur across the whole wavelength excursion the effect of this is minimised by selecting a 10 nm bandwidth for the probe. In retrospect it has been noted through discussion with Paolo Foggi at L.E.N.S that CaF_2 although having a cubic crystal structure has a slight birefringence causing a modulation instability in the continuum due to the rotation. In this respect it is thought that a translational rather than rotational movement of the disk would give more favourable results. This has indeed been shown to be the case at L.E.N.S where work is ongoing in understanding the experimental principles of continuum generation.

2.2.3 European User Facilities

Although we have facilities to undertake time resolved chemical studies at BNFL much of the work had little commercial significance to BNFL's business interests. Access and collaborations with other facilities throughout Europe allowed us to pursue investigation of photochemical phenomena in areas of fundamental interest in addition to providing experience of the relevant techniques for transient spectroscopy. The systems at the European Laboratory For Non-Linear Spectroscopy (L.E.N.S. Florence), Rutherford Appleton Laboratory (R.A.L. Chilton, Oxon) and the Max Born Institute für Nichtlinear Optik und Kurzzeitspektroskopie (M.B.I. Berlin) are briefly described and the relevant parameters discussed.

The European Laboratory for Non-Linear Spectroscopy (L.E.N.S) at the University of Florence is one of a number of research laboratories (including the Max Born Institute for Laser Spectroscopy (Berlin)) funded under the European Community Large Scale Facilities Initiative to provide access for workers from other European countries. We have taken advantage of this initiative to perform femtosecond pump-probe experiments at L.E.N.S on a variety of molecular systems. This not only allowed us to undertake the experiments but also helped us to learn about the techniques appropriate for transient spectroscopy.

In order to fully characterise the transient response of a system it is necessary to obtain both transient spectra and kinetics. During our stay in Florence over two periods in 1996 and 1998, we obtained transient spectra for time delays ranging from 0 to 500 ps for a series of compounds thought to undergo Excited State Proton Transfer (ESIPT) and in some cases the formation of Twisted Intramolecular Charge Transfer (TICT) states.

Transient pump-probe spectra were obtained at L.E.N.S using a laser system similar to that described in Section 2.1, but with an ~ 70 fs Spectra-Physics Tsunami Ti:Sapphire Oscillator used as the seed laser for the regenerative amplifier. Approximately 150 fs pulses at 800nm and a repetition rate of 1 kHz are delivered at the front end of the system. The experimental system has been described previously[8], however some of the important features are reiterated below.

For pump-probe experiments, the desired wavelengths are derived from an OPO and a white light continuum for pump and probe respectively. The pump beam at 800 nm is used to drive a custom built OPO producing ~ 120 fs pulses in the spectral region 1.2 to 1.5 μm. This output can be used to generate 2nd and 3rd harmonics (600 - 750 nm and 400 - 500 nm respectively). Further pump wavelengths can be derived from the 2nd and 3rd harmonics of the regenerative amplifier and by mixing the OPO output with the harmonics. In this manner, most pump wavelengths are obtainable. However, it is clear that pump stability is dependent on the complexity of the technique used to generate the desired wavelength. Typically, no more than 5 mW is used to pump the sample.

The probe light is temporally delayed and used to generate a white light continuum in a CaF_2 window (continuously translated), producing a stable probe beam across a broad frequency excursion (200 - 1000 nm). The probe is divided into signal and reference beams and focused collinearly with the pump onto the sample. Dispersion in the continuum means that there is a slight discrepancy in time zero across the spectra (of the order 500 fs from red to blue components). The dispersion of the continuum is given in Fig. 2.2.7.

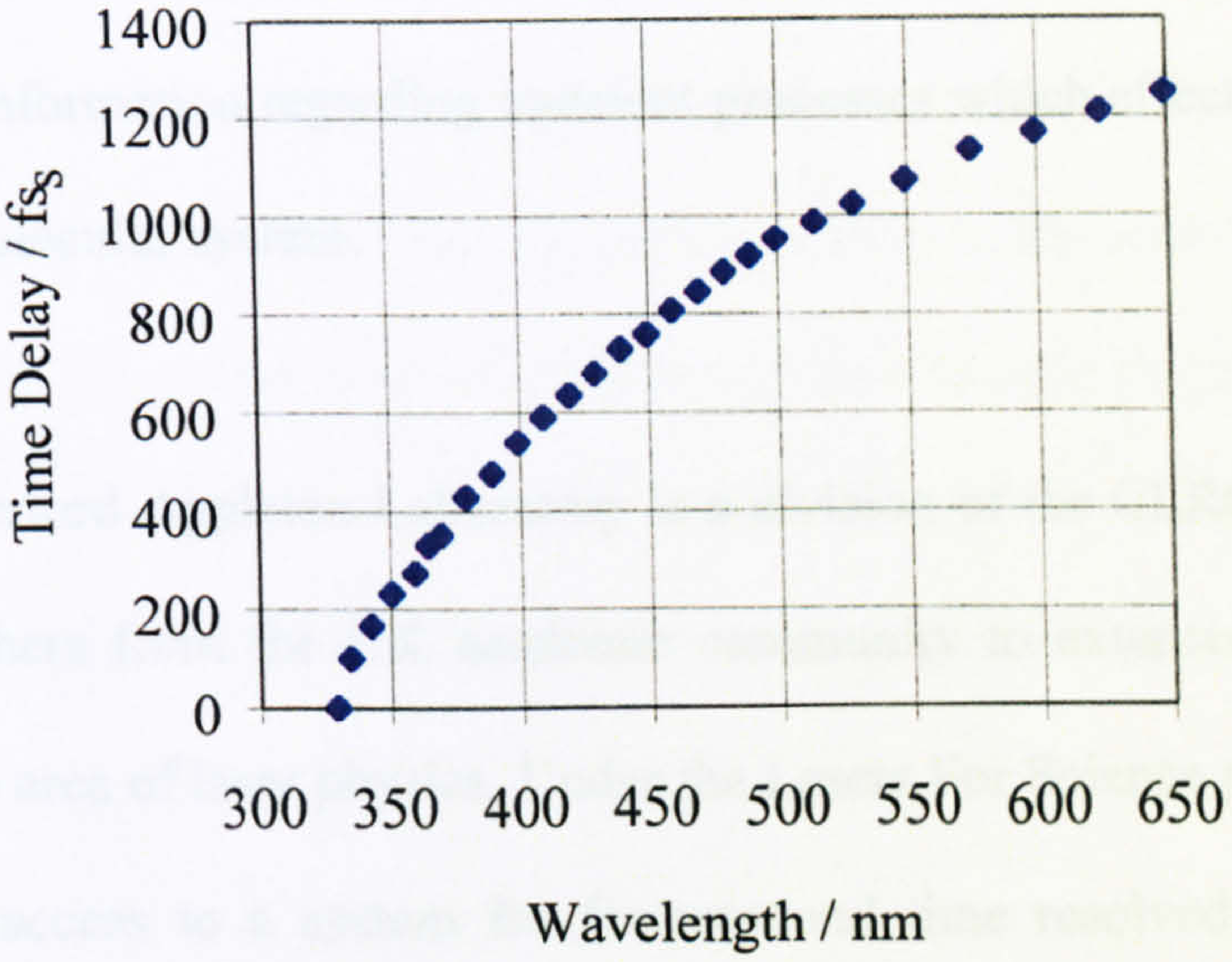

Fig. 2.2.7 Measured time dispersion of white light continuum generated in CaF_2 (Courtesy Of Paolo Foggi, LENS).

Samples are prepared to give 1.0 OD at the pump wavelength in the pathlength of the cell (2 mm). The cell is constructed from Teflon with CaF_2 windows to allow good transmission of UV wavelengths. The sample is flowed to reduce problems of heat conduction and photoproduct generation at the focus, which can reduce the signal stability.

Following the sample cell the pump is blocked and the signal and reference beams pass through a pair of pinholes into a spectrometer. The spectra are dispersed onto different parts of a CCD camera. Captured signals are analysed by a computer and changes in transmission of the molecular system are made by equation 2.2.1. For samples with significant fluorescence, subtraction of the fluorescence signal (with the pump on and probe off) can also be selected. Fluctuations of the background (pump off) of ± 1% are readily obtainable and adequate for the type of transients observed in our molecular systems.

The full spectra at visible wavelengths of a molecule may be taken at ultrashort times to provide information regarding transient processes which effect the excited state absorption of a molecular system.

The Rutherford Appleton Laboratory is a division of the CLRC which provides access to researchers from the UK academic community to extensive research tools, particularly in the area of laser physics. Under the Lasers For Science program at R.A.L. we have gained access to a system for femtosecond time resolved single frequency kinetics. The recently developed apparatus employs the use of custom designed optical parametric amplifier technology to offer two synchronised and widely tuneable ultrashort pulses[9].

The laser system is similar to that described in Section 2.1 and is based on a Ti:Sapphire oscillator (Spectra Physics Tsunami) and a Ti:Sapphire regenerative amplifier (Spectra Physics Spitfire) pumped with a Q-switched intracavity frequency doubled Nd:YLF laser (Spectra Physics Merlin). The fundamental output is tuneable from 770 - 840 nm with pulse energies of approximately 500 μJ at 1 kHz.

Transient absorption measurements may be undertaken at a variety of wavelengths with pump tunability from an OPA and other non-linear frequency mixing techniques from 200 - 2200 nm. The probe wavelength is selected by 10 nm bandpass filter from a continuum generated in a 1 cm flowing water cell. The continuum produced is high power but multifilament, which ultimately limits the resolution of the system to ~ 500 fs due to third order dispersion.

Signal processing is carried out by dividing signal and reference photodiode outputs in an analogue circuit to reduce pulse to pulse jitter and then measurement using a digital lock-in amplifier (EG&G 7206). The lock-in frequency of around 200 Hz is derived from a chopper in the pump arm, which superimposes a modulation only on the signal diode.

Transient kinetics are obtained by setting a time delay look-up table of user defined time delays. To reduce systematic errors due to sample degradation and laser misalignment, the delay values are sampled in random order for a duration set by the time constant of the lock-in. The detection limit of the system is of the order of 10^{-4} of absorption.

Access to facilities at the Max Born Institute für Nichtlinear Optik und Kurzzeitspektroskopie (Berlin) was also gained under the EU Large Scale Facilities Initiative. The Institute specialises in providing laser facilities for research collaboration in the areas of atomic, molecular, cluster and solid state physics, UV and XUV spectroscopy, laser development, quantum optics, chemical physics and biophysics. Access was granted in order to undertake measurements of ESIPT in 3-hydroxyflavone in the region of the first absorption band at or around the absorption maximum.

The MBI system is based on a custom built chirped mirror dispersion compensated Ti:Sapphire laser oscillator capable of generating 10 fs laser pulses from the design of the ETH ultrafast laser group in Zurich[10]. Amplification is initially in a regenerative cavity (after appropriate pulse stretching) and subsequently in a bowtie amplifier to bring the output to approximately 3 mJ after recompression. The output is continuously monitored by a single shot second harmonic FROG (frequency resolved optical gating) instrument to give simultaneous measurement of pulse width and spectrum (and by the use of custom algorithms, phase). The pulses produced in this manner are typically < 50 fs FWHM, 1 kHz and with a spectral extent centred around 800 nm. Shorter pulses are obtained by loosely focusing the beam into a 2 m lossy hollow glass fibre waveguide filled with krypton gas at ~ 1 mbar. The high intensity of the laser pulses due to the confinement in the waveguide and the 2 m pathlength in the krypton provides significant spectral broadening due to SPM despite the low χ^3 of the gas. Pulse compression with gratings and prisms can then produce pulses of approximately 10 - 20 fs duration with energy in the region of 50 % of the input due to losses in the fibre. This is a simple and efficient method of providing high energy pulses of this duration although the beam quality is significantly reduced.

Transient absorption measurements were performed in the same manner as detailed previously (section 2.2.1) with the following exceptions[11]. Pump and probe pulses were derived from frequency doubling components of the spectrum created in the fibre waveguide[12] by angle tuning a pair of BBO crystals to provide the desired wavelengths (this restricts the bandwidth of the pulses to the acceptance angle of the crystal). Following generation the two beams are independently compressed in double pass prism pairs and then directed to the sample using all reflective optics. The sample is flowed through a dye laser jet to produce a pathlength of approximately 200 μm. Solutions of 6 mmol concentration were used to give significant absorption at the pump wavelength. Changes in the probe transmission were monitored using a silicon photodiode and read to computer via a time gated analogue to digital converter at the laser repetition rate. The probe was referenced to a second photodiode measuring probe intensity prior to the sample jet. Changes in transmission of 10^{-4} are achievable providing many experiments are averaged to provide good statistics. The resolution of the system is of the order of 70 - 100 fs. Presently only pump and probe wavelengths at the second harmonic and fundamental are available for experiments (360 - 440 nm and 720 - 880 nm respectively).

2.2.4 Data analysis

Fitting of transient kinetic data was undertaken for the most part using Microsoft Excel based macros written for the purpose. Following the arguments of Foggi et al[8] we assume a model such that the transient absorption signal can be reproduced by the convolution of the system response, R(t) and the instrumental response, I(t);

$$S(\tau) = \int_{\infty}^{0} R(t)I(t)dt \qquad 2.2.2$$

The system response is defined by the model chosen to represent the chemical system under examination. For a simple system where the depopulation time of a state is much longer than the population time R(t) can be characterised by;

$$R(t) = A\left[1 - \exp\left(-\frac{t}{T_1}\right)\right] \qquad 2.2.3$$

where, A, is a parameter proportional to the ground state absorbance. The selection of an instrumental response for the experimental apparatus itself is not a trivial exercise and we have either fitted a Gaussian function to data from molecular systems with instantaneous response (ground state bleach of beta carotene) or cross-correlation data obtained prior to and immediately after experimental runs.

Initially data is fit to single exponential kinetics and if indications in the residuals and χ^2 values show evidence of potential additional components, appropriate parameters are added to the fitting routines. For the purposes of this thesis χ^2 is a figure of merit defined as;

$$\chi^2 = \frac{(x_i - f_i)^2}{f_i^2} \qquad 2.2.4$$

where x_i and f_i are the measured and expected values respectively.

2.3 Femtosecond Laser Ablation

In this section I describe the experimental apparatus built for femtosecond laser ablation together with the methods employed for analysis and preparation of samples after ablation.

2.3.1 Experimental System For Ultrashort Laser Ablation

As has been shown earlier in section 1.5, the advantages of laser material processing with ultrashort pulses include precise ablation threshold, reduced laser fluence, much reduced heat affected zone and improved energy coupling to the surface due to reduced (if not eliminated) plasma shielding. These advantages translate well in precise micromachining applications. With this in mind, a femtosecond laser micromachining workstation was developed in order to facilitate the production of high value, low volume components for other BNFL projects.

A number of factors determine the choice of experimental technique employed. Principally the arrangement must be flexible enough to deal with a variety of different substrate materials and feature sizes with particular emphasis on reproducibility and fast "turn around".

From an experimental standpoint there are a number of approaches which may be employed. In the simplest arrangement the laser beam is focused onto a target substrate and the substrate translated in one or more dimensions. In this case, minimum feature sizes are determined principally by the diffraction limited spot size (although for ultrashort pulses this is not necessarily the case). For high resolution, high complexity applications (such as integrated circuits) a more complex imaging system may be employed, whereby the laser is imaged onto the target via a preformed mask or aperture.

Within the bounds of our brief to produce relatively simple devices with feature sizes of the order 50 μm, it is clear that the added complexity of the second approach (including the fabrication of masks for projection imaging) is not suitable. Initial work has been undertaken using the first approach and a third technique involving the manipulation of the laser beam onto a static substrate has been evaluated for use as a fast prototyping method.

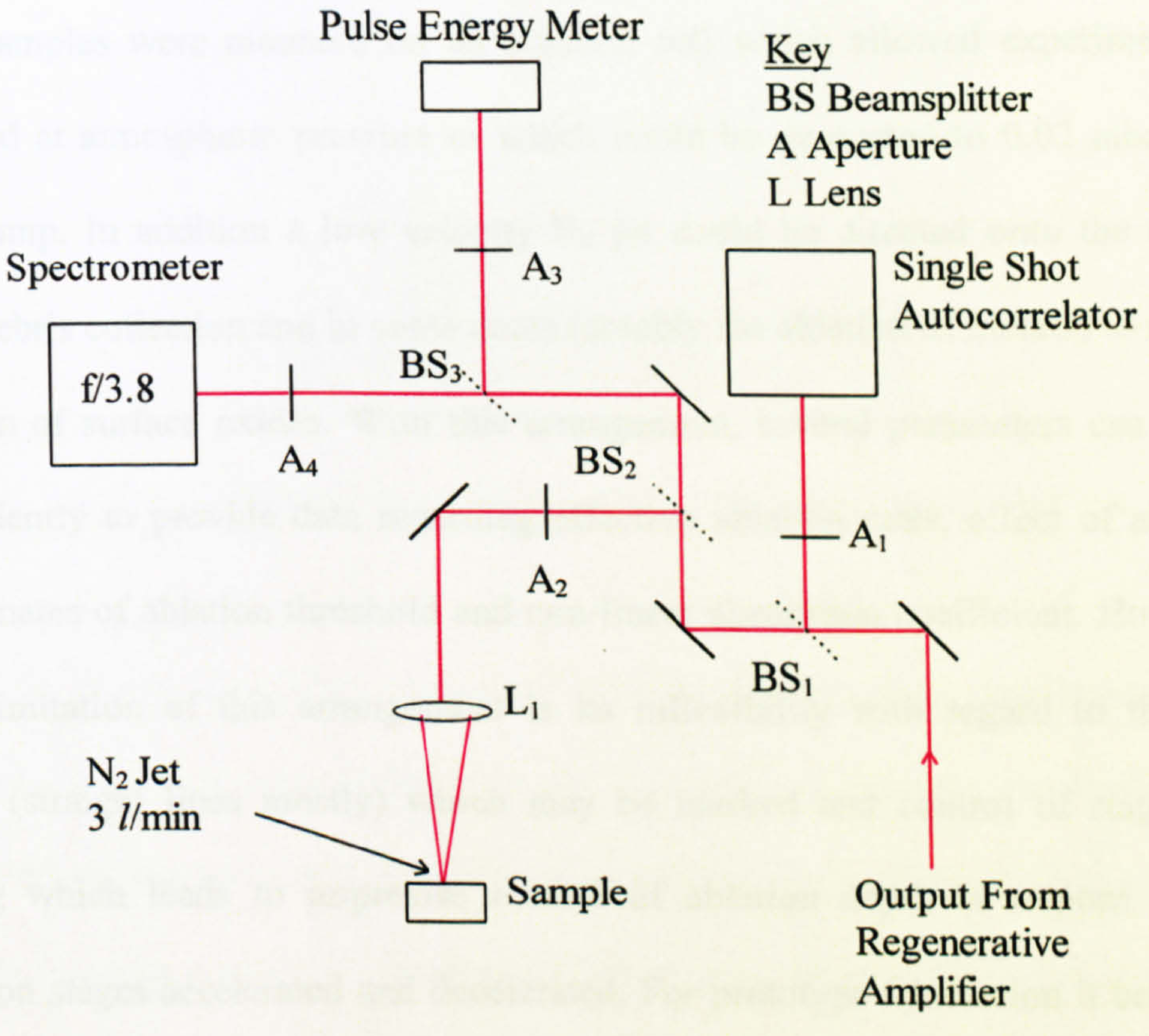

Fig. 2.3.1 Experimental arrangement for laser ablation.

The optical system for fundamental studies of femtosecond laser ablation is given in Fig. 2.3.1. Effectively there are four beam lines created using 50:50 ultrafast beamsplitters and attenuators (reflective neutral density filters) so that pulse width, energy and spectrum can be monitored throughout the experiments. In preliminary studies to gauge the potential of the technique the substrate was translated under a focused laser beam using a two axis positioning system (Photon Control UPC-SD motion controller), providing a resolution of 0.5 μm. The pulses were focused using a fused silica plano convex lens with a focal length f = 100 mm (ϕ = 25 mm). The laser beam diameter at the lens was approximately 8 mm, so the effective f# was ~ 12.5. The calculated PFD (see section 1.4.2) and GVD introduced by the lens was insignificant (~ 5 fs). However, for shorter pulses, or when precise control of the pulse length are required at the surface a reflective focusing element should be employed.

Samples were mounted on an ablation cell which allowed experiments to be performed at atmospheric pressure or which could be evacuated to 0.02 mbar using a rotary pump. In addition a low velocity N_2 jet could be directed onto the surface to reduce debris collection and in some cases (notably the ablation of metals) to reduce the formation of surface oxides. With this arrangement, several parameters can be varied independently to provide data regarding effective ablation rates, effect of atmosphere and estimates of ablation threshold and non-linear absorption coefficient. However, the severe limitation of this arrangement is its inflexibility with regard to the type of patterns (straight lines mostly) which may be marked and control of stage velocity profiling which leads to imprecise control of ablation depth in regions where the translation stages accelerated and decelerated. For prototype fabrication it became clear at an early stage that a more flexible system was required.

The work-station for prototype fabrication is given in Fig. 2.3.2 and consists of a beam delivery system based on a pair of orthogonally arranged temperature stabilised galvonometer mirrors (silver coating with SiO_2 protective overcoat) which scan the beam onto a standard flat field lens (fθ corrected, f_{eff} ~ 190 or 350 mm depending on required field). The scanhead provides two axis beam deflection with a 15 mm input aperture within the scan field. Mechanical limit stops at the full scan angle (± 20°) protects the XY mirrors from unintentional collisions.

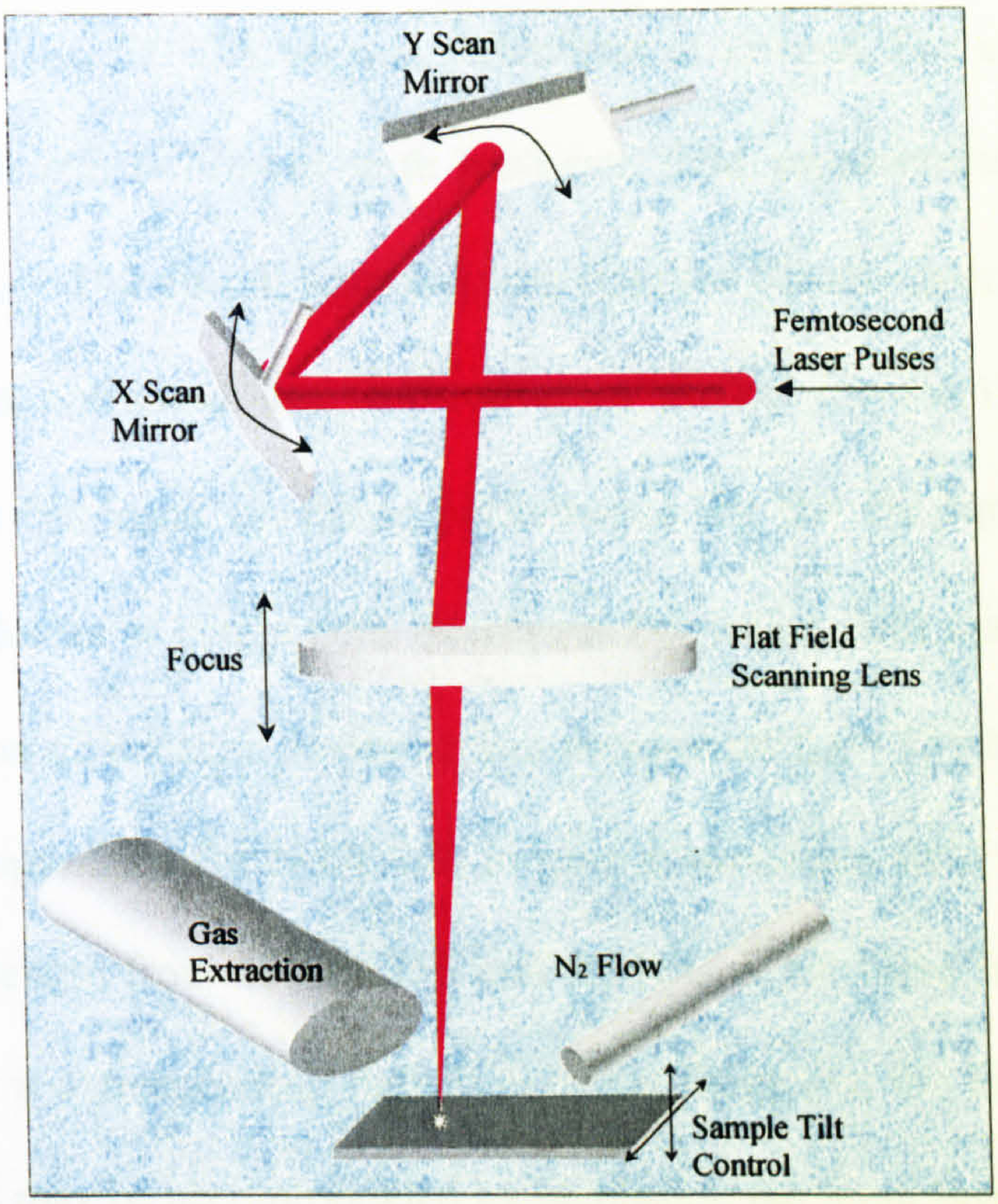

Fig. 2.3.2 Schematic of galvonometer based laser scanning system.

The digital scanning controller (DSC) provides two axis control of the galvonometer mirrors using digital scanning techniques. Computer host commands, via a user interface, are translated from the active bus into appropriate servo signals and, by extension, scanner positions. Vector scanning is used, where each vector is subdivided into a sequence of incremental points (XY pairs). Scan patterns are created either as Hewlett Packard Graphic Language (HPGL) files in CorelDraw or directly as XY-pairs using the correct language protocols. Manipulation of objects created in this manner is performed in a dedicated interface program (Job Editor) which communicates via the DSC. The Job Editor also provides interface with such parameters as scan speed and shutter control.

The type of lens adopted in the ablation scheme is dependent on the experimental parameters. A summary of the lenses used for ablation experiments is given in Table 2.3.1 below with various parameters of interest. For experiments at the fundamental wavelength (~790nm) with moderate field requirements (< 100 cm^2) a three component $f_{eff} = 190$ mm fθ scanning lens (Omitec Electro-optics "Lasonar") may be used. Although optimised and anti-reflection coated for Nd:YAG operation at 1.063 μm the lens has good operating performance for the fundamental wavelength despite reflection losses at component interfaces. For larger field operations (as in the case of the Nitration of Benzene device) a four component $f_{eff} = 350$ mm fθ lens may be employed (again optimised for Nd:YAG) to give a maximum field of ~500 cm^2. The increase in focal length from 190 to 350 mm leads to a 1.8 times increase in the $1/e^2$ spot diameter and a corresponding reduction in the fluence at the focus for equivalent input energy. This may be accommodated by increasing the input beam diameter from 8 to 15 mm, to bring the system to the equivalent f#. Reflection losses are significant for both lenses and in the four element lens amount to a reduction in pulse energy at the substrate of approximately 50% of the input energy.

Commercially available fθ lenses are inappropriate for use with the second harmonic of the laser at ~ 395 nm, due to absorption in the coatings and glass components. Necessarily fθ correction requires the use of high dispersion glass such as SF10, which is incompatible with UV light due to transmission losses. In addition GVD in glass is highly significant. In this case a singlet lens of fused silica was adopted and ray trace analysis showed that with the plano surface to the infinite conjugate aberrations could be balanced to give adequate scanning performance over a limited scan range.

Table 2.3.1 Pulse stretching due to PFD and GVD in fθ lenses.

Lens Type	Wavelength mm	Focal length mm	F Number	PFD / fs On Axis	PFD / fs At Max θ	GVD / fs On Axis
Fused Silica	790 nm	150 mm	19	5.48	28.77	< 0.1
Fused Silica	395 nm	150 mm	19	16.94	88.95	0.7
3 element fθ	790 nm	190 mm	24	20.55*	90.85*	14.28
4 element fθ	790 nm	350 mm	24	20.55*	143.11*	24.75

* Approximation assumes singlet fused silica lens.

The parameters for group velocity (GVD) and pulse front distortion (PFD) are also given in table 2.3.1. For the fθ lenses the figures for both phenomena have been estimated by making the assumptions that the lenses are single element and are made from fused silica. Whilst the assumptions are clearly inadequate to characterise the lenses rigorously they serve to illustrate the possible magnitude of pulse distortion. Taking the f = 350 mm lens as an example, the pulse stretching due to GVD amounts to a maximum of 14 fs pulse stretch for a 150 fs input pulse and compares to a 21 fs stretch due to PFD (which is independent of pulse width and assuming a 12mm beam diameter). However, PFD is not linear across the lens aperture due to the r^2 dependence. For a maximum scan angle (calculating an annulus of 12mm at the extreme of the aperture) the PFD will be of the order of 143 fs! Whilst this amounts to a 63% change in pulse width, we do not appear to experience a measurable drop in ablation rate at large scan angles with Pyrex substrates. This seems to indicate that the ablation rate for Pyrex is relatively insensitive to pulse width for this range (150 - 300 fs), as one might expect, as the pulse width is still much shorter than the electron-phonon relaxation time (~1 ps). However, the result illustrates that a different optical arrangement would be necessary to deliver well-defined, short pulses to the target (achromatic or reflective optics).

Alignment of the optical arrangement in the first instance was achieved by removing the scan lens and overlapping a back reflection from the target with the incoming beam at a pinhole by manipulating the sample holder. Replacing the lens, the various component back reflections were also aligned to the pinhole. The focal plane of an fθ lens is always perpendicular to the optical axis, so a small tilt of the lens with respect to normal incidence of the laser beam will introduce a similar tilt of the focal plane. This is evident for the 350 mm focal length lens as a change in ablation rate (characterised by a loss of visible optical emission from the plasma) from one end of a long scan to another at near ablation threshold. Fine adjustment of the target can be achieved by monitoring the plasma and introducing small angular modifications until a constant ablation rate can be observed throughout a long scan. Misalignment is indicated both by the loss of the characteristic kHz buzz of the expanding plasma and the development of a self-focusing filament (in thick samples) which can be seen to move towards the surface as the correct angular adjustment is applied. Gross misalignment may require iteration between angular adjustments and lens-target distance.

2.32 Sample Analysis

Samples were optically polished and cleaned prior to ablation with acetone and methanol using the drop-drag technique. Fused silica samples were made from Spectrosil B, 10 or 25 mm in diameter and 6 mm thick, polished to λ/5 per face at 633 nm (Optical Works). Silicon and Pyrex samples were provided by the BNFL micro-engineering group and used as provided, details (where appropriate) are given in the appropriate results section. Metal samples were polished to near optical flatness using a sub-micron abrasive.

Analysis of femtosecond micromachined components has been accomplished using a variety of complementary microscope techniques. Initial investigation was principally undertaken qualitatively using optical microscopy and device dimensional characterisation (typically in the range of 50 - 500 μm) was performed on a confocal microscope[13]. Investigation of microstructure has been performed using ESEM[14] and AFM[15] techniques. Each method has significant advantages at particular resolutions and all methods have been used to fully analyse the ablated samples.

Probably the most useful technique for quantifying the features of the ablated samples is confocal microscopy. The technique employs a laser beam to scan across the sample surface and the signal is detected by a CCD camera. The reflected light is directed through an aperture confocal with the focal point on the sample surface. This severely restricts the depth of field by allowing only in-focus light to pass to the CCD. As the sample is scanned through the focal plane, the in-focus points produce the most intense signals, corresponding to the height of the stage relative to the starting position. The information is then compiled to recreate a 3-dimensional image of the surface. Features of the order of 1 μm are readily resolvable.

A high quality confocal image depends on the reflected signal being within a particular intensity range. A sample with poor or inhomogeneous reflectivity will not produce a strong enough signal for imaging. Because the majority of our samples were of glass or Pyrex, which exhibit poor reflectivity at normal incidence (~ 4%), samples were sputter coated with a few tens of nanometers of gold, both enhancing and homogenising the reflected signal (clearly ablated regions are much less reflective (due to enhanced roughness) than unablated glass).

Environmental scanning electron microscopy (ESEM) is conceptually similar to conventional SEM and produces high quality images at a range of magnifications up to 10^5 with exceptional depth of field. In this respect the ESEM is an excellent tool for high resolution imaging of fine surface microstructures. The ESEM differs from the SEM in that operation is at higher pressure and uses secondary electrons from ionised environmental gas to produce an image. Due to the neutralising effect of the positively charged gas ions, negative charge accumulation is much reduced (although not eliminated) and non-conducting and even biological materials may be analysed. For this reason ESEM is a suitable technique for imaging ablated regions in non-conducting media such as fused silica without significant sample preparation.

Atomic force microscopy (AFM) uses a scanning technique to acquire high resolution, 3-dimensional reconstruction of surfaces. A very sharp tip on the end of a flexible cantilever approaches the surface. Atomic forces between the tip and the surface cause the cantilever to bend. A laser beam, reflected from the cantilever detects movement to provide depth profiling. No sample preparation is required to use this technique. The resolution of the technique is superior to ESEM and evidence of atoms can be seen on some special samples (graphite). The upper range is limited to 4 μm in the Z direction. The AFM has been used to characterise samples with dimensions below approximately 1 or 2 μm in order to analyse microstructure and near fluence ablation.

Further analysis has been undertaken using a conventional Talisurf surface profiler to give cross-sectional data and information regarding residual surface roughness.

---

[1] J. Squier, F. Salin, G. Mourou and D. Harter, *Opt. Lett.* 16(5): pp324-326 (1991).

[2] D.E. Spence, P.N.Kean and W. Sibbett, *Opt. Lett.* 16(1): pp42-44 (1991).

[3] H. Weichel and L. S. Pedrotti, *Electro-opt. syst. Des.* 8 (22-36): p61 (1976).

[4] T. Hasche, S. Ashworth, E. Riedle, M. Woerner and T. Elsaesser, *Chem. Phys. Lett.* 244: p164 (1995).

[5] R. Fork, C. V Shank, C. Hirliman, R. Yen and W. J. Tomlinson, *Opt. Lett.* 8: p1 (1983).

[6] R. Alfano, *The Supercontinuum Laser Source*, Springer-Verlag (1989).

[7] R. Fork, C. Brito-Cruz, P. Becker and C. V Shank, *Opt. Lett.* 12 (7): pp483-485 (1987).

[8] P. Foggi, L. Pettini, I. Santa, R. Righini and S. Califano, *J. Phys. Chem.* 99: pp7439-7445 (1995).

[9] P. Matousek, A. Parker, P. Taday , W. Parker and M. Towrie, *J. Chem. Phys.* 107(23):pp9807-9817 (1997).

[10] A. Stingl, M. Lenzner, C. Spielmann, F. Krausz and R. Szipocs, *Opt. Lett.* 20(6): pp602-604 (1995).

[11] O. Duhr, E. T. J. Nibbering and G. Korn, *Appl. Phys. B- Lasers&optics*, 67: pp525-527 (1998).

[12] E. T. J. Nibbering, O. Duhr and G. Korn, *Opt. Lett.* 22(17): pp1335-1337 (1997).

[13] A. Wennerberg, R. Ohlsson, B.-G. Rosen and B. Andersson, *Med. Eng. Phys.* 18(7): pp548-556 (1996).

[14] G. D. Danilatos, Microsc. Res. Tech, 25(5-6): pp.354- 361 (1993).

[15] V. S. Edel'man, *Pribory I Teknical Eksperimenta (English translation)*, 5: pp25-49 (1989).

Chapter 3: Pump-Probe Spectroscopy:

ESIPT To Oxygen (3-Hydroxyflavone and Derivatives)

The following chapter presents experimental results obtained using the laser systems and techniques detailed in Section 2.2. The main thrust of the research has been in understanding and quantifying the mechanisms involved in the transient kinetics of 3-hydroxyflavone (I), which may undergo ESIPT to form a tautomer after excitation with 350 nm light. Previous work by our group[1] has shown that the addition of certain substituents to the 4' position of the phenyl ring of I can anomalously affect the fluorescence emission and this has been attributed to switching between charge and proton transfer. With this in mind, transient spectra of a number of 3-hydroxyflavones, containing various substituents, have been measured in a variety of solvent environments to examine the effect of the substituents upon the ultrafast dynamics of the excited state.

The structure of I and a number of substituted derivatives are given in Fig. 3.0.1 These compounds have been synthesised at the University Of Central Lancashire by Stuart Ormson and Xavier Poteau.

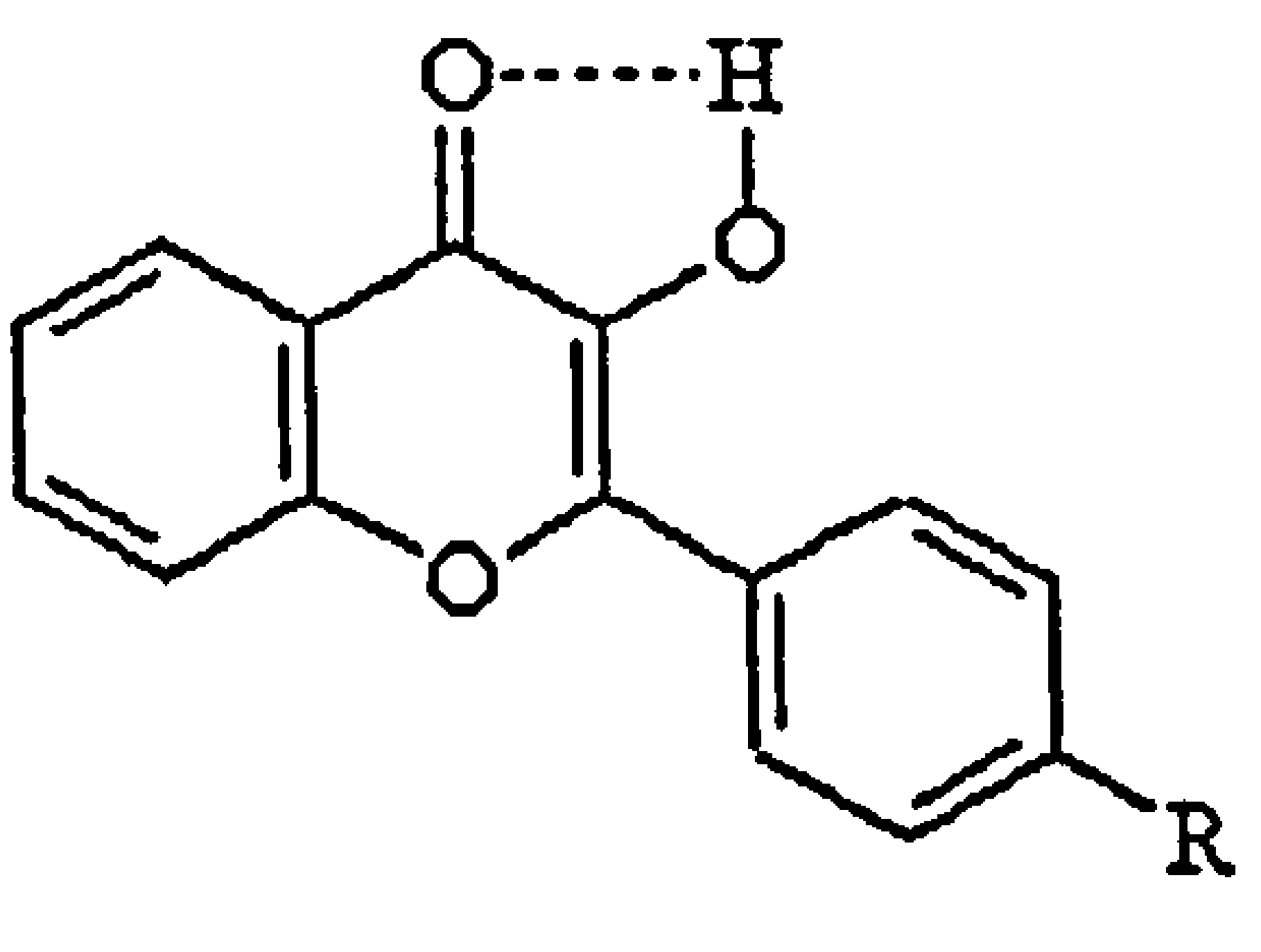

I: R = H
II: R = Cl
III: R = CH_3
IV: R = OCH_3
V: R = CN
VI: R = $N(CH_3)_2$
VII: R = $N(CH_3)_2$ & H replaced with CH_3

VIII: R=

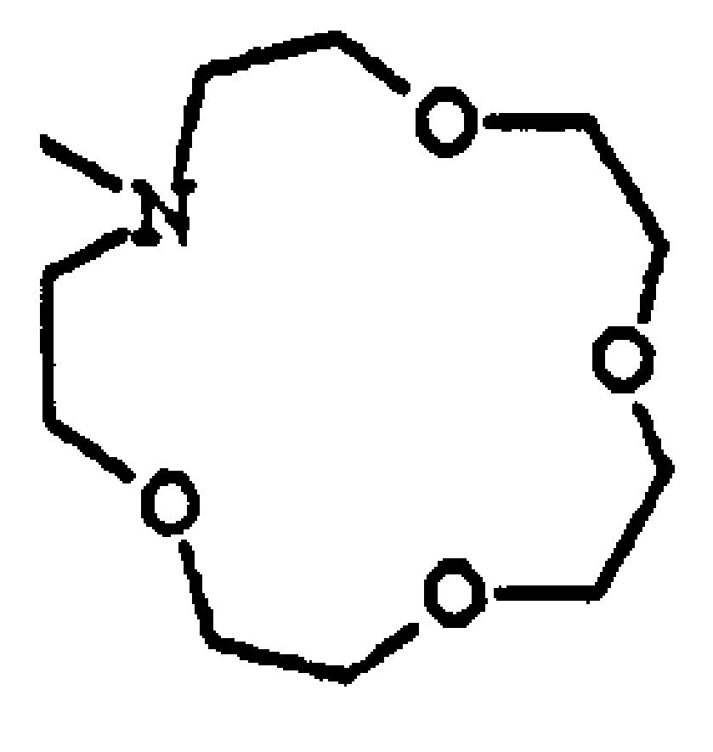

Fig. 3.0.1 Structure of normal form of I and various substituted derivatives.

3. 1 3-Hydroxyflavone

The prior research on 3-hydroxyflavone is extensive and has been discussed in Section 1.4.2. Presented here are the results of several experiments undertaken to elucidate the effect of the proton transfer process on the excited state dynamics of this molecule.

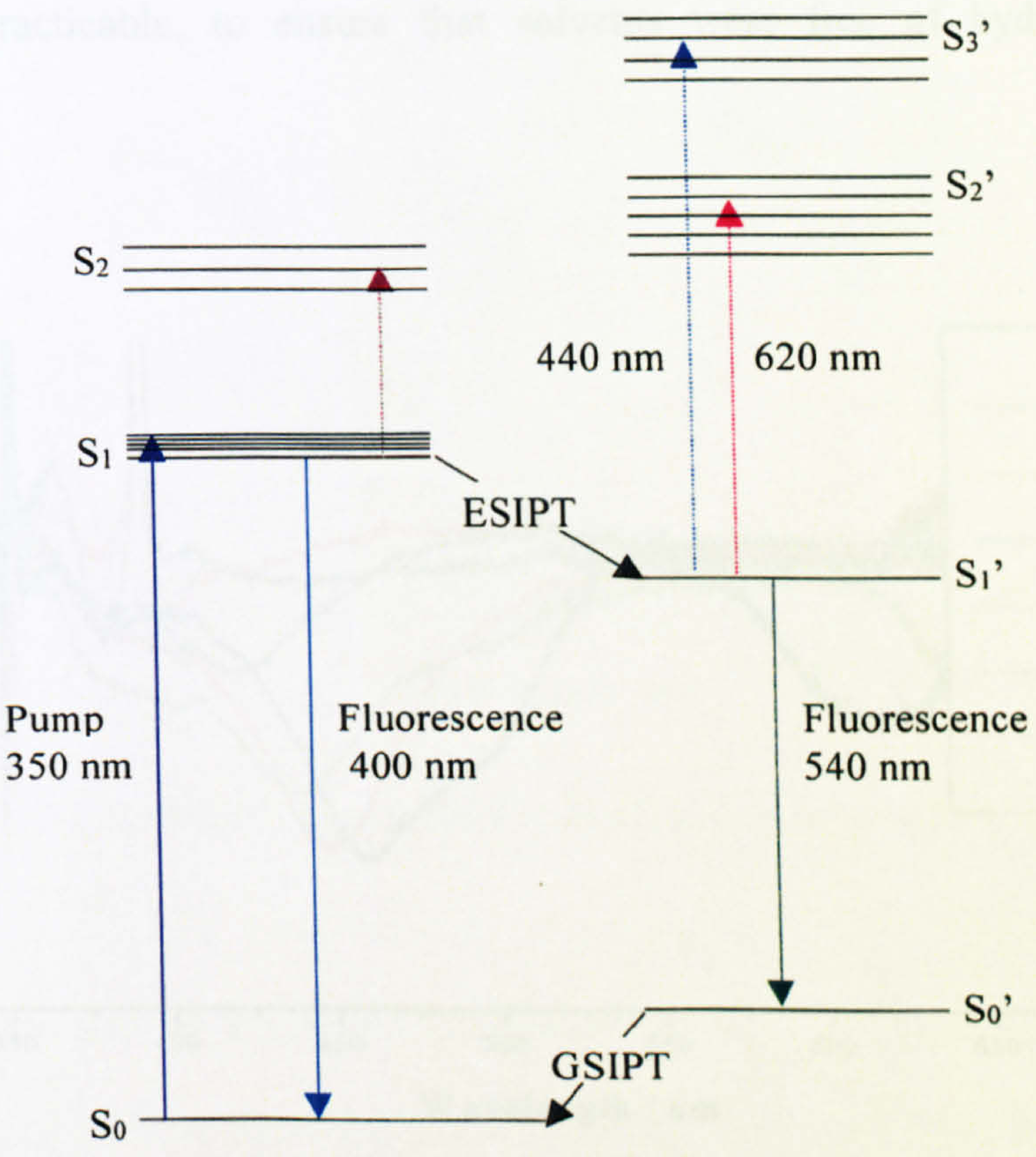

Fig. 3.1.1 Excited state processes in **I** (ESIPT: excited state intramolecular proton transfer, GSIPT: ground state intramolecular proton transfer).

We start with the model of excited state processes in **I** (Fig. 3.1.1) proposed by Schwartz et al[2] and introduce modifications as the experimental results dictate. The notation in the diagram will be adopted where appropriate throughout the text. Where appropriate the model is modified to fit the observed excited state dynamics.

Transient absorption spectra of **I** in spectroscopic grade methylcyclohexane, ethanol and acetonitrile were recorded following femtosecond excitation using the ultrafast laser facility at LENS in Florence (previously described in Section 2.3.3). These three solvent systems were chosen as representing examples of a non-polar, non-interacting solvent (methylcyclohexane, MCH); a polar, hydrogen-bonding solvent (ethanol); and a polar, non-hydrogen-bonding solvent (acetonitrile). Particular care was taken, where practicable, to ensure that solvents were free of hydrogen bonding impurities.

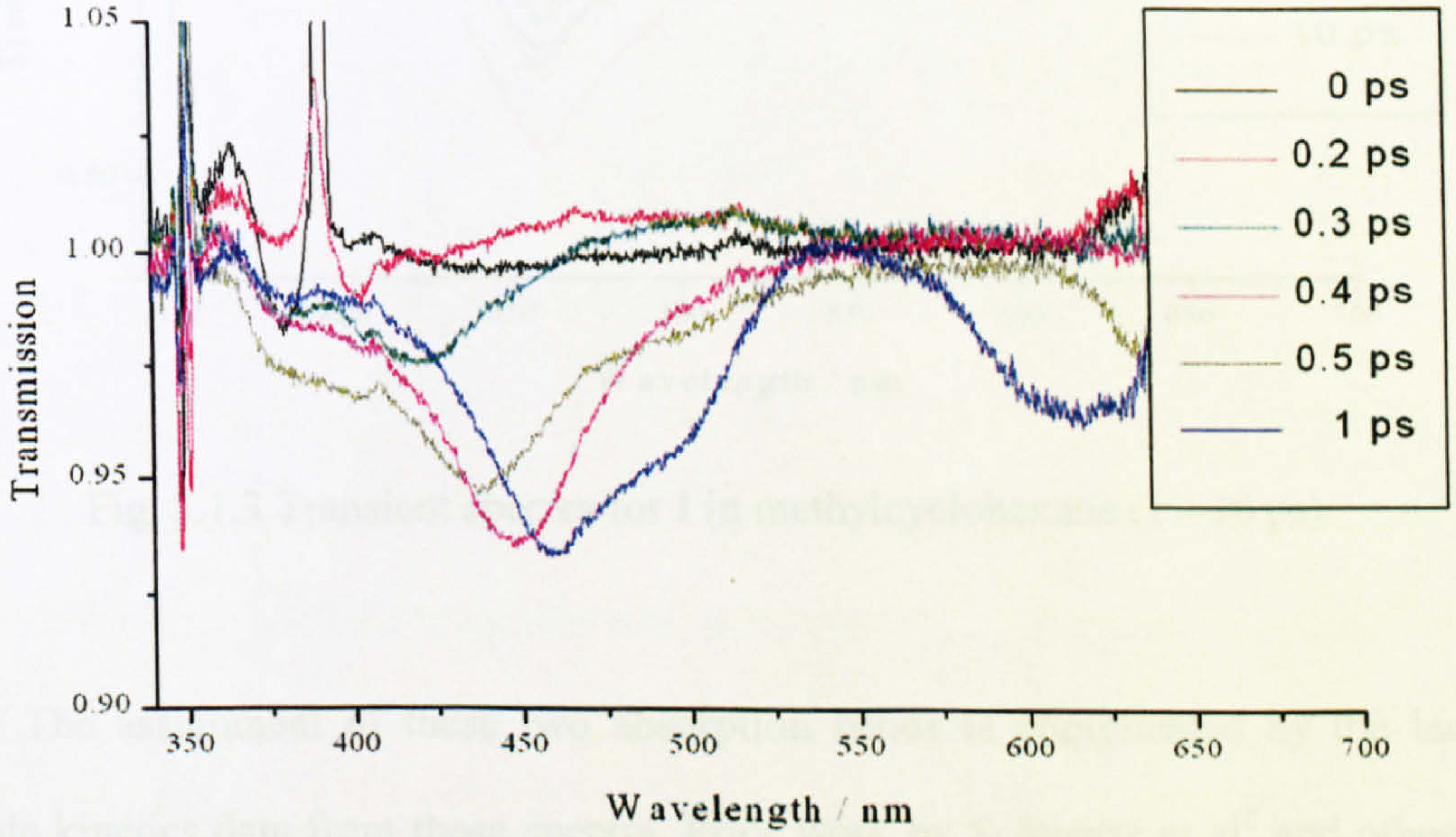

Fig. 3.1.2 Transient spectra for **I** in methylcyclohexane (0 - 1 ps).

For **I** in MCH (1 mM solution), the spectra at short delay times (200-500fs) exhibit transient absorption in the region of 350-475 nm with the spectral peak moving to the red at the later times (figure 3.1.2). At delay times of 1 ps and greater, the transient absorption is principally in the 400-500 nm region (figure 3.1.3) with a clear peak at approximately 450 nm and a shoulder around 490 nm. There is also gain at wavelengths above approximately 500 nm due to stimulated emission. The shape of these spectra after approximately 1 ps appear to be independent of the time delay between the pump and probe, although there are the expected variations in overall intensity with delay time.

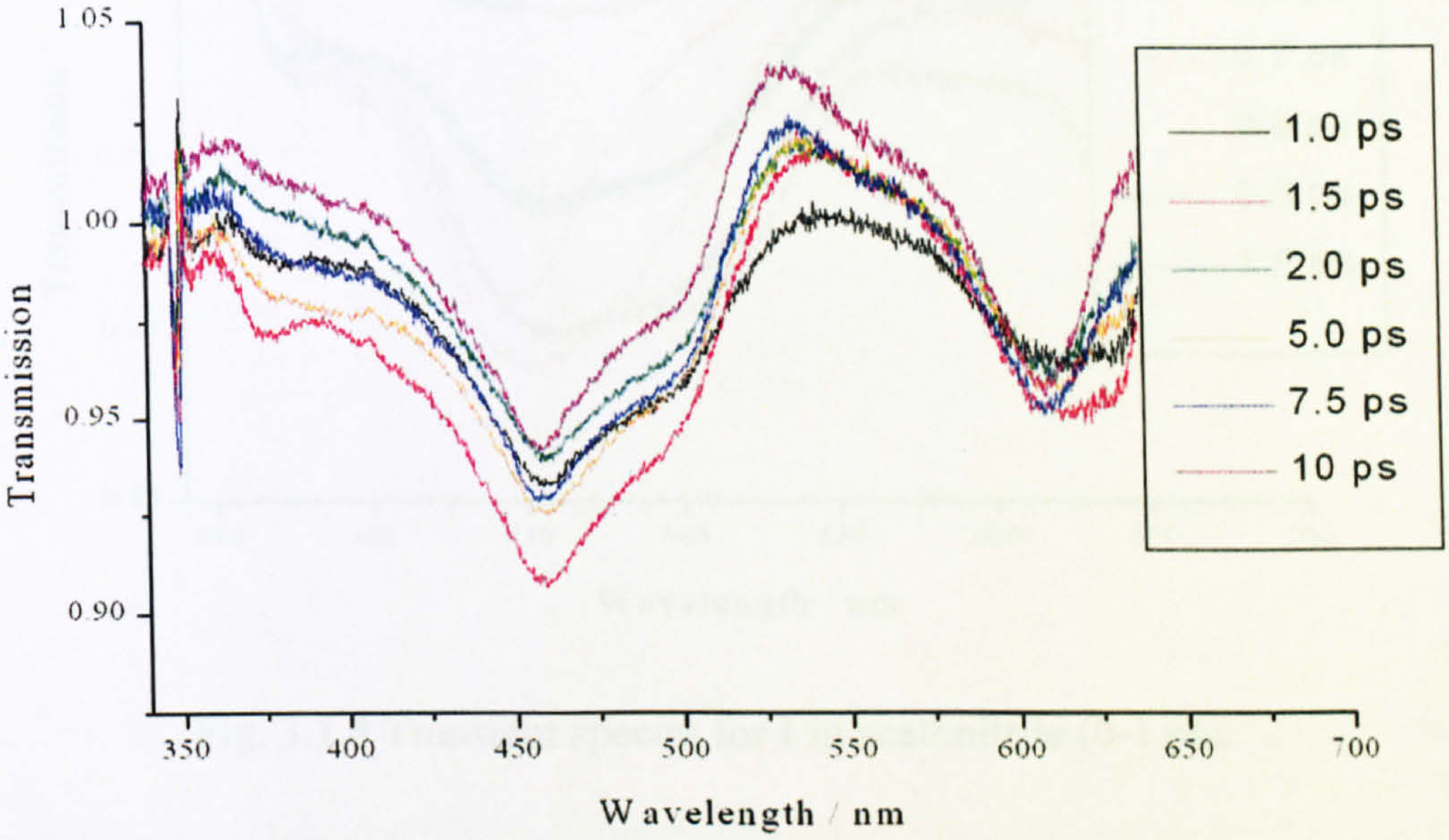

Fig. 3.1.3 Transient spectra for **I** in methylcyclohexane (1 - 10 ps).

The assignment of these two absorption bands is complicated by the lack of accurate kinetics data from these spectra. Prior work by Schwartz et al[2] and others has assigned the emission at 500 nm to the tautomeric excited state and the lower energy absorption band to the S_1'-S_2' transition of the tautomeric species. Almost certainly the red edge of the higher energy absorption band (400-500 nm) is associated with absorption from the S_1' state to some higher excited state of the tautomeric form which we term S_3'. The change in the shape of this band from short delay times until it reaches its steady state condition (1 ps) suggests a movement on the excited state potential energy surface towards equilibrium due to stabilisation of the charged tautomer by the solvent, although we accept that this peak shift is convoluted to a large extent with the dispersion of the continuum, a discussion of which is given in Chapter 2.2.3.

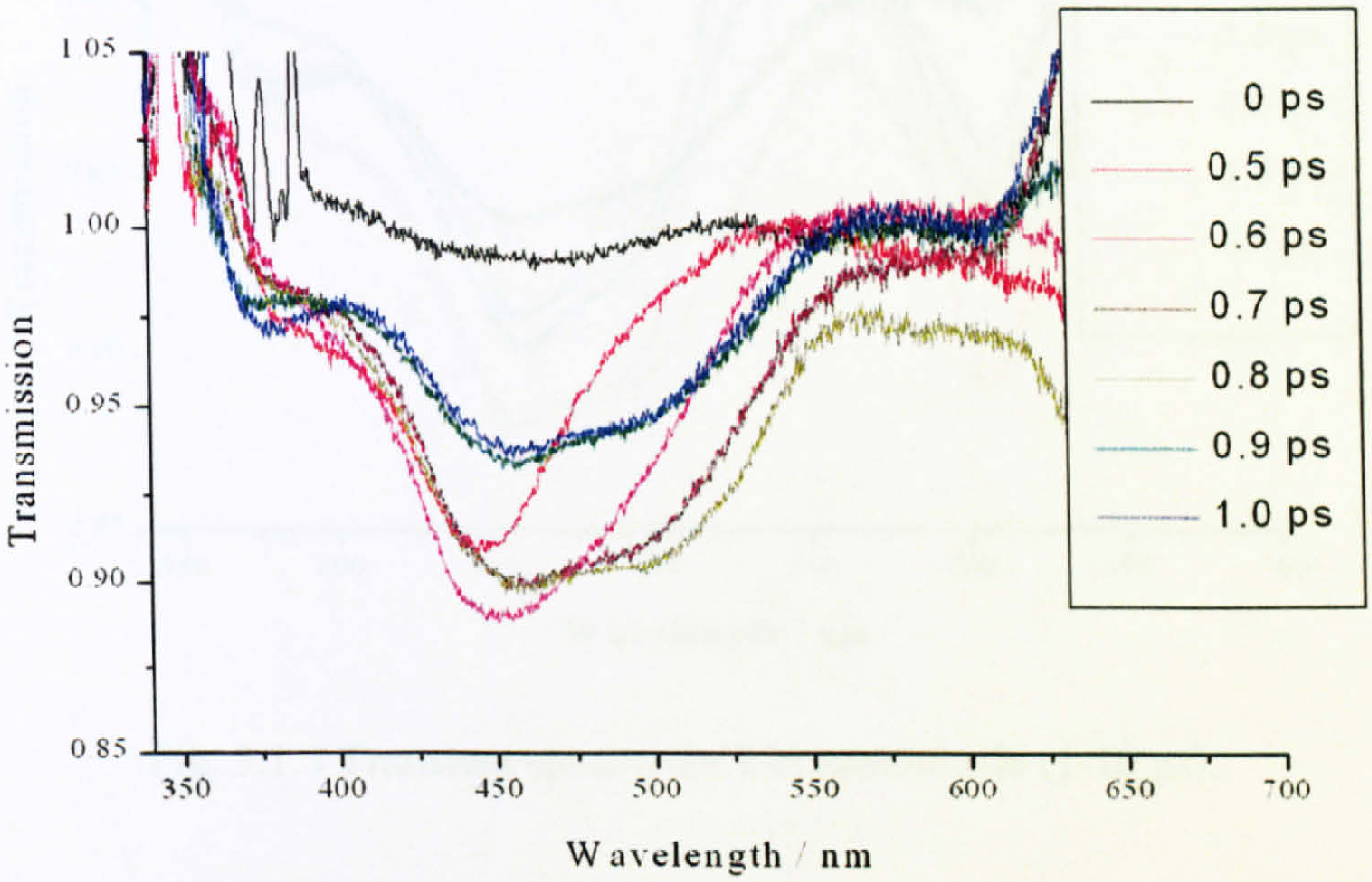

Fig. 3.1.4 Transient spectra for **I** in acetonitrile (0-1 ps).

The transient spectra for **I** (1 mM solution) dissolved in acetonitrile are given in Fig. 3.1.4 and Fig. 3.1.5 for 0-1ps and 1-10 ps respectively. The spectra appear to evolve in a similar fashion to that observed in methylcyclohexane and no obvious effect of solvent polarity is apparent in these spectra.

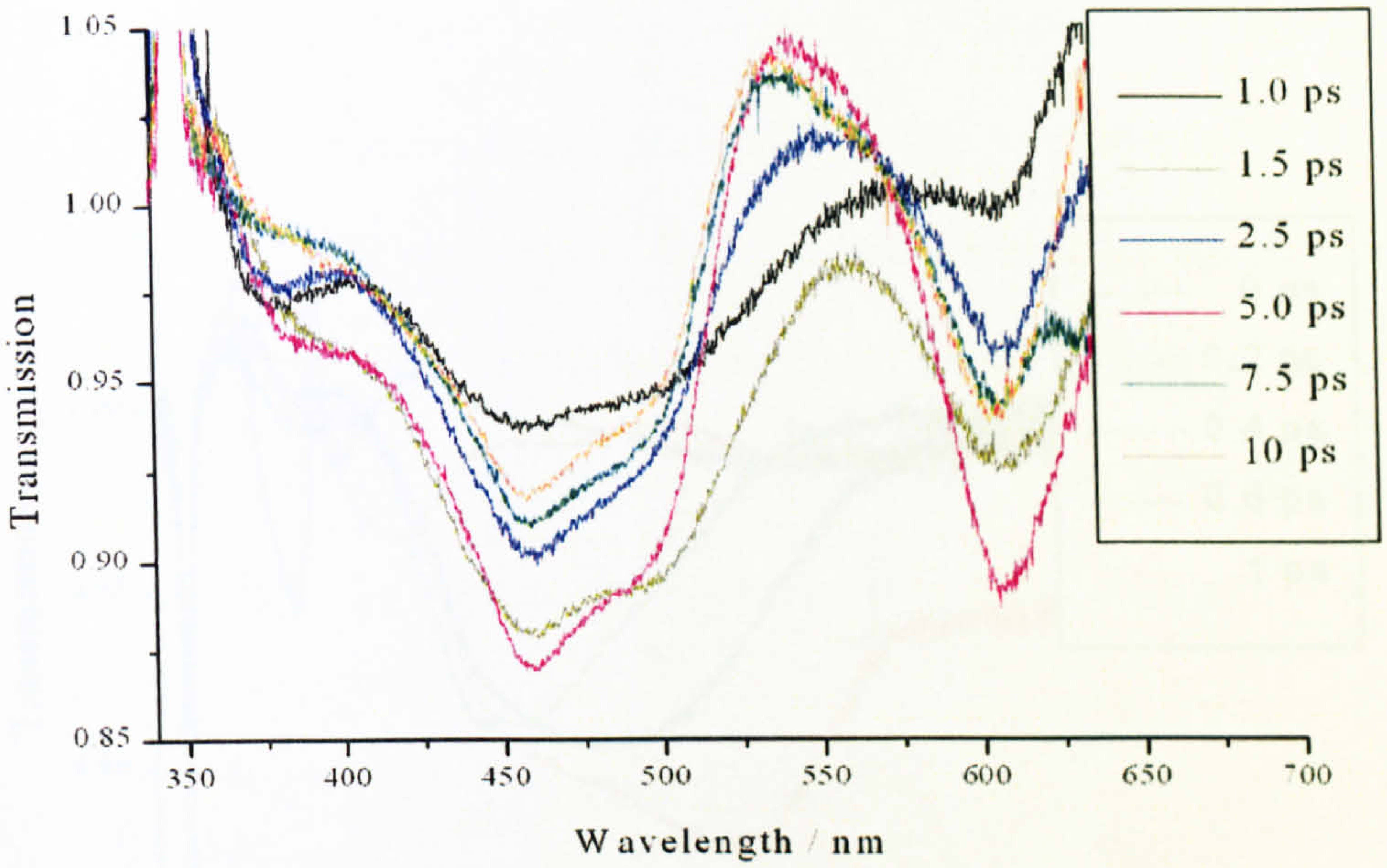

Fig. 3.1.5 Transient spectra for **I** in acetonitrile (1-10 ps).

The transient spectra for **I** dissolved in ethanol show a marked difference to those in the previously described non-hydrogen bonding solvents (Fig. 3.1.6 and Fig. 3.1.7 for 0-1 ps and 1-10ps respectively). The initial time-dynamics are similar in that a peak in absorption shifts from ~ 400 nm to form a broad absorption feature from 425-550 nm. However, a larger Stokes shift to a peak at ~525 nm is observed with a shoulder at around 450 nm after 1 ps. This contrasts with the methylcyclohexane spectra, which showed a peak at 450 nm and a shoulder around 525 nm. In ethanol we are perhaps observing a shift in molecular population to a lower energy state due to solvent stabilisation of the tautomer. For longer time scales we see an apparent peak shift back to the 450 nm band due to the grow-in of stimulated emission around 530 nm, as one would expect. For longer time-scales the spectra are identical in form to those observed for methylcyclohexane as solvent.

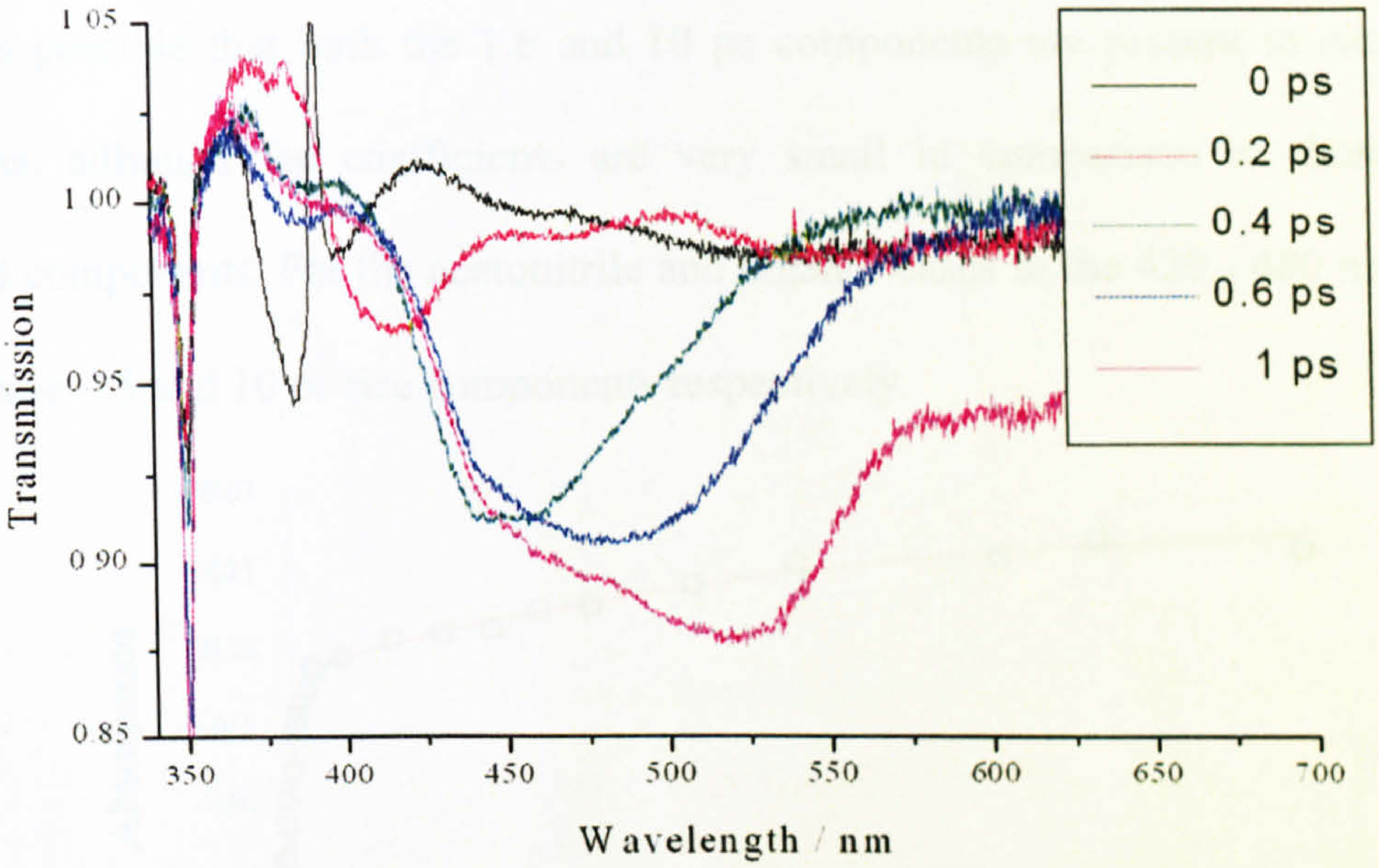

Fig. 3.1.6 Transient spectra for **I** in ethanol (0-1 ps).

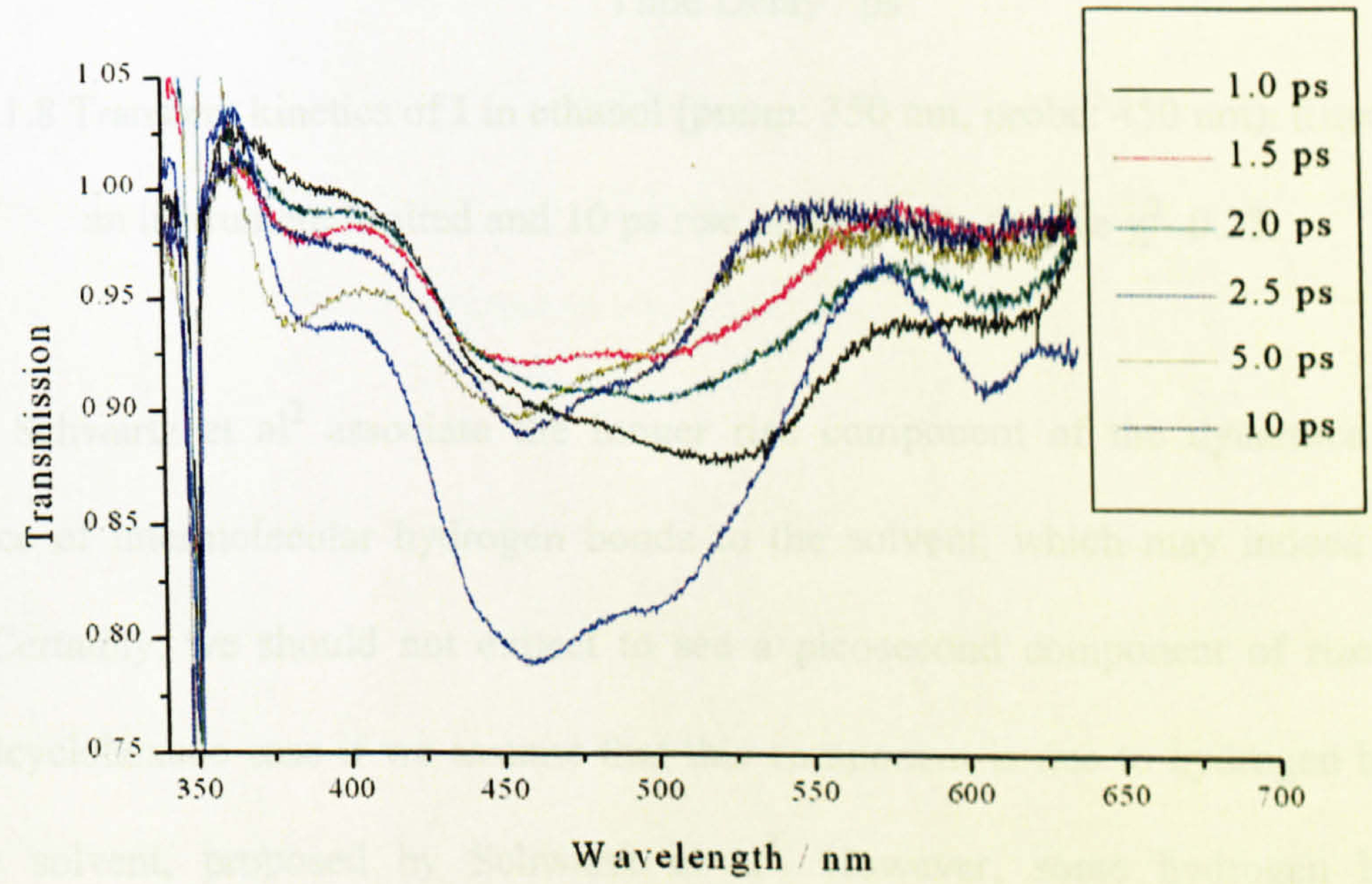

Fig. 3.1.7 Transient spectra for **I** in ethanol (1-10 ps).

methylcyclohexane solution, we see a small ps rise component in the 420 - 480 nm region of the excited state spectra. However, a significant component of rise is observed at 585 nm of ~10 ps and a much faster component of ~ 1.6 ps is clearly resolved at 620 nm. It is possible that both the 1.6 and 10 ps components are present in each of the transients, although the coefficients are very small in comparison to those of the resolved components. For the acetonitrile and ethanol cases in the 420 - 480 nm region, we observe ~ 5 and 10 ps rise components respectively.

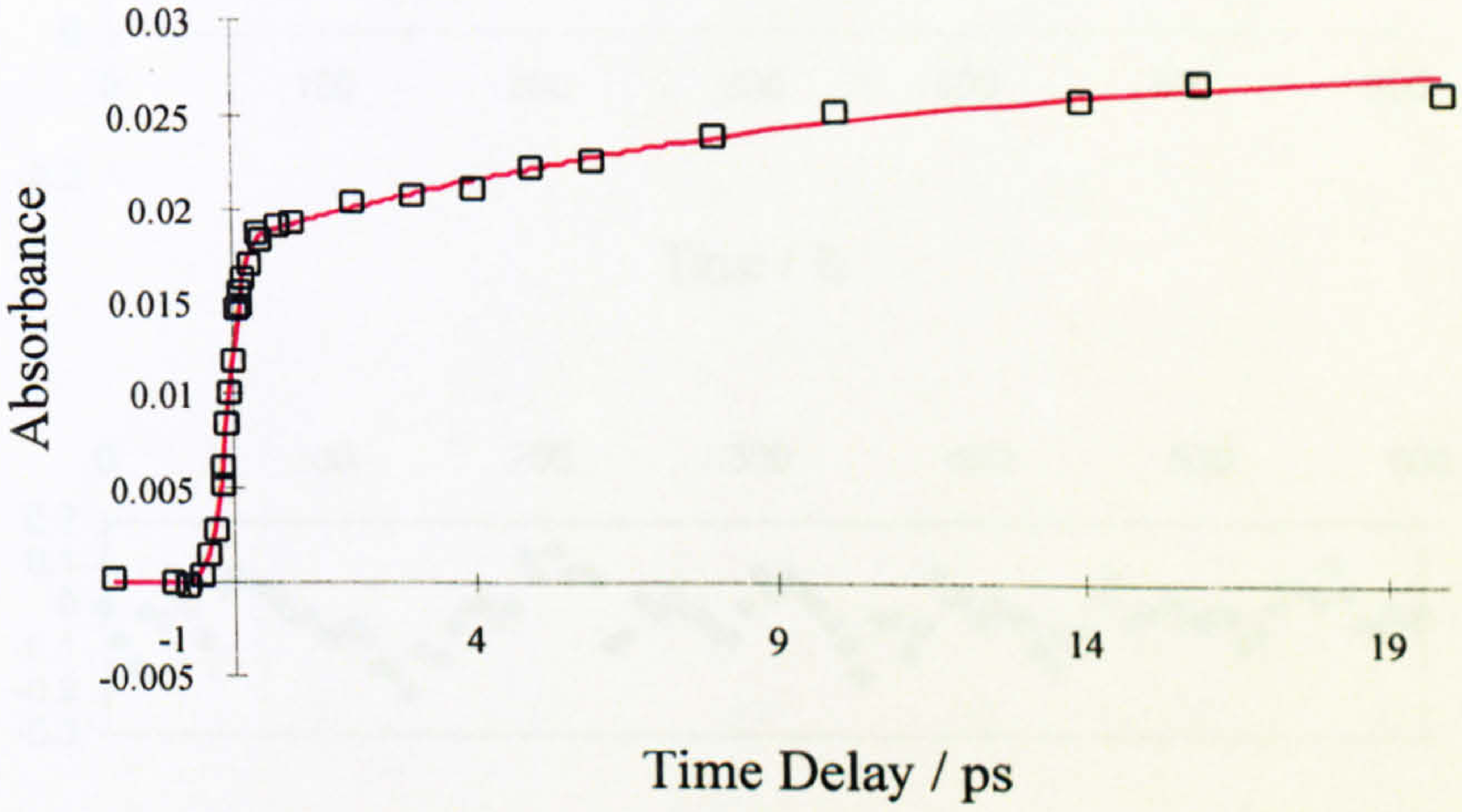

Fig. 3.1.8 Transient kinetics of **I** in ethanol (pump: 350 nm, probe: 450 nm). fitted with an instrument limited and 10 ps rise components to give χ^2~0.23.

Schwartz et al[2] associate the longer rise component of the dynamics to the presence of intermolecular hydrogen bonds to the solvent, which may indeed be the case. Certainly, we should not expect to see a picosecond component of rise in the methylcyclohexane case if we assume that this component is due to hydrogen bonding of the solvent, proposed by Schwartz et al[2]. However, some hydrogen bonding impurities are no doubt present and these could potentially cause the component observed in these transients. The fast component of rise in the kinetics has been assigned to the ESIPT and a dependence on solvent environment. If we accept this

PAGE

MISSING

IN

ORIGINAL

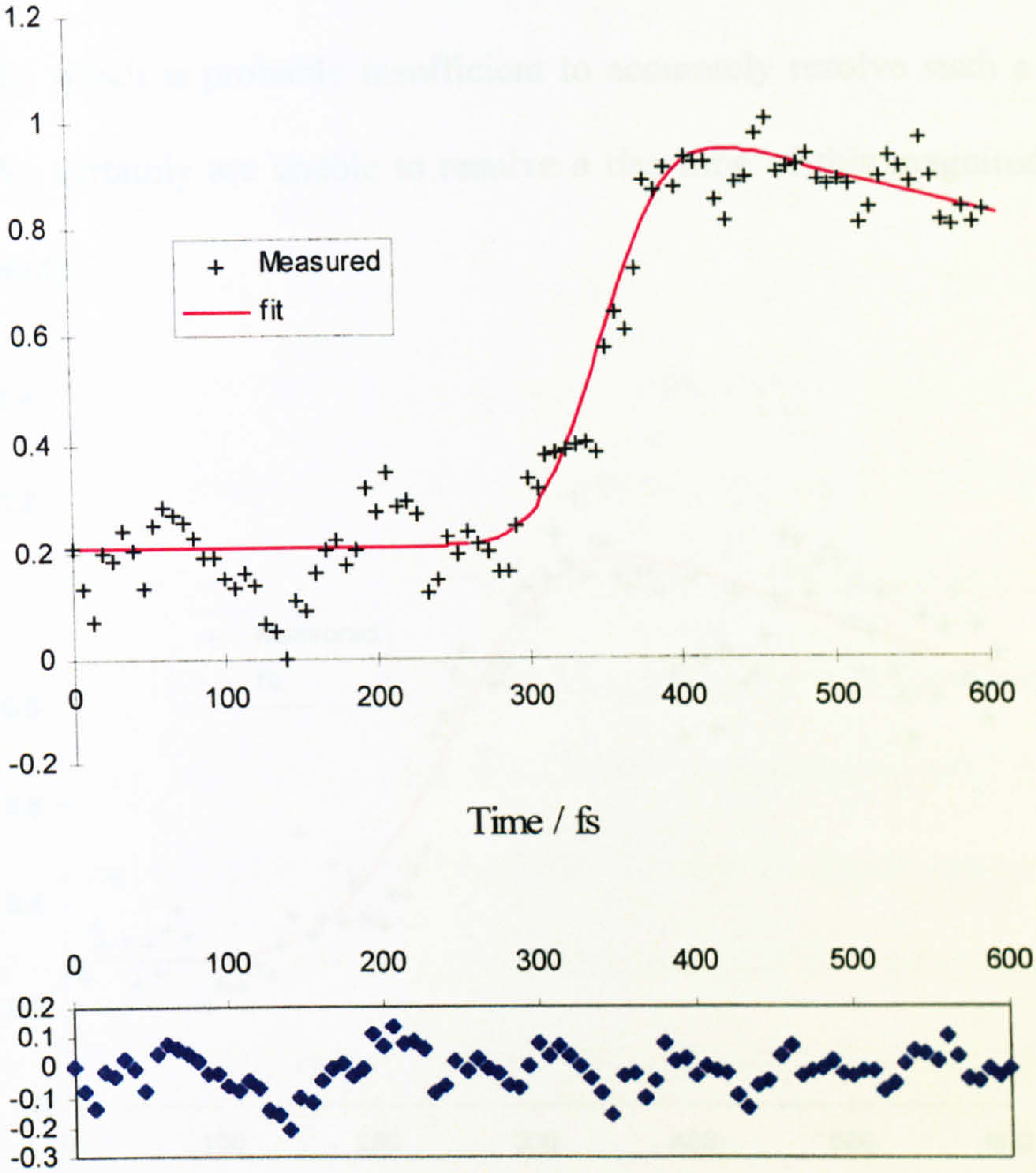

Fig. 3.1.9 Transient absorption of **I** in methylcyclohexane

(pump: 360 nm, probe: 440 nm). Fit to instrument limited rise and 1 ps decay

component to give χ^2~0.62.

A typical transient is given in Fig. 3.1.9 for **I** in methylcyclohexane at 440 nm which was excited with a UV pulse at 360 nm, along with the instrumental function (time integrated cross diffraction measurement). It is clear that the response at this point in the spectrum is instrument limited indicating that the proton transfer event in this solvent is considerably less than 70 fs and indeed significantly less than the 120 fs observed by Schwartz et al[2]. This might be attributed to the deconvolution method used by Schwartz et al to extract the rise component. Careful scrutiny of the experimental section of the paper reveals that the instrumental function for the experiment was of the order of 250 fs, which is probably insufficient to accurately resolve such a 100 fs rise component. We certainly are unable to resolve a rise time of this magnitude from our RAL experiments.

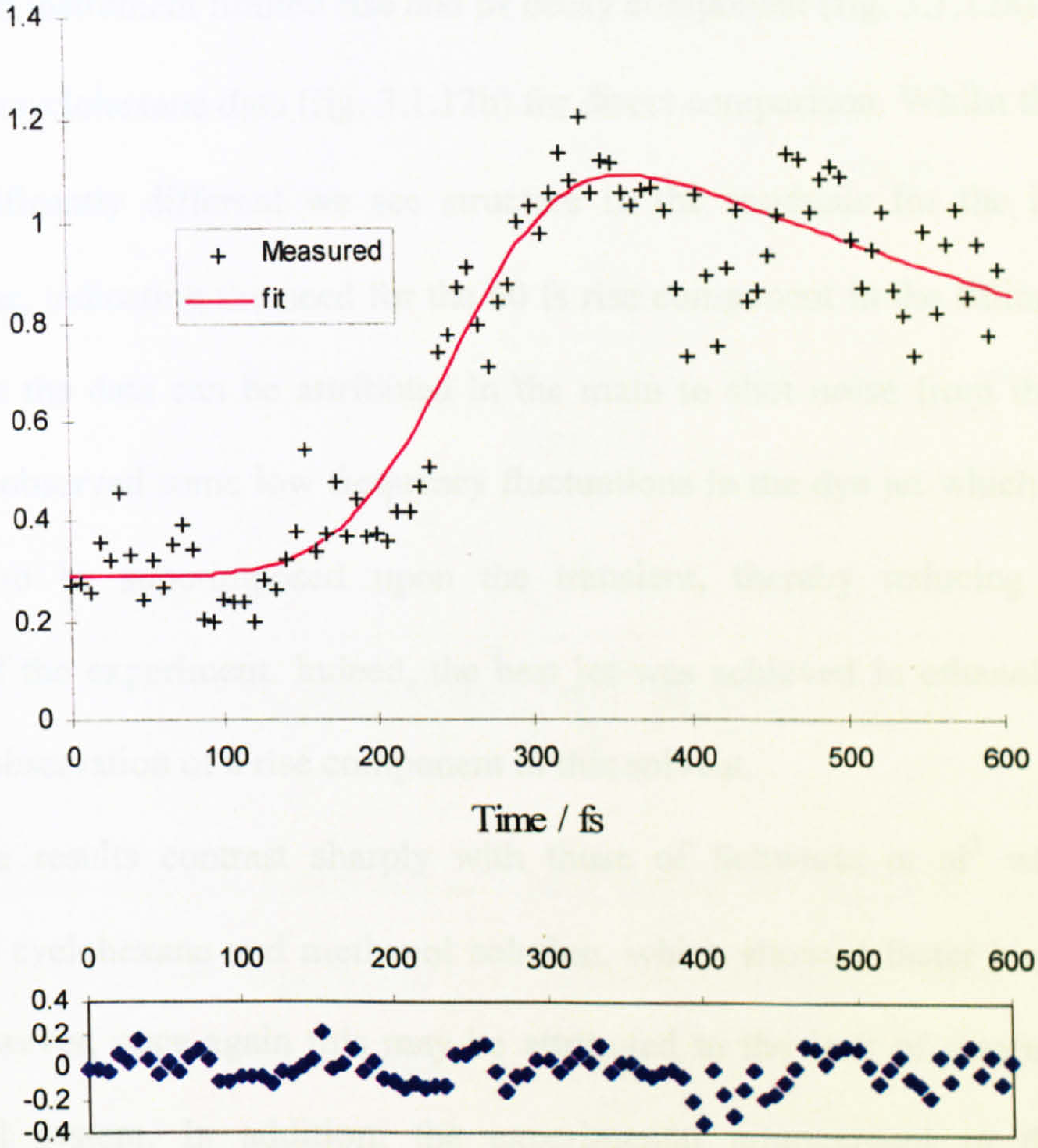

Fig. 3.1.10 Transient absorption of **I** in acetonitrile (pump: 360 nm, probe: 440 nm). Fit to instrument limited rise and 1 ps decay component to give χ^2~1.12 (over the peak).

Observations in acetonitrile solution (Fig.3.1.10) seem to confirm our initial results with no resolvable rise component observed at 440 nm. This contrasts with observations of **I** in ethanol, which seem to require a rise component of the order of 60 fs (Fig. 3.1.11) to give a satisfactory fit (χ^2 = 0.51). We also observe a decay component on a ps timescale which may be due to the decaying edge of the blue absorption region as observed in the spectra. However, no such component was observed for the RAL experiments and may be a consequence of the difference in experimental parameters (concentration and excitation wavelength). The same data is fitted using an instrument limited rise and ps decay component (fig. 3.1.12a) and plotted with the methcyclohexane data (fig. 3.1.12b) for direct comparison. Whilst the χ^2 values are not significantly different we see structure in the residuals for the instrumental function alone, indicating the need for the 60 fs rise component in the fitting algorithm. The noise on the data can be attributed in the main to shot noise from the detection, however we observed some low frequency fluctuations in the dye jet which cause some oscillations to be superimposed upon the transient, thereby reducing the overall sensitivity of the experiment. Indeed, the best jet was achieved in ethanol which may explain the observation of a rise component in this solvent.

These results contrast sharply with those of Schwartz et al[2] who observed transients in cyclohexane and methanol solution, which showed faster kinetics for the alcohol. However, once again this may be attributed to the lack of resolution of their experimental system. In addition, the experimental arrangement in the Schwartz experiment involved excitation (pump) well above the S_0—S_1 transition (~350 nm) at 296 nm. This may explain the discrepancy with respect to the fast time component. Vibrationally hot molecules of **I** may undergo significantly different kinetics. Indeed, the potential energy landscape of higher order singlet states would certainly differ from the S_1 state.

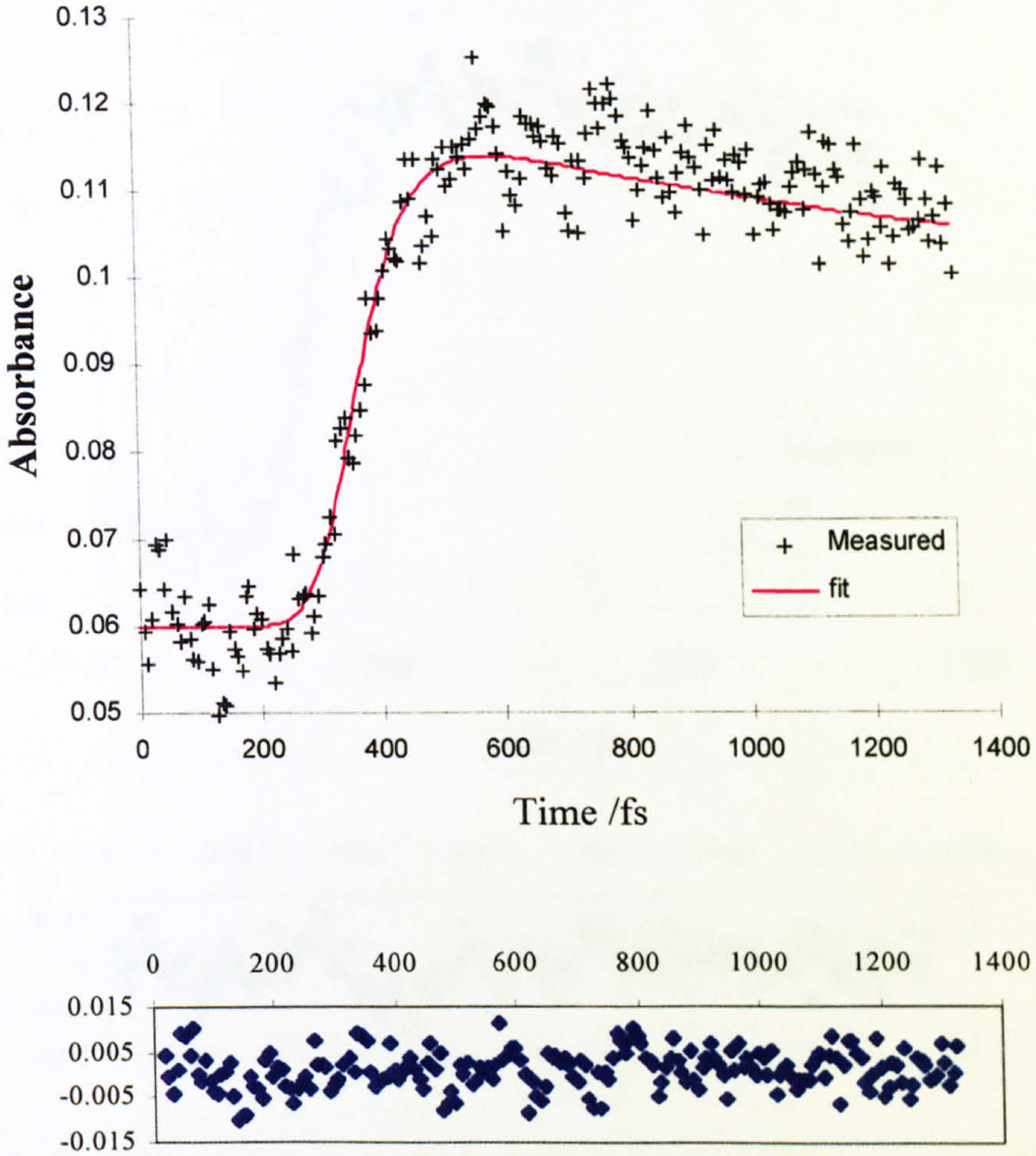

Fig. 3.1.11 Transient absorption of **I** in ethanol (pump: 360 nm, probe: 440 nm). The best fit occurs for a rise component of 61 fs and a decay component of the order of 1 ps, giving a χ^2~0.5.

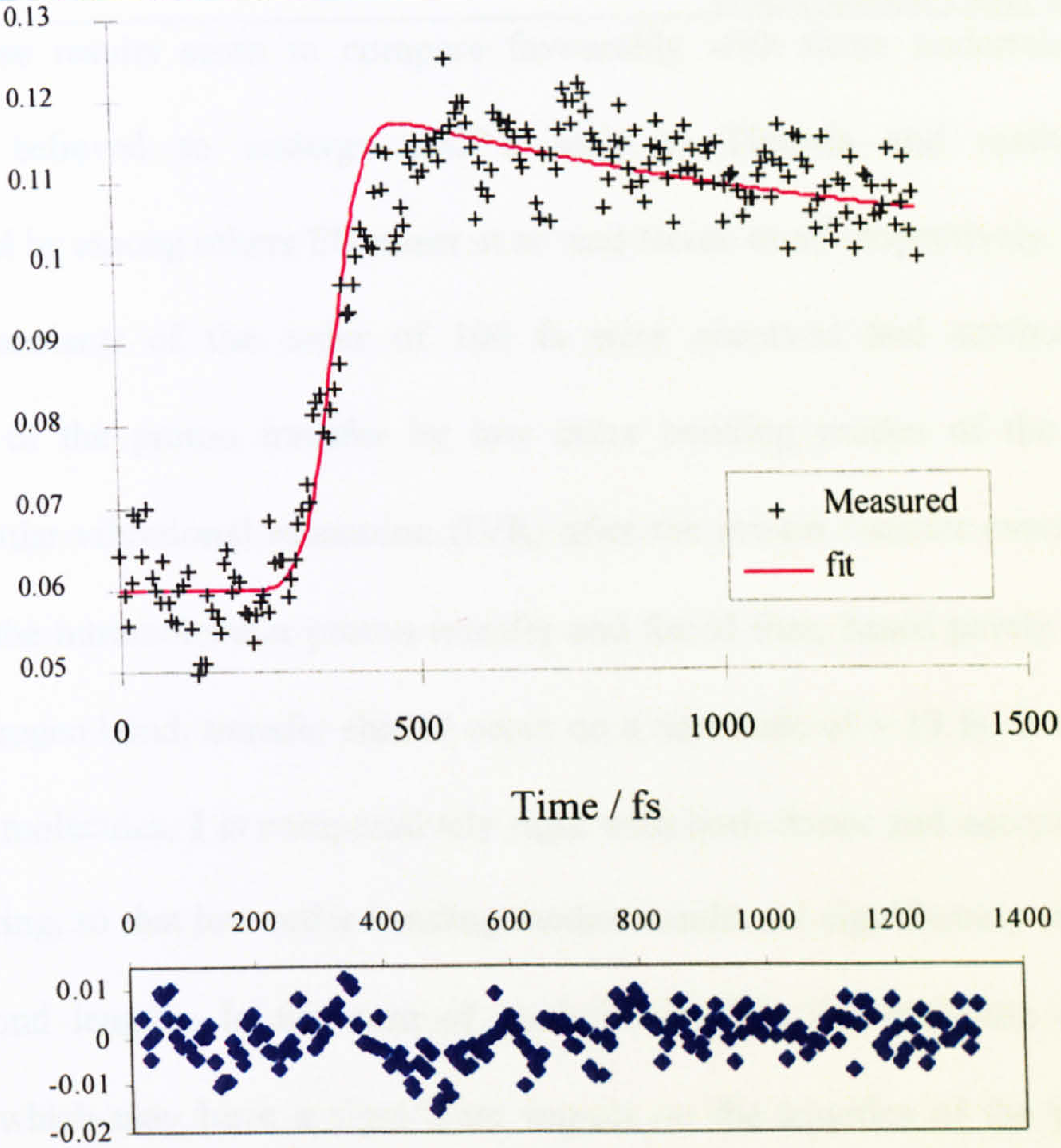

Fig. 3.1.12a Transient absorption of **I** in ethanol (pump: 360 nm, probe: 440 nm). Fit with instrumental rise and ps decay component (note the structure in the residuals around time zero), $\chi^2 \sim 0.62$.

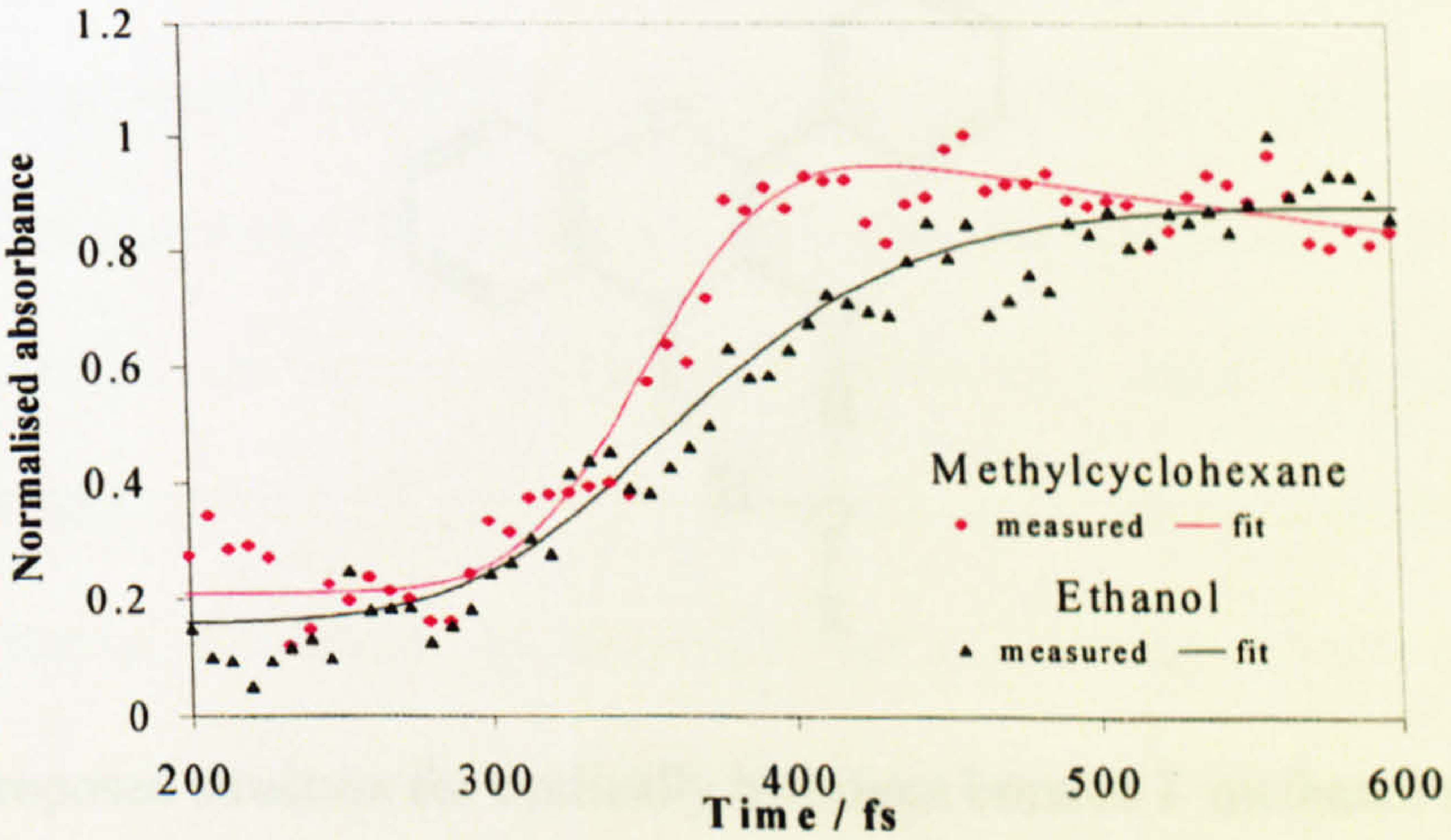

Fig. 3.1.12b Direct comparison of transients from **I** in methylcyclohexane and ethanol (pump: 360 nm, probe: 440 nm).

These results seem to compare favourably with those undertaken for other molecules believed to undergo ESIPT such as Tinuvin and methyl salicylate investigated by among others Elsaesser et al[3] and Herek et al[4] respectively. In both these systems transients of the order of 100 fs were observed and attributed to either mediation of the proton transfer by low order bending modes of the molecule or intramolecular vibrational relaxation (IVR) after the proton transfer event. Herek et al modelled the intramolecular proton transfer and found that, based purely on the length of the hydrogen bond, transfer should occur on a timescale of ~ 13 fs. In comparison to these two molecules, **I** is comparatively rigid with both donor and acceptor moeties on the same ring, so that low order bending modes should not significately mediate the O_4-H—O_3 bond lengths. In the case of methyl salicylate the molecule can form two rotamers which may have a significant impact on the kinetics of the proton transfer motion. Tinuvin has significantly more degrees of freedom in comparison to **I** and is also free to rotate about an inter-ring bond (See Figures 1.4.6 and 1.4.13 for the structures of methyl salicylate and Tinuvin respectively).

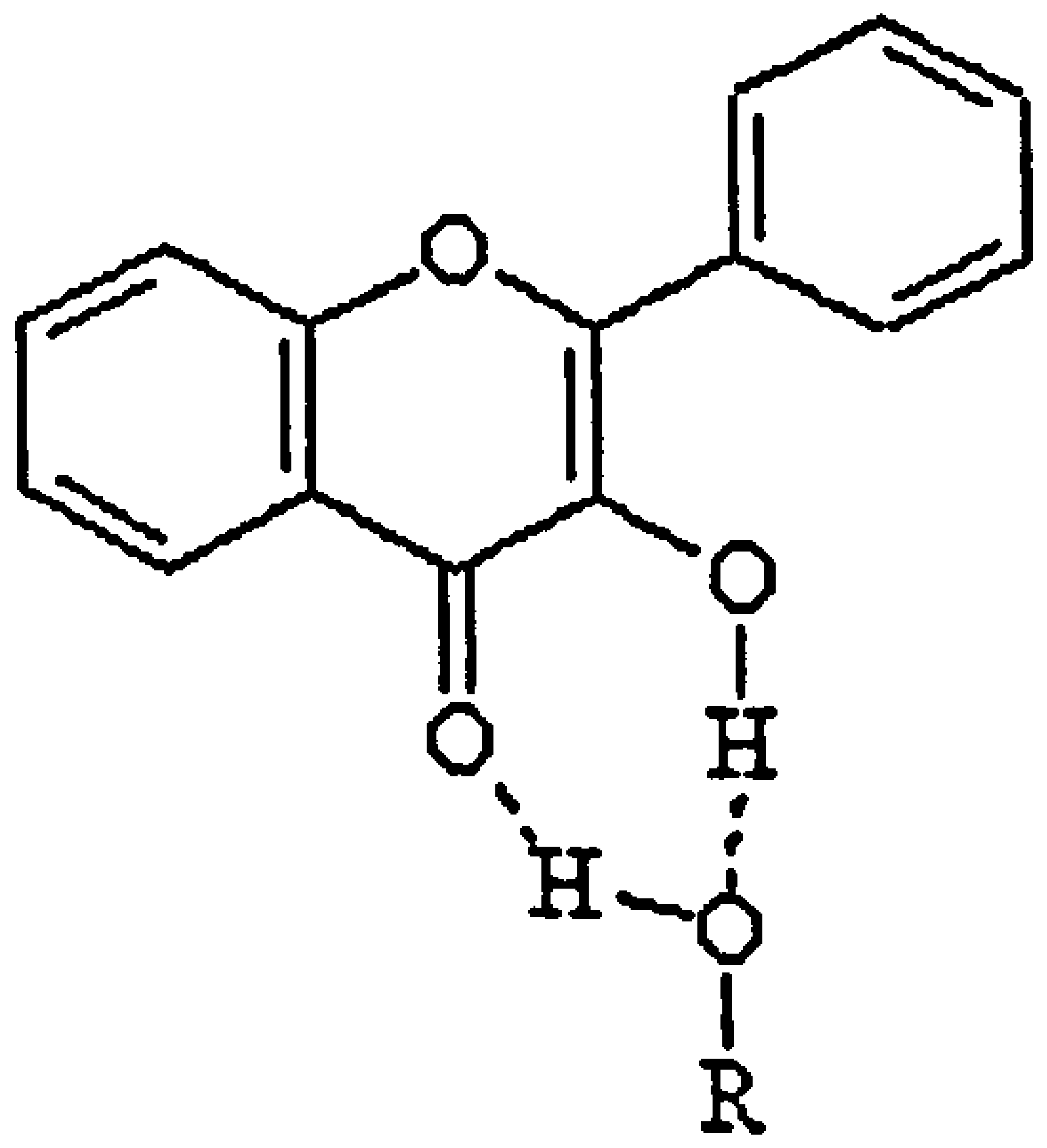

Fig. 3.1.13 Proposed structure for cyclically hydrogen bonded **I** methanol monosolvate.

Whilst we observe the opposite effect on the kinetics for intramolecular proton transfer in going from non-interacting to hydrogen bonding solvent environments, we consider this to be consistent with the arguments put forward by Schwartz et al[2] to explain the anomalous behaviour. The presence of intermolecular hydrogen bonds will considerably influence the kinetics. In the case of a mono-solvated molecule (Fig. 3.1.13), proton transfer can occur mediated by the intermolecular hydrogen bonds. Such a process involves either a two step motion or concerted proton transfer. Systems such as 7-azaindole which form dimeric proton transfer complexes have been observed to undergo such a dual proton motion with what appears to be biphasic kinetics with a slow (picosecond component) and a faster ~ 200 fs component which has been observed to be dependent on the excess energy of the excitation[5]. With this in mind we suggest that proton transfer mediated by intermolecular hydrogen bonds could occur on a comparable or slightly slower timescale than observed for the non-interacting case. Certainly, considering the problem on a probabilistic basis, the probability of two protons moving along the appropriate reaction co-ordinates must be low in comparison with a single comparable event. However, resonance Raman spectra of the molecule in a variety of solvents should elucidate the mechanism by which protic solvents effect the intramolecular hydrogen bond but this is, unfortunately, beyond the scope of this thesis.

In conclusion, we have observed the behaviour of **I** under excitation with UV laser pulses at 350 nm and 360 nm. Transient absorption measurements show small spectral and kinetic differences in behaviour for an alcohol solvent environment, confirming the earlier work of Ormson et al[6]. Measurement of the ultrafast ESIPT event also shows such a dependence, with non-interacting and polar solvent environments showing an instrument limited response and an appreciable rise component for a hydrogen bonding solvent of ~ 60 ± 10 fs. We attribute this behaviour to the presence of mono-solvated **I** complexes, which may undergo either a dual intermolecular proton transfer to the solvent, or intramolecular proton transfer along the O_4-H—O_3 reaction co-ordinate.

3.2 4'-Chloro-3-hydroxyflavone

Spectra observed for 4'-chloro-3-hydroxyflavone (**II**) in methylcyclohexane, show time dependent behaviour similar to that observed for the unsubstituted molecule (Fig. 3.2.1 and 3.2.2 for 0-1 ps and 1-16 ps respectively). Within 500 fs a broad ~ 50 nm absorption feature is observed with a peak at approximately 440 nm which shifts to form a broad peak at 470 nm with a full width at half maximum of ~ 75 nm within 1 ps, when motion of this band can be said to be complete. A second absorption feature is observed which grows in within 1 ps from the long wavelength region to form a peak at ~ 620 nm with a width of ~ 25 nm and a long tail towards 700 nm. Stimulated emission from the tautomer S_1' state is observed at 530 nm within 1 ps and a long timescale anti-Stokes shift is observed to approximately 520 nm.

Spectra observed in acetonitrile (Fig.3.2.3 & 3) and ethanol (Fig. 3.2.5 & 6) solution show similar behaviour, although the appearance of the stimulated emission band appears to be delayed (~ 4ps for acetonitrile, ~ 16 ps for ethanol) with respect to the cyclohexane case. This is consistent with the observations for unsubstituted **I**, which showed a weak dependence of the spectral observations on the solvent.

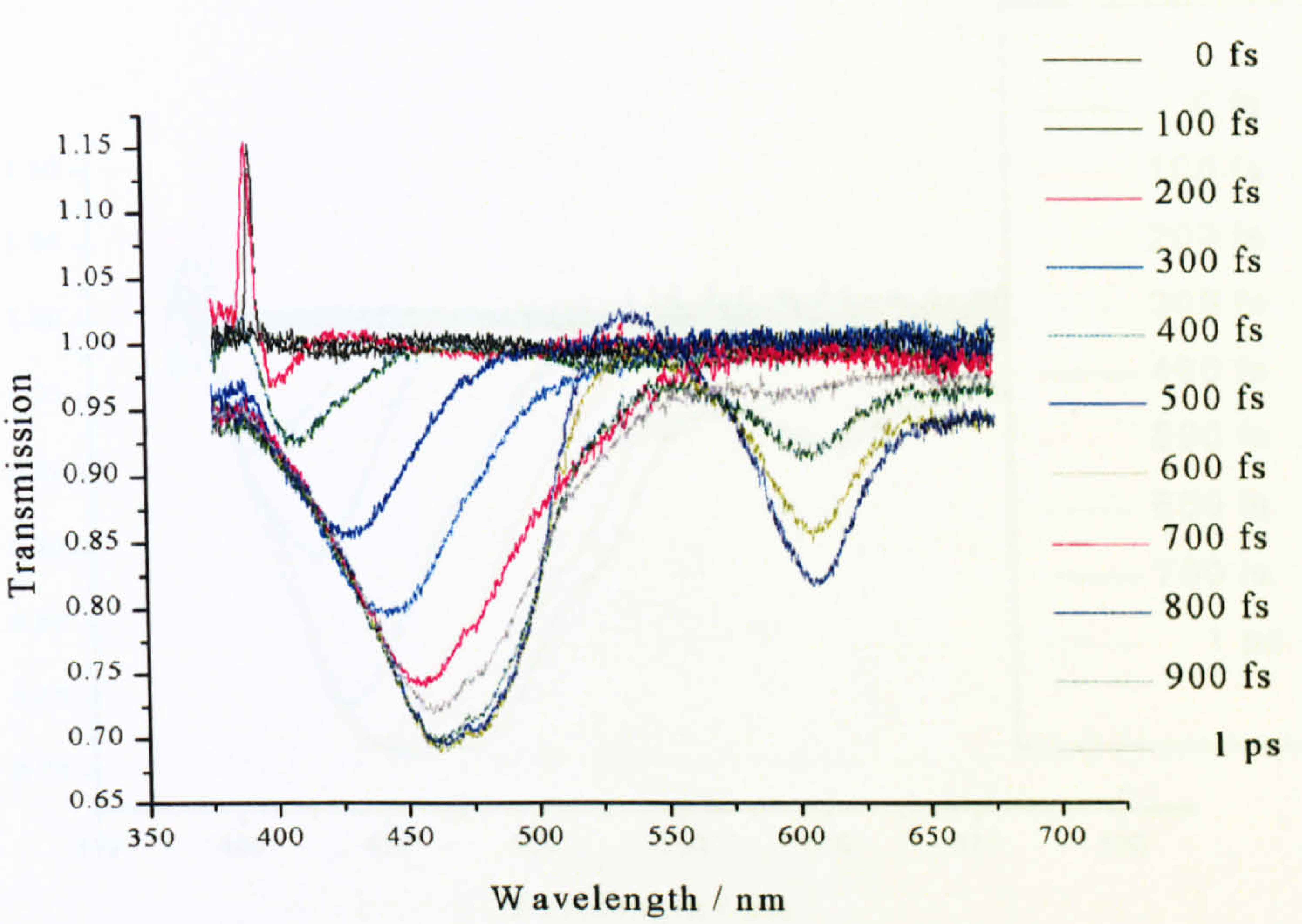

Fig. 3.2.1 Transient spectra for **II** in methylcyclohexane (0-1 ps).

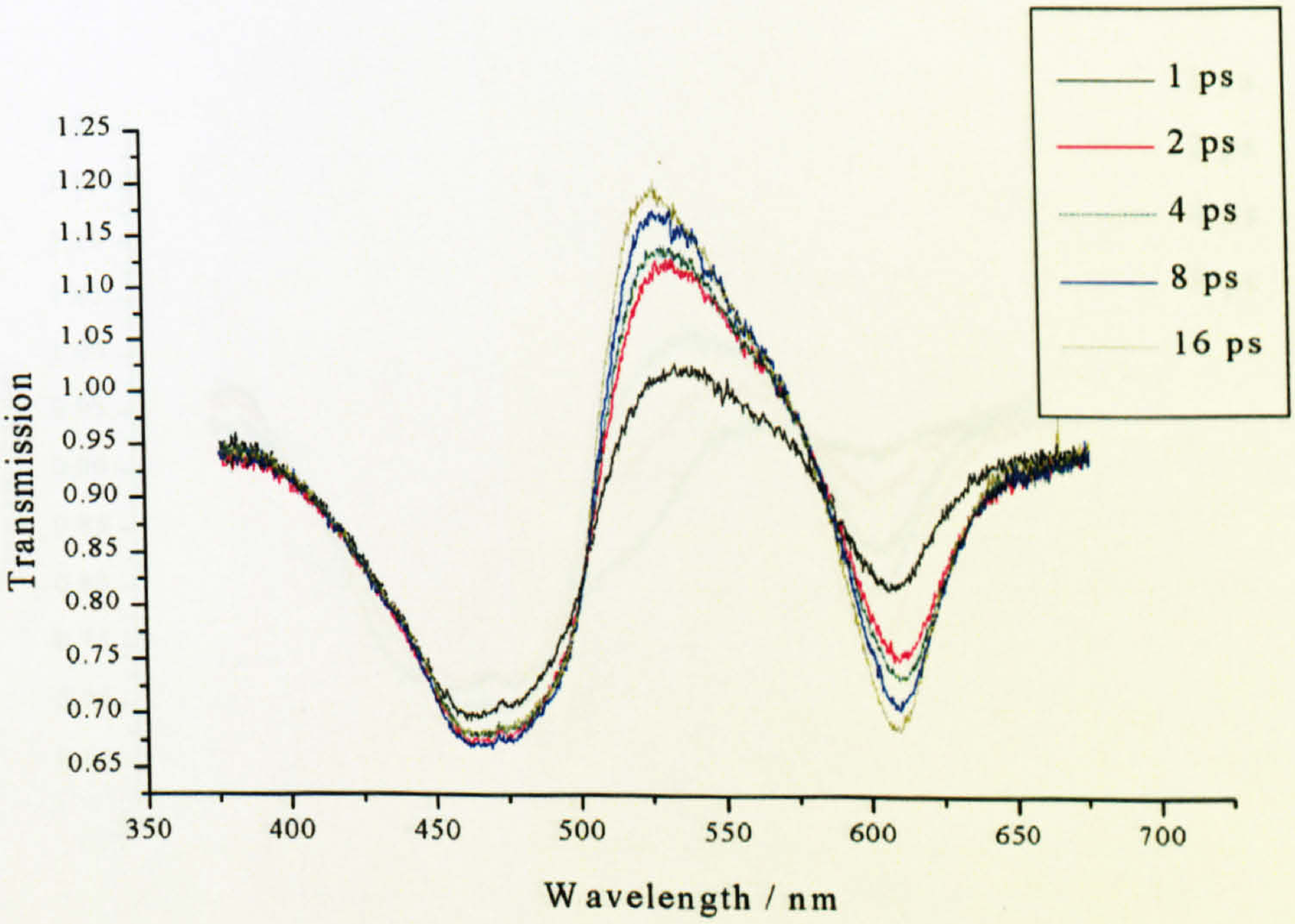

Fig. 3.2.2 Transient spectra for **II** in methylcyclohexane (1-16 ps).

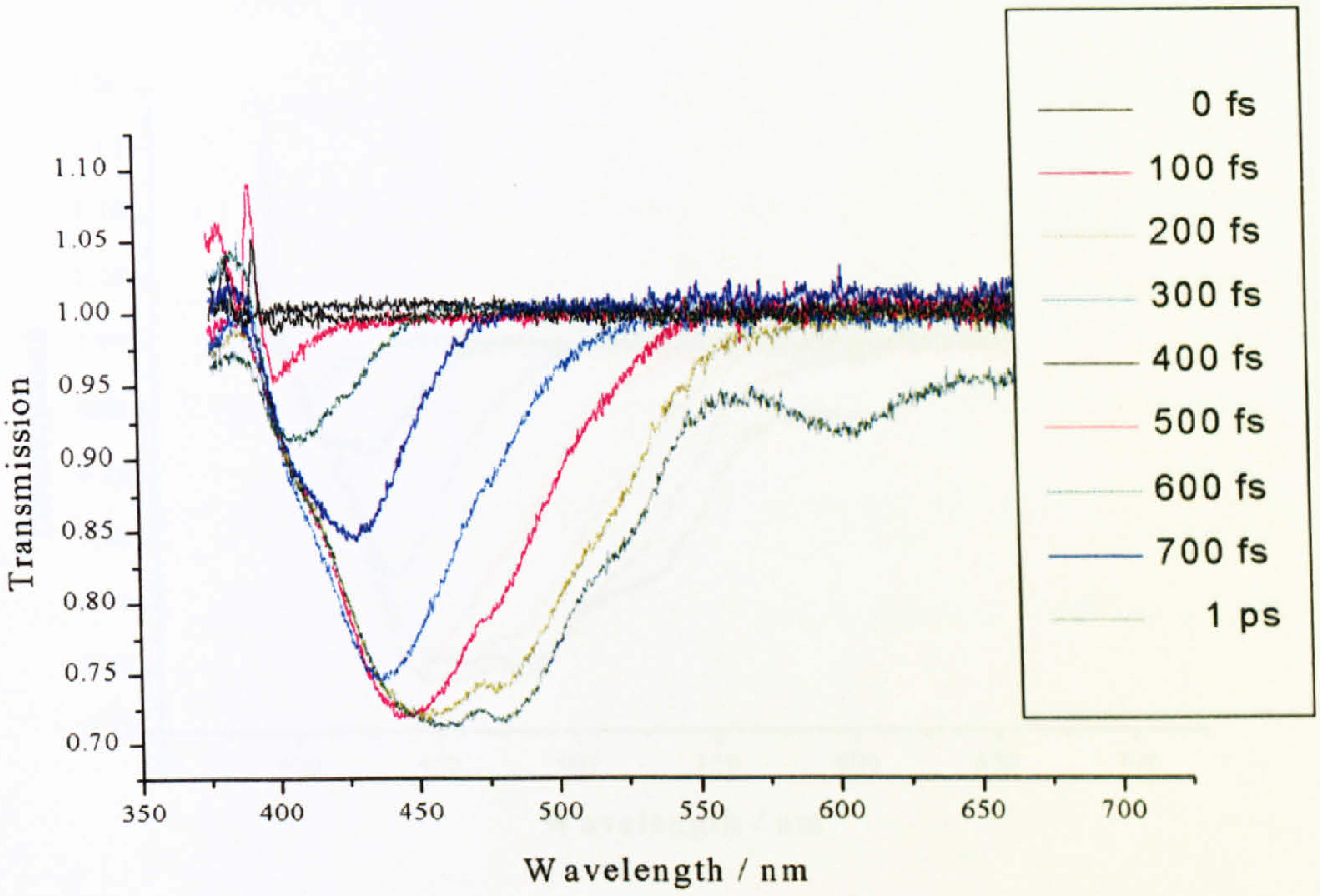

Fig. 3.2.3 Transient spectra for **II** in acetonitrile (0-1 ps).

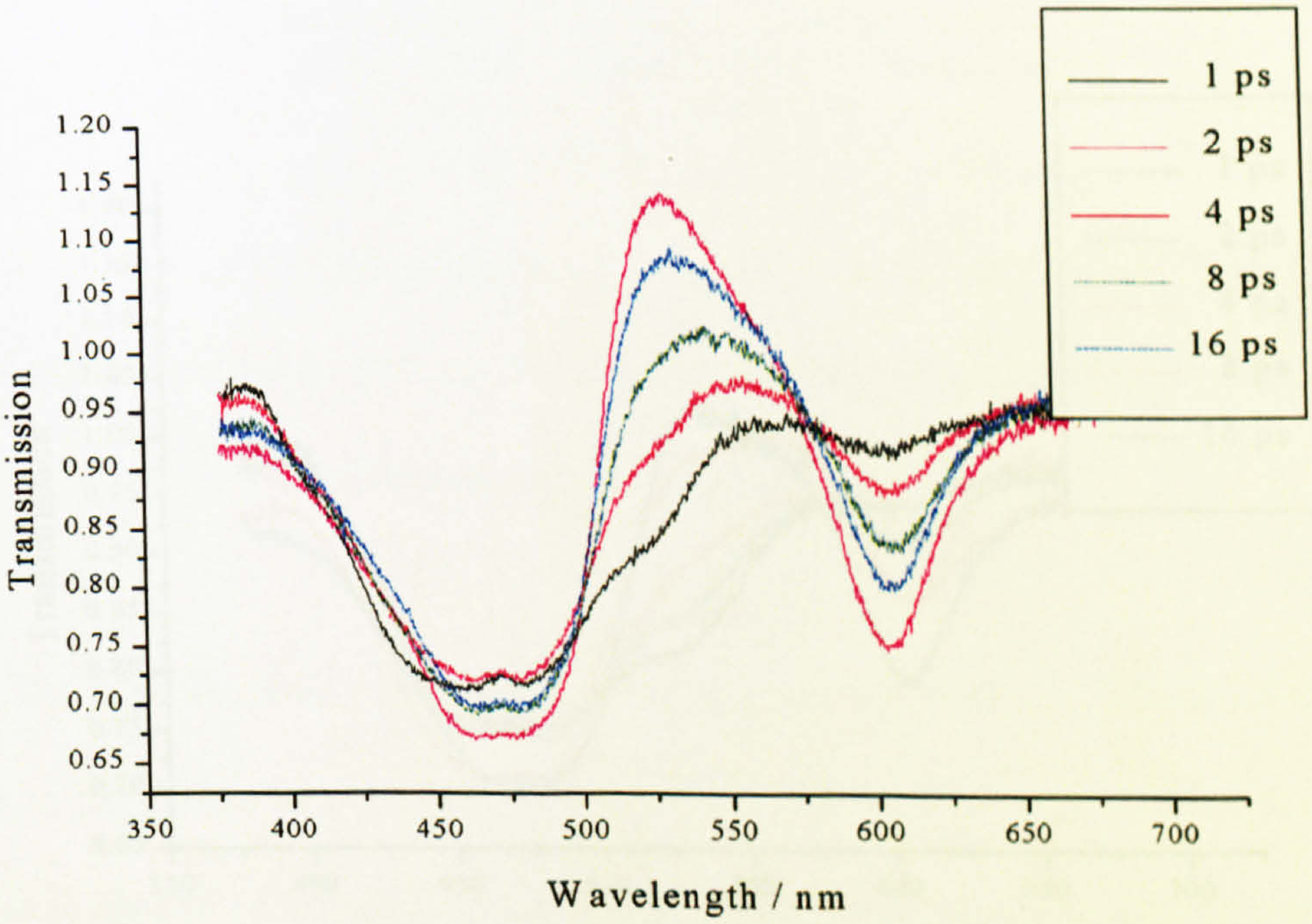

Fig. 3.2.4 Transient spectra for **II** in acetonitrile (1-16 ps).

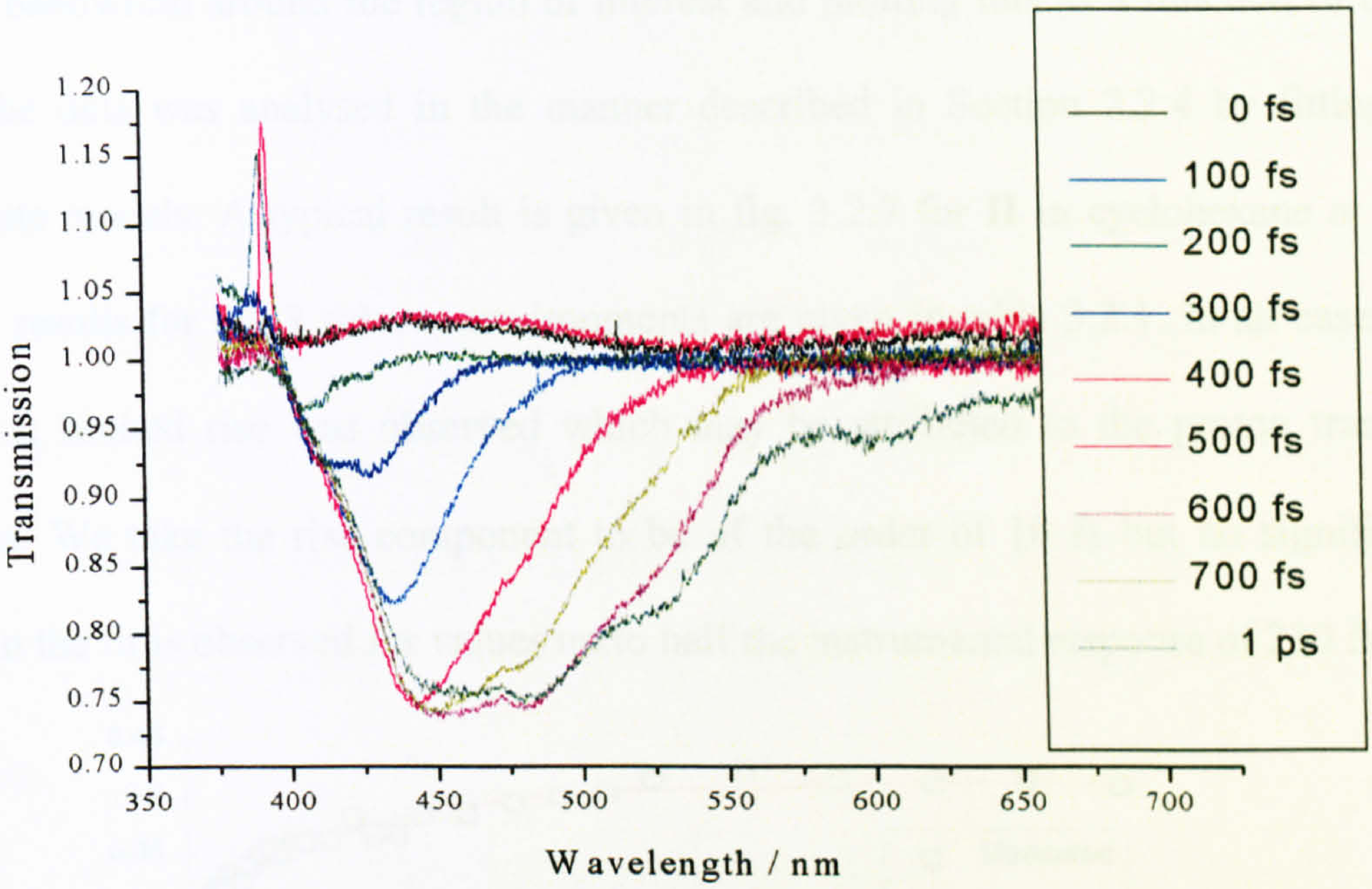

Fig. 3.2.5 Transient spectra for **II** in ethanol (0-1 ps).

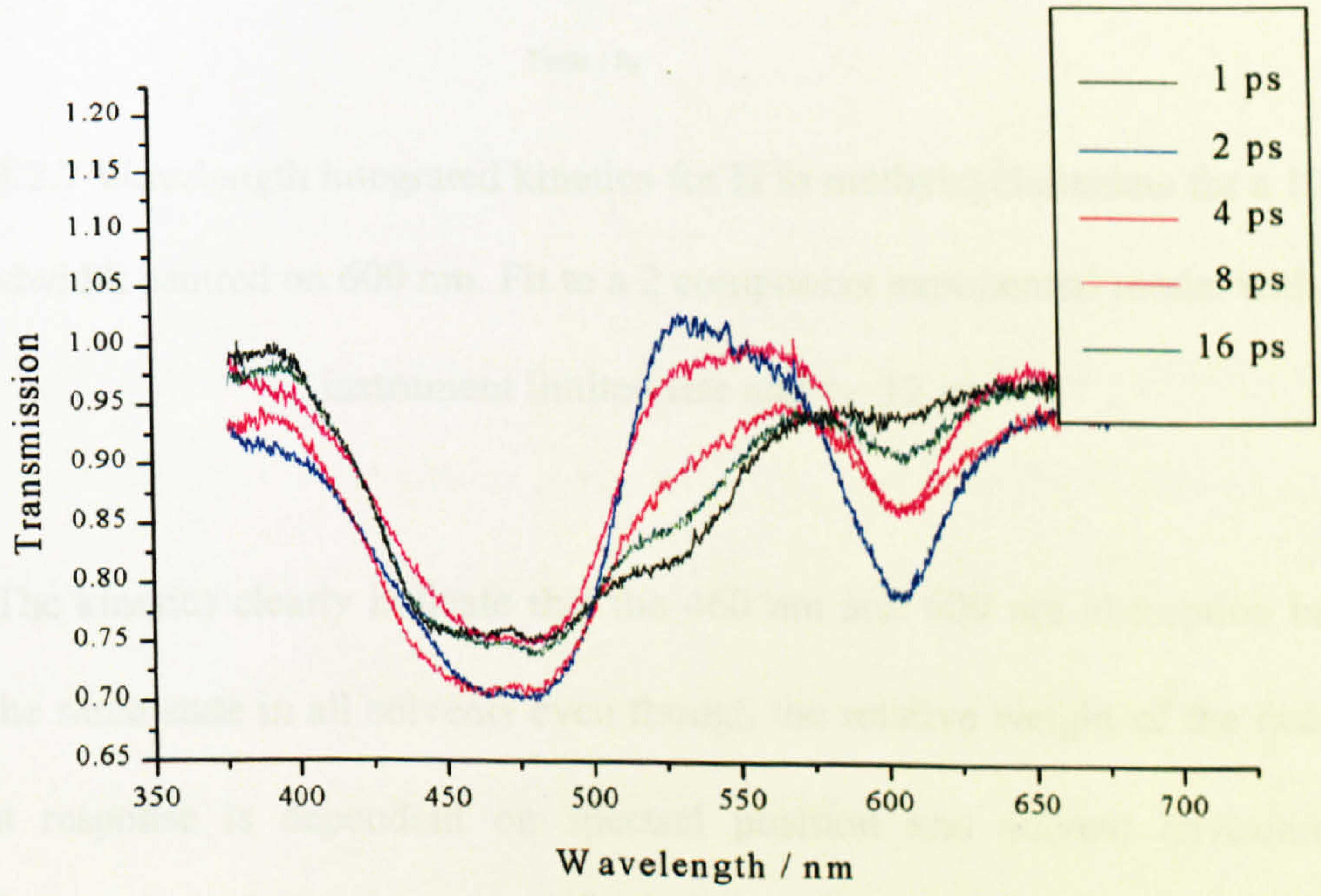

Fig. 3.2.6 Transient spectra for **II** in ethanol (1-16 ps).

Kinetics data for each of the relevant spectral regions was extracted by averaging a 10 nm bandwidth around the region of interest and plotting this as a function of time delay. The data was analysed in the manner described in Section 2.2.4 by fitting to appropriate models. A typical result is given in fig. 3.2.7 for **II** in cyclohexane at 600 nm. The results for the 3 solvent environments are given in table 3.2.1. In all cases an instrument limited rise was observed which may be attributed to the proton transfer dynamics. We take the rise component to be of the order of 10 fs but no significant change in the fit is observed for values up to half the instrumental response of 230 fs.

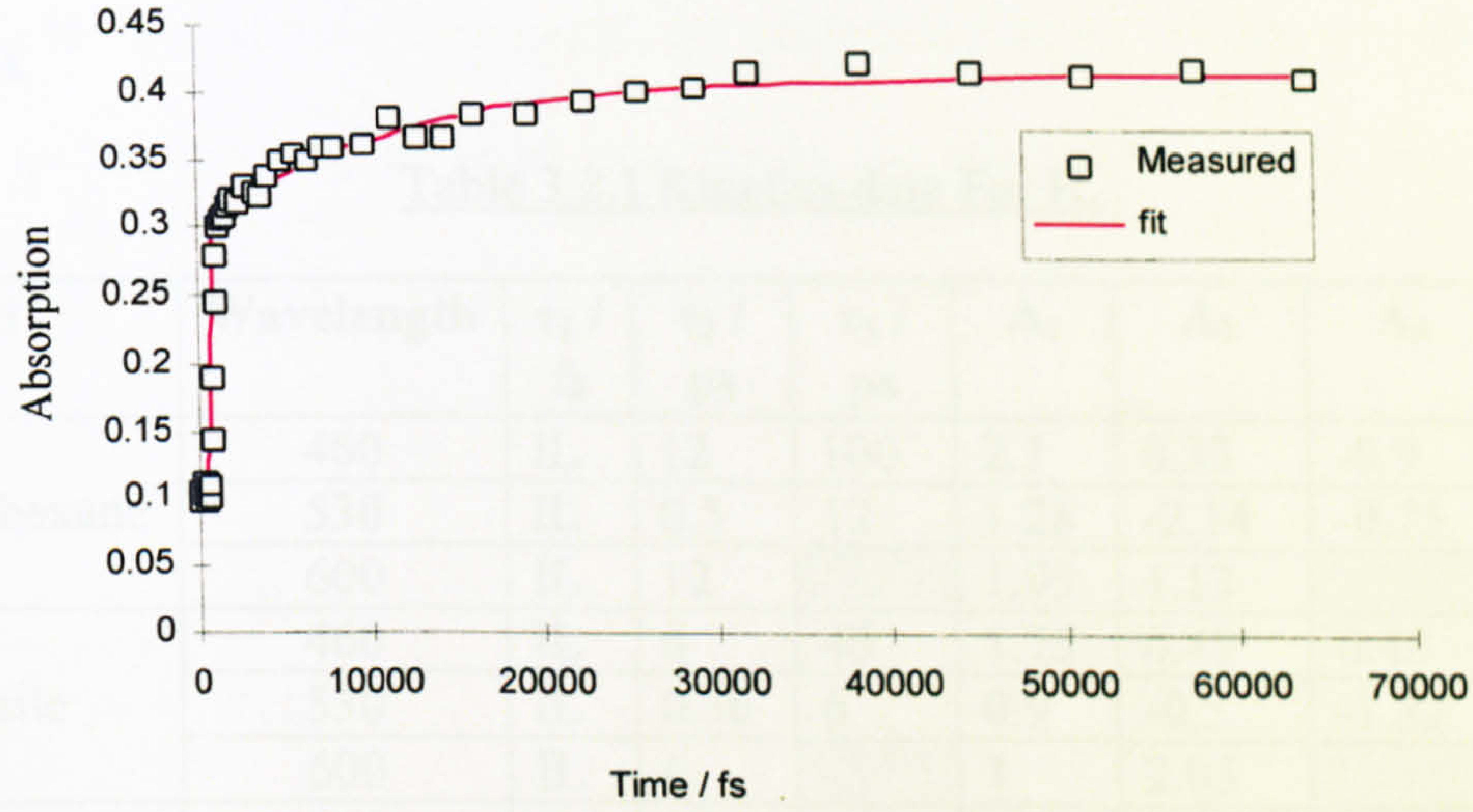

Fig. 3.2.7 Wavelength integrated kinetics for **II** in methylcyclohexane for a 10 nm bandwidth centred on 600 nm. Fit to a 2 component exponential model with an instrument limited rise and τ_2~12 ps.

The kinetics clearly indicate that the 460 nm and 600 nm absorption bands are due to the same state in all solvents even though the relative weight of the fast to slow transient response is dependent on spectral position and solvent environment. At 530 nm, we observe an instrument limited rise in absorption followed by fast decay into spontaneous emission in all environments investigated, however the time constants involved vary dramatically with solvent. For methylcyclohexane we observe a ~ 500 fs time constant for the rise in population to the emissive potential surface, indicating the presence of a secondary process which hinders the fluorescence on this timescale. A similar such component is present for the acetonitrile solution with a time constant of the order of 360 fs. Such a fast component is completely absent from the ethanol kinetics indicating once again the importance of intermolecular hydrogen bonds. The increase in the rate constant for acetonitrile may indicate some dependence on the polarity of the solvent, however it is clear that further work is required to confirm this hypothesis.

Table 3.2.1 Kinetics data For **II.**

Solvent	**Wavelength**	τ_1 / fs	τ_2 / ps	τ_3 / ps	A_1	A_2	A_3	χ^2	A_1/ A_2
Methylcyclohexane	460	IL	12	100	2.1	0.33	-0.9	0.02	6.36
	530	IL	0.5	12	1.28	-2.14	-0.75	0.15	
	600	IL	12		1.95	1.13		0.06	1.73
Acetonitrile	460	IL	6	40	1.75	0.49	0.48	0.08	3.57
	530	IL	0.36	6	0.9	-0.3	-1.32	0.08	
	600	IL	6		1	2.05		0.04	0.49
Ethanol	460	IL	12	ns	1	0.13		0.2	7.69
	530	IL	11		1	-1.6		0.07	
	600	IL	12		0.85	1.75		0.13	0.49

The picosecond time constants, observed for all spectral regions and solvents are comparable with those observed at RAL for I and are certainly within experimental error. We observe identical time constants for ethanol and methylcyclohexane indicating the possibility of protic impurities in the non-interacting solvent. The longer time constants observed in some spectral regions are indicative of the excited state decay, which typically occurs on a nanosecond timescale, too long for us to accurately determine and hence the discrepancy in the long time component.

3.3 4'-Methyl-3-hydroxyflavone

Transient spectra for 4'-methyl-3-hydroxyflavone (**III**) in methylcyclohexane solution are given in Fig. 3.3.1 and 3.3.2 (for 0 to 1 ps and 1-16 ps). Similar behaviour is observed to that of the 4'-chloro substituent. However, where the chloro species gives a broad absorption peak in the 450 nm region, for the methyl substituent we see a pronounced peak at 450nm with a shoulder at 500 nm with a corresponding emission state profile as in the unsubstituted case. Acetonitrile solutions give a comparable result to that of the unsubstituted compound. For ethanol solutions, we observe an absorption shoulder at 500 nm and for short time scales the population of this state appears to exceed that of the 450 nm band; for longer time-scales this distinction is lost due to the growth and spectral shift of the emission band around 530 nm (Fig. 3.3.3).

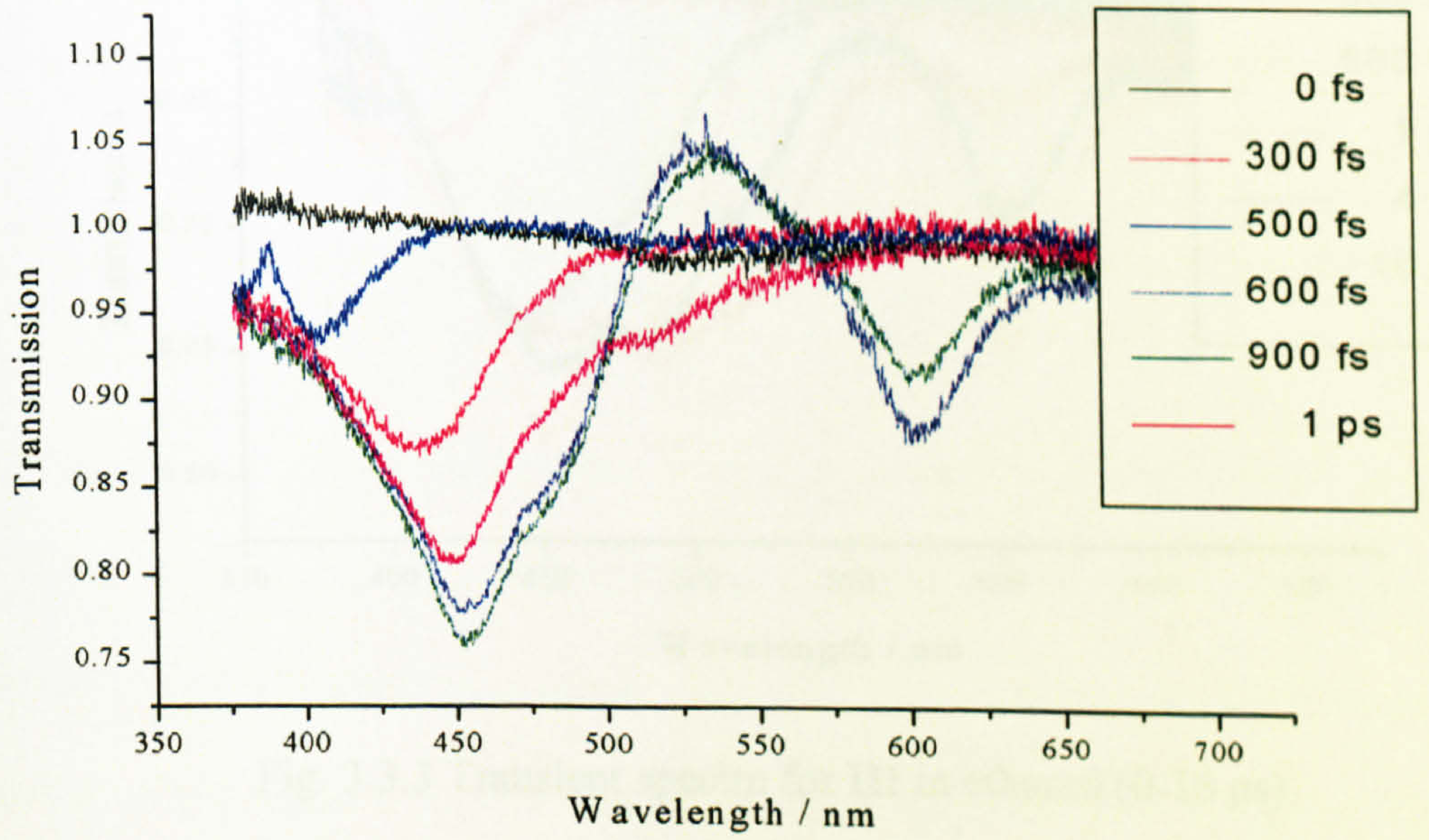

Fig. 3.3.1 Transient spectra for **III** in methylcyclohexane (0-1 ps).

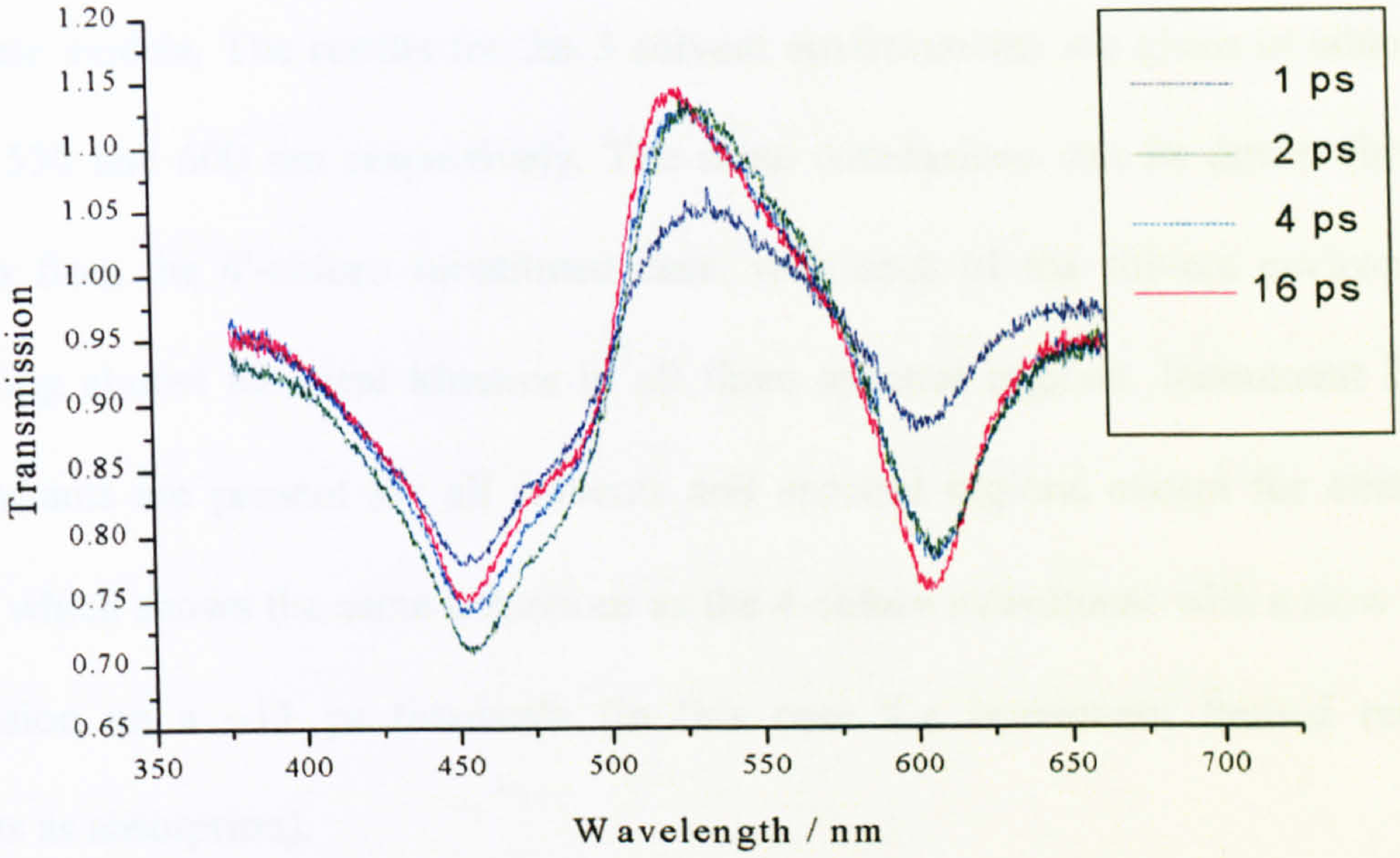

Fig. 3.3.2 Transient spectra for **III** in methylcyclohexane (1-16 ps).

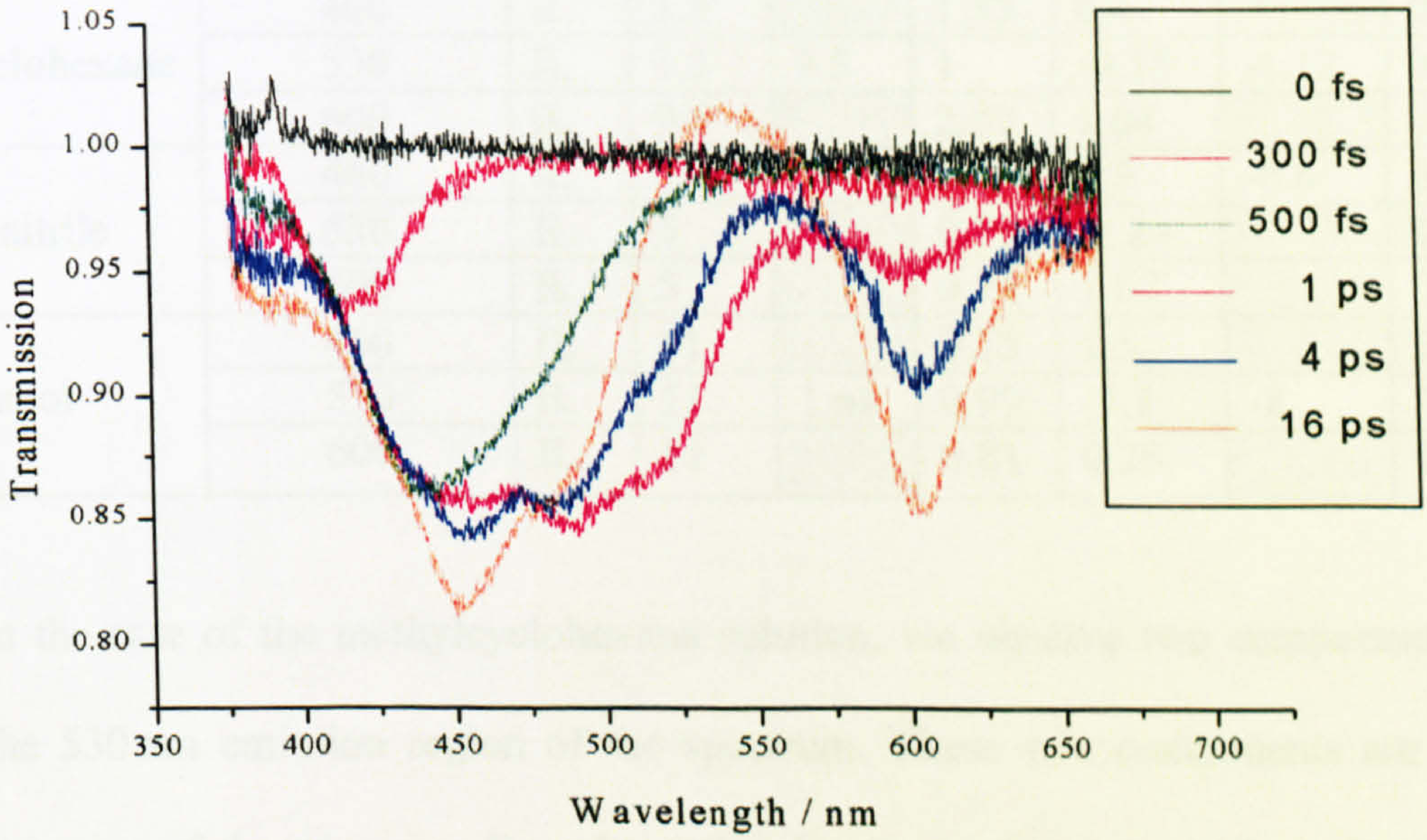

Fig. 3.3.3 Transient spectra for **III** in ethanol (0-16 ps).

Kinetics data for each of the relevant spectral regions was extracted by averaging a 10 nm bandwidth around the wavelength of interest and plotting this as a function of time delay. The data was analysed in the manner described in Section 2.2.4 by fitting to appropriate models. The results for the 3 solvent environments are given in table 3.3.1 for 460, 530 and 600 nm respectively. The same conclusions can be drawn for these results as from the 4'-chloro substituted case, with each of the solvent environments reproducing almost identical kinetics in all three spectral regions. Instrument limited time constants are present for all solvents and spectral regions except for ethanol at 530 nm, which shows the same behaviour as the 4-chloro substituent with a slow rise in transmission on a ~11 ps timescale (in this case the instrument limited response manifests as absorption).

Table 3.3.1 Kinetics data for **III**.

Solvent	**Wavelength**	τ_1 / **fs**	τ_2 / **ps**	τ_3 / **ps**	**A_1**	**A_2**	**A_3**	χ^2
Methylcyclohexane	460	IL	1.5		1.55	0.4		0.35
	530	IL	1.5	9.5	1	-0.15	-1.12	0.16
	600	IL	9.5		2.07	1.04		0.08
Acetonitrile	460	IL	5	50	0.84	0.7	-0.6	0.05
	530	IL	4		0.72	-1.84		0.21
	600	IL	5		0.74	1.67		0.12
Ethanol	460	IL	11		0.75	1.5		0.13
	530	IL	11	1 ns	0.99	-1.3	-8	0.05
	600	IL	11		0.81	0.26		0.06

In the case of the methylcyclohexane solution, we observe two components of rise in the 530 nm emission region of the spectrum. These two components are also observed in one of the corresponding absorption bands. In the acetonitrile and ethanol solutions only a single decay component is observed (notwithstanding the long decays which correspond to the lifetime of the tautomer).

3. 4 4'-Methoxy-3-hydroxyflavone

Transient spectra for 4'-methoxy-3-hydroxyflavone (**IV**) are given in Fig. 3.4.1 for methylcyclohexane from 0-8 ps. In this case we observe very noisy spectra possibly due to the poor solubility of this compound in cyclohexane. The spectra reproduce the features observed for other substituents although we observe a strong emission spike in the kinetics around time zero, which masks any short time dynamics of the 450 nm band. The behaviour of **IV** in acetonitrile and ethanol essentially mimics that of other derivatives (Fig. 3.4.2 and 3 respectively).

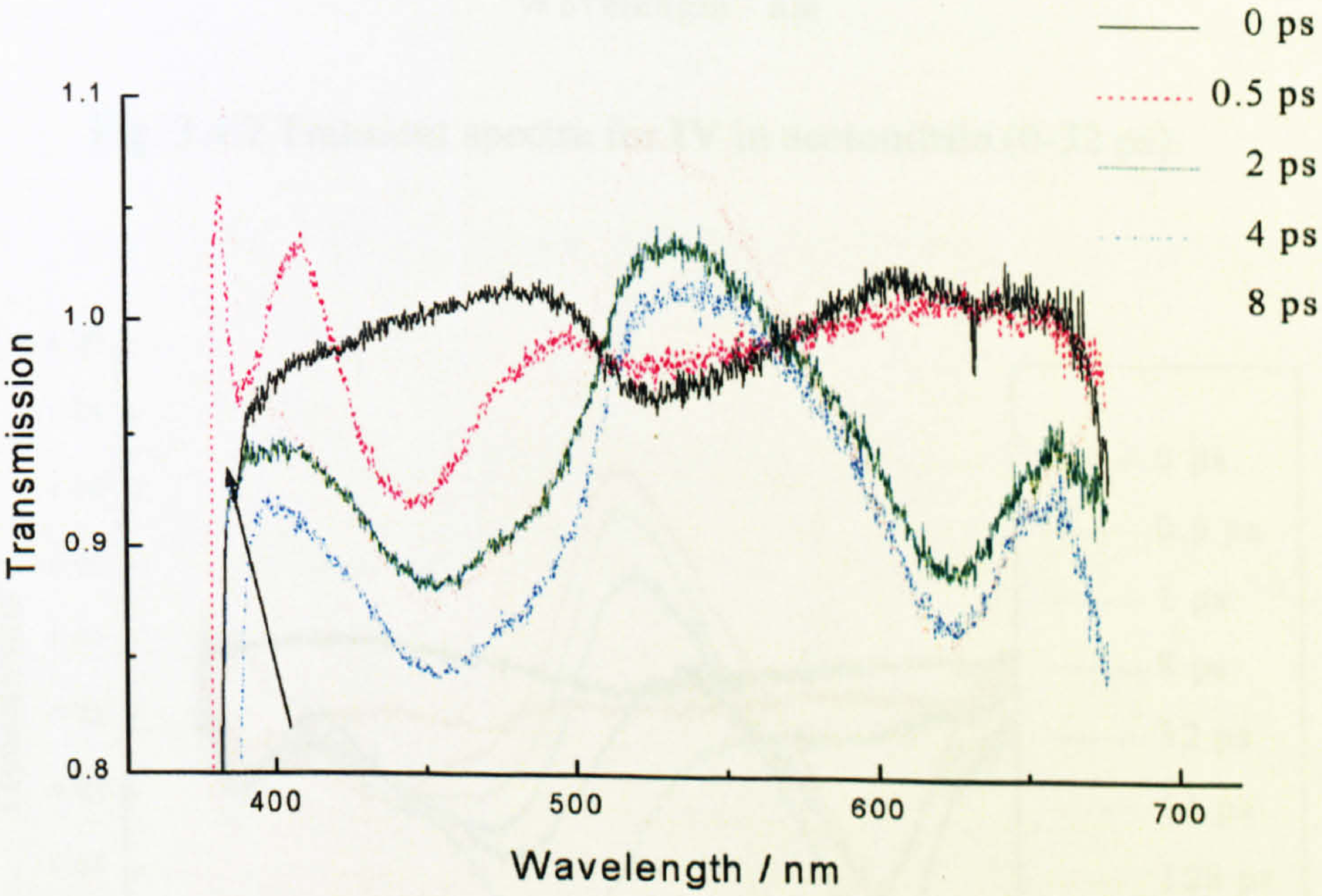

Fig. 3.4.1 Transient spectra for **IV** in methylcyclohexane (0-8ps).

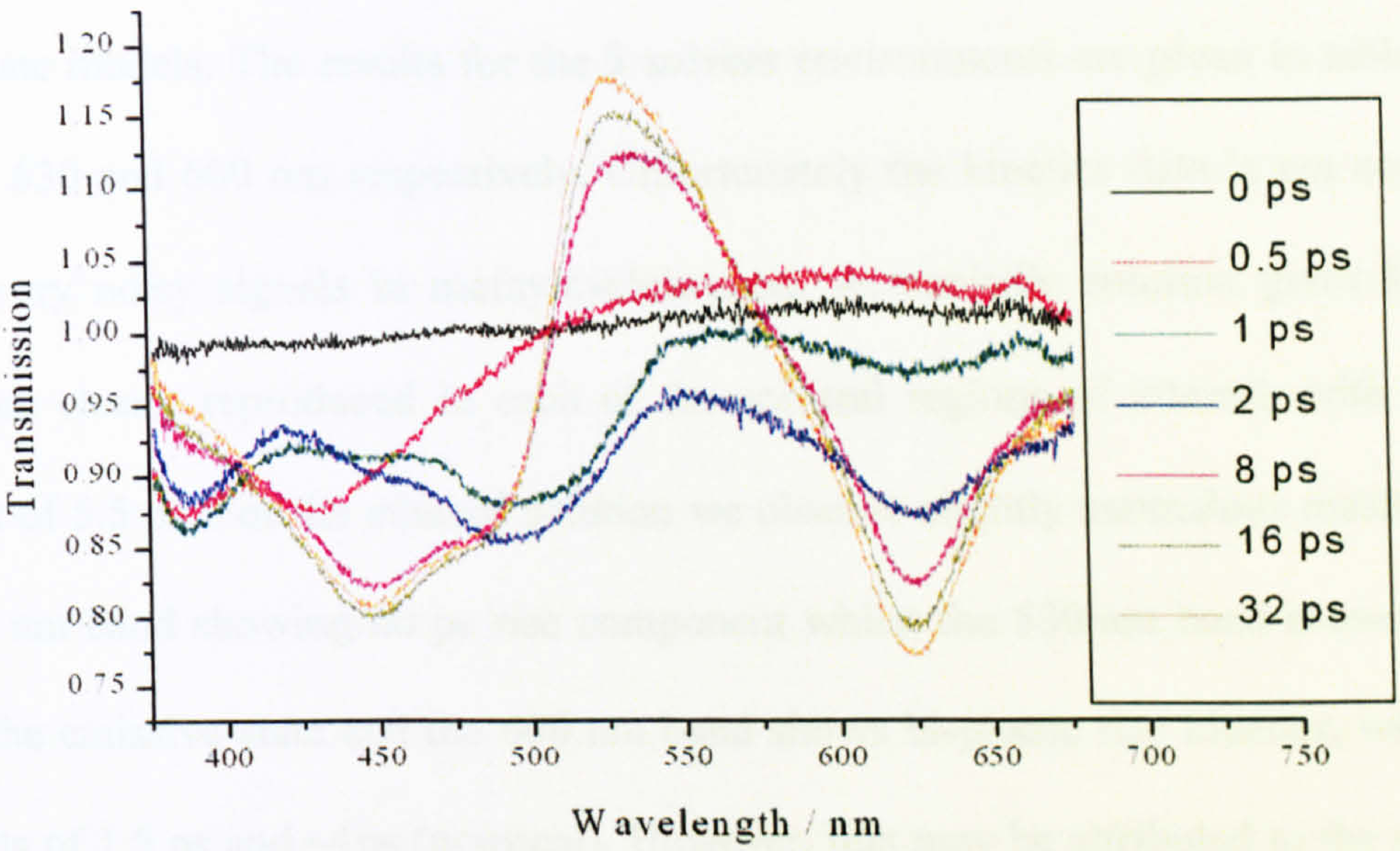

Fig. 3.4.2 Transient spectra for **IV** in acetonitrile (0-32 ps).

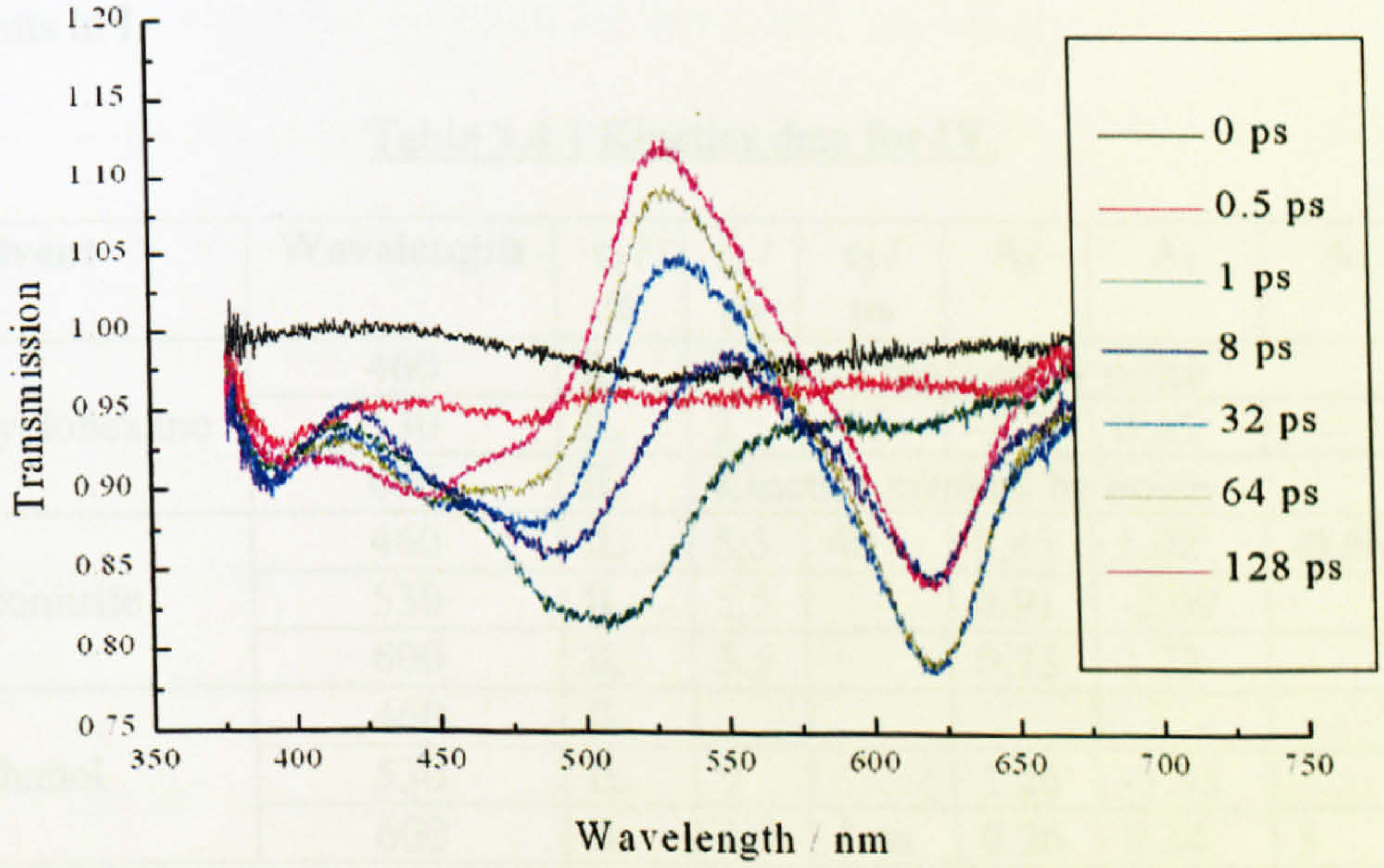

Fig. 3.4.3 Transient spectra for **IV** in ethanol (0-32 ps).

Kinetics data for each of the relevant spectral regions was extracted by averaging a 10 nm bandwidth around the region of interest and plotting this as a function of time delay. The data was analysed in the manner described in Section 2.2.4 by fitting to appropriate models. The results for the 3 solvent environments are given in table 3.4.1 for 460, 530 and 600 nm respectively. Unfortunately the kinetics data is not complete due to very noisy signals in methylcyclohexane. Acetonitrile solution gives kinetics which are clearly reproduced in each of the spectral regions of interest, with a time constant of 5.5 ps. For the ethanol solution we observe slightly anomalous results, with the 460 nm band showing no ps rise component whilst the 530 nm band shows a 9 ps rise to the emissive state and the 600 nm band shows bi-phasic rise kinetics, with time constants of 1.5 ps and ~1ns (nominal). However, this may be attributed to the noise as illustrated by the χ^2 value of ~ 2. Certainly, the kinetics are ambiguous and there are no significant indications that **IV** shows any different behaviour to that observed for other substituents in **I**.

Table 3.4.1 Kinetics data for **IV**.

Solvent	**Wavelength**	τ_1 / fs	τ_2 / ps	τ_3 / ps	A_1	A_2	A_3	χ^2
Methylcyclohexane	460	IL	Kinetics masked by noise					
	530	IL	3		-1.2	0.35		0.27
	600	IL	Kinetics masked by noise					
Acetonitrile	460	IL	5.5	40	0.45	1.02	-0.66	0.17
	530	IL	5.5		0.91	-2.09		0.14
	600	IL	5.5		0.75	1.73		0.31
Ethanol	460	IL						0.37
	530	IL	9		1.26	-1.95		0.22
	600	IL	1.5	1 ns	0.26	0.34	5	1.94

3.5 4'-Cyano-hydroxyflavone

Transient spectra for 4'-cyano-hydroxyflavone (V) show significant differences to those for other substituted **I** in ethanol and acetonitrile solutions. Unfortunately the compound proved relatively insoluble in methylcyclohexane and no transient could be resolved with a lower concentration. For **V** in acetonitrile solution (Fig. 3.5.1 for 0-128 ps) we observe the presence of a weak stimulated emission band at 400 nm at short timescales which is masked by absorption at later times. This is most likely associated with the normal Franck-Condon excited state of the molecule. As for the other substituted molecules we observe short time evolution of an absorption band in the region from 420 - 550 nm and indeed for the 4'-cyano compound tails of the absorption are observed throughout the measured wavelength region. Within 1 ps we observe a peak-shift to approximately 490 nm. Growth of a second absorption band centred around 600 nm occurs after 1 ps and we see a corresponding decay from the 500 nm band. Interestingly the growth of an emissive state around 550 nm does not occur on the timescale of the observations suggesting a significant reduction in the quantum efficiency of the fluorescent state. A red shift is evident in the spectral peaks, however this is most probably due to the decreased influence of the emissive state, which masks the absorption for compounds **II-IV**.

Transient spectra for ethanol solutions show no apparent difference to those for acetonitrile and are given in Fig.3.4.2. In contrast to the other substituents, we observe decay of the 450 nm band which at first glance appears to correspond to the rise in absorption in the 600 nm region (illustrated by arrows on the figure).

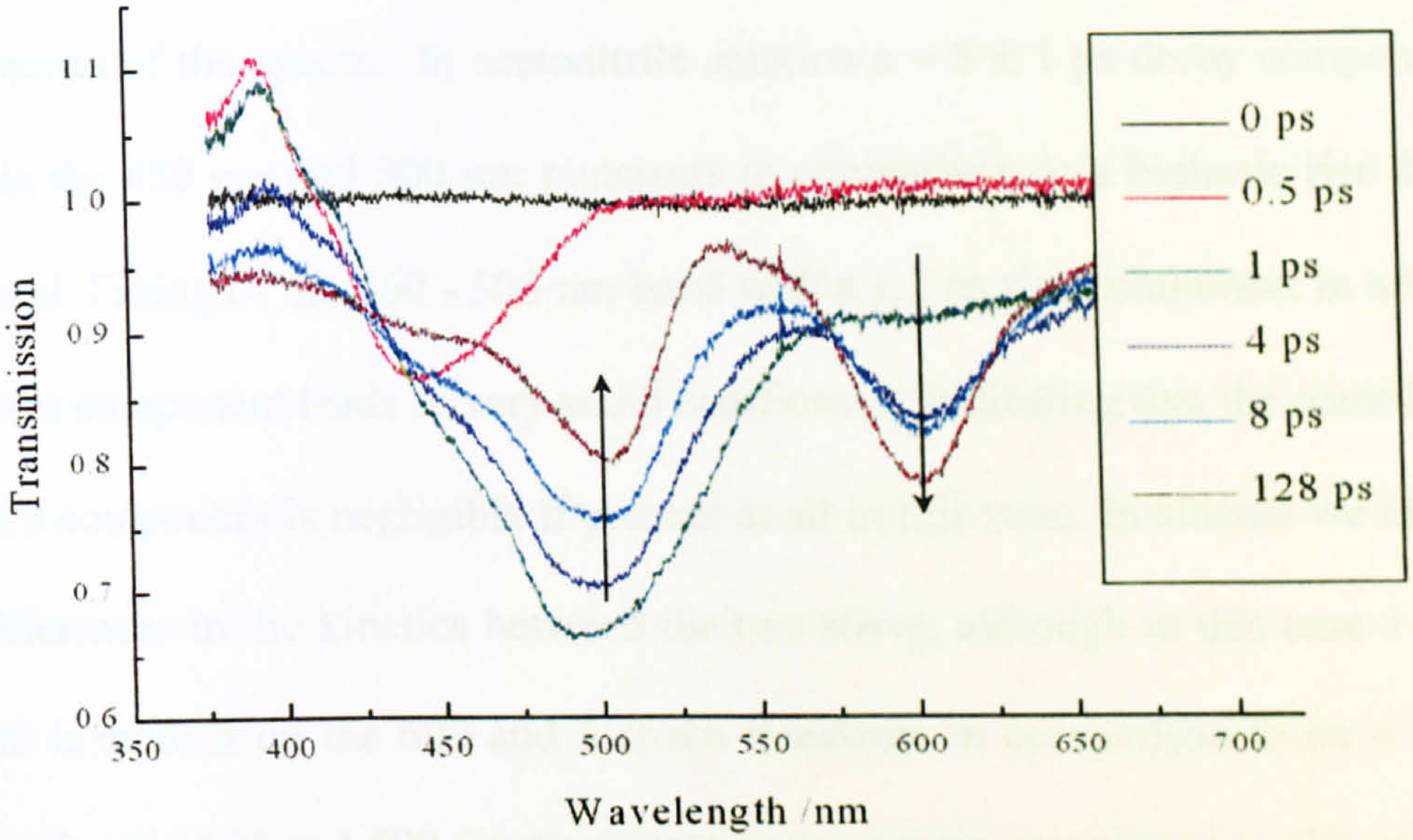

Fig. 3.5.1 Transient spectra for **V** in acetonitrile (0-128 ps).

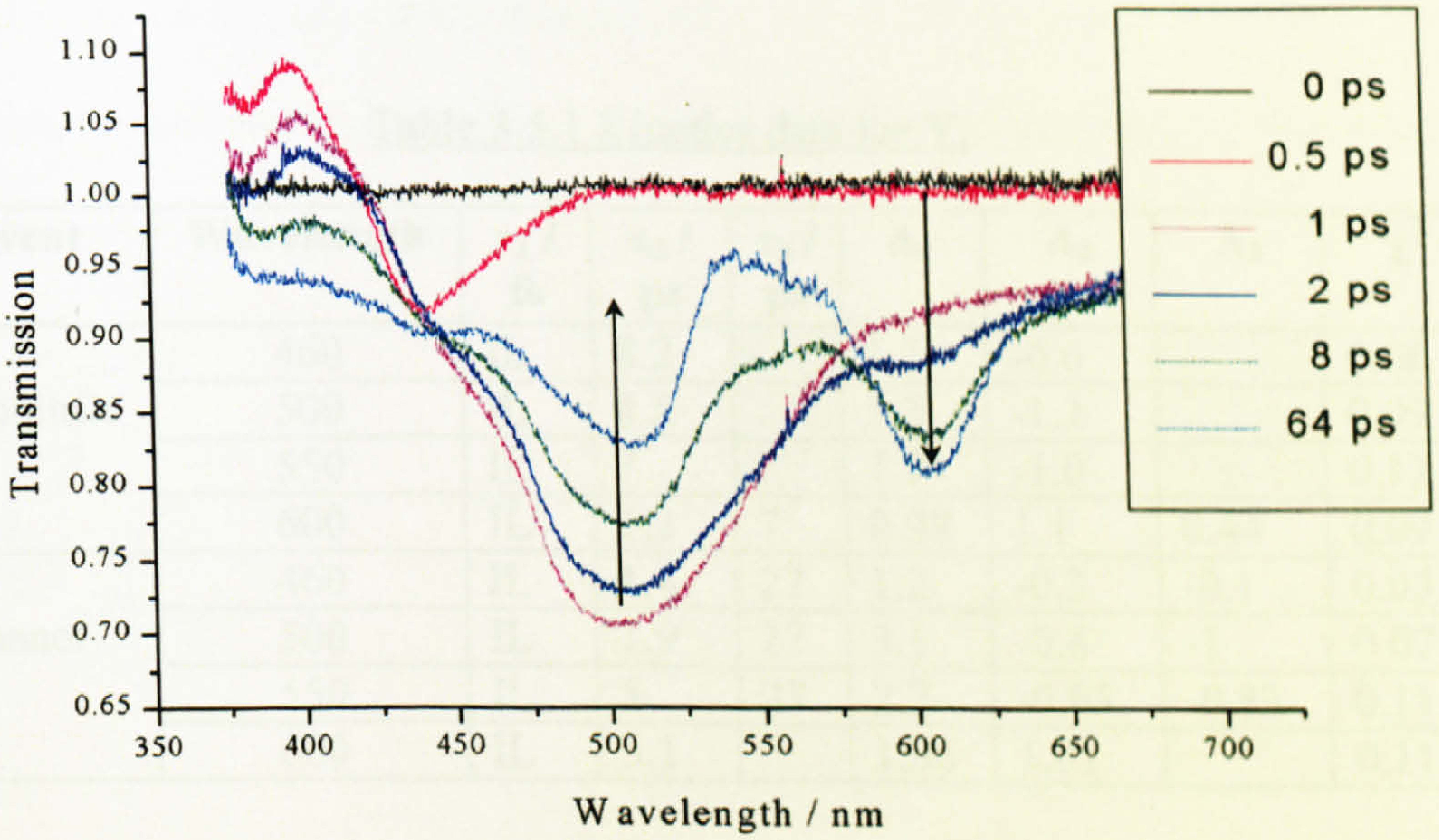

Fig. 3.5.2 Transient spectra for **V** in ethanol (0-64 ps).

Kinetic re-constructions from the spectra (as described previously) are given in Table 3.5.1 for ethanol and acetonitrile solutions at 460, 500, 550 and 600 nm. In both solvents we observe slight differences in the behaviour between the 450-500 nm and 600 nm regions of the spectra. In acetonitrile solution a ~ 8 ± 1 ps decay component is observed in the 450 nm and 500 nm transients in comparison to a biphasic rise for the 600 nm band. Fitting of the 460 - 500 nm band with a 1.2 ps rise component in addition to the slower component leads to very small coefficients, indicating that the contribution from such a component is negligible if present at all in this state. In ethanol we observe similar differences in the kinetics between the two states, although in this case a ~ 5 ps component is evident on the 600 and 550 nm transients in comparison to an ~ 1-2 ps component for the 450 and 500 nm transients. A long time component is also required to fit the data adequately, although the lifetime of this component is too long to be accurately determined (and is taken here to be 27 ps for best fit) given the timescale of our data.

Table 3.5.1 Kinetics data for **V**.

Solvent	**Wavelength**	τ_1 / **fs**	τ_2 / **ps**	τ_3 / **ps**	A_1	A_2	A_3	χ^2
Acetonitrile	460	IL	8.2		1.5	-0.6		0.06
	500	IL	8.5		3.3	-1.2		0.09
	550	IL	7		1.7	-1.0		0.12
	600	IL	1.2	7	0.98	1.1	0.44	0.09
Ethanol	460	IL	1.4	27	1.2	-0.3	-0.1	0.03
	500	IL	1.9	27	3.1	-0.6	-1	0.07
	550	IL	5	27	2.2	-0.95	-0.83	0.11
	600	IL	5.1		1.06	1.01		0.11

The results for the kinetics indicate that the cyano substituent has a significant impact on the transient dynamics in comparison with other **I** derivatives, which appear to mimic that of the parent system.

In compounds **I-IV**, the rise of the stimulated emission indicative of the formation of the excited tautomer is biphasic. The fast component is usually also present in the rise of the transient absorption in both the blue and red spectral regions, but the slower component is usually only associated with increased transient absorption in the red. These two components appear to be due to ESIPT in "bare" and solvated molecules respectively. In **V**, alone of all the 3-hydroxyflavones, we observe a redistribution of intensity between the two transient absorption bands, with increased absorption in the red at longer delay times at the expense of the blue band. On the basis of the assignment of the transient absorption bands, this might suggest that "bare" **V** molecules are being dynamically solvated and that this is the cause of the absorption changes. However, this process is not observed for any of the compounds **I-IV** and it is perhaps more appropriate to assign the unique behaviour of **V** to its cyano substituent.

Alone of the various substituents used in this work, the cyano group is electron withdrawing in nature and could interact with the negative charge developed by the proton transfer process as shown in Fig. 3.5.3. This could account for the observed transient absorption changes.

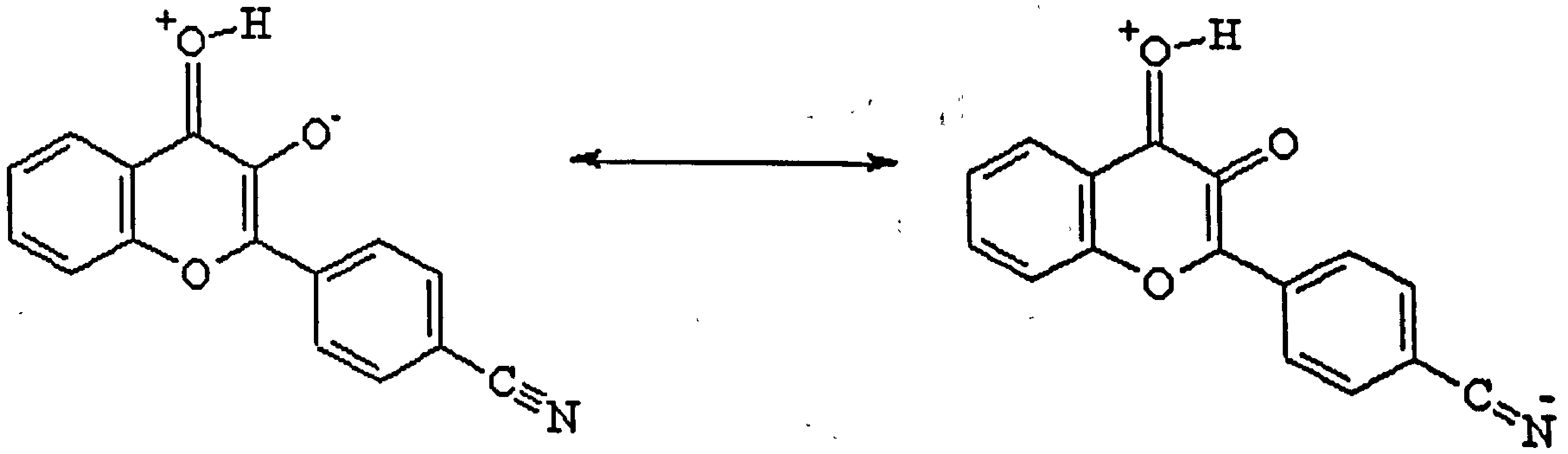

Fig. 3.5.3 Interaction of cyano substituent with the charged tautomeric state created after ESIPT.

3.6 4'-*N*, *N*-Dimethylamino-3-methoxyflavone

It has been shown in the literature that substitution of a dimethylamino group in a fluorescent molecule can lead to the presence of a second fluorescence state which has been attributed to a, so called, twisted intramolecular charge transfer (TICT) state[7]. Such fluorescent states of a molecule have been observed to be strongly dependent on solvent environment, in particular on viscosity. The influence of solvent friction on the relative orientations of the donor and acceptor parts of the molecule leading to the formation of the emitting state is crucial: the twisting motion of the TICT mechanism is a large amplitude motion which can be stopped by very high viscosity conditions obtained with temperature or solvent polarity changes. Polarity plays an important role due to the charge separation of the TICT state (highly dipolar) which leads to solvent dependent peak intensity and mean frequency of the Stokes shifted TICT emission.

In order to see how such a substituent would affect the proton transfer dynamics of the 3-hydroxyflavone molecule, we have undertaken transient spectral measurements on the three compounds shown in Fig.3.0.1 4'-*N*,*N*-dimethylamino-3-hydroxyflavone (VI), 4'-*N*,*N*-dimethylamino-3-methoxyflavone (VII) and 4'-(1"-aza-4",7",10",13"-tetraoxacyclopentadecyl)-3-hydroxyflavone (VIII). The results for **VII** are presented first since the behaviour for this system is less complex due to the absence of ESIPT and the results improve our understanding of the other two systems.

In order to try to separate the two excited state mechanisms observed for **VI** we investigated the spectral properties of 4'-*N*,*N*-dimethylamino-3-methoxyflavone (**VII**) which cannot undergo proton transfer, but may form a TICT state. Transient spectra for **VII** in methylcyclohexane (Fig. 3.6.1) show initial weak absorption with two peaks at

~ 410 and 460 nm and a long tail to the red. For longer time-scales we see the formation of a broad emission centred at 430 nm with a bandwidth of ~ 30 nm. Within 1 ps we see the formation of a further broad (100 nm) absorption band with a peak around 550 nm. The observed spectra are not well resolved in terms of the signal amplitude in this solvent and restrict us to qualitative analysis as extraction of kinetics data is impractical. The formation of a TICT state will be less favouable in a non-polar solvent such as methylcyclohexane, but the evolution of the spectra on a timescale of tens of picoseconds is probably indicative of a process such as this.

For **VII** in acetonitrile (fig. 3.6.2) we observe absorption in a broad band at 400 nm to approximately 430 nm at short timescales, corresponding to excited state absorption of the local excited state. An emissive state with a peak at 460 nm is present within 500 fs and we observe this to red shift to 490 nm and increase in intensity within 2 ps. The shifting of the emission peak causes a corresponding movement of the edge of the 420 nm absorption band. Such a slow Stokes shift of the emission cannot be attributed to the continuum dispersion, which is of the order of 200 fs across the observed spectral region (450-500 nm).

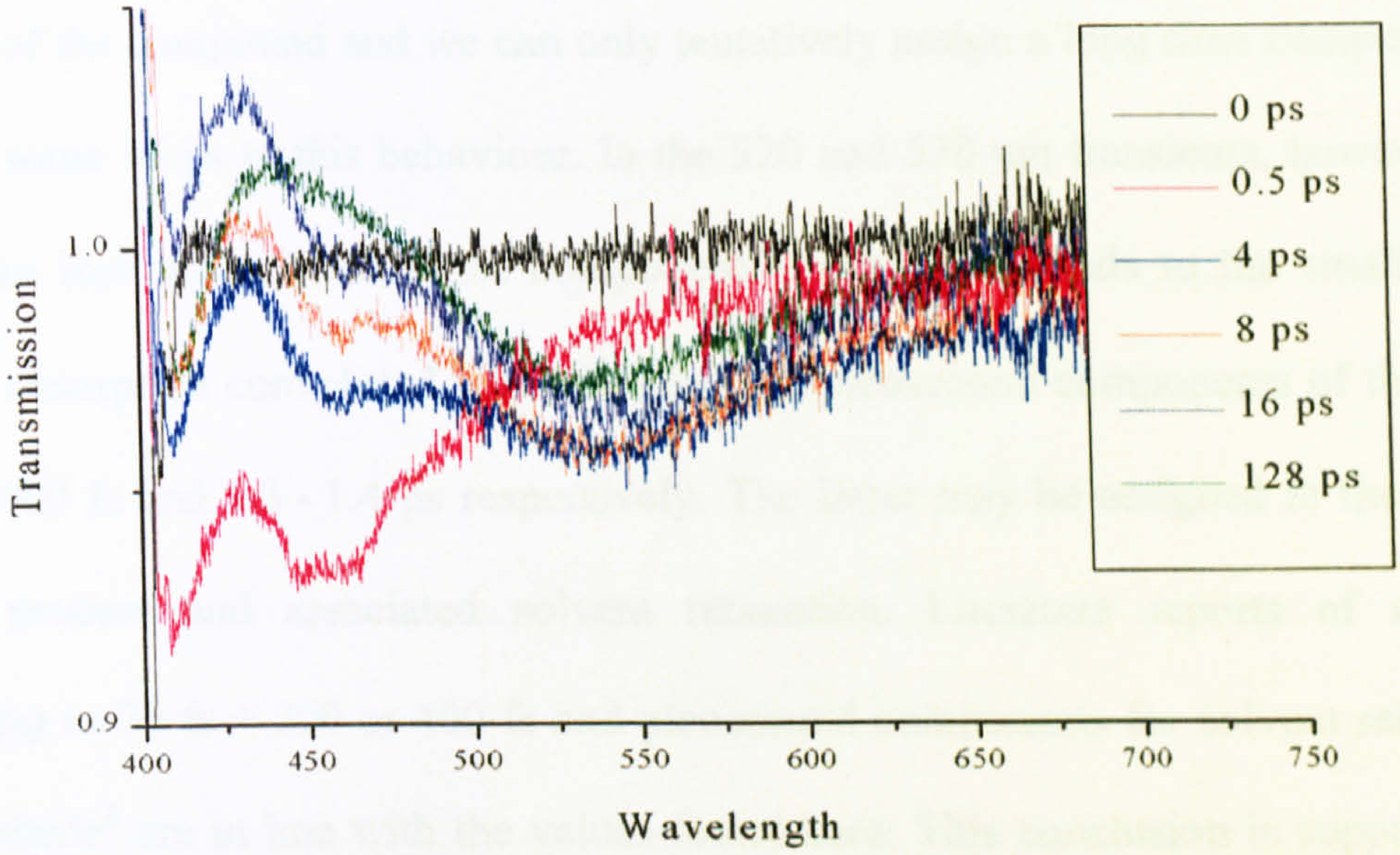

Fig. 3.6.1 Transient spectra of **VII** in methylcyclohexane (0-128 ps)

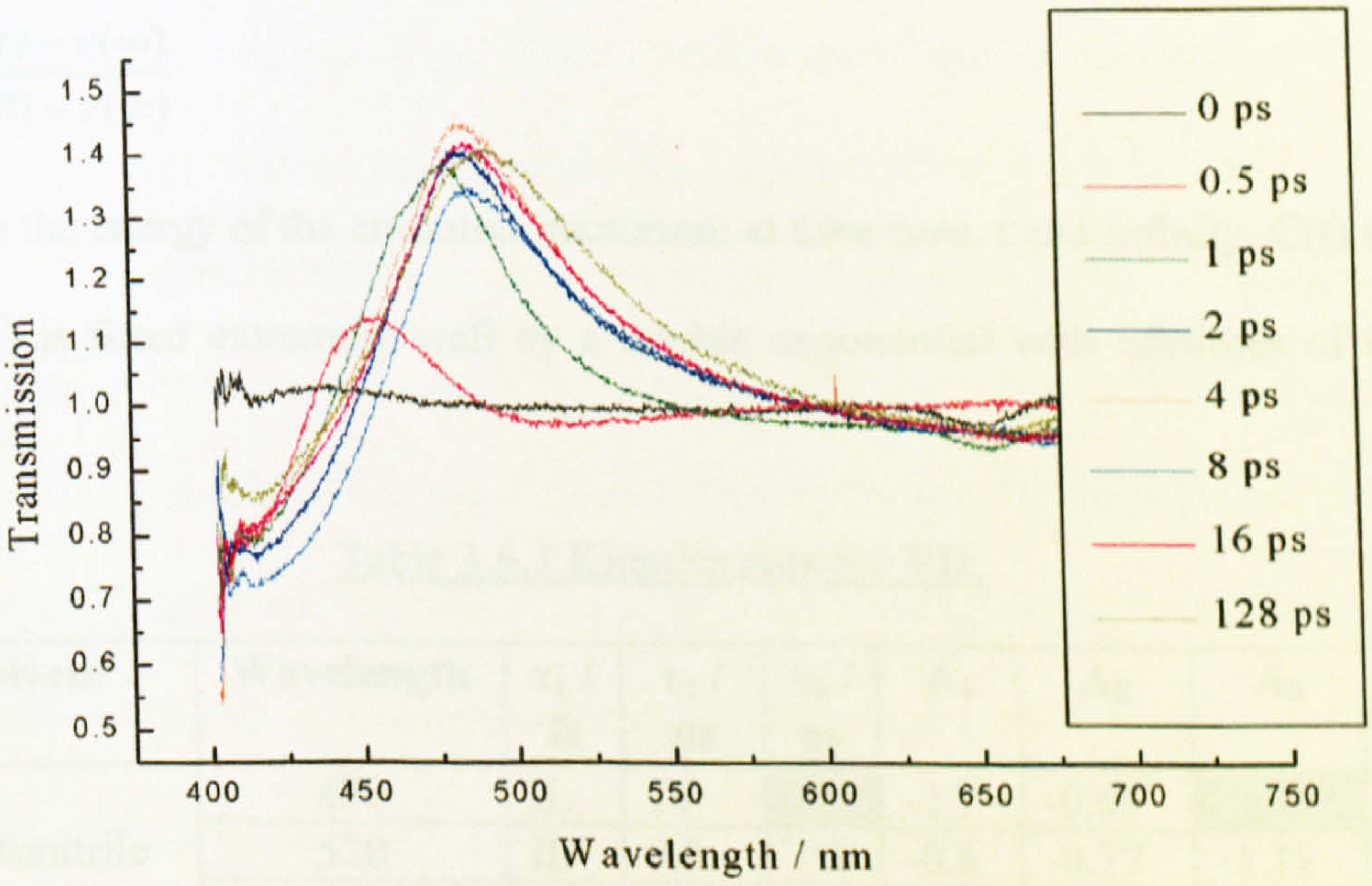

Fig. 3.6.2 Transient spectra of **VII** in acetonitrile (0-128 ps).

The wavelength integrated kinetics for **VII** are given in table 3.6.1. In the case of **VII** in acetonitrile solution at 470 nm, we see an instrument limited rise component which is contaminated by large amplitude noise over the peak. This masks the fast response of the compound and we can only tentatively assign a long time component of decay of some 16 ps to this behaviour. In the 520 and 570 nm transients, however, we observe an instrument limited rise component which corresponds to the small initial transient absorption convoluted with ultrafast and picosecond components of the order of 300 - 400 fs and 1.3 - 1.4 ps respectively. The latter may be assigned to the charge transfer process and associated solvent relaxation. Literature reports of ultrafast (50-100 fs) or 70 fs + 200 or 400 fs and picosecond components for solvent relaxation in acetonitrile[8] are in line with the values found here. This conclusion is supported by the time dependent Stokes shift (TDSS) shown in Fig. 3.6.3. The TDSS, C(t), has been calculated from[12]

$$C(t) = \frac{\nu(t) - \nu(\infty)}{\nu(0) - \nu(\infty)} \tag{3.1.1}$$

where ν is the energy of the emission maximum at time zero, t and infinity. C(t) versus t (fig. 3.6.3) is fitted extremely well by a double exponential with lifetimes of 0.4 and 1.3 ps.

Table 3.6.1 Kinetics data for **VII**.

Solvent	**Wavelength**	τ_1 / **fs**	τ_2 / **ps**	τ_3 / **ps**	A_1	A_2	A_3	χ^2
Acetonitrile	470	IL	16	▨	-2.7	-0.61	▨	1.7
	520	IL	0.3	1.3	-0.6	-0.77	-1.18	0.6
	570	IL	0.4	1.4	0.67	-0.75	-0.31	0.1
Ethanol	470	IL	2.6	18	-4.4	-3.6	6.51	0.5
	520	IL	0.3	15	1.4	-1.7	-3.2	0.4
	550	IL	0.3	18	0.7	-0.64	-1.9	0.1

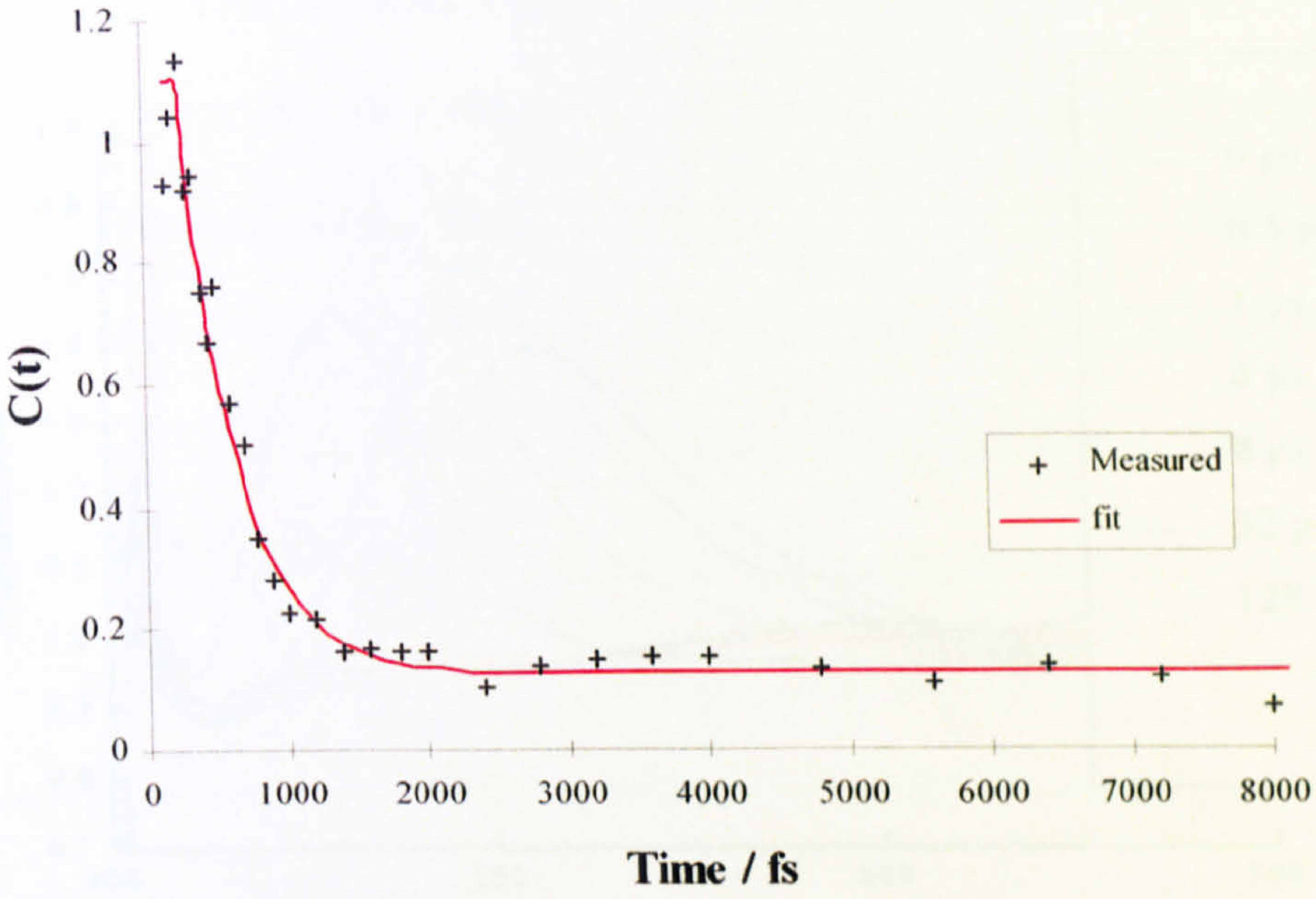

Fig.3.6.3 Time-dependent Stokes shift (C(t)) for **VII** in acetonitrile. Fit to 2nd order exponential decay ($\tau_1 = 0.4$ ps, $\tau_2 = 1.3$ ps to give $\chi^2 \sim 0.6$).

For **VII** in ethanol (Fig. 3.6.4) we observe similar spectra to those for acetonitrile solution, with an emissive species formed within 500 fs at ~ 450 nm, which then undergoes a spectral shift to ~ 520 nm. However, in this case we see a significantly slower response of the system with the motion of the band occurring throughout the period of the observations (128 ps). This is further evidenced by the extracted kinetics of the 520 and 570 nm transients which show both an ultrafast component of the order of 400 fs and a 15 - 18 ps component, significantly slower than observed for the acetonitrile case. The 470 nm band shows a decay of the order of 18 ps which corresponds to the long time rise observed in the 520 and 570 nm transients which is not surprising given the spectral shift of the band. This assignment is further supported by the TDSS data in figure 3.6.5.

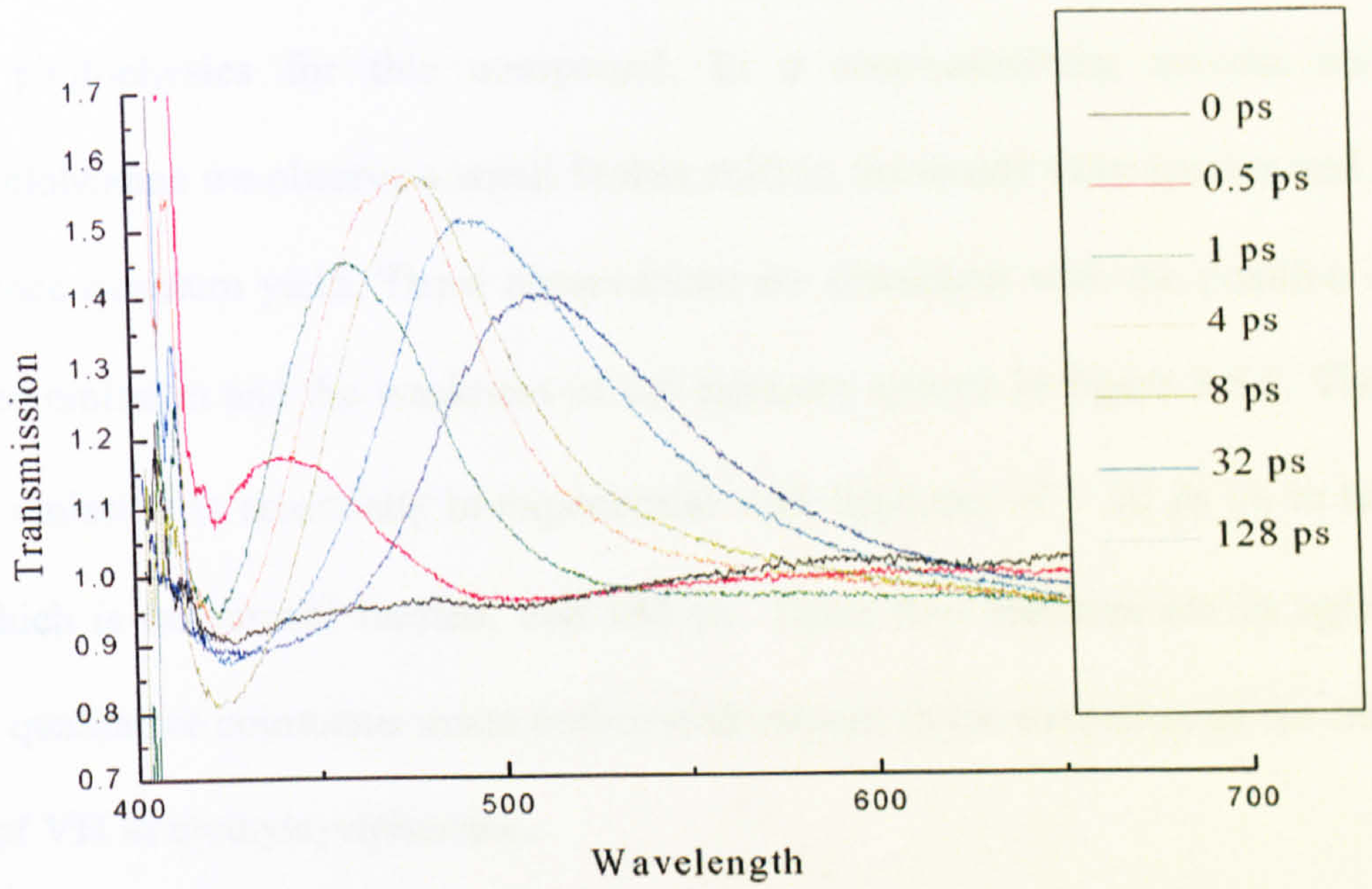

Fig. 3.6.4 Transient spectra of **VII** in ethanol (0-128 ps)

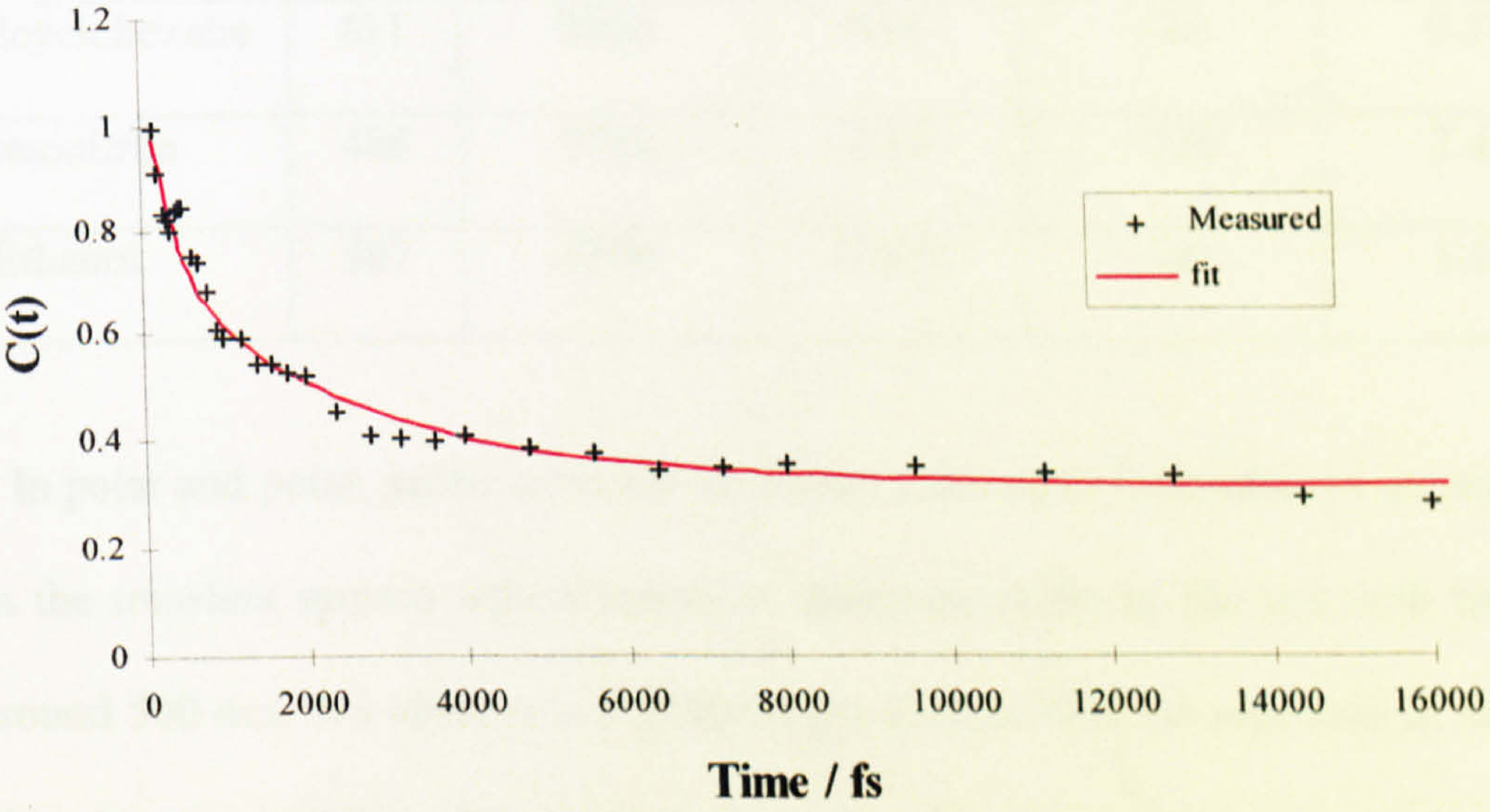

Fig. 3.6.5 Time-dependent Stokes shift (C(t)) for **VII** in ethanol. Fit to 3rd order exponential decay ($\tau_1 = 0.3$ ps, $\tau_2 = 2.6$ ps and $\tau_2 = 18$ ps to give $\chi^2 \sim 0.11$).

The spectra and extracted kinetics data for **VII** together with its steady state and time resolved emission properties Table 3.6.2, give us a fairly consistent view of the solution photophysics for this compound. In a non-interacting solvent such as methylcyclohexane we observe a small Stokes shift in the steady state spectra and a low fluorescence quantum yield. These observations are consistent with the position of the stimulated emission and the weakness of the transient spectra in figure 3.6.1. The time resolved emission is essentially bi-exponential with lifetimes of ~ 20 ps (τ_f in table) a value which is instrument limited, and 180 ps. These two lifetimes are in agreement with the qualitative comments made earlier with respect to the evolution of the transient spectra of **VII** in methylcyclohexane.

Table 3.6.2 Steady state and time resolved emission properties of **VII** in solution[9].

Solvent	λ_{max} nm	Stokes Shift (cm^{-1})	ϕ_f	τ_f^1 ps	τ_f^2 ns
Methylcyclohexane	411	2300	0.06	~20	0.18
Acetonitrile	486	5700	0.48	~250	2.43
Ethanol	507	5800	0.403	~40	1.14

In polar and polar, protic solvents we observe the rapid formation of an emissive state in the transient spectra whose emission spectrum shifts to the red with time, to peak around 500 nm. We observe a slightly larger Stokes shift for solutions in ethanol, which is to be expected from the steady state results. We also see a slower component in the Stokes shift for ethanol solutions, and this suggests that the presence of intermolecular hydrogen bonds have a significant effect on the dynamics of the solvation and/ or the charge transfer process. However, whether the latter process involves twisting (as suggested by Ormson et al[1]), or purely charge transfer (as proposed by Chen et al[10]), is unresolved by the transient spectral data presented here. It is clear, however, that the polar solvents favour the formation of a strongly emissive (high ϕ_f and longer $\tau^2{}_f$ values) and heavily Stokes shifted excited state.

3. 7 4'-*N*, *N*-Dimethylamino-3-hydroxyflavone

Transient spectral measurements, were undertaken for **VI** in four solvent environments, in order to elucidate the effect of the TICT mechanism with respect to polarity (to a minor extent) and viscosity on the ultrafast dynamics of the excited state.

The transient spectra for **VI** excited at 400 nm in methylcyclohexane solution are given for delays of 0 - 64ps in fig. 3.7.1. The excited state spectra resemble those of 3-hydroxyflavone albeit slightly red shifted due to the influence of the dimethylamino substituent.

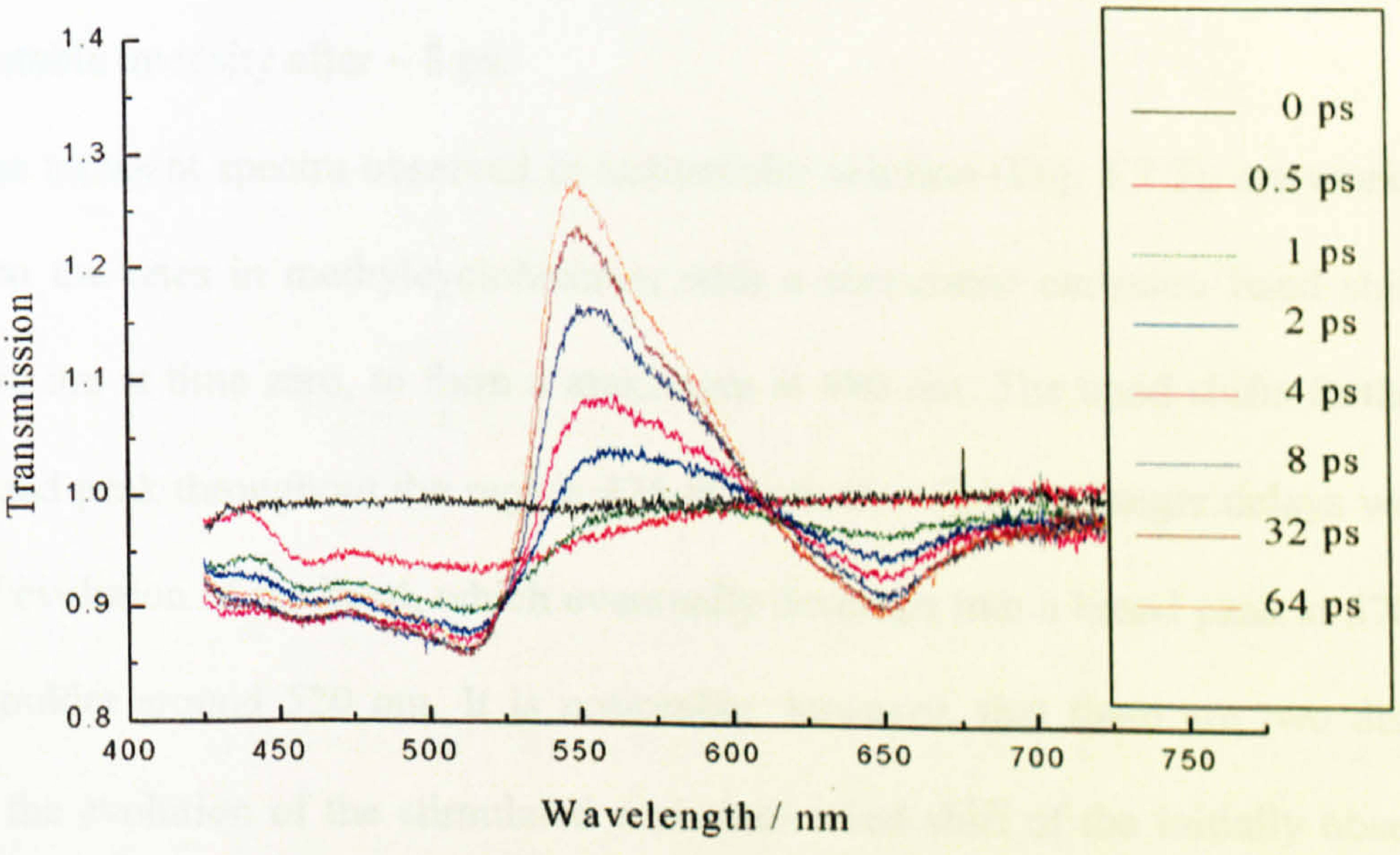

Fig. 3.7.1 Transient spectra for **VI** in methylcyclohexane (0-64 ps).

At a delay of 500 fs, transient absorption occurs across most of the spectral range and there is evidence (in the light of spectra at longer delays) that there is some stimulated emission between 550 and 600 nm. Identical comments may be made about the spectrum at a delay of 1 ps, but here transient absorption is also observed between

600 and 700 nm. At even longer delay times the three spectral regions become more and more distinct:- transient absorption from 425 to approximately 530 nm and from 610 to 750 nm and stimulated emission between.

The shape of the stimulated emission band appears to change with time. The band exhibits a peak at approximately 550 nm and a shoulder around 580 nm. The ratio of intensities at these two wavelengths (550:580) clearly increases with increased delay. However, it is possible that this is simply caused by changes in the transient absorption, which can be reasonably be assumed to be occuring over this wavelength range. It is also noticeable that the intensity of the stimulated emission changes in a similar manner to that of the red transient absorption. However, the blue transient absorption band reaches a stable intensity after ~ 8 ps.

The transient spectra observed in acetonitrile solution (Fig. 3.7.2), are markedly different to the ones in methylcyclohexane, with a stimulated emission band shifting from ~ 450 nm at time zero, to form a maximum at 480 nm. The band shifts further to form a broad peak throughout the region 475-600 nm in ~ 2ps. At longer delays we see continued evolution of the band, which eventually develops into a broad peak at 570 nm with a shoulder around 520 nm. It is noticeable, however, that there are two distinct events in the evolution of the stimulated emission- a red shift of the initially observed emission band and the growth of the emission at 570 nm, whose maximum emission wavelength appears to be invariant with time delay. The small range of the transient absorption at the blue end of the spectrum may be the result of competition with the stimulated emission which occupies a greater wavelength range in acetonitrile compared to methylcyclohexane. However, the absence of transient absorption in the red is in marked contrast to the situation in methylcyclohexane.

Similar results are observed for **VI** in ethanol solution (Fig. 3.7.3). Although in this solvent we see more distinction between the two emission bands, the kinetics of the spectral evolution appears comparable. We also observe more transient absorption (albeit weak at delays >500 fs) at longer wavelengths than in acetonitrile.

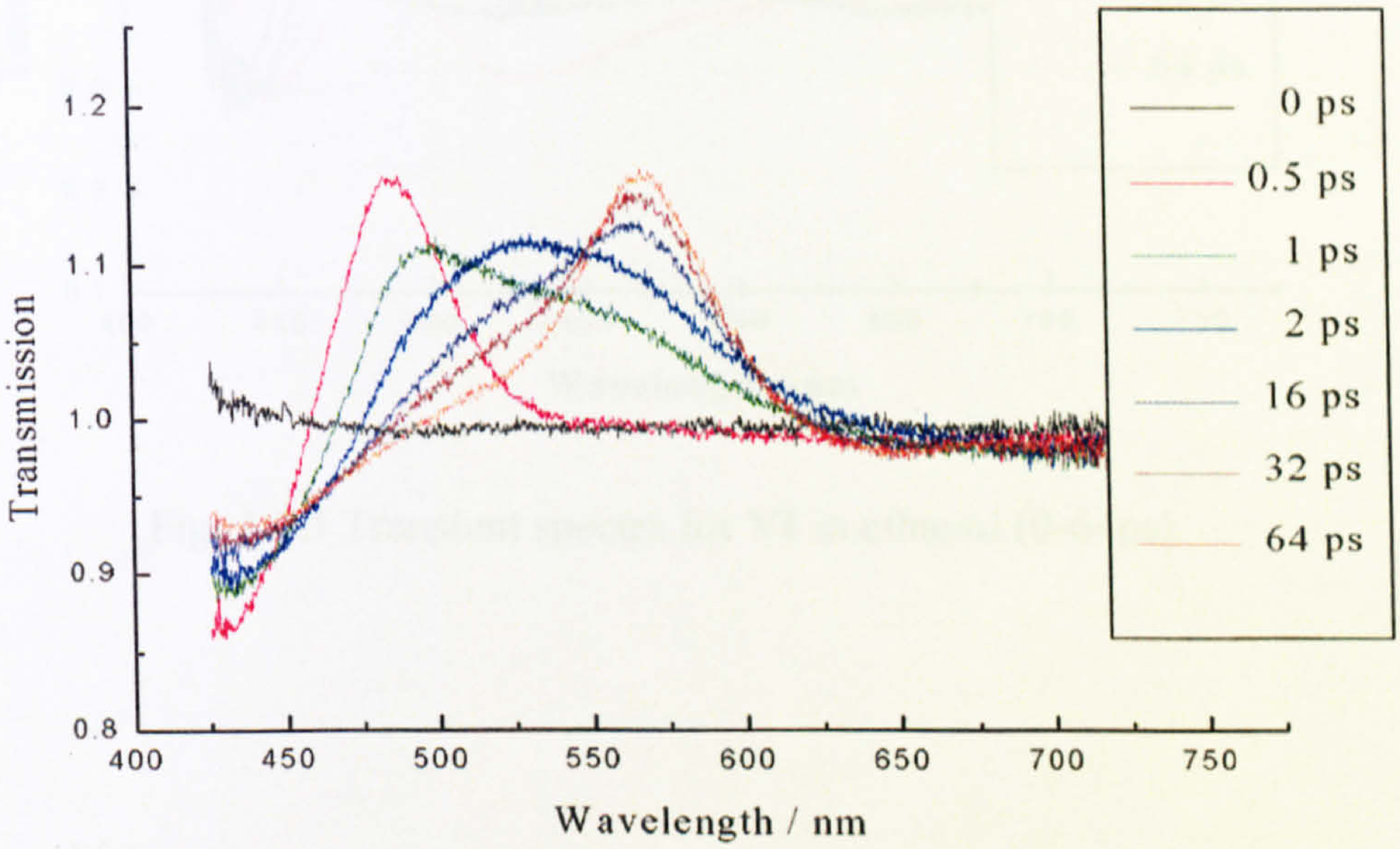

Fig. 3.7.2 Transient spectra for **VI** in acetonitrile (0-64 ps).

Spectra observed for **VI** in 1-decanol solution (Fig. 3.7.4), however, show markedly different behaviour. In this case, we see the formation of two distinct stimulated emission bands, with peaks at 475 nm and 560 nm, which do not converge throughout the measurement period (128 ps). In fact, part of the 475 nm band is observed to decay within this time to form a weak absorption band at shorter wavelength. There are also strong transient absorption bands lying between the two absorption bands and at the red end of the spectrum. This behaviour is markedly different to the behaviour of **VI** in the two other polar solvents.

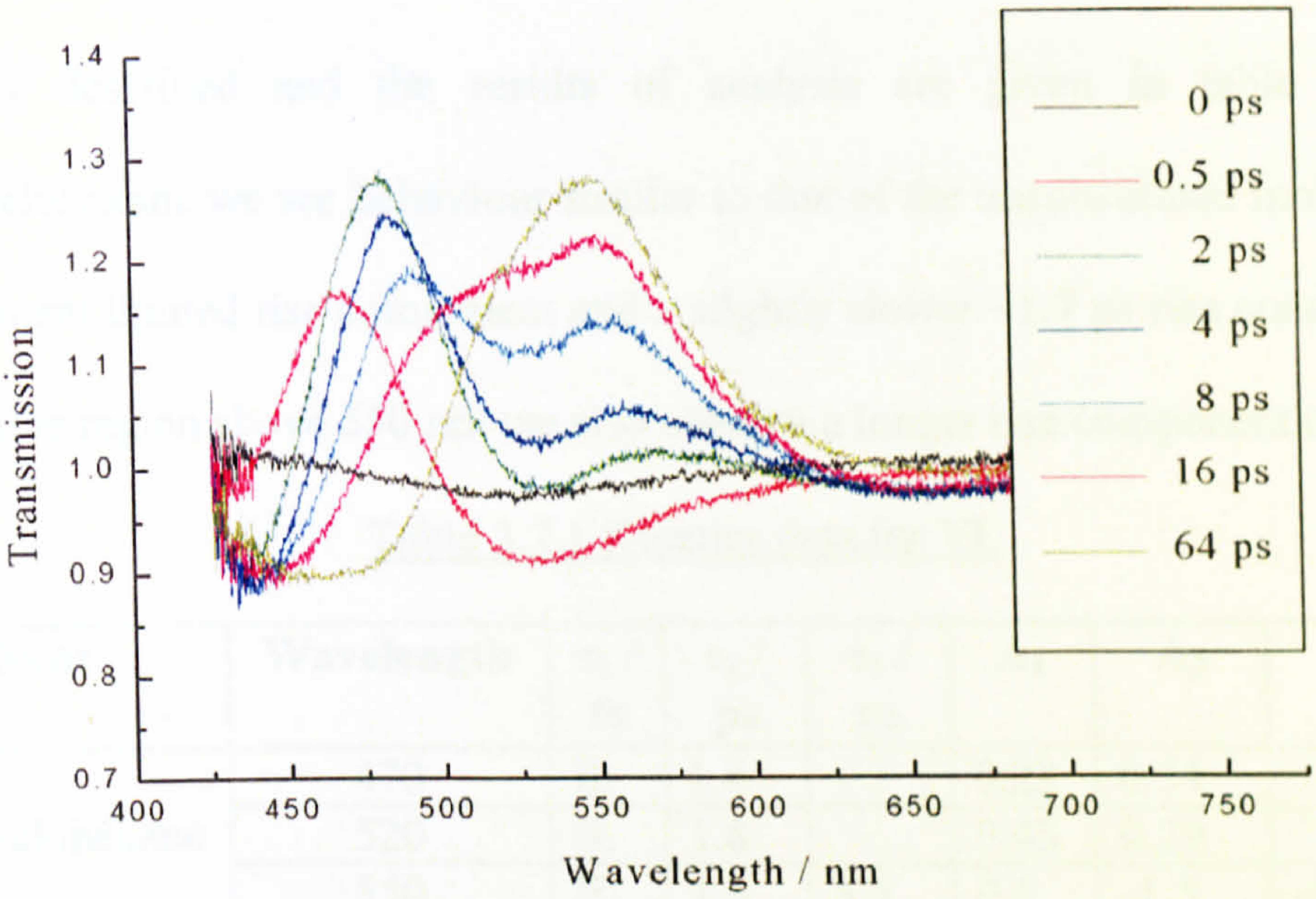

Fig. 3.7.3 Transient spectra for **VI** in ethanol (0-64ps).

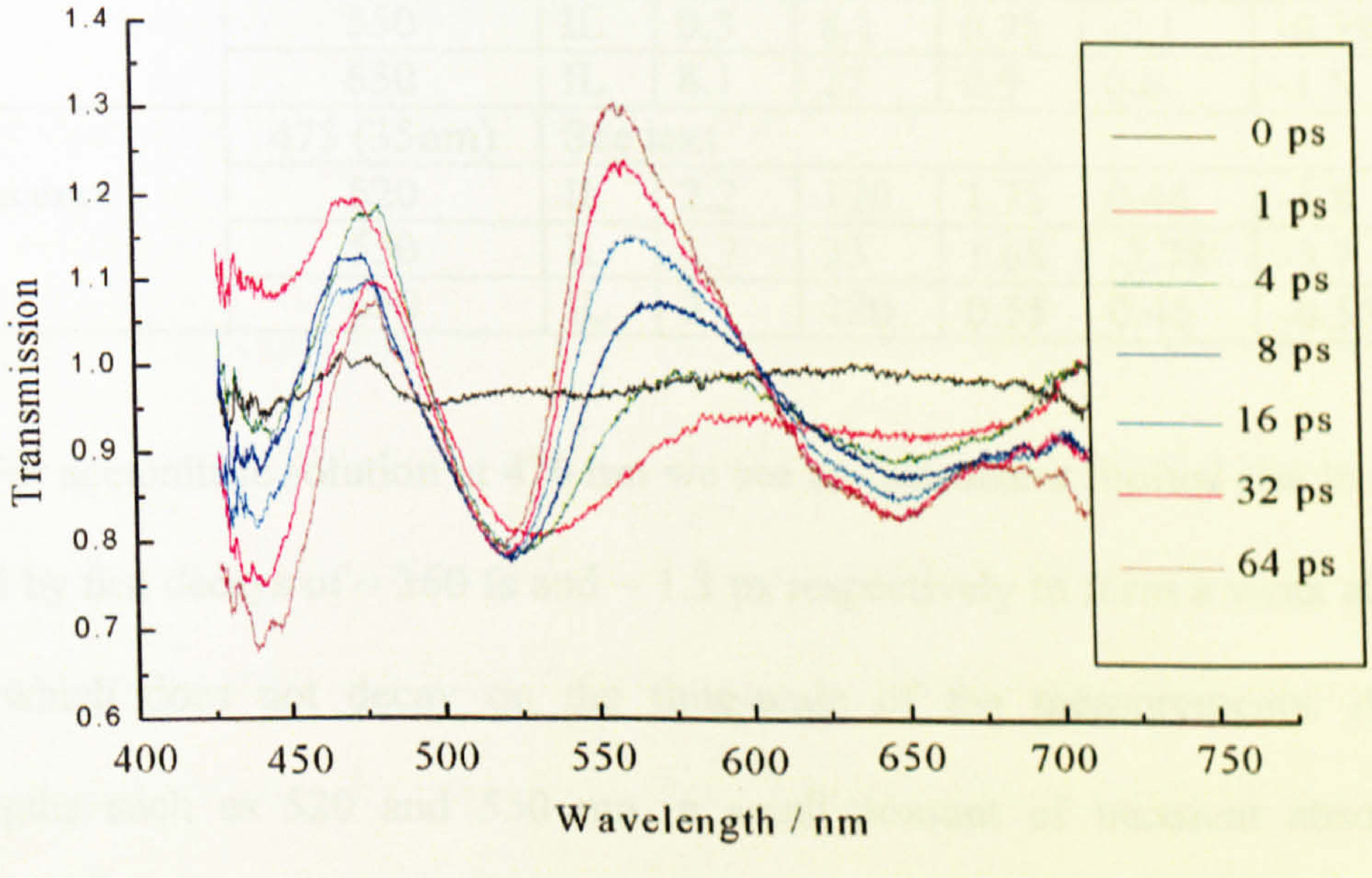

Fig. 3.7.4 Transient spectra for **VI** in 1-decanol (0-64ps).

Time integrated kinetics for **VI** have been obtained from the spectra as previously described and the results of analysis are given in table 3.7.1. For methylcyclohexane we see behaviour similar to that of the unsubstituted molecule, with an instrument limited rise component and a slightly slower ~1.7 ps rise component. For the emissive region above 550 nm we also observe a longer rise component of ~ 8.5 ps.

Table 3.7.1 Kinetics data for **VI.**

Solvent	**Wavelength**	τ_1 / fs	τ_2 / ps	τ_3 / ps	A_1	A_2	A_3	χ^2
Methylcyclohexane	470	IL	1.6		0.23	0.34		0.53
	520	IL	1.8		0.43	0.29		0.27
	550	IL	1.6	8.5	0.4	-1.5	-0.6	0.33
	550	IL	5.6		0.14	-0.88		0.4
	650	IL	1.6	8.5	0.27	0.27	0.44	0.11
Acetonitrile	470	IL	0.36	1.3	-1	0.95	0.24	0.05
	520	IL	0.27	33	0.69	-1.32	0.6	0.04
	570	IL	0.33	33	0.44	-0.93	-0.5	0.06
Ethanol	470	IL	0.28	8.6	-1.7	2.5	-0.31	0.08
	520	IL	0.3	8.1	1	-0.7	-1.6	0.15
	550	IL	0.3	8.1	0.75	-2.1	-0.39	0.09
	650	IL	8.1	27	0.9	0.6	-1.5	0.02
1-Decanol	475 (35nm)	See text						
	520	IL	2.2	120	1.75	0.44	-1.8	0.55
	550	IL	3.7	33	1.68	-2.78	-3.7	0.45
	650	IL	3	120	0.55	0.45	-0.55	0.11

For acetonitrile solution at 470 nm we see an instrument limited rise in emission followed by fast decays of ~ 360 fs and ~ 1.3 ps respectively to form a weak absorption feature which does not decay on the time-scale of the measurements. At longer wavelengths such as 520 and 550 nm, a small amount of transient absorption is observed initially which is then transformed to a stimulated emission signal with a rise time of approximately 300 fs. At 520 nm, the stimulated emission then decays with a lifetime of 33 ps, where as the 550 nm emission continues to increase - again with a lifetime of 33 ps. The three lifetimes of ~ 300 fs, 1.3 ps and 33 ps are also appropriate for fitting the TDSS data for **VI** in acetonitrile (Fig. 3.7.5), although the middle lifetime needs to be a little longer than 1.3 ps for the optimal fit which has time constants of $\tau_1 = 0.3$ ps (A_1=-0.57), τ_2 =1.6 ps (A_2=-1.6), τ_3 = 33 ps (A_3=-0.3) to give a χ^2 of ~ 0.56.

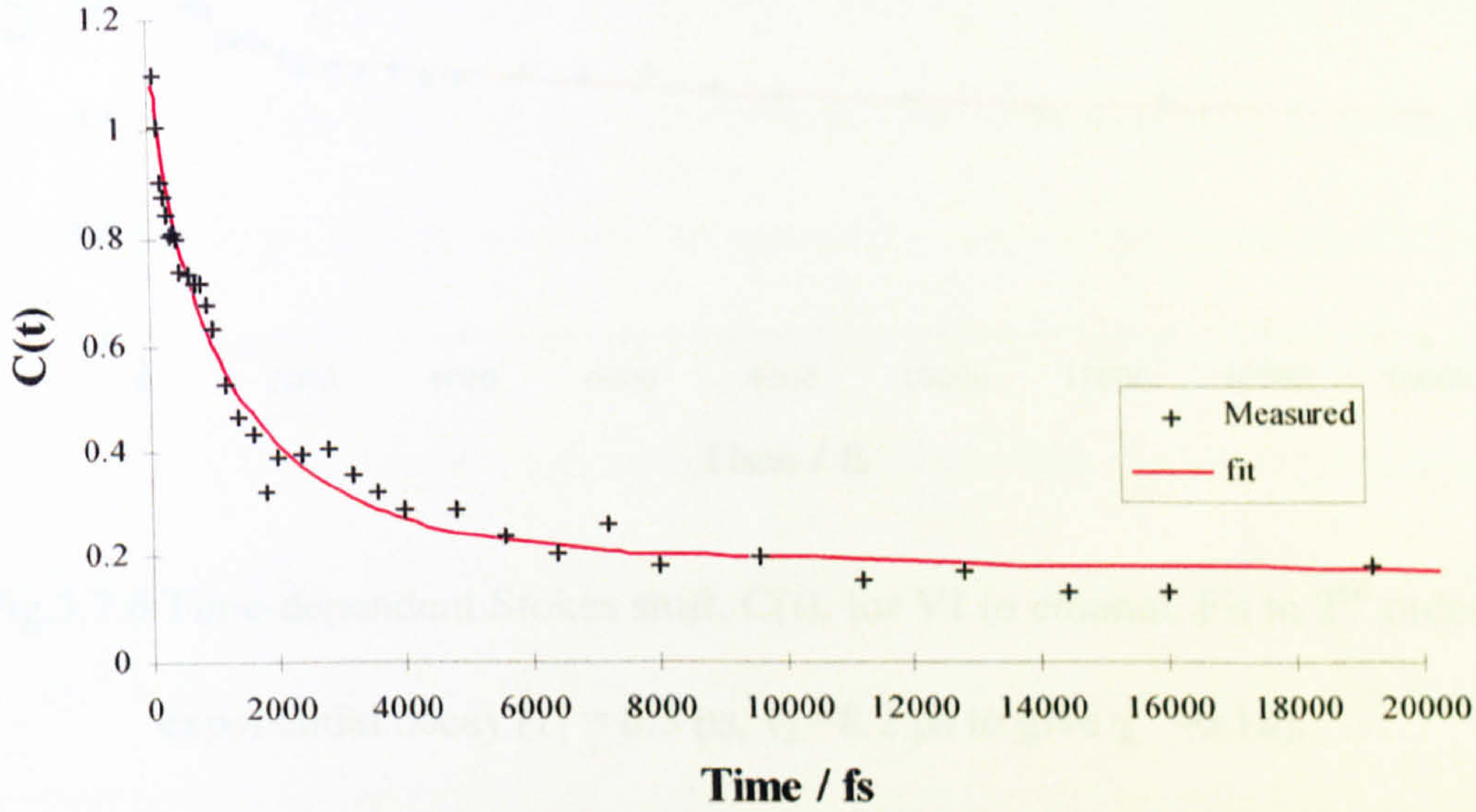

Fig.3.7.5 Time-dependent Stokes shift, C(t), for **VI** in acetonitrile. Fit to 3 rd order exponential decay ($\tau_1 = 0.3$ ps, τ_2 =1.6 ps, τ_3 = 33 ps to give χ^2 ~ 0.56).

The kinetic behaviour in **VI** in ethanol is similar to that observed for the compound in acetonitrile, i.e. we see similar fast dynamics (τ_1 ~ 300 fs), but in this case we observe only a single picosecond component in the 8 ps range. The kinetics clearly show the transient state at 470 nm decaying into a second state, components of which are at 520 and 550 nm. In ethanol the transient absorption in the red is sufficiently intense to enable its kinetics to be fitted. We find that it displays instrument limited and 8 ps risetimes and a 27 ps decay. Finally the TDSS data for **VI** in ethanol is shown in fig. 3.7.6 where the kinetic components of 300 fs and 8 ps are once again reproduced.

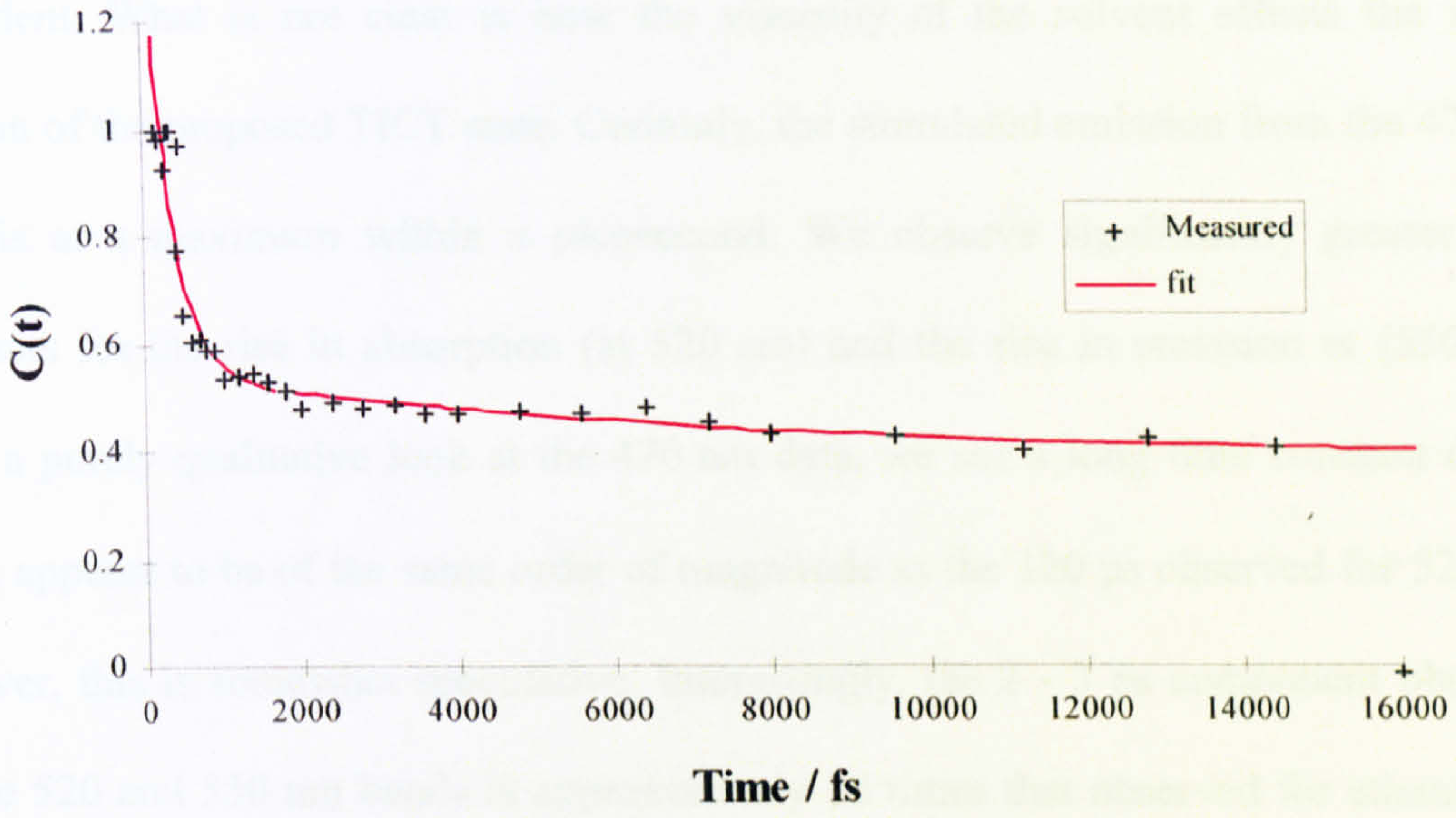

Fig.3.7.6 Time-dependent Stokes shift, C(t), for **VI** in ethanol. Fit to 2nd order exponential decay (τ_1 = 0.3 ps, τ_2 =8.2 ps to give χ^2 ~0.18).

Solutions of **VI** in 1-decanol show significantly different kinetics to those observed in other solvents. In this case we observe stimulated emission bands at 470 nm and 550 nm, however the time dependent Stokes shift observed for ethanol and acetonitrile does not occur. The kinetics of the 470 nm band show large amplitude variations (even with integration over the whole band), such that the dynamics could not be resolved. These large amplitude oscillations are most likely noise, however time integrated kinetics at 520 nm and 550 nm show no such oscillations and are comparable in quality to all the other data obtained at LENS. Further investigation of this emission band is clearly desirable, in order to fully characterise the excited state dynamics of this molecule. Attempts to fit the transient absorption around 440 nm were similarly thwarted.

It is evident that the Stokes shift of the stimulated emission is strongly viscosity dependent. What is not clear is how the viscosity of the solvent effects the initial creation of the proposed TICT state. Certainly, the stimulated emission from the 470 nm band is at a maximum within a picosecond. We observe significantly greater time constants for the rise in absorption (at 520 nm) and the rise in emission at (550 nm). From a purely qualitative look at the 470 nm data, we see a long time constant decay, which appears to be of the same order of magnitude as the 120 ps observed for 520 nm, however, this is somewhat speculative. Interestingly, the 2 - 3 ps component observed for the 520 and 550 nm bands is approximately 10 times that observed for ethanol and acetonitrile, correlating with the viscosity change between the two solvents (ethanol ~ 1.037 at 300 K, 1-decanol ~ 10.16 at 300 K). However, this may be a coincidence and further experimental observations are required to establish this hypothesis. Certainly the effect of viscosity is a dramatic one, both in terms of the changes in the time constants and the absence of a time-dependent Stokes shift. The other comment which can be made is that the decay of the transient absorption at 520 and 650 nm (with time constants of 120 ps in each case) appears to correlate with the rise in the stimulated emission band, albeit the latter has a faster time constant.

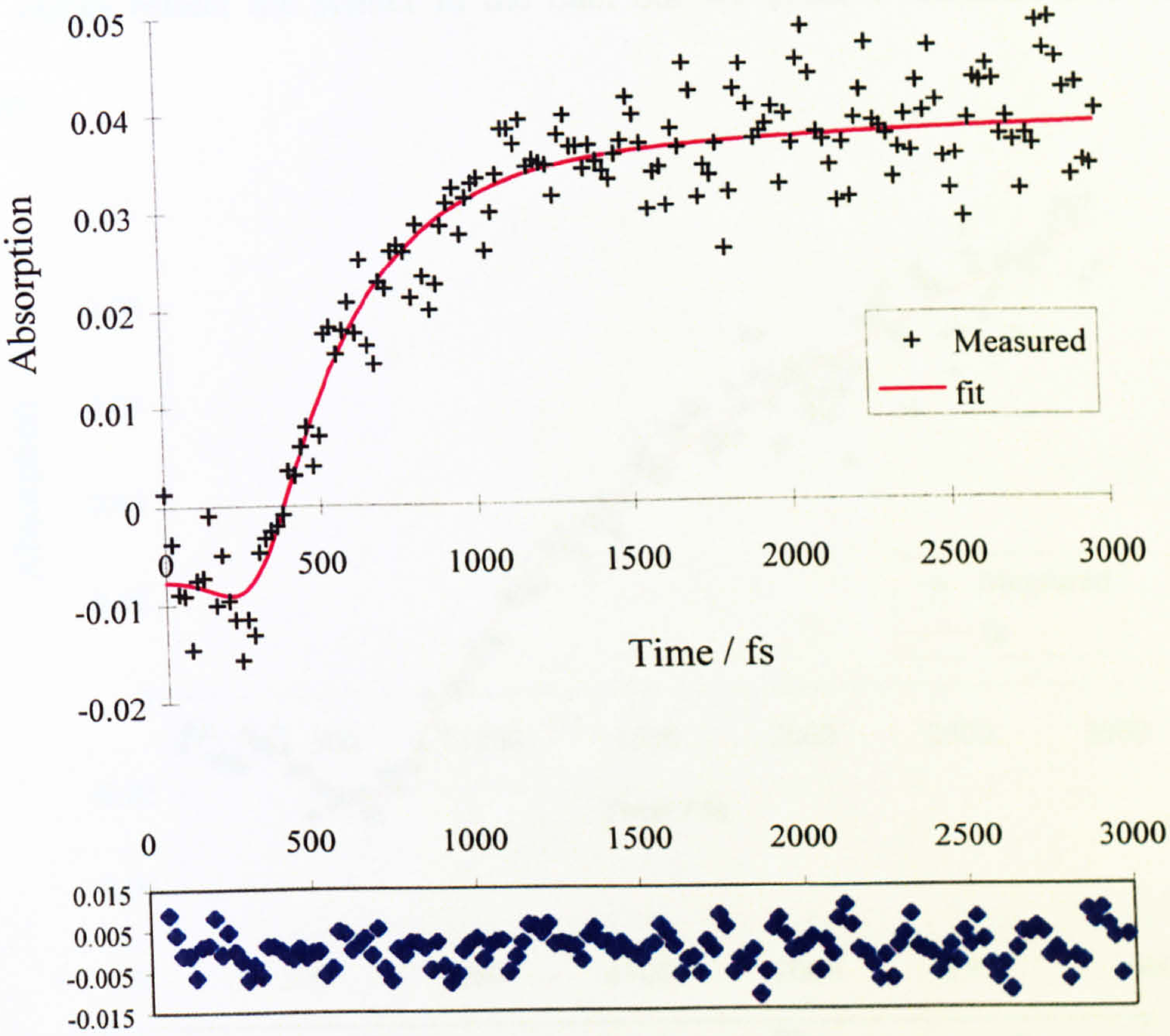

Fig. 3.7.7 Single wavelength transient absorption of **VI** in ethanol solution (Pump: 395 nm, Probe: 430 nm). Fit to 300 fs and 1.6 ps rise components to give $\chi^2 \sim 0.9$.

In addition to the kinetics reconstructed from the LENS data, single wavelength kinetics for ethanol and methylcyclohexane solutions of **VI** have been undertaken using the recently developed BNFL pump-probe apparatus discussed in Chapter 2, Section 2.2 in the blue region of the transient absorption. Fig. 3.7.7 and Fig. 3.7.8 show transient absorption measurements for ethanol solutions of **VI** at 430 and 450 nm respectively. In each case we observe a small transient emission at time zero followed by 300 fs and 8.6 ps components of rise confirming the results obtained for the reconstructed kinetics.

The χ^2 values reflect the scatter in the data but we observe reasonable fitting in the residuals.

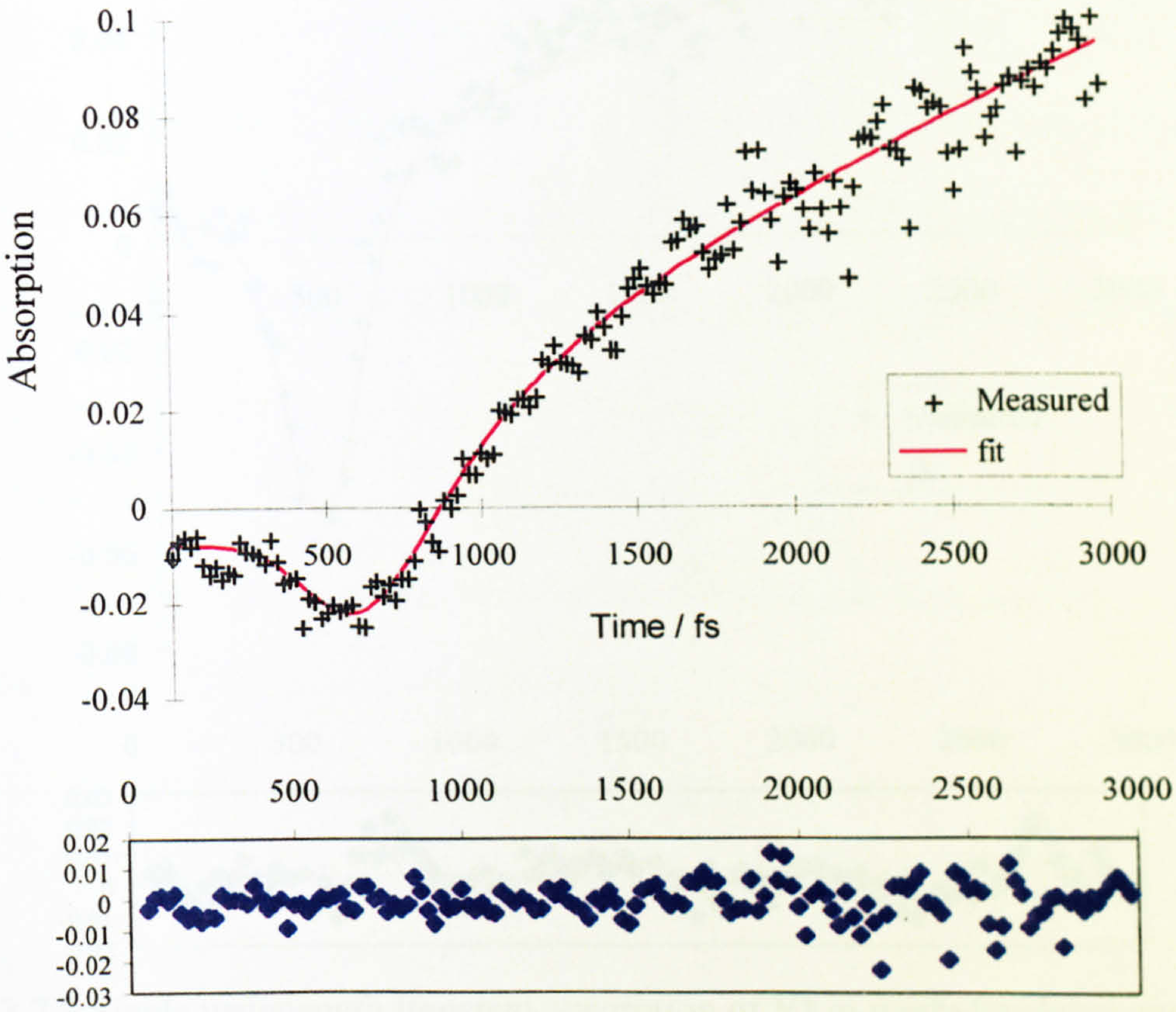

Fig. 3.7.8 Single wavelength transient absorption of **VI** in ethanol solution (Pump: 395 nm, Probe: 450 nm). Fit to 290 fs and 8.6 ps rise components to give χ^2 ~0.95.

Transient absorption of methylcyclohexane solutions of **VI** at 450 nm is given in Fig. 3.7.9. Once again, we observe similar behaviour to that given in the reconstructed kinetics with an instrument limited and 1.6 ps component present, albeit that the data is contaminated at time zero by an instantaneous emission spike which may be a stimulated Raman peak.

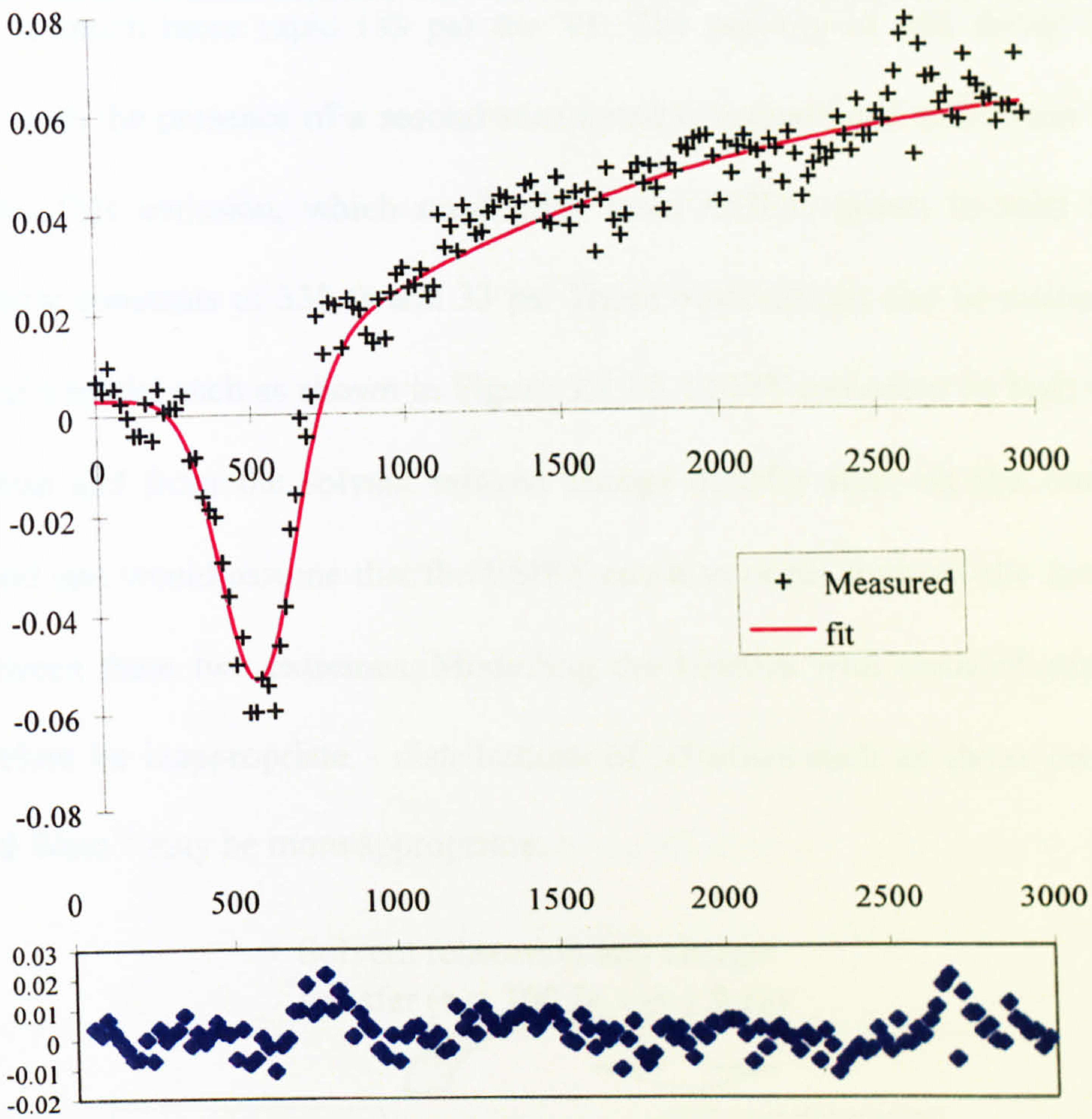

Fig. 3.7.9 Single wavelength transient absorption of **VI** in methylcyclohexane solution (Pump: 395 nm, Probe: 450 nm). Fit to instrument limited rise and 1.6 ps components to give χ^2 ~0.95. The result is contaminated by instantaneous emission at time zero.

An understanding of the excited state processes for **VI** in solution which has led to the data presented here can perhaps be best obtained by first considering the behaviour of **VI** in acetonitrile. The transient spectra (Fig. 3.7.2) and derived kinetics (Table 3.7.1) show many similarities to those for **VII** where proton transfer is impossible. In both **VI** and **VII** the initial stimulated emission band undergoes a red shift, with virtually identical time constants, to yield stimulated emission peaking around 500 nm. In **VII** the emission decays with a nanosecond lifetime (Table 3.7.1) but the decay is much more rapid (33 ps) for **VI**. The rapidity of this decay is clearly associated with the presence of a second stimulated emission band at 570 nm for **VI** in acetonitrile. This emission, which must arise from ESIPT, grows in with two very different time constants of 330 fs and 33 ps. These observations can be rationalised on the basis of a model such as shown in Figure 3.7.10. ESIPT can occur in both the initial excited state and from the solvent relaxed charge transfer state on the basis of the kinetics and one would assume that the ESIPT can also occur from all the intermediate states between these two extremes. Modelling the kinetics with sums of exponentials may therefore be inappropriate - distributions of lifetimes such as those proposed by James and Ware[11] may be more appropriate.

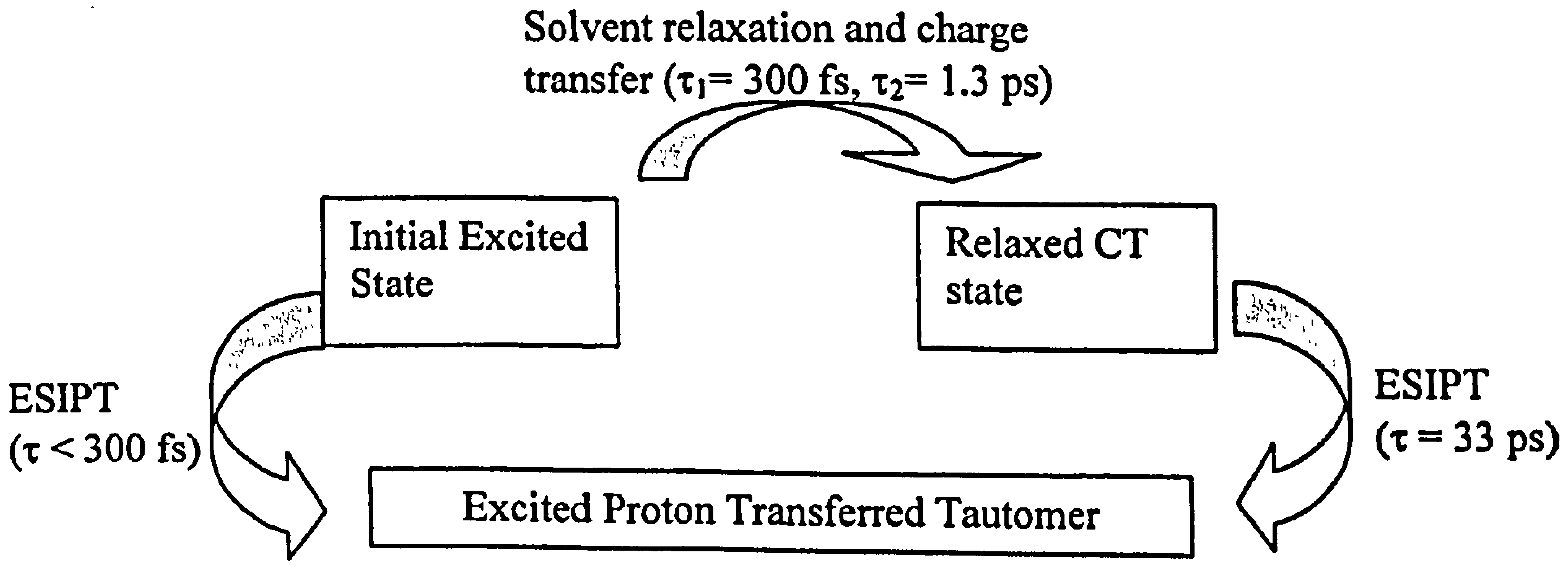

Fig. 3.7.10 Scheme for **VI** in acetonitrile, incorporating both ESIPT and charge transfer processes.

The time constants observed for the solvent relaxation / charge transfer process are identical for **VI** and **VII** in acetonitrile and compare well with the literature values of 0.1, 0.86 and 1.85 ps (for coumarin dyes)[12]. The solvent cage around the excited molecule of **VI** and / or its electronic structure following solvent relaxation and charge transfer are obviously very different. This is perhaps a truism but is vividly illustrated by the two different proton transfer rates which are derived from the kinetics, differing by a factor of 100. It may be that faster kinetics for ESIPT are observed with better time resolution as undertaken for **I**, however further work of this nature is sadly beyond the scope of this thesis.

The steady state and time resolved emission properties of **VI** in acetonitrile (Table 3.7.2) fit in well with the model proposed in figure 3.7.10 and the above discussion. The emission spectrum, contains two strongly Stokes shifted bands and their decay profiles exhibit fast (instrument limited) and slower (hundreds of ps) components. The slower decays are complex, but the instrument limited decay reflects the ultrafast and 33 ps components observed in the transient spectra. There is a marked contrast between the fluorescence quantum yields of **VI** and **VII** in acetonitrile, with the latter (0.48) being nearly an order of magnitude greater than the former (0.07). This reflects the high proportion of the excitation energy which is channelled into ESIPT via the two routes in Fig. 3.7.10 and the low emission yield of the excited tautomer (0.04 for **I** in acetonitrile[1]).

Table 3.7.2 Steady state and time-resolved emission properties of **VI** in solution[13].

Solvent	λmax nm	Stokes Shift (cm^{-1})	ϕ_f	τ_f^1 ps	τ_f^2 ns	τ_f^3 ns
Methylcyclohexane	551	6950	0.16	IL	1.36	
Acetonitrile	507, 560	5400, 7250	0.07	IL	0.37	0.5-1.0
Ethanol	520	5350	0.27	IL	1.75	
1-Decanol	498, 550	4550, 6450				

The behaviour observed for the transient spectra of **VI** in ethanol can be understood using a very similar model to that used for acetonitrile as solvent, with one major difference; there is no evidence from the kinetics of **VI** in ethanol that the relaxed charge transfer state undergoes ESIPT. That is to say, there is no direct parent-daughter relationship between the two states. This is almost certainly due to solute-solvent intermolecular hydrogen bonding, which may prevent the intramolecular proton motion. The reduction in ESIPT is reflected in the emission yield for **VI** which is much higher in ethanol than in acetonitrile, although the longer excited state lifetime of the proton transferred tautomer in ethanol may also help to increase ϕ_f. The steady state emission spectrum is not structured for **VI** in ethanol; a single band peaking around 520 nm is observed. The emission maximum reflects the contribution of the charge transfer state to the overall emission and the absence of the ESIPT decay route for the charge transfer state removes the dip in the emission spectrum which causes the two bands observed for **VI** in acetonitrile.

The transient spectra observed for **VI** in methylcyclohexane are very different to those for the two solvents discussed above. There is significant transient absorption over most of the spectral range covered at all decay times and there is only one single stimulated emission band whose spectral position changes only slightly with decay time. On the basis of the assignments made for **VI** in acetonitrile and ethanol, the stimulated emission may be considered to originate from the excited proton transferred tautomer. The shape and spectral position of the emission is also in agreement with the stimulated emission from **I** in methylcyclohexane (Fig. 3.1.4) when the red-shift in the absorption properties of **VI** with respect to **I** is taken into account.

The origins of the transient absorption appear to be similar to those proposed for **I-V** when the spectral shape, position and kinetics are considered. The absence of any transient absorption above approximately 570 nm at a delay of 500 fs, suggests that there is little or no excited tautomer present resulting from ESIPT. This would also explain the weakness/absence of any stimulated emission at this early delay time. The transient absorption at ~ 500 fs can therefore be largely assigned to the initially excited state. In the absence of any evidence for solvent relaxation processes, the two time constants of 1.6 and 8.5 ps can be assigned to the ESIPT from the bare and impurity solvated molecules of **VI** respectively. The longer of these components compares favourably with the 10 ps lifetime observed for **I** in methylcyclohexane. However, the 1.6 ps component is considerably longer than the instrument limited value observed for **I**. This may reflect the fact that the proton transfer event is bound up with the charge transfer and that the 1.6 ps lifetime component represents a convolution of the two processes. Alternatively, it may be that the electron-donation properties of the *N,N*-dimethylamino group reduce the acidity and/or basicity of the excited state hydroxyl and carbonyl functions, such that ESIPT is no longer as favourable as it is in **I**. Such a lifetime for proton transfer is not inconceivable if the event is moderated by other motions on the excited state than simply along an intramolecular hydrogen bond.

The behaviour of **VI** in 1-decanol also appears to fit with the above model, even though we observe no significant time-dependent Stokes shift of the blue stimulated emission band. We have not been able to obtain meaningful kinetics for the blue transient absorption and stimulated emission bands, but there appears to be a qualitative correlation between the increased transient absorption and decrease in the stimulated emission and the spectral changes observed at 550 and 650 nm. The kinetic component with a lifetime of 2-4 ps presumably relates to charge transfer/ESIPT occurring in the initial excited state together with a small amount of solvent reorganisation. The increased lifetime for this component can be matched with the increased viscosity of

1-decanol. The 120 ps component represents ESIPT from the partially relaxed charge transfer excited state - again the lifetime is increased over the values seen in ethanol and acetonitrile due to increased viscosity. It is impossible to deduce whether the increased lifetimes of the kinetic components in 1-decanol are due to the slower rate of diffusion of the solvent such that the solvent relaxation and reorientation (to allow the progression of ESIPT) processes are much slower or whether a TICT state is involved, whose rate of formation would also be greatly reduced in a more viscous solvent such as 1-decanol.

3. 8 4’-(1”-Aza-4”,7”,10”,13”-Tetraoxacyclopentadecyl)-3-Hydroxyflavone

The 4’-(1”-aza-4”,7”,10”,13”-tetraoxacyclopentadecyl)-3-hydroxyflavone (**VIII**) molecule has been examined by our group[14] and others[15] as a potential environmental sensor, using the ability of the 15-crown-5 moiety to selectively complex metal ions and act as a charge donor group in a charge transfer or TICT process as previously described for **VI** and **VII**. Transient absorption measurements were undertaken for **VIII** at LENS in a range of solvents analogous to those chosen for **VI** and **VII**. The spectra which were obtained are very similar to those for **VI** and it would appear that an identical model (Fig. 3.7.7) may be used to describe the photophysics of **VIII**.

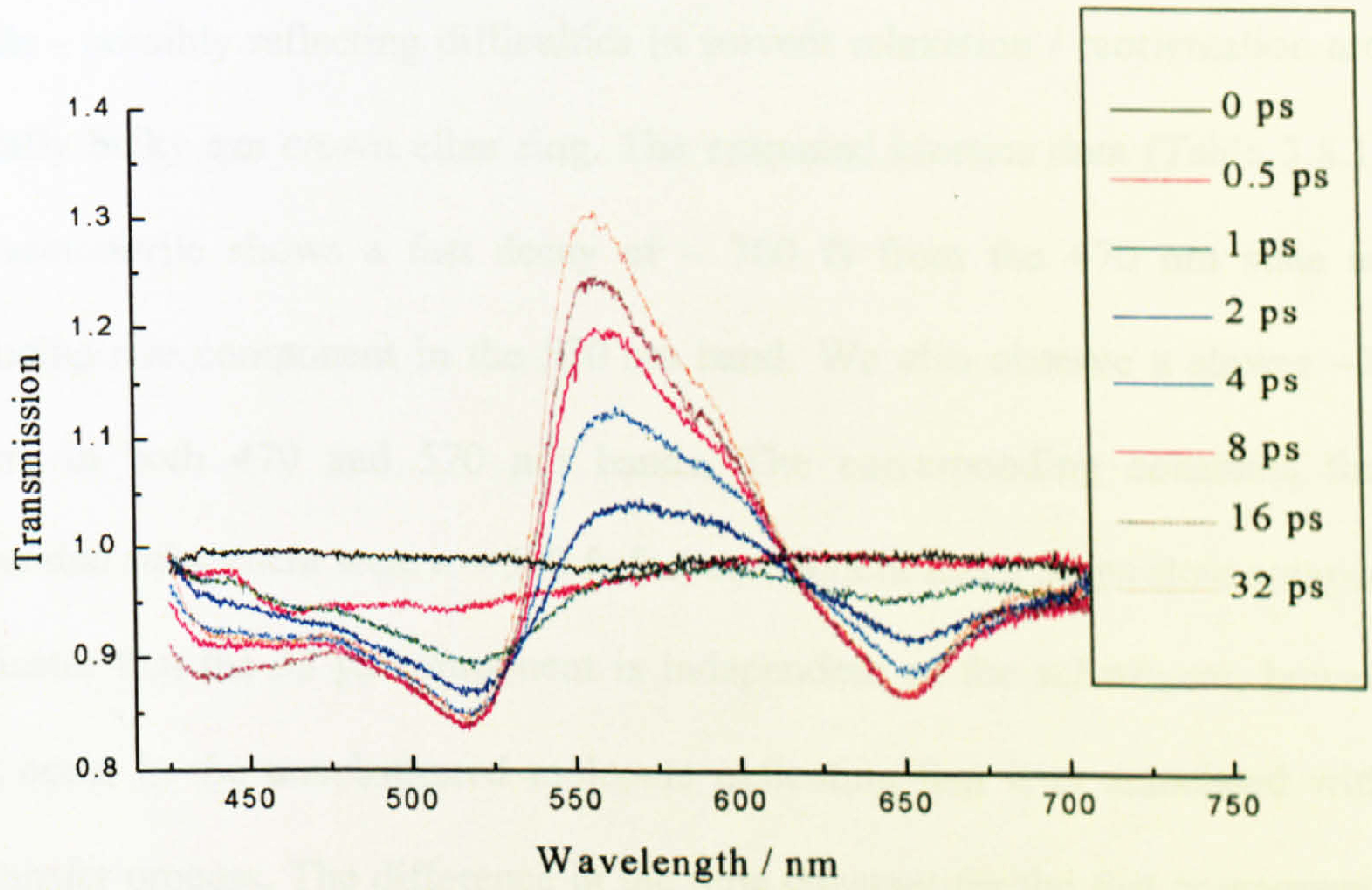

Fig. 3.8.1 Transient spectra of **VIII** in methylcyclohexane (0-32ps).

The transient spectra for **VIII** excited at 350 nm in methylcyclohexane for delays of 0-32 ps are given in Fig. 3.8.1. The spectra are virtually identical to those for **VI** in methylcyclohexane (Fig. 3.7.1). However, there are changes in the time constants describing the evolution of the spectral bands (Table 3.8.1). An instrument limited component is observed at all wavelengths, in an identical fashion to **VI**, but the two picosecond components are increased for **VIII**; ~3 ps (from 1.6 ps for **VI**) and 15 ps (from 8.5 ps for **VI**).

For acetonitrile solutions of **VIII** we observe the initial formation of an emission band at 470 nm, the peak of which shifts to approximately 500 nm on a timescale of ~ 2 ps and undergoes a subsequent decay (Fig. 3.8.2). A second emissive region evolves with a peak around 570 nm on a similar timescale as the decay from the 470 nm band but we do not observe the merging of the two emission bands as observed for **VI**. The initial emission band at 470 nm does not undergo as large a Stokes shift as for **VI** in acetonitrile - possibly reflecting difficulties in solvent relaxation / reorientation around the sterically bulky aza crown ether ring. The extracted kinetics data (Table 3.8.1) for **VIII** in acetonitrile shows a fast decay of ~ 700 fs from the 470 nm state and a corresponding rise component in the 570 nm band. We also observe a slower ~32 ps component in both 470 and 570 nm bands. The corresponding constants for the dimethylamino substituent were a ~ 300 fs fast component and a 33 ps slow component. This indicates that the 33 ps component is independent of the substituent, however it does not occur in the unsubstituted molecule indicating that it is associated with the charge transfer process. The difference in the time constant for the fast component may be due to the increased size and mass of the crown substituent (with respect to the dimethylamino substituent) which would lead to a substantial change in the effect of solvent viscosity and reorientation with respect to the change in charge distribution in the solute. Alternatively the 0.7 ps component may reflect two components of ~ 300 fs and ~1 ps (as observed for **VI** in acetonitrile at 470 nm) which are convolved to give a value of 700 fs.

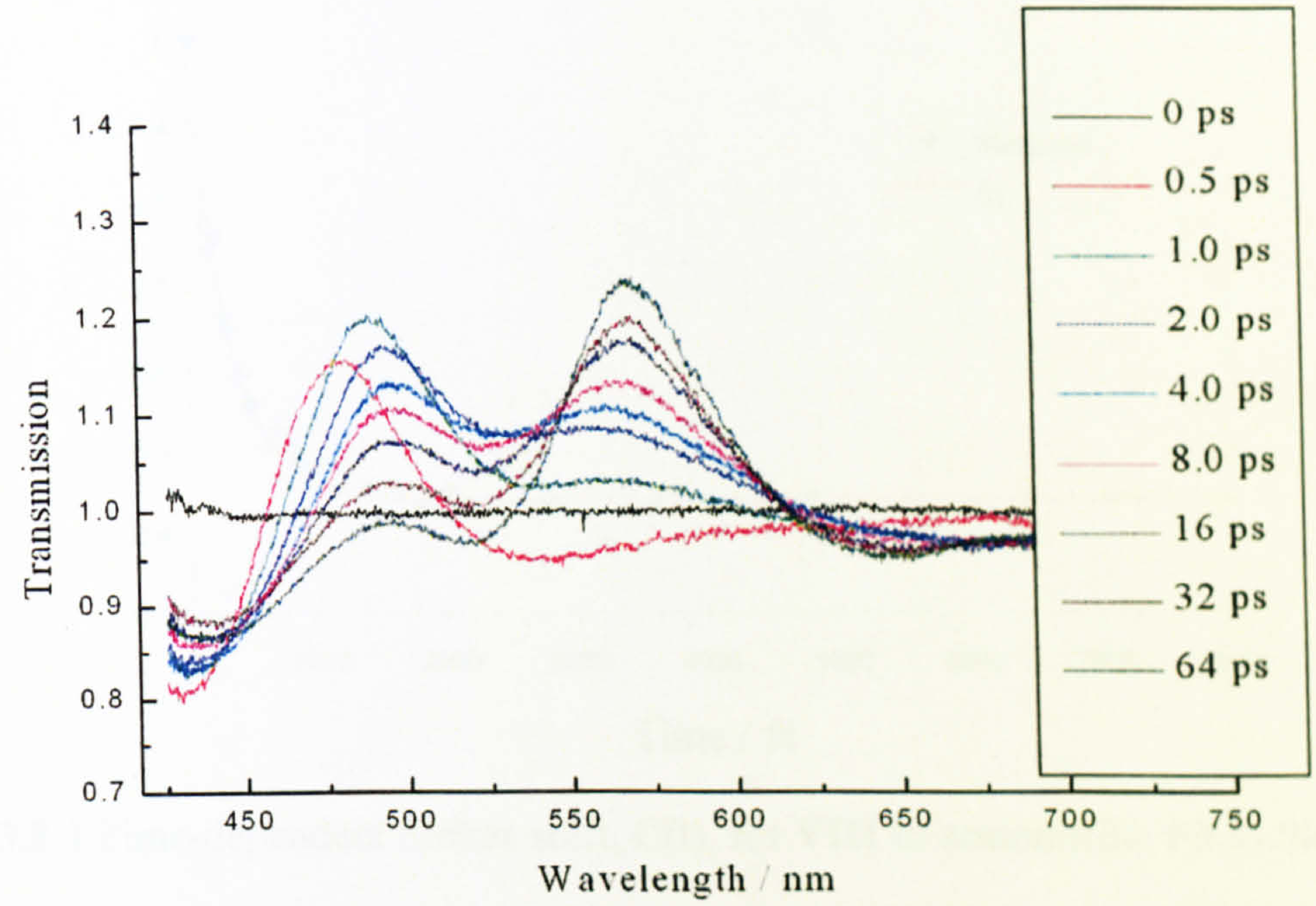

Fig. 3.8.2 Transient spectra of **VIII** in acetonitrile (0-64ps).

The time dependent Stokes-shift for acetonitrile solutions of **VIII** is given in fig. 3.8.3. Here we see a far more rapid shift (310 fs) of the blue stimulated emission band than observed in the transient kinetics. This may indicate that the conclusion regarding the 700 fs transient is correct. Although no longer component is observed, this may be due to the grow-in of the green stimulated emission, which masks any slower dynamics.

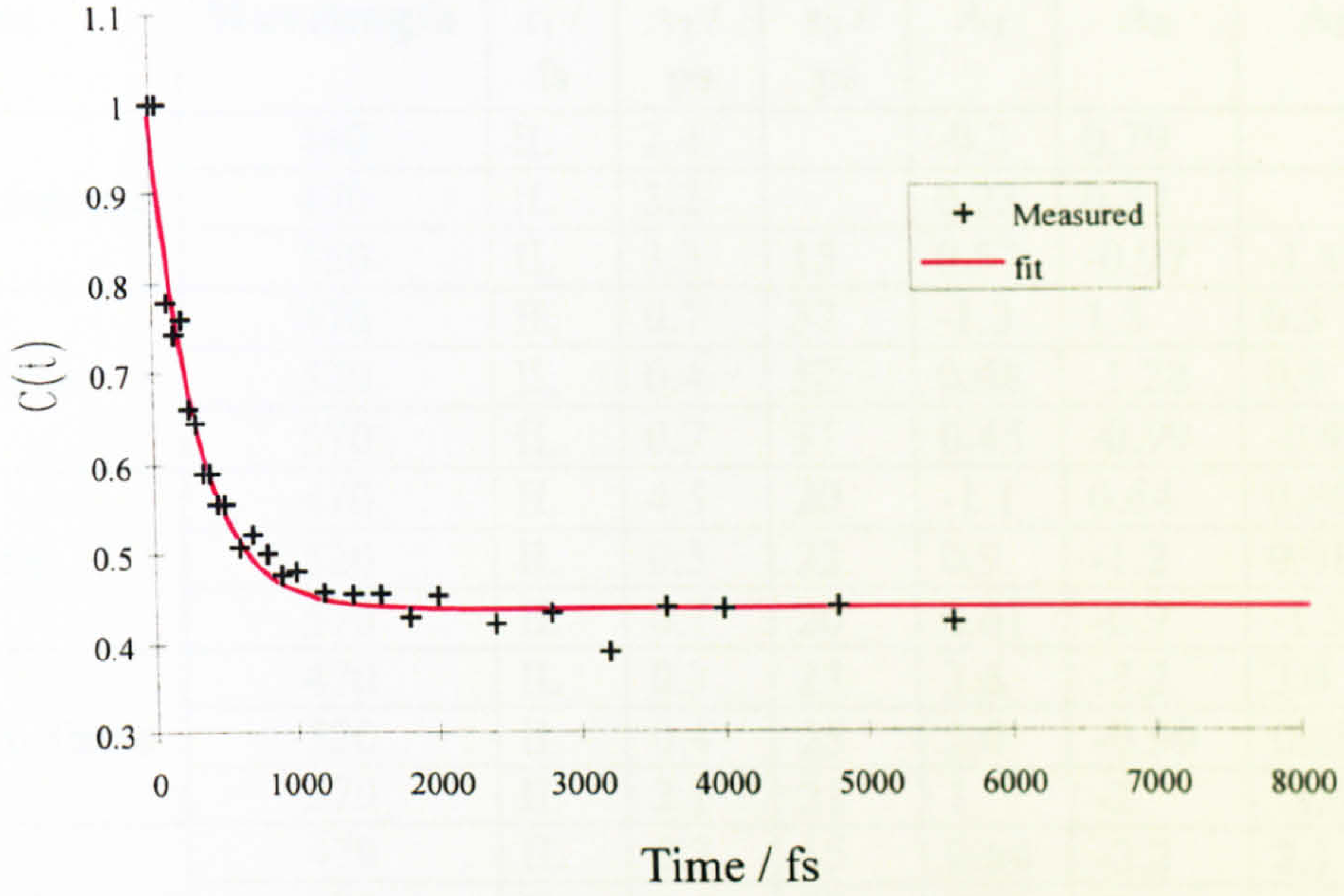

Fig. 3.8.3 Time-dependent Stokes shift, C(t), for **VIII** in acetonitrile. Fit to Single exponential decay ($\tau_1 = 0.31$ ps to give $\chi^2 \sim 0.03$).

The spectra observed for **VIII** in ethanol solution (Fig. 3.8.4) are very similar to those observed for **VI**. Whilst there is clearly a discontinuity in the Stokes shift between the two excited state populations, there is a clear superposition of the spectra at long delay times. The kinetics data does not indicate as clear a parent-daughter relationship between the two states as in **VI**, but this may be because we have not used enough components in the analysis of the data. However, as in the case for **VIII** in methylcyclohexane, the extracted time constants exhibit an increase compared to the corresponding values for **VI**. The TDSS data confirms the time constants found for the blue emission band with components of 0.2 and 15 ps being reproduced - whilst the fast component (0.2ps) is faster than that extracted from the kinetics this is probably within error given the instrumental response of the LENS system.

Table 3.8.1 Kinetics data for **VIII.**

Solvent	**Wavelength**	τ_1 / fs	τ_2 / ps	τ_3 / ps	A_1	A_2	A_3	χ^2
Methylcyclohexane	440	IL	2.4		-0.2	0.79		0.51
	470	IL	3.2		0.23	0.32		0.12
	550	IL	3.3	15	0.57	-0.97	-1.41	0.35
Acetonitrile	470	IL	0.7	32	-1.3	1.3	0.5	0.28
	520	IL	0.4	32	0.68	-1.28	0.9	0.07
	570	IL	0.7	31	0.45	-0.99	-0.99	0.1
Acetone	470	IL	4.5	20	-1.1	0.64	0.86	0.7
	520	IL	0.5	23	0.9	-1.2	0.91	0.6
	570	IL	0.7	20	0.61	-0.9	-1.5	0.25
1,2-Dichloroethane	470	IL	0.3	23	3.6	-5.2	3.4	0.41
	520	IL	0.4	25	2.0	-0.99	0.68	0.13
	570	IL	2.1	21	1	-2	-3.5	0.3
Ethanol	470	IL	0.3	15	0.64	-2.2	2.1	0.03
	520	IL	2.5	27	0.32	-0.45	-1.1	0.15
	570	IL	1.5	21	0.56	-0.78	-1.5	0.13
1-Decanol	470	IL	0.3	85	2.2	-3.2	2.1	1.5
	520	IL	3	88	1.5	0.4	-1	0.6
	570	IL	2.4	85	1.4	-2.7	-2	0.73

We observe a change in the colour of the ethanol solution of **VIII** after the experiment from green to red, potentially indicating contamination by metal ions from the steel of the experimental arrangement. No change in the absorption of the solution was observed. However, the presence of metallic ions in solution may have led to unexpected changes in the photophysics of **VIII** in ethanol.

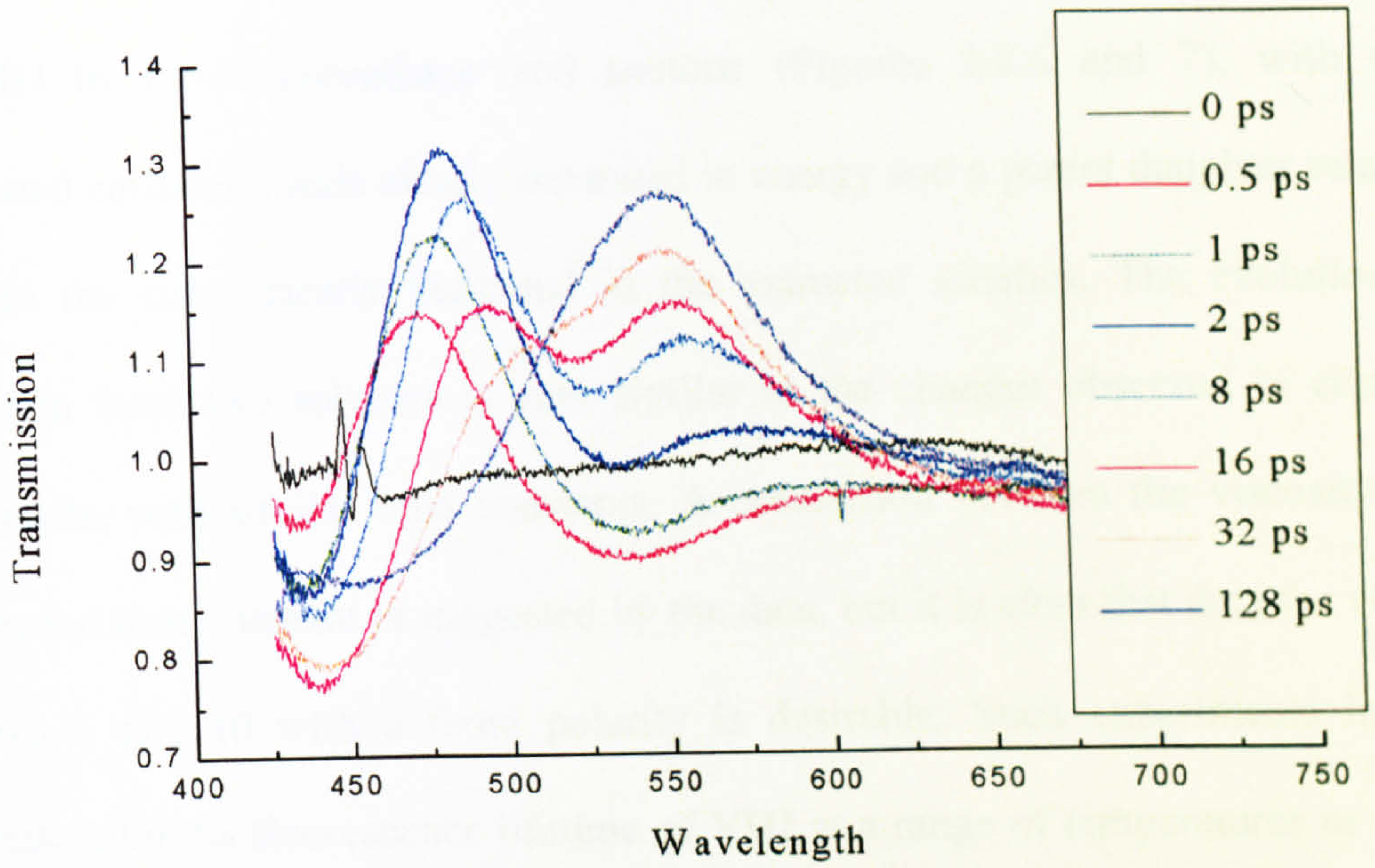

Fig. 3.8.4 Transient spectra of **VIII** in ethanol (0-128 ps).

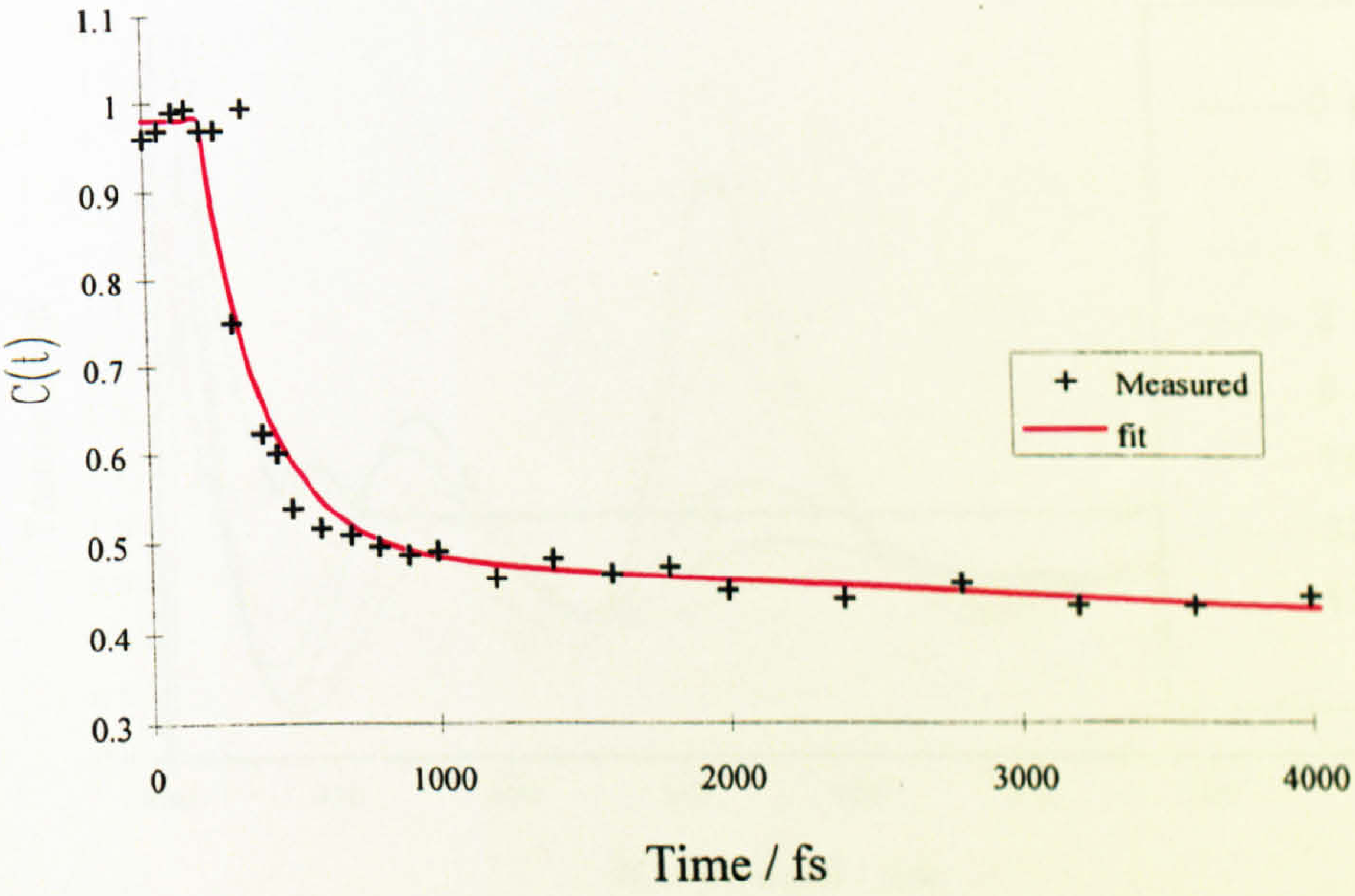

Fig. 3.8.5 Time-dependant Stokes shift for **VIII** in ethanol. Fit to 2nd order exponential decay ($\tau_1 = 0.2$ ps, $\tau_2 = 15$ ps to give $\chi^2 \sim 0.19$).

Similar behaviour to that observed for acetonitrile solutions of **VIII** is observed for **VIII** in 1,2-dichloroethane and acetone (Figures 3.8.6 and 7), with the two stimulated emission bands clearly separated in energy and a parent daughter relationship between the states clearly indicated in the extracted kinetics. The evolution of the spectra in these two solvents is very similar to the changes observed in ethanol and acetonitrile, with similar time constants. A connection between the viscosity and the picosecond time constant is suggested by the data, but it is clear that data for viscosities between 1 and 10 with a fixed polarity is desirable. Such experiments have been undertaken for the fluorescence lifetime of **VIII** at a range of temperatures in a number of solvents down to 77 K using single photon counting at the BESSY (Berlin) and SRS Daresbury, U.K.) synchrotron sources and confirm these conclusions[10].

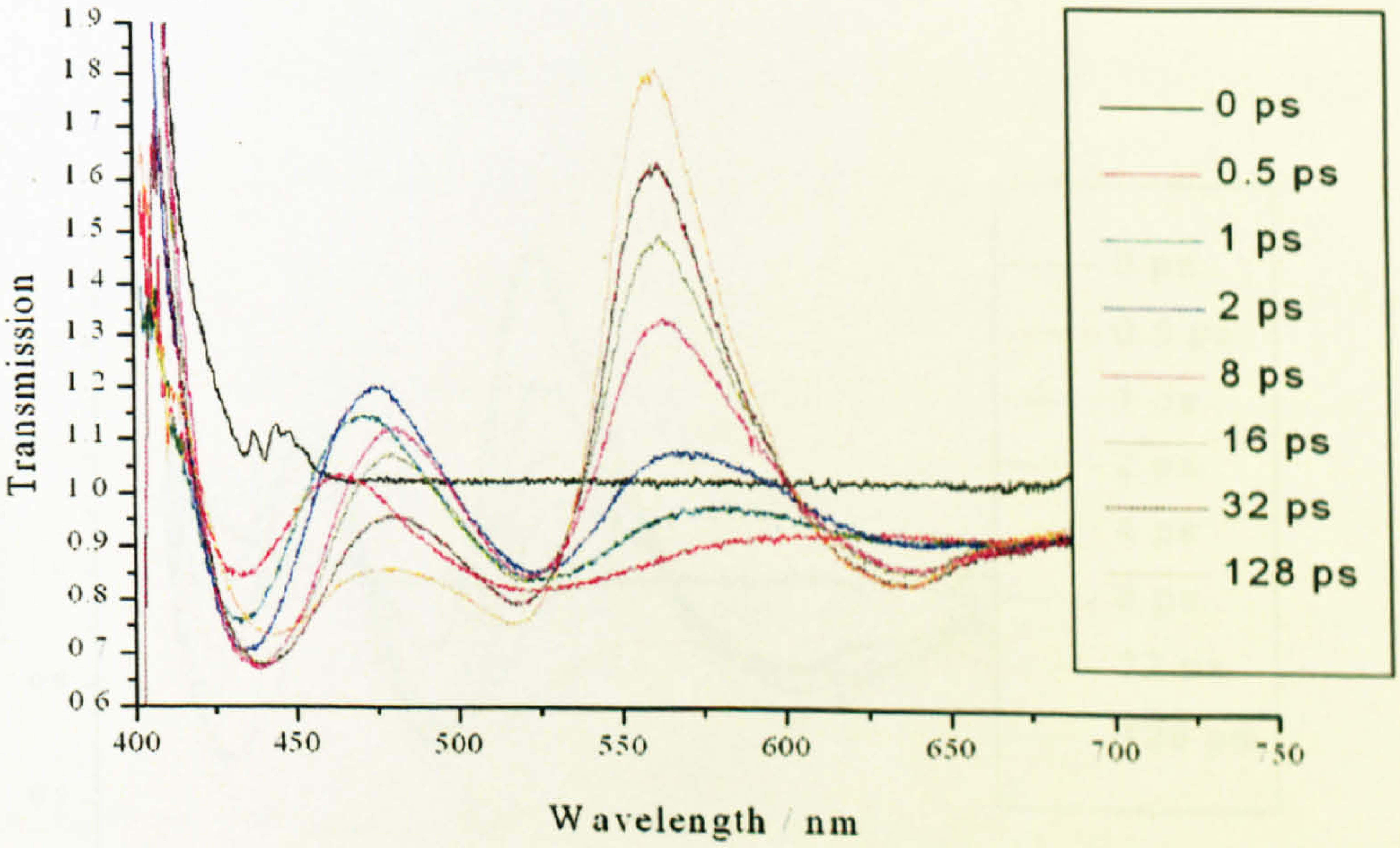

Fig. 3.8.6 Transient spectra of **VIII** in 1,2-dichloroethane (0-128 ps).

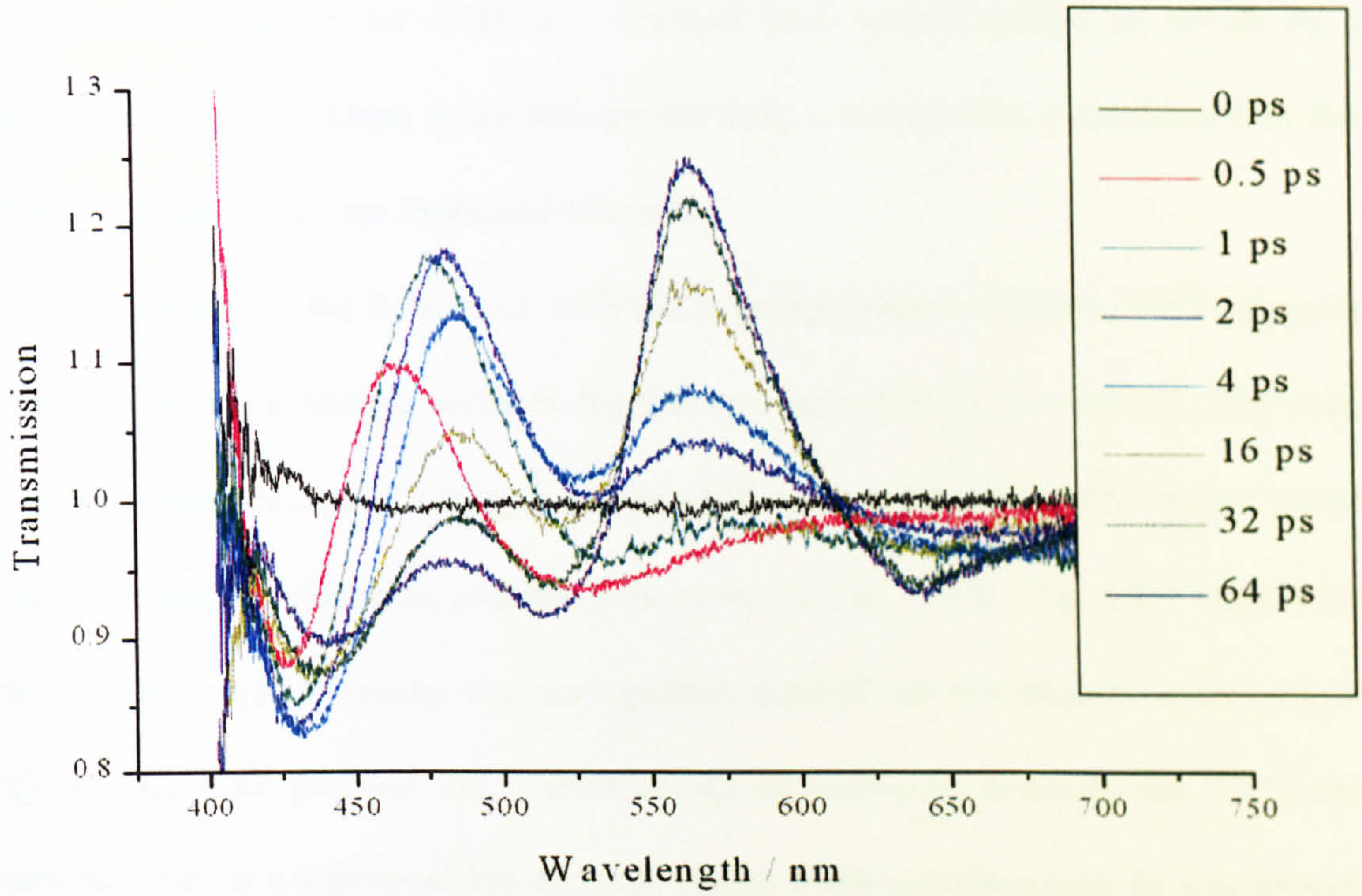

Fig. 3.8.7 Transient spectra of **VIII** in acetone (0-64 ps).

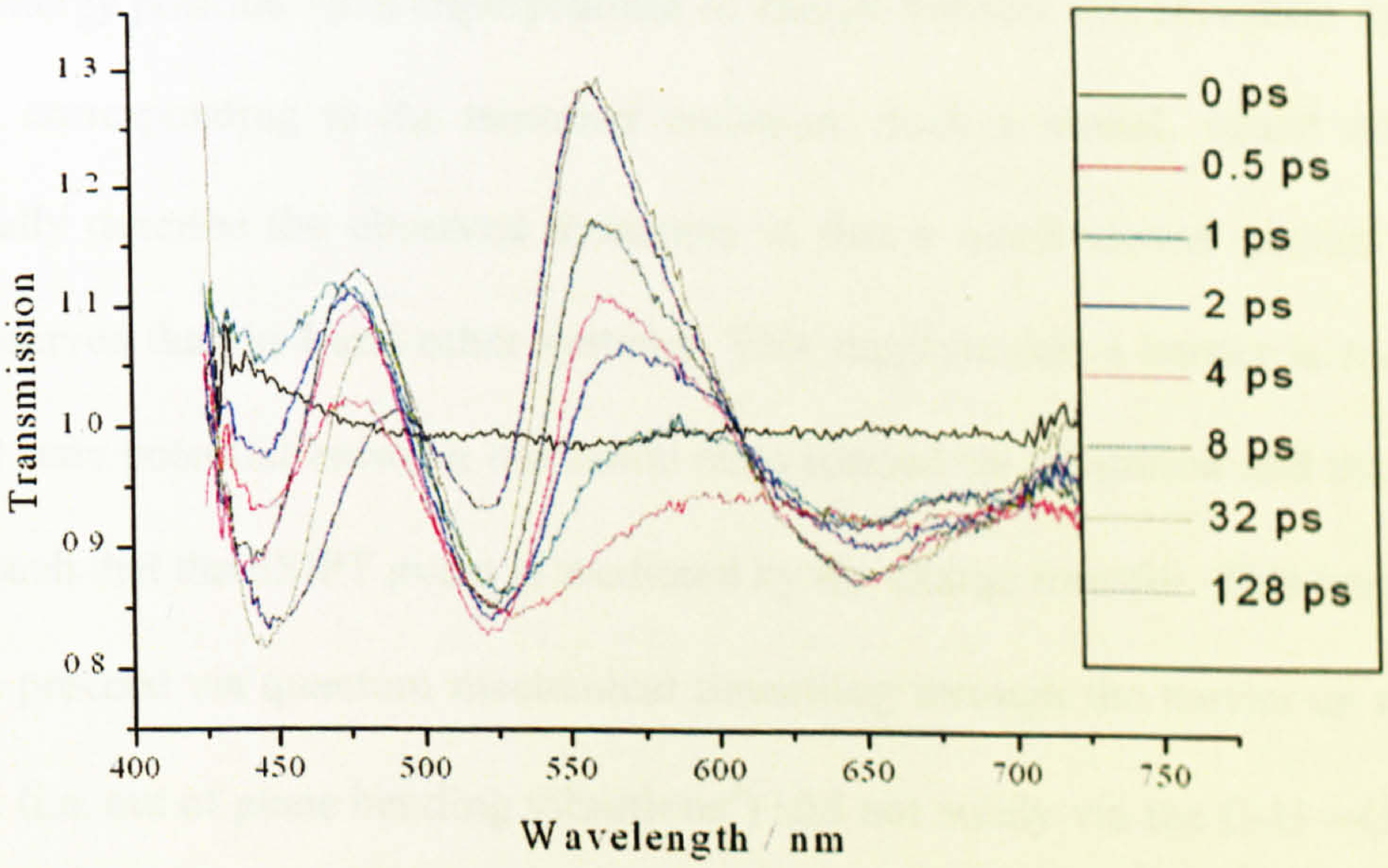

Fig. 3.8.8 Transient spectra of **VIII** in 1-decanol (0-128 ps).

Transient spectra for **VIII** in 1-decanol over a time range of 0-128 ps are presented in Fig. 3.8.8. Once again the spectra bear a remarkable resemblance to those of **VI** in 1-decanol as do the extracted kinetics.

It is clear that the behaviour of **VIII** is comparable with that of **VI** suggesting that the excited state energy surfaces for the two substituents are similar. The results lead us to suggest potential energy surfaces with axes representing the charge transfer and proton transfer relaxation pathways as given in Fig. 3.8.9. Fig. 3.8.9 represents a barrier-less potential, whereby the wavepacket created on the excited state potential energy surface may proceed via a multiplicity of pathways towards the TICT state, tautomeric state, or a superposition of these states. Such a surface may be inappropriate for the observed dynamics, in that it implies an ultrafast time scale for the ESIPT step as in the case of **I**. The movement of the wavepacket on the excited state potential is indicated by the strong Stokes shift from the initial emission band at 470 nm towards the minimum energy position via a superposition of charge transfer and solvation dynamics at 570 nm, corresponding to the tautomer emission. Such a model, whilst attractive, does not fully describe the observed dynamics in that a much slower proton transfer event is observed than in **I** and other systems. This suggests that a barrier is formed on the excited state potential between the initial state formed on excitation and the excited tautomer, such that the ESIPT event is mediated by the charge transfer. This implies that ESIPT can proceed via quantum mechanical tunnelling through the barrier or via some other route (i.e. out of plane bending vibrations[3]) and not solely via the O-H—O stretch. However, since the absence of stimulated emission around 570 nm does not imply that ESIPT has not occurred, merely that an emissive potential has not been formed, such an excited state potential should not be dismissed. In the case of 3-hydroxyflavone itself, the stabilisation of the highly vibrationally excited molecule and, in particular, planarisation by the solvent is thought to play a role in the rise of the fluorescence[2].

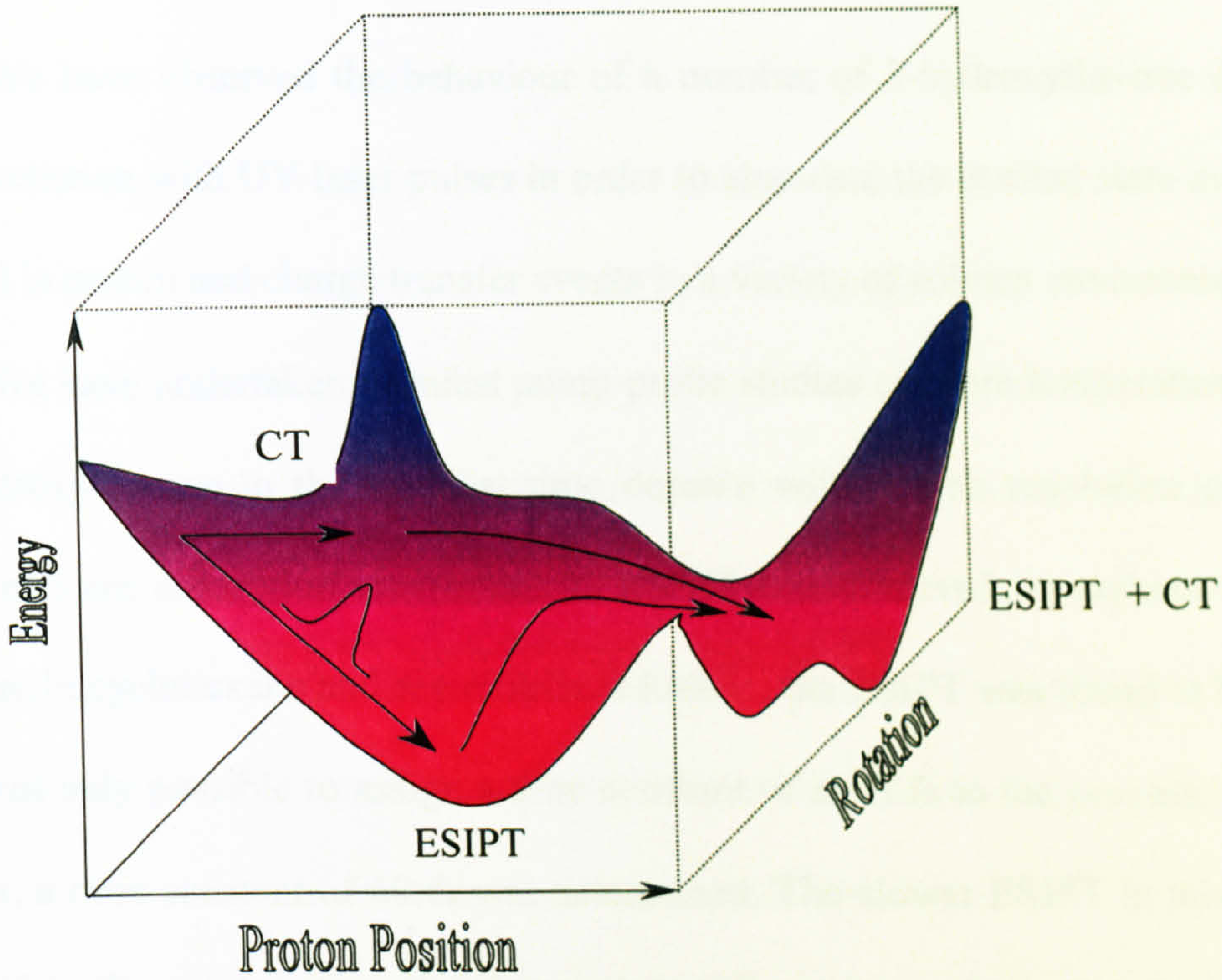

Fig. 3.8.9 Barrier-less potential energy surface as a model for molecules undergoing charge transfer and ESIPT processes.

In conclusion, it would seem that dimethylamino and aza-crown-ether derivatives of 3-hydroxyflavone undergo two excited state processes, the dynamics of which are strongly dependent on solvent polarity and viscosity. Experimental results suggest a model with a strongly solvent dependent barrier between the two fluorescent states of the molecules. A significant separation of the states present in a highly sterically hindered environment (1-decanol) and kinetics indicate a parent-daughter relationship between the charge transfer and ESIPT fluorescent states in some solvent environments.

3.9 Conclusions

We have observed the behaviour of a number of 3-hydroxyflavone derivatives under excitation with UV laser pulses in order to elucidate the excited state mechanisms involved in proton and charge transfer events in a variety of solvent environments.

We have undertaken ultrafast pump-probe studies of room temperature solutions of 3-hydroxyflavone in the ultrafast time domain with a time resolution of less that 35 fs. Transient absorption attributable to ESIPT was observed throughout the visible spectrum. In cyclohexane and acetonitrile solutions, the ESIPT was found to be so rapid that it was only possible to assign a time constant of ≤ 35 fs to the process. In ethanol, however, a time constant of 60 fs was determined. The slower ESIPT in this solvent is attributed to the greater strength of the solute-solvent interactions. In all three solvent environments a transient in the 1-10 ps range was also observed and we attribute this behaviour to the presence of monosolvated 3-hydroxyflavone complexes, which may undergo either a dual intermolecular proton transfer to the solvent, or intramolecular proton transfer directly along the O_a-H—O_b reaction co-ordinate. The influence of substituents in the 4' position of the phenyl ring of 3-hydroxyflavone has also been investigated and we observe unusual behaviour for a cyano substituent in polar solvents and for dimethylamino (VI) and aza-Crown (VIII) substituents. The anomalous behaviour of VI and VIII is explained in terms of a charge transfer state which has been postulated and experimentally confirmed previously[15,1], although our results do not allow us to definitively determine if the state formed has a 'twisted' conformation in the excited state as previously postulated. We observe fast transients on the order of 300 and 700 fs for the time dependent stokes shift of the CT emission band in acetonitrile for **VI** and **VIII** respectively, which we attribute to solvent reorganisation and stabilisation of the charge transfer state. The observed difference in the timescale for reorganisation is explained in terms of the difference in mass of the substituents.

The results of transient absorption measurements of **VI** and **VIII** lead us to suggest potential energy surfaces with axes representing the charge transfer and proton transfer relaxation pathways. A potential energy surface is proposed whereby the excited state wavepacket proceeds initially towards the superposition state where a local minimum exists for the CT emission. A pathway corresponding to the relaxation or quenching of the CT state is then available for the subsequent creation of a tautomeric emissive potential well, which is the global minimum of the excited state. The decay of the initial CT emissive state is mediated by solvent interaction and, in this case, the behaviour of both **VI** and **VIII** may be described by modifying the height of the potential energy barrier between the two minima for the various solvent environments. In the case of 1-decanol solutions for both molecules and, to an extent, 1,2-dichloroethane solutions of **VIII**, we clearly observe separation of the CT and ESIPT states and a clear parent-daughter relationship in the kinetics, indicating that a significant barrier is present on the excited state potential. Similar behaviour is also suggested by the acetone and acetonitrile kinetics of **VIII**. However, in this case the energy barrier appears to be less significant although the emissive states remain distinct, and there is clear evidence in the kinetics for a parent-daughter relationship. Conversely, in the case of the ethanol solutions of both molecules and acetonitrile solution of **VI**, we see a distinct shift of the CT emission into that of the ESIPT state. This may indicate a broad potential minimum between the two states, with no barrier, suggesting strong solvent interaction. Indeed we are probably observing dynamic solvent interactions with the potential energy surface, such that the minimum position is shifted in time from the CT state to the ESIPT state via an equilibrium position.

We have shown a dynamic interaction between two excited state processes in 3-hydroxyflavone derivatives, the dynamics of which are strongly dependent on solvent polarity and viscosity. Experimental results suggest a model with a strongly solvent dependent barrier between the two fluorescent states of the molecules. A significant separation of the states present in a highly sterically hindered environment (1-decanol) and kinetics indicate a parent-daughter relationship between the CT and ESIPT fluorescent states. Further investigation of the excited states of these derivatives with better time resolution (such as that available at MBI) or at infra-red wavelengths in the region of the C-N and H-O bond energies would further elucidate the role of solvent in these reactions.

---

[1] S. M. Ormson, R.G. Brown, F. Vollmer & W. Rettig, *J.Photochem.Photobiol.A: Chem.*, 81: p65 (1994).

[2] B. J. Schwartz, L. A. Peteanu & C. B. Harris, *J. Phys. Chem.*, 96: p 3591 (1992).

[3] T. Elsaesser, *Femtosecond Chemistry* J. Mantz & L. Woste (Eds), Chapter 18, (1995).

[4] J. L. Herek, S. Pedersen, L. Banares & A. H. Zewail, *J. Chem. Phys.* 97 (12): pp9046-9061 (1992).

[5] A. Douhal, S. Kim & A. H. Zewail, *Nature*, 378: p260 (1995).

[6] S. M. Ormson, D. LeGourrierec, R.G. Brown & P. Foggi, *J.Chem Soc.Chem.Commun.*, p2133 (1995).

[7] W. Rettig, *Angew. Chem. Internat. Ed.*, 25: p971 (1986).

[8] P. J. Rossky & J. D. Simon, Nature, 370: p263 (1994).

[9] R. G. Brown, R. J. Clark and S. Ormson, *Unpublished data.*

[10] Chen et al, *J. Phys. Chem.* 97, p2618 (1993).

[11] D. R. James and W. R. Ware, *Chem. Phys. Lett.*, 120, pp455-459 (1985).

[12] E. W. Castner. Jr & M. Marconcelli, J. Molec. Liquids, 77: pp1-36 (1998)

[13] R. G. Brown, R. J. Clark and S. Ormson, *Unpublished data.*

[14] X. Poteau, S. Ameer-Beg, D. Le Gourrierec, R. G. Brown, C. Holmes, D. Matthew & W. Rettig, *BESSY Annual Report,* Berlin (1997).

[15] A. D. Roshal, A. V. Grigorovich, A. O. Doroshenko, V. G. Pivovarenko, A. P. Demchenko, *J. Phys. Chem. A*, 102: pp5907-5914 (1998).

Chapter 4: Ultrashort Pulse Laser Ablation.

Femtosecond laser ablation has been investigated as a method for producing highly controlled surface modifications on a variety of substrate materials with the aim of producing low cost micro and macro size prototype devices of interest to BNFL's advanced materials group. In order to facilitate the production of such devices, some fundamental aspects of the ablation process have been investigated and a micro-machining workstation has been developed (see chapter 2). This chapter is necessarily divided into two sections, dealing with the fundamental aspects of laser ablation and prototype fabrication respectively. In section 4.1 we present quantitative and qualitative results of laser ablation for glasses, semiconductors, polymers and metals. In section 4.2, prototype device fabrication is discussed and some results presented.

4.1 Fundamental Parameters

4.1.1 Glasses

Two types of glass were investigated for use as substrates for microchemical devices, fused silica (spectrosil B) and Pyrex 7070 (borosilicate glass). Results for each material are presented below.

Fused Silica

The interaction between visible light and practically transparent materials like glasses is expected to be negligible (see fig. 4.1.1). The bandgap for fused silica is ~ 8 eV, so that in the linear optical regime, laser light at 790nm ($h\nu = 1.6$ eV) should be transmitted. However, for very high light intensities of the order of 1 GWcm^{-2}, multiphoton absorption (in the case of fused silica absorption of ~5 photons) results in a finite penetration depth in glasses. Electronic and/or thermal excitation below damage and ablation thresholds can lead to incubation effects associated with colour centres[1] (section 1.5).

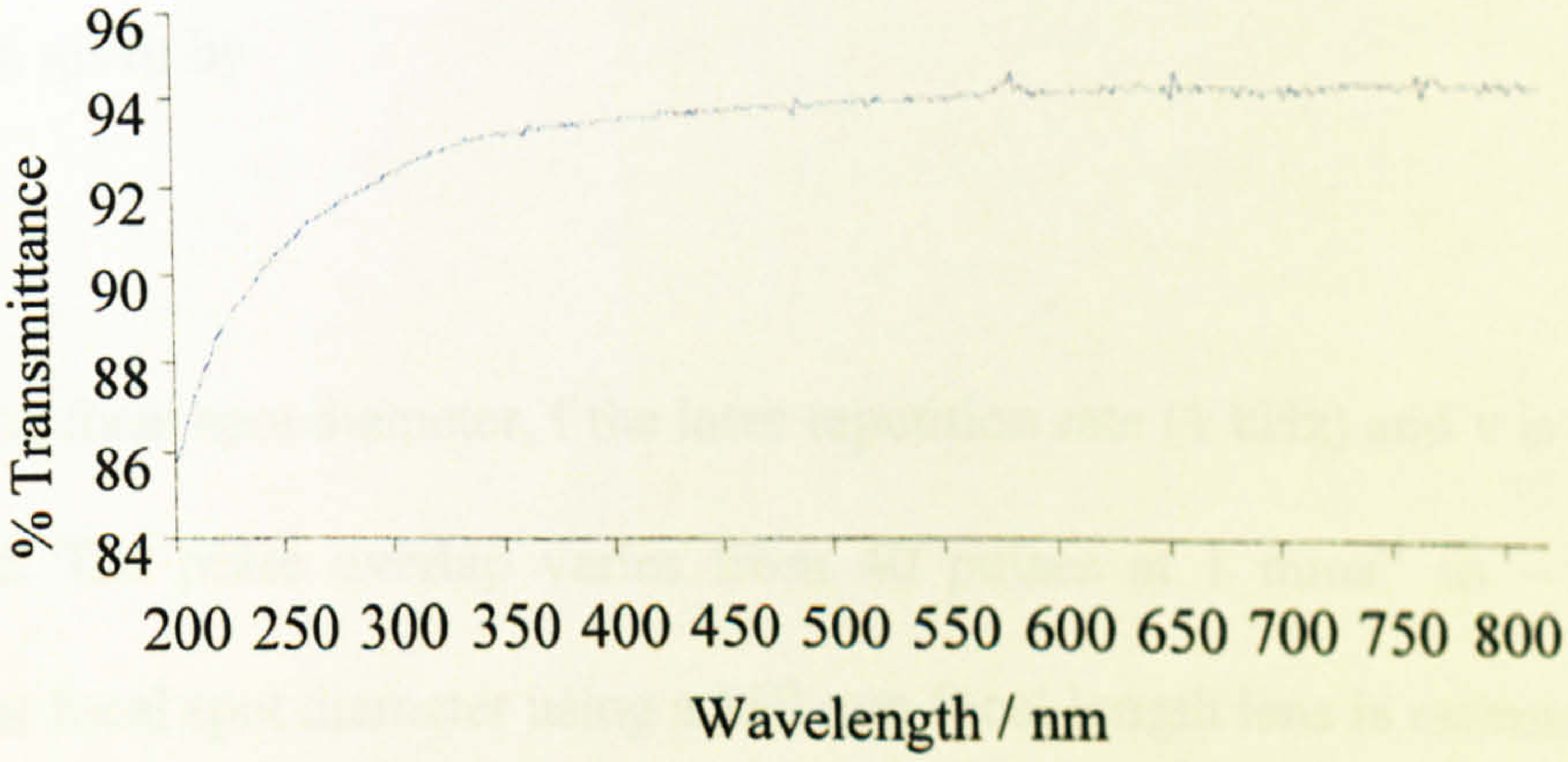

Fig. 4.1.1 Transmission Spectrum Of Spectrosil B.

Samples of Spectrosil B synthetic fused silica of 10 mm diameter, 6 mm thickness were ablated by scanning the sample through the focused laser beam at various stage velocities to produce a track. Typically the laser fluence was kept constant while varying the scan speed during an experiment, a track being produced for each scan speed. Fig. 4.1.2 shows how the track depth measured using a confocal microscope varied with scan speed for various incident fluences.

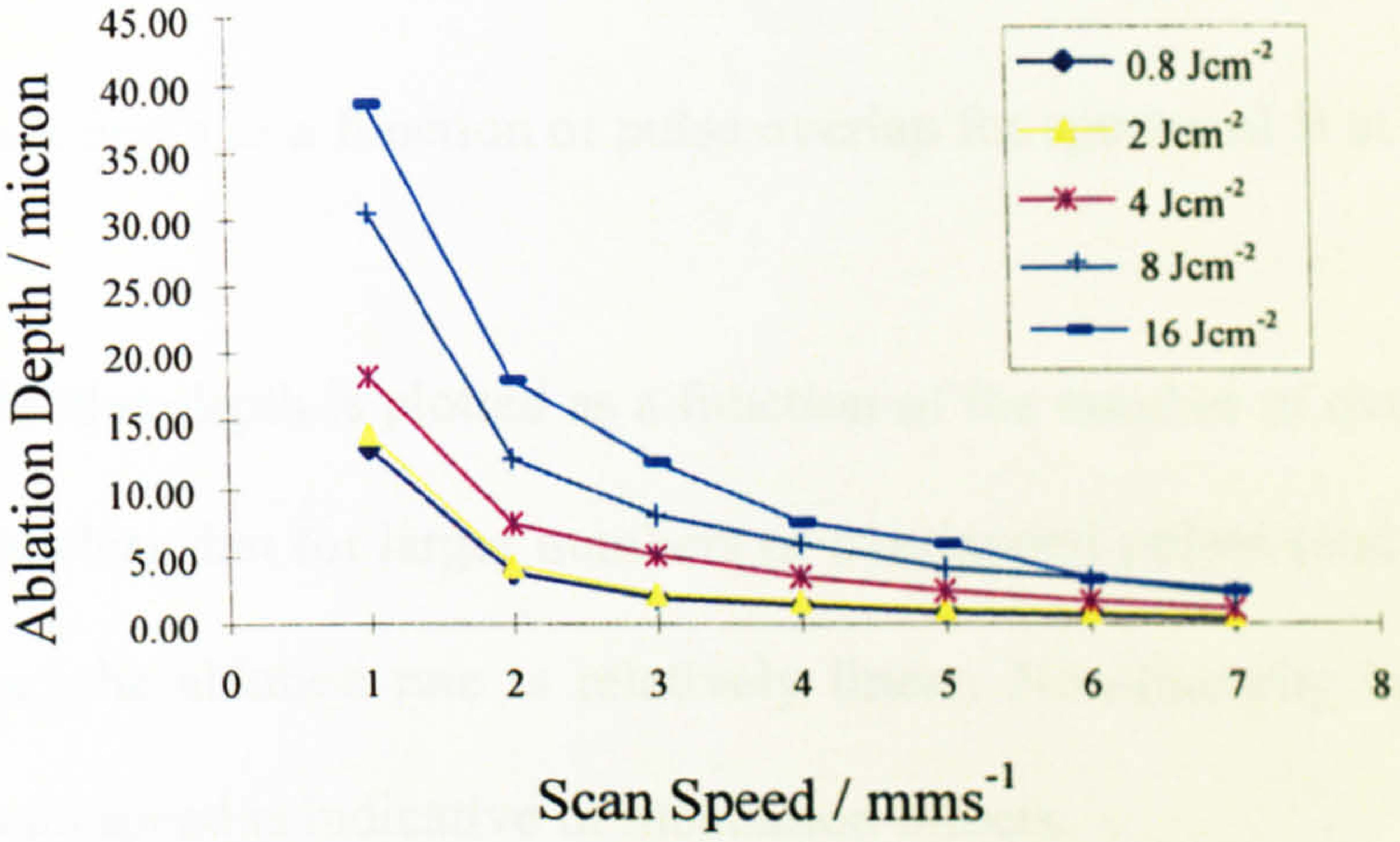

Fig. 4.1.2 Track depth as a function of scan speed for ablation of spectrosil B at various incident fluences.

Increasing scan speed corresponds to decreasing numbers of pulses overlapping at each point, given by

$$N = \frac{\phi f}{v} \qquad 4.1.1$$

where ϕ is the focal spot diameter, f the laser repetition rate (1 kHz) and v is the velocity of the stage. The pulse overlap varies from 40 pulses at 1 mms^{-1} to ~ 6 pulses at 7 mms^{-1}. The focal spot diameter using a 150 mm focal length lens is estimated from the ablated track width at high fluence and pulse overlap to be approximately 40 μm.

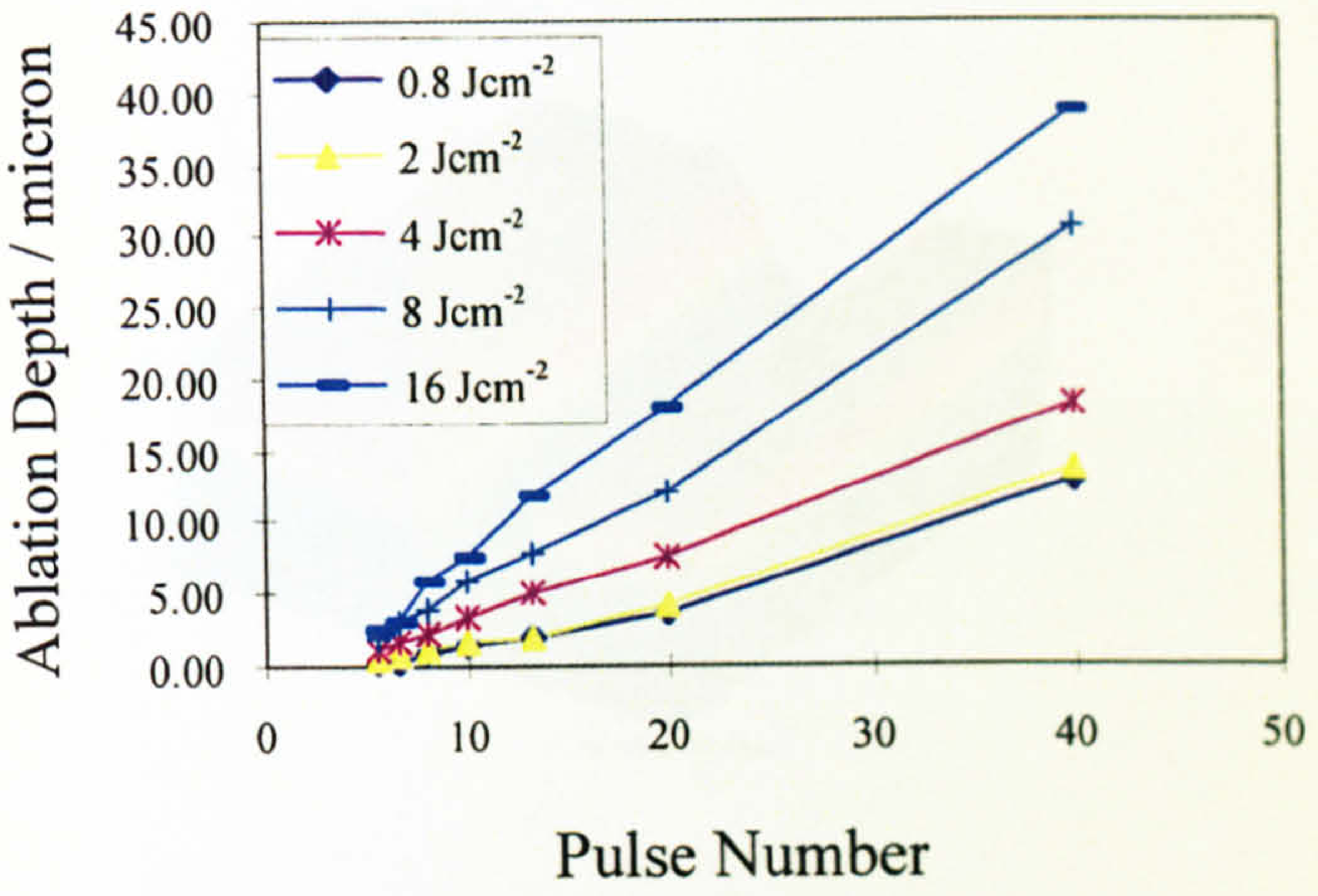

Fig. 4.1.3 Track depth as a function of pulse overlap for spectrosil B at various fluences.

The ablation depth is plotted as a function of the number of overlapped pulses in Fig. 4.1.3. It is clear that for larger numbers of overlapped pulses (and to a lesser extent higher fluence) the ablation rate is relatively linear. Non-linearity in the case of low fluence and scan speed is indicative of incubation effects.

A typical confocal microscope image is shown in fig. 4.1.4. The image can provide information on track depth, width and to a lesser degree residual surface roughness. Track cross-sections at fast scan speeds [low numbers of overlapped pulses] reflect the focused intensity profile and resemble an inverted Gaussian, as one would expect from the measured beam M^2 value (see section 2.1). However, ablation at higher fluences and with greater numbers of overlapped pulses results in more triangular cross-sectional geometries.

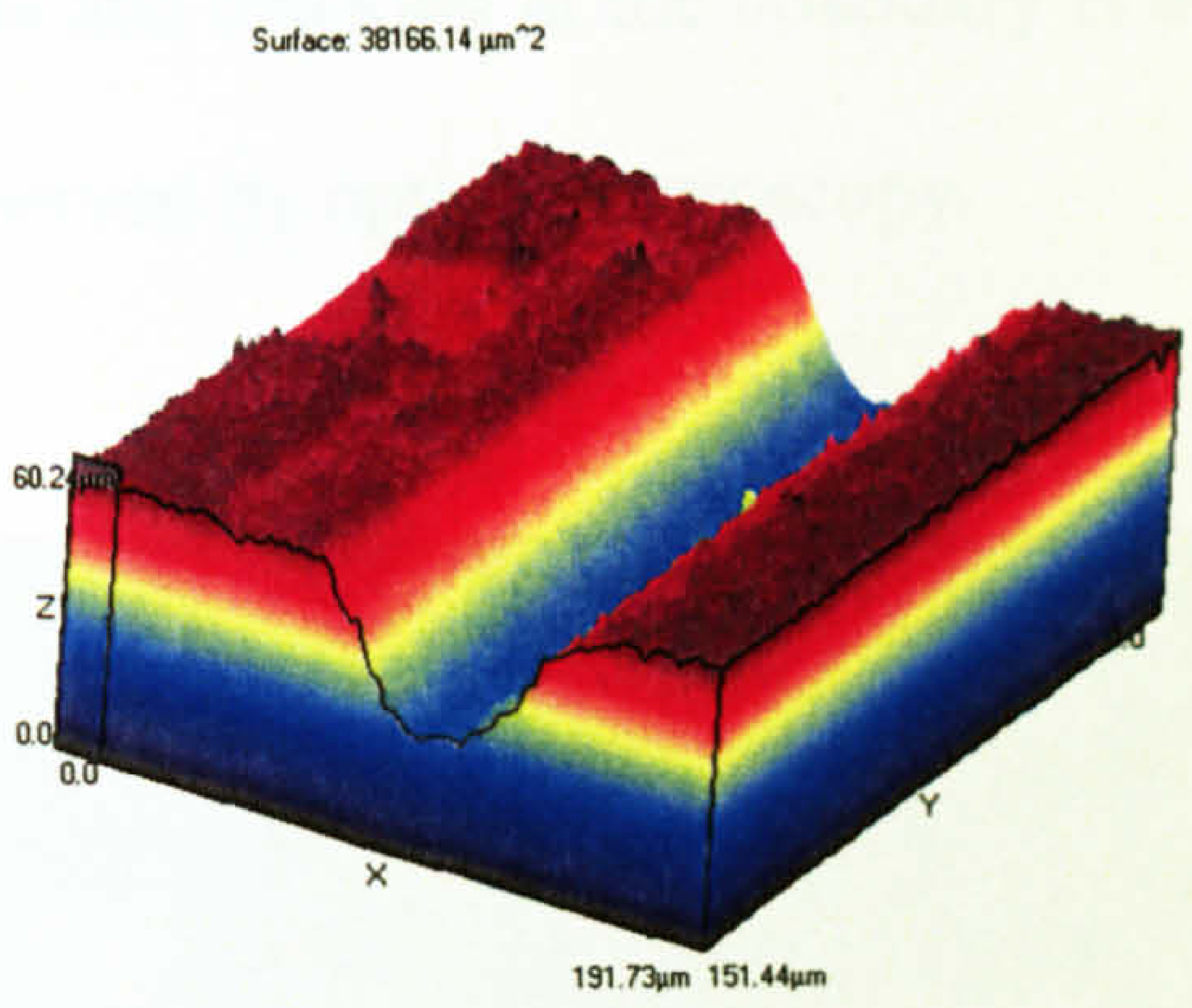

Fig. 4.1.4 Typical confocal microscope image of ablated fused silica at ~ 50 Jcm^{-2} and with a ~7 mms^{-1} Scan Velocity.

Analysis of ablated samples was primarily undertaken using optical microscopy. However, information regarding the residual microstructure was obtained by imaging in an environmental scanning electron microscope (ESEM, see section 2.3.2). Typical ESEM images of ablated fused silica are shown in fig. 4.1.5 for scan velocities of 1, 4 and 7 mms^{-1} at a fluence of ~ 4 Jcm^{-2} in air. Good contrast is obtained between the microstructure and the smooth surface of the glass due to charging at microstructural boundaries. However, track geometries cannot be inferred due to the large depth of field of the microscope. Clearly the area over which microstructure is observed increases with decreasing scan velocity (increasing pulse overlap). The microstructural features appear to be on the same scale (~ 1 µm) for all scan speeds, but appear to be distributed more homogeneously for the 1 mms^{-1} scan velocity. For both the 7 and 4 mms^{-1} velocities, the boundary between the microstructure and apparently unstructured glass substrate is not well defined and no particular orientation of the microstructure relative to the scan direction is observed. The 1 mms^{-1} scan shows good contrast between the microstructure and unstructured substrate and cracking at the boundary is evident (notably near the top of the micrograph) as observed by optical microscopy.

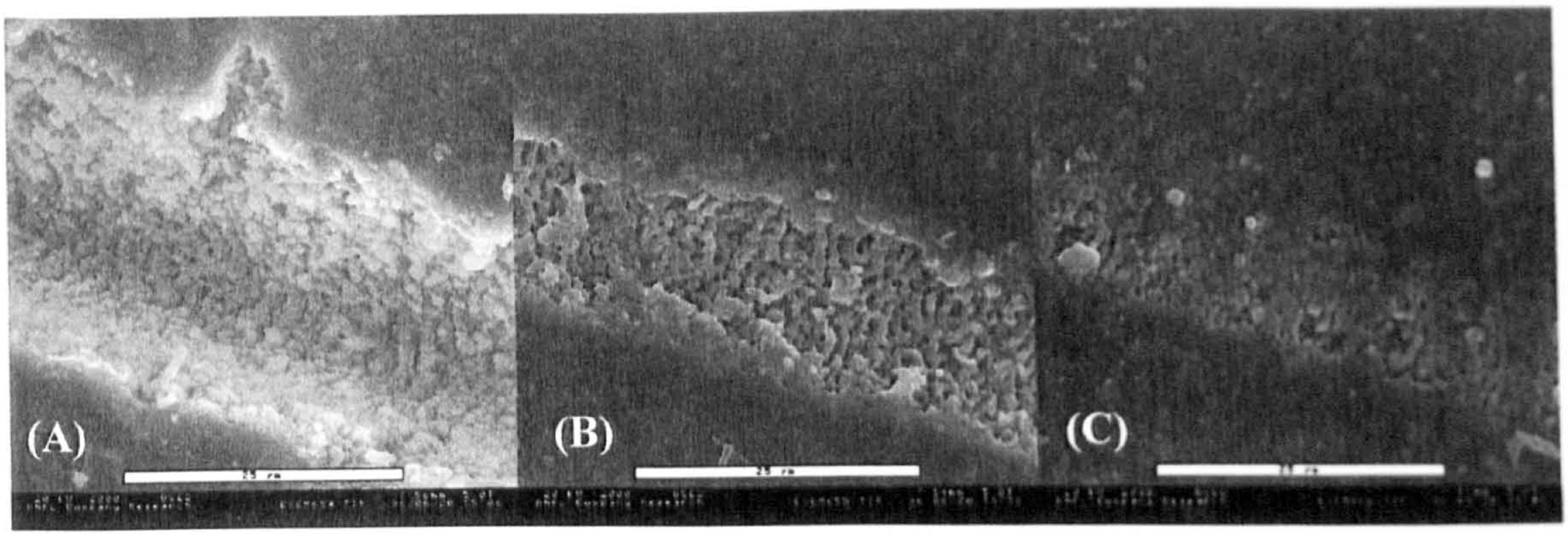

Fig. 4.1.5 ESEM image of fused silica ablated in air at 4 Jcm^{-2}.

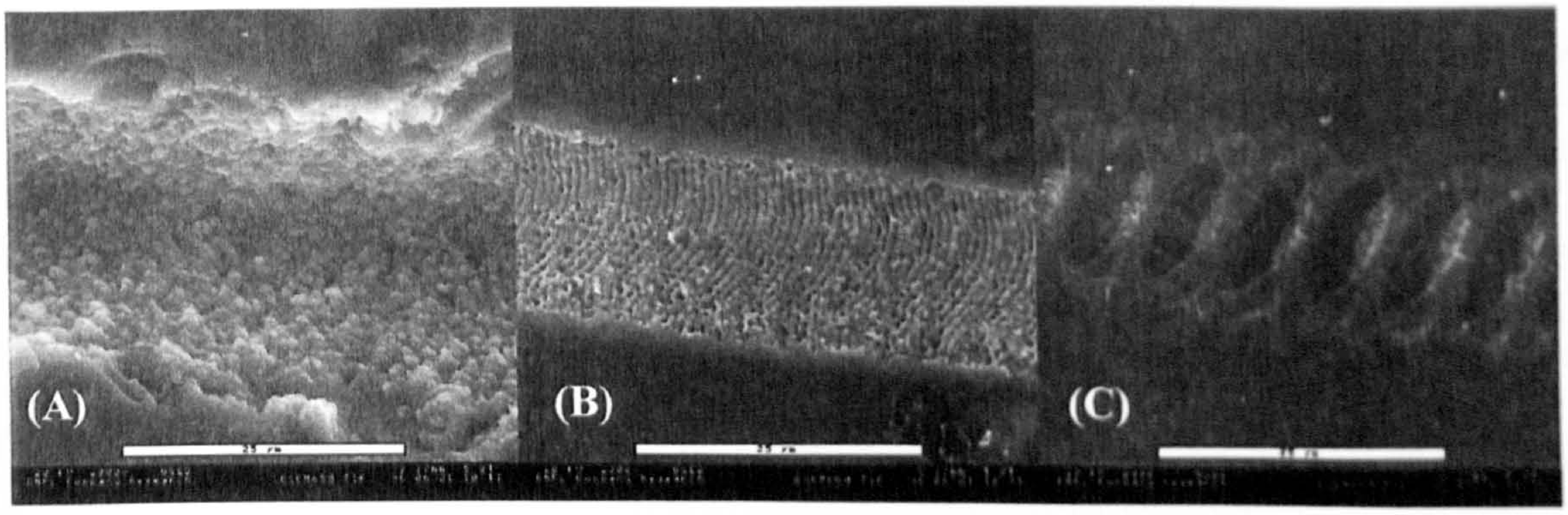

Fig. 4.1.6 ESEM Image Of Fused Silica Ablated In Vacuum at 4 Jcm^{-2}. (A) v = 1 mms^{-1}, (B) v = 4 mms^{-1}, (C) v = 7 mms^{-1}.

For direct comparison to fig 4.1.5, fig. 4.1.6 shows the residual microstructure after ablation in vacuum (2.4×10^{-2} mbar) at approximately the same fluence. The slow speed scan appears very similar to that ablated at ambient pressure, with evidence of edge cracking (perhaps even more evident). The images of the 7 and 4 mms^{-1} scans, however, are strikingly different to those seen at ambient pressure. The 4 mms^{-1} scan shows highly ordered microstructure, with a pitch of ~ 0.7 μm oriented in an arc perpendicular to the scan direction. The radius of curvature of the microstructure may correspond to the beam diameter (~ 40 μm) however, the pitch is much less than the pulse to pulse separation of ~ 4 μm. The boundary between the microstructure and the unstructured surface is also well defined in contrast to the ambient case. The scan at 7 mms^{-1} clearly illustrates the effect of incubation on the ablation rate. The microstructure is clearly confined to regions where higher integrated fluence has been deposited, other areas appear to have been altered but no microstructure is observed. The microstructured regions are separated by ~ 6.9 μm, approximately the scan velocity but much less than the width (~ 17 μm) of the altered surface. Both the tracks ablated in air and in vacuum show approximately Gaussian profiles as observed with both confocal and AFM microscopy, however the microstructures are clearly pressure dependent. The size of the microstructured features is clearly reduced at the lower pressure and we propose that this is due to a reduced solidified melt thickness for the low pressure case. In vacuum, the vaporisation temperature of the glass is reduced so that for a comparable fluence the ablation rate is higher. This means that although the penetration depth remains constant, a greater volume of material will be removed and so the remaining melt solidification depth will be reduced (in comparison to that at ambient pressure). In addition, this hypothesis may explain the presence of a well-defined boundary in the vacuum case. At ambient pressure, the dynamics of the vapour-liquid phase boundary are likely to be unstable and the vapour will transfer more heat to the liquid phase. In the partial vacuum, more energy will be removed from the surface by the vapour, due to the reduced vapour pressure. Further measurements of the pressure dependence on both ablated volume and the residual microstructure are required to confirm this hypothesis.

The appearance of microcracking at the track edges indicates the presence of high stresses in these regions. Under single scan conditions the microcracks tend to appear for scan speeds below 3 mms^{-1} and at higher fluence. However, samples subjected to multiple overscans have been observed to suffer the same problem. Kruger and Kautek[1] have suggested that this is due to shock abrasion of the material by the rapidly expanding glass vapour and the appearance of these cracks are shown to be dependent on both fluence and pulse number.

In order to minimise edge cracking a milling technique was developed, where by the required width and depth for a given device could be ablated using a series of raster patterns overwritten on the sample. Initially, a series of lines (n) were written with a separation of approximately 10 μm at 5 mms^{-1} (fluence ~ 4 Jcm^{-2}) to give the required width. A second "layer" of (n-1) lines was then ablated, offset by 5 μm from the initial raster pattern. Subsequent "layers" were then ablated to provide the required depth and track geometry. The technique is illustrated in a series of confocal images in Fig. 4.1.7. The pictures correspond to increasing numbers of "layers". A cross-section of a track milled to required dimensions in fused silica and sectioned using a diamond saw is given in Fig. 4.1.8(a & b). The result is a high quality track with smooth edges and no cracking. The residual microstructure is also significantly reduced in scale and the surface roughness is < 1 μm rms (measured using a Talysurf surface profiler).

Fig. 4.1.7 A series of confocal images illustrating the laser milling technique.

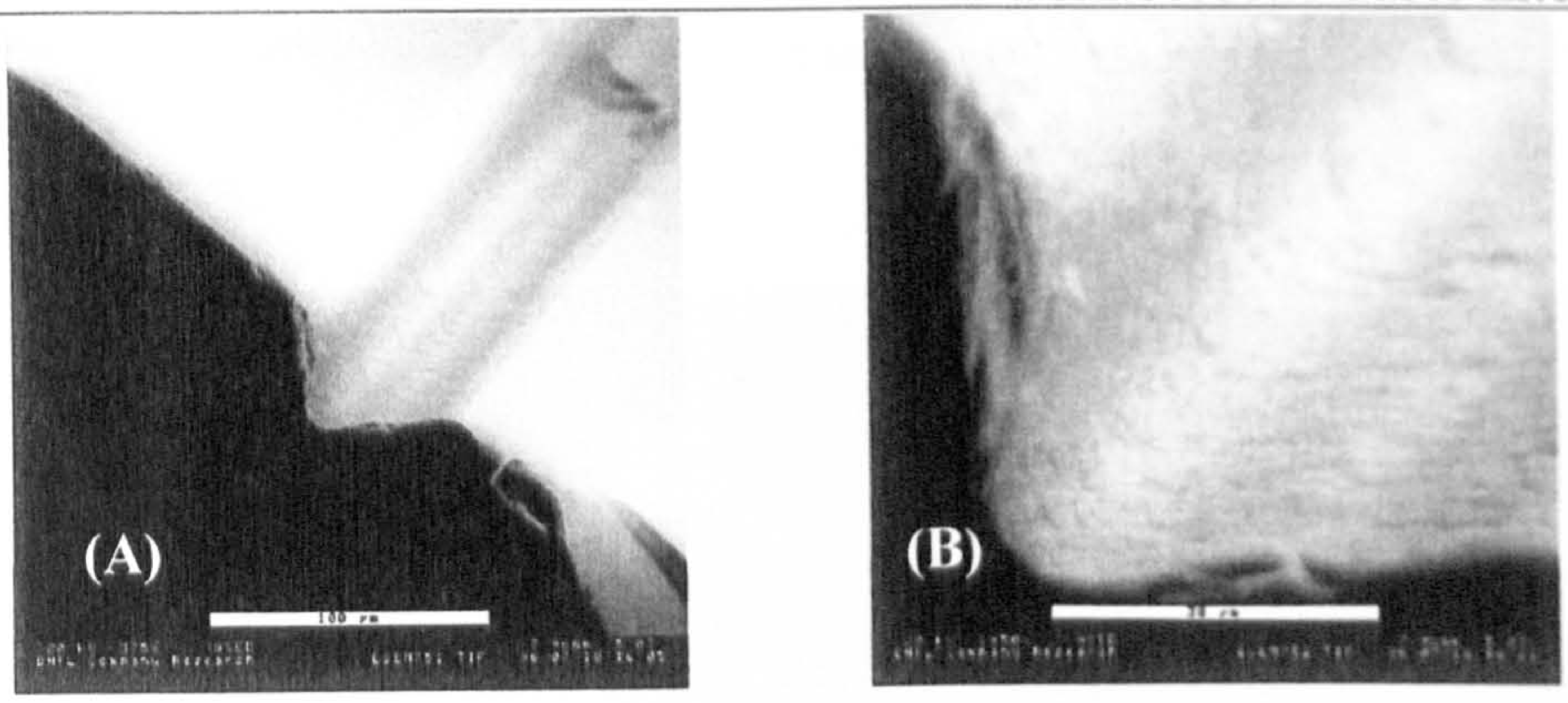

Fig. 4.1.8 ESEM image of laser milled fused silica,
(A) 375 × magnification, (B) 1450 × magnification.

Pyrex 7070

Studies of Pyrex 7070 Borosilicate glass have been undertaken and show some similarities to fused silica ablation. Fig. 4.1.9 shows the depth of the ablated track as a function of scan speed and incident laser fluence. We see similar behaviour to that of fused silica ablation as we would expect, but Pyrex exhibits a reduced incubation effect, supporting the findings of Kruger and Kautek[1]

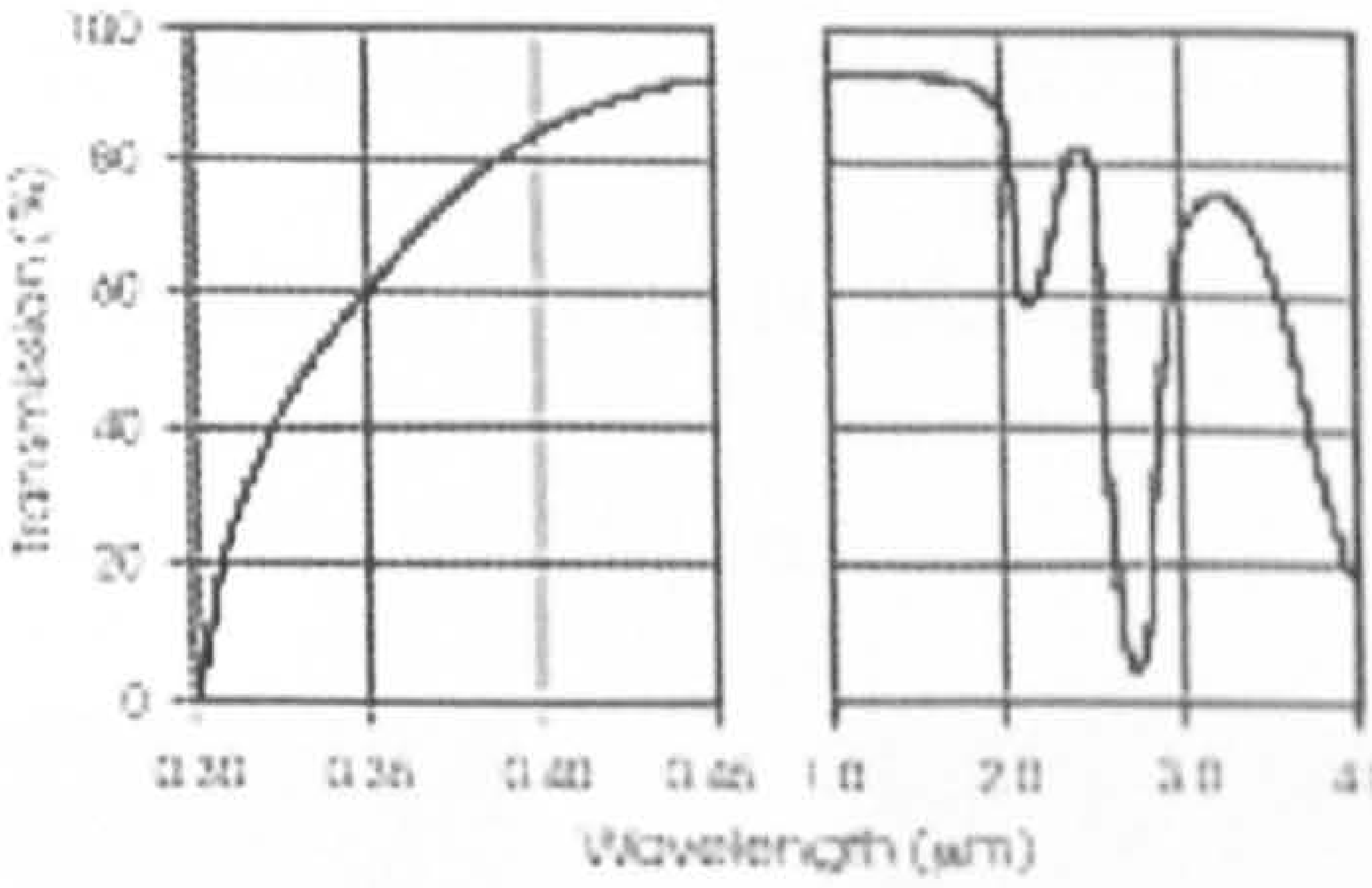

Fig. 4.1.9 Transmission Spectrum Of Pyrex 7070.

ESEM images of Pyrex ablated at 4 Jcm^{-2} are given in Fig. 4.1.10 for direct comparison with the fused silica results (Fig. 4.1.5). The residual microstructure shows a similarity to that shown for fused silica, but we see a well-defined boundary between the structured and unstructured substrate in the Pyrex case (as indeed we did for fused silica ablated in vacuum).

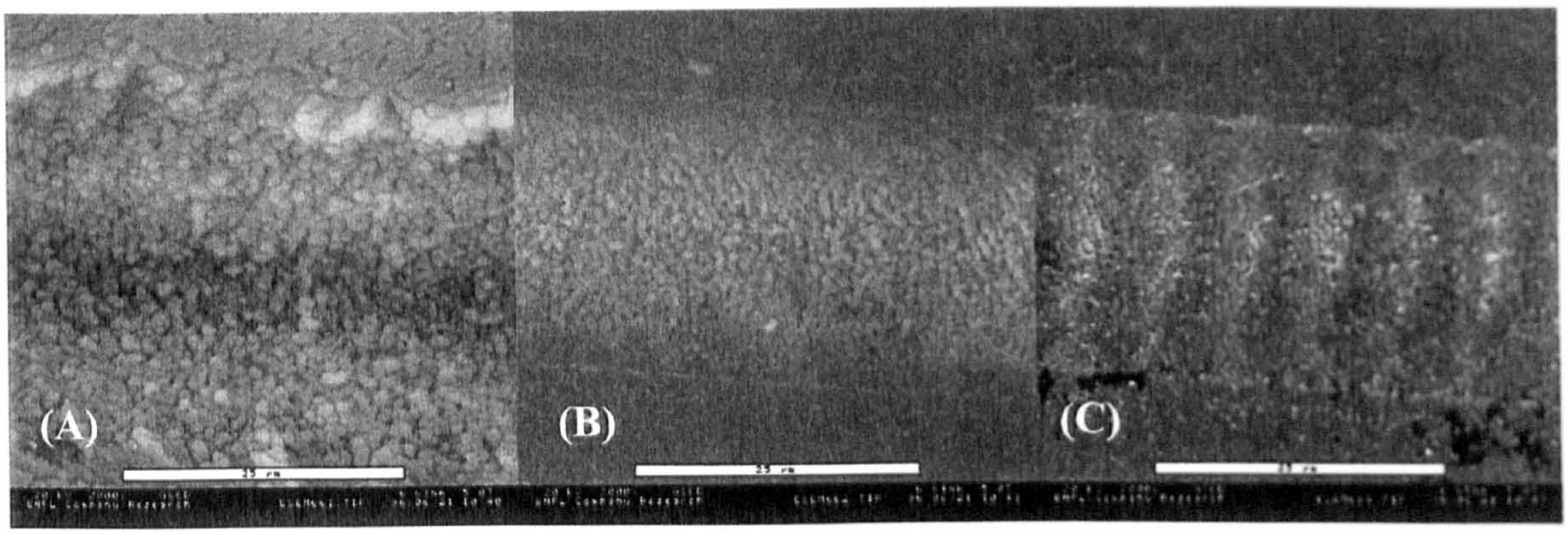

Fig. 4.1.10 ESEM images of laser ablation of Pyrex 7070 in air at 4 Jcm^{-2}.

(A) v = 1 mms^{-1}, (B) v = 4 mms^{-1}, (C) v = 7 mms^{-1}.

The problem of microcracking still occurs in Pyrex, as we can see from the 1 mms^{-1} scan in Fig. 4.1.10. However, the scale of the damage is less pronounced, which we expect, for a material with better thermal qualities than fused silica. Microstructuring by laser milling (as described above) has been shown to be effective in reducing edge cracking and an example of a milled track is given in Fig. 4.1.11. We see no apparent edge cracking, and similar residual surface morphologies (as for the single scan case), with features of the order of 0.5 μm.

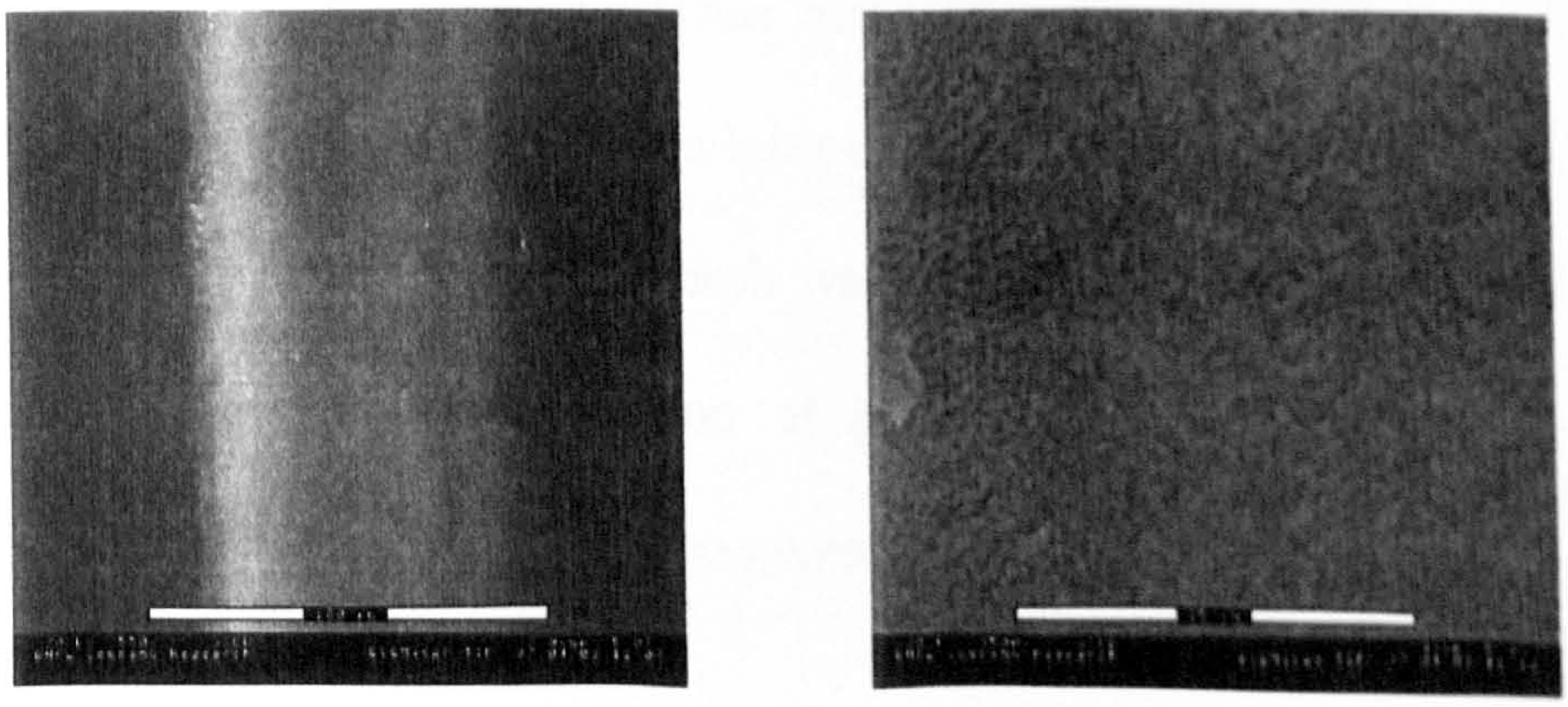

Fig. 4.1.11 ESEM Image Of Laser Milled Pyrex (4 Jcm^{-2}).

4.1.2 Semiconductors

The interaction of ultrashort pulses with semiconductors has been of significant interest to the scientific community for some years, as we have already seen in section 1.5.2. We have looked in detail at the ablation of silicon for the microstructuring of chemical microdevices and make direct comparisons with the ablation of gallium arsenide (GaAs).

p-type Silicon

The ablation threshold for silicon has been measured[2] to be of the order of 0.2 Jcm^{-2} at 610 nm; similar to that of metals (Au ~0.3 Jcm^{-2}). The primary absorption process for visible laser processing is by single photon absorption (silicon has an in-direct bandgap of ~ 1.12 eV at 300 K). However, the high intensities generated by ultrashort pulses may also lead to multiphoton absorption to the direct bandgap of 4 eV. The absorption spectrum for silicon is given below in Fig. 4.1.12.

Ablation of p-type silicon (boron doped to 1 part in 10^4) oriented with the 100 plane parallel to the substrate surface has been undertaken at 790 and 395 nm (the fundamental and second harmonic of the laser system respectively). Qualitative analysis shows that whilst ablation occurs for both wavelengths the microstructural properties are remarkably different. A comparison of ablation at 790 nm for 170 fs pulses, picosecond and nanosecond pulses is also given.

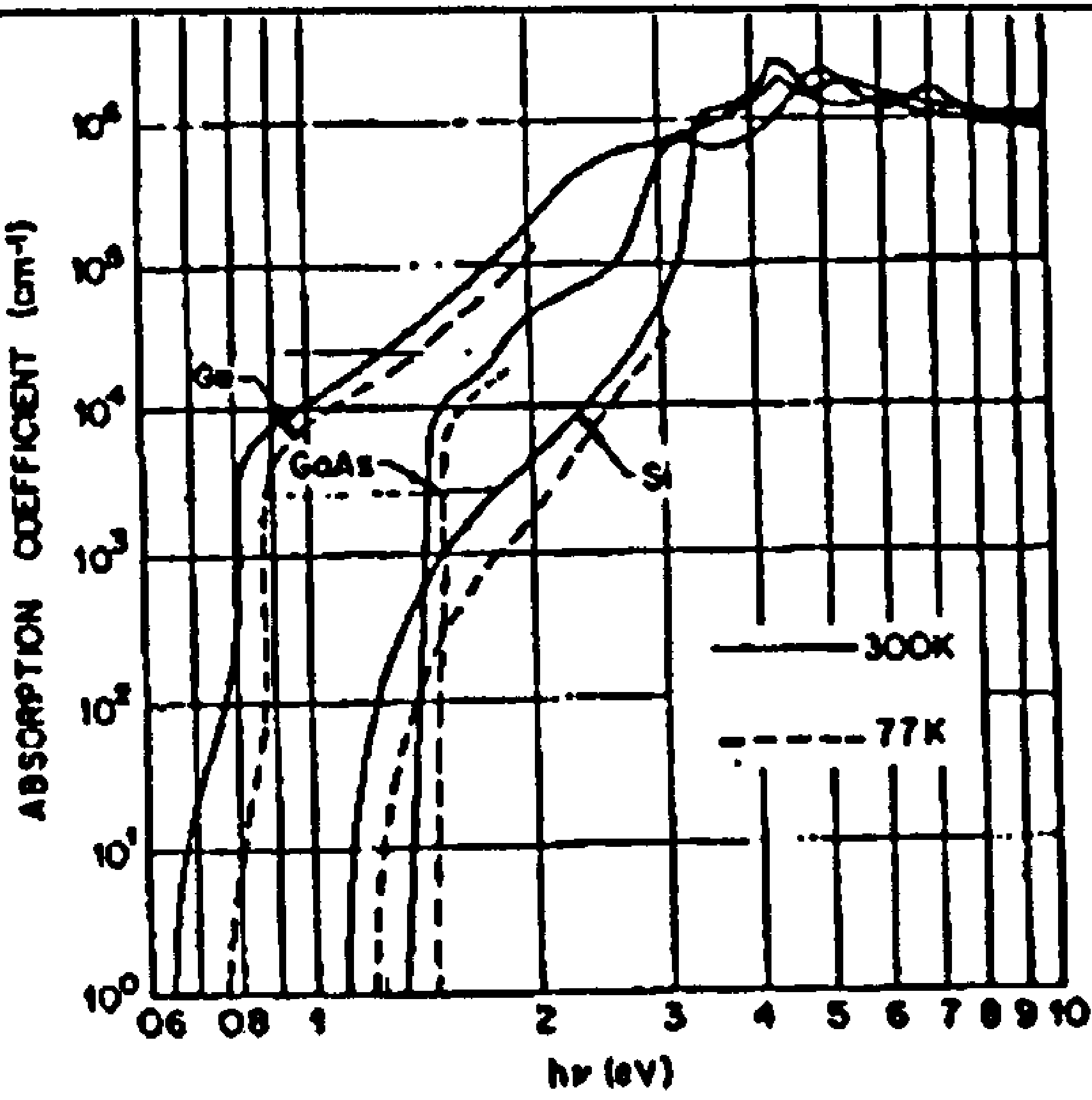

Fig. 4.1.12 Absorption spectrum of silicon and gallium arsenide at room temperature (reproduced From reference[3]).

Fig. 4.1.13 shows a graph of ablation rate vs incident laser fluence for tracks ablated on silicon using the scanning galvo system at a speed of 10 mms^{-1}. Laser fluence was calculated by assuming a beam diameter of 100 μm, which is consistent with the maximum ablated beam diameter given on the second y-axis of Fig. 4.1.13. Clearly the trend does not conform to the expected Beer-Lambert behaviour. We suggest that this is due to an increase in the intensity dependent absorption in the silicon substrate reducing the absorption depth. The ablation rate is clearly at odds with the linear absorption coefficient at this wavelength (~ 4 × 10^3 cm^{-1}), which implies an ablation rate per pulse of ~ 2.5 μm. The result contrasts with work by Ilhemann et al[4] at 248 nm (500 fs) which showed typical Beer-Lambert behaviour and Krüger and Kautek[2] at 612 nm (300 fs) who reported non-linear behaviour which deviated from the Beer-Lambert law but which could be fitted to a model incorporating an intensity dependent absorption coefficient (given by $\alpha = \alpha_1 + \alpha_2.I$). The ablation rate per pulse also contrasts with the rate quoted for 612 nm ablation at 1 J cm^{-2} of approximately 40 nm / pulse averaged for

1000 laser pulses. This may indeed be a consequence of a change in absorption coefficient, however a result given below for 500 overlapped pulses at 50 μJ shows a significant reduction in ablation rate compared to the 10 pulse case given in Fig. 4.1.13.

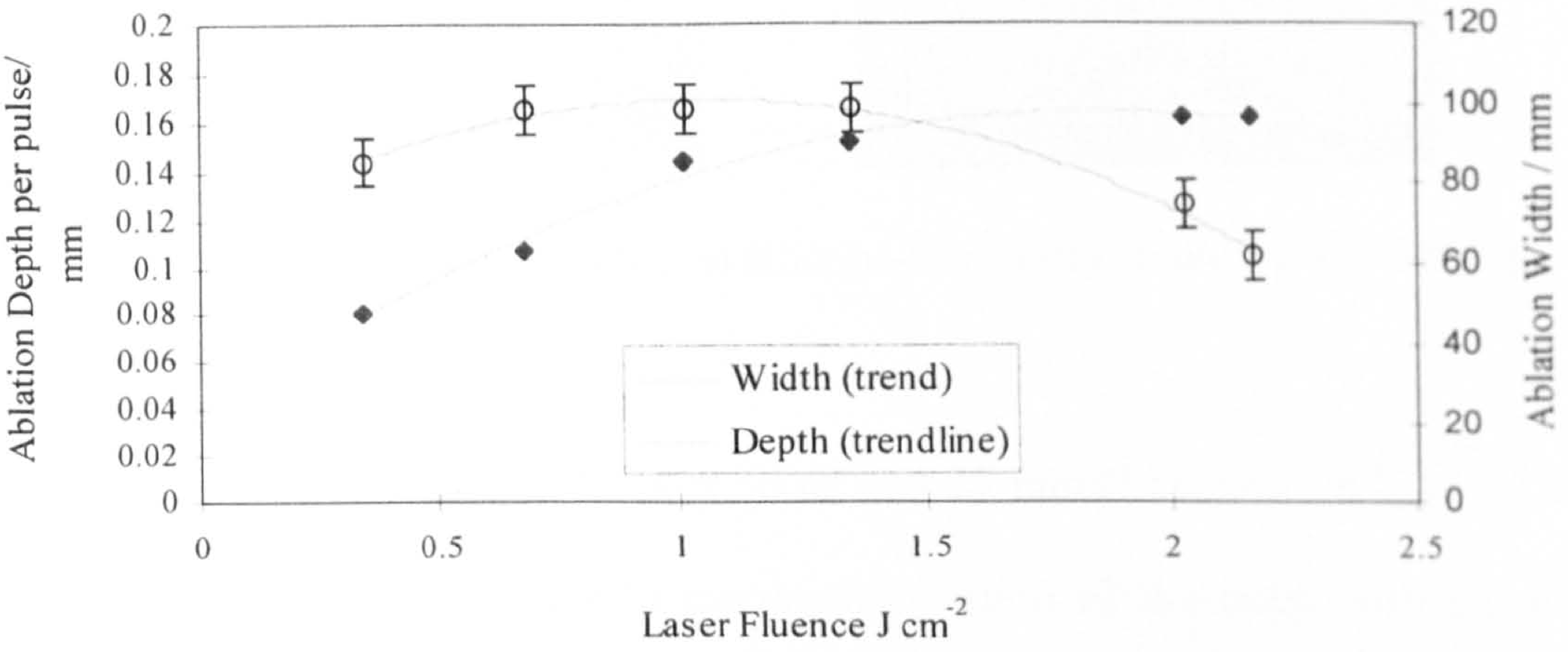

Fig 4.1.13 Ablation rate as a function of laser fluence for silicon ablated at 790 nm (a polynomial fit is given as an aid to the eye).

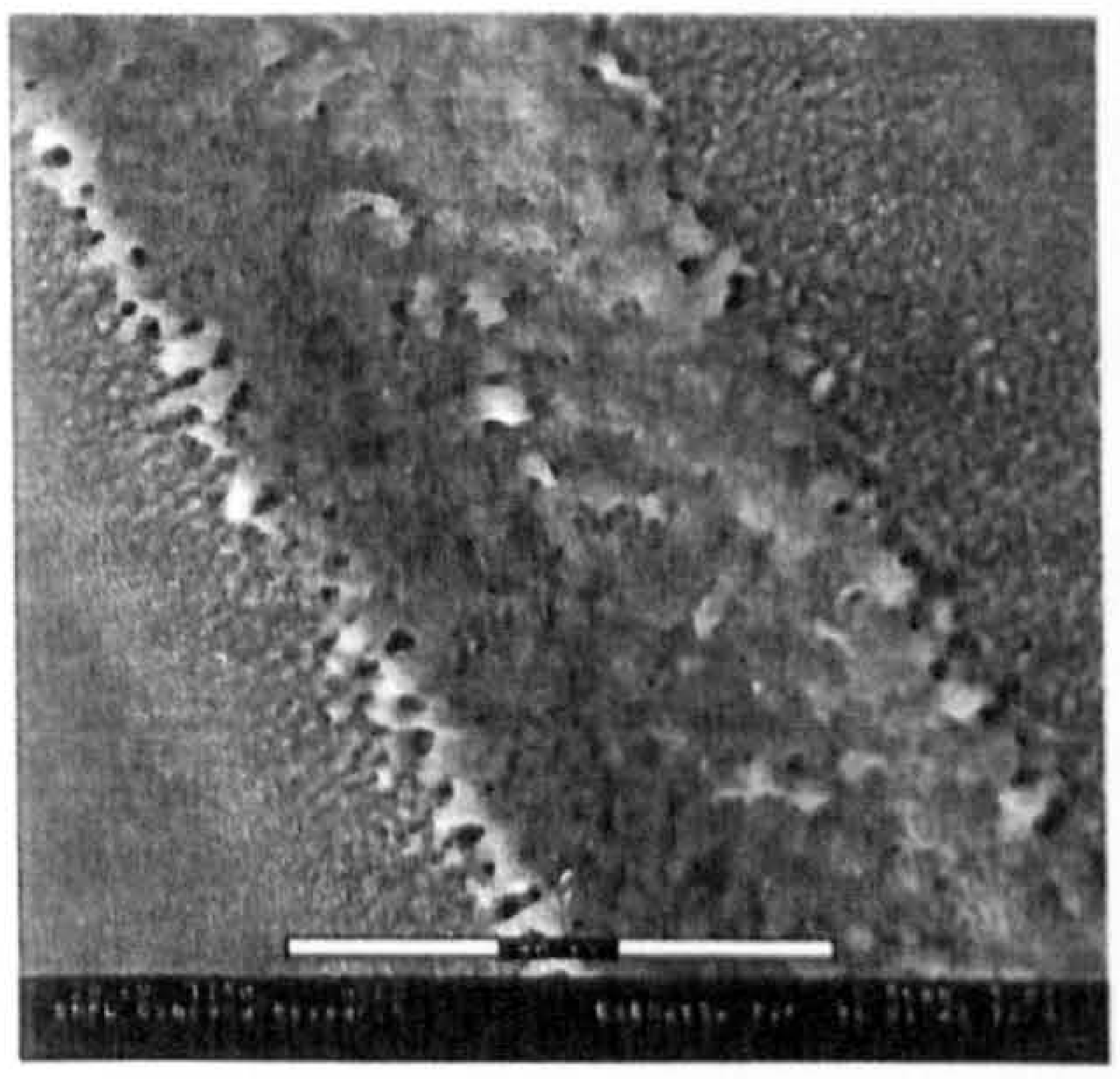

Fig. 4.1.14 ESEM image of ablated silicon at 50 μJ (F~0.6 Jcm^{-2}).

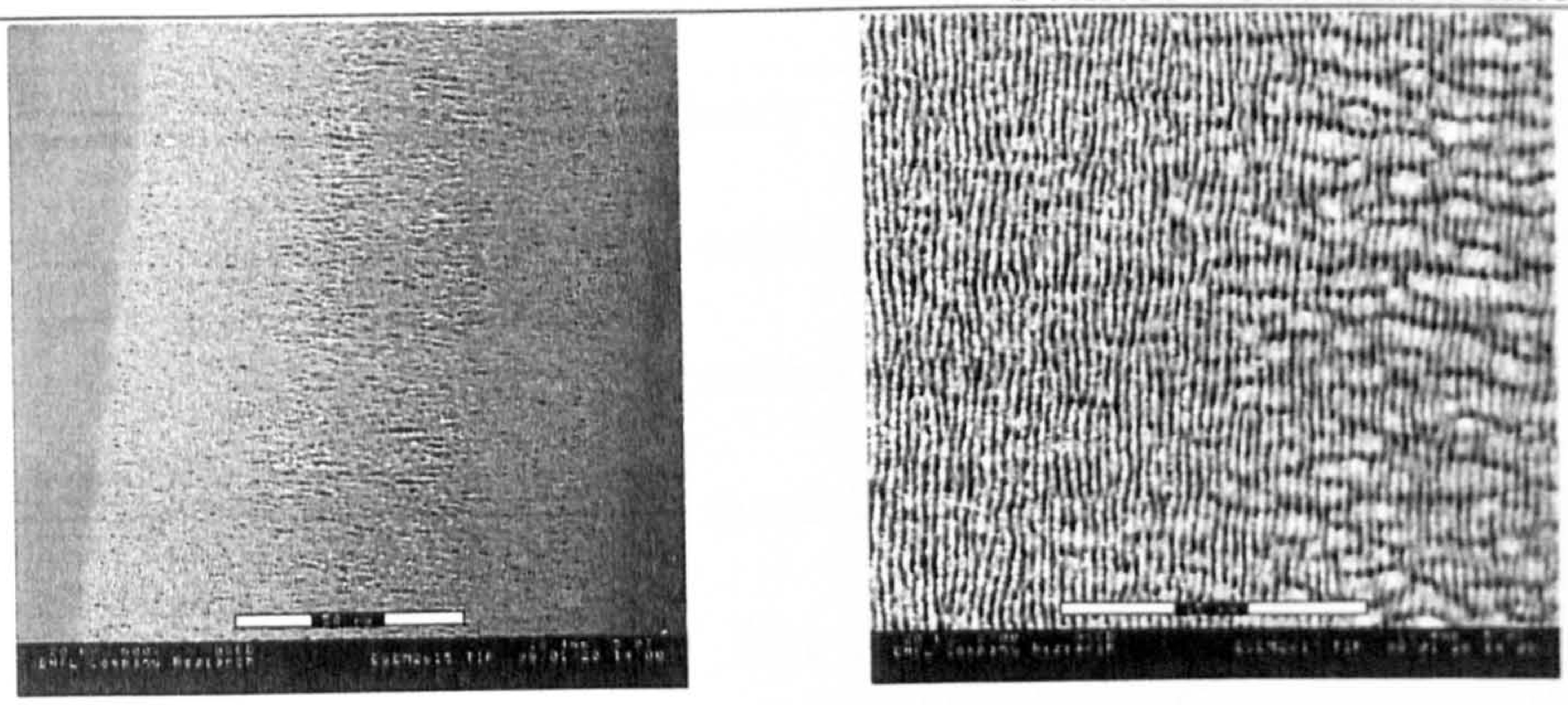

Fig. 4.1.15 ESEM image of ablated silicon ~ threshold fluence (~0.2 Jcm^{-1}).

An example of silicon ablated at 50 μJ and 10 mms^{-1} is given in Fig. 4.1.14. A re-solidified melt layer is evident in the central portion of the track with an uneven boundary between this region and a second microstructured region, which displays 0.5 μm periodicity parallel to the scan direction. Comparison with a further scan at near threshold fluence, in Fig. 4.1.15, show the same microstructure in the wings of the intensity profile, but not the apparent melting in the central, high intensity region of the track. Here, we suggest, is qualitative evidence of a transition from an ablation regime dominated by non-linear interactions (low fluence, high intensity) to that of a regime with a significant linear contribution (high fluence, high intensity). This is supported by the presence of the fine rippled microstructure in the wings of both images, and the presence of such a rippled structure in the central part of the low fluence case. A higher magnification image (also shown in fig 4.1.15) shows the transition region between the wings and central portion. It is evident that the parallel ripple structure continues into the central region, but a lower frequency ripple is present perpendicular to it. The presence of a perpendicular ripple structure cannot be attributed to the scan speed (pulse separation at 10 mm s^{-1} with a beam diameter of ~100 μm is ~10 μm). Previous work has suggested that the periodic microstructures in dielectric materials could be attributed to stress relaxation. However, this is clearly not the case in crystalline silicon, which should have a depth independent stress vector (i.e. stress dependent microstructure will be independent of ablation depth in crystalline materials). Work by Von der Linde and Saurbrey[5] on time resolved melting of metallic materials (and indeed earlier work on semiconductors) show the presence of time dependent ripple structures, which they attribute, not to acoustic surface waves in the melt pool, but Newton's rings formed by interference between the beams reflected from the solid-melt surface and the melt-vacuum interface. It is possible that such an interference effect might lead to areas of higher intensity at the liquid-vapour boundary in the ablative regime, and that the periodicity of such interference would be dependent on the melt depth and hence the intensity (in the non-linear regime). Clearly, more rigorous experimental and theoretical study is required in this area to elucidate the processes behind the development of this residual microstructure.

Multiple overscans of a track (shown in Fig. 4.1.16) revealed microstructure similar to that observed by Kruger and Kautek[2]. We also observe (as mentioned above) a pronounced reduction in ablation rate from 0.158 to 0.033 μm / pulse at 50 μJ for one (10 pulses) and fifty (500 pulses) overscans respectively. A reduction of this magnitude may be accounted for by the geometries of the ablation sites, which show very steep side walls and very pronounced residual microstructure. Measurement of the residual depth surface roughness gives a value of ~ 5.85 μm with some features with dimensions approaching 10 μm in dimensions. Clearly target dimensions of 50 - 100 μm with residual roughness of the order of 1 μm are not achievable using femtosecond near IR pulses without employing another technique.

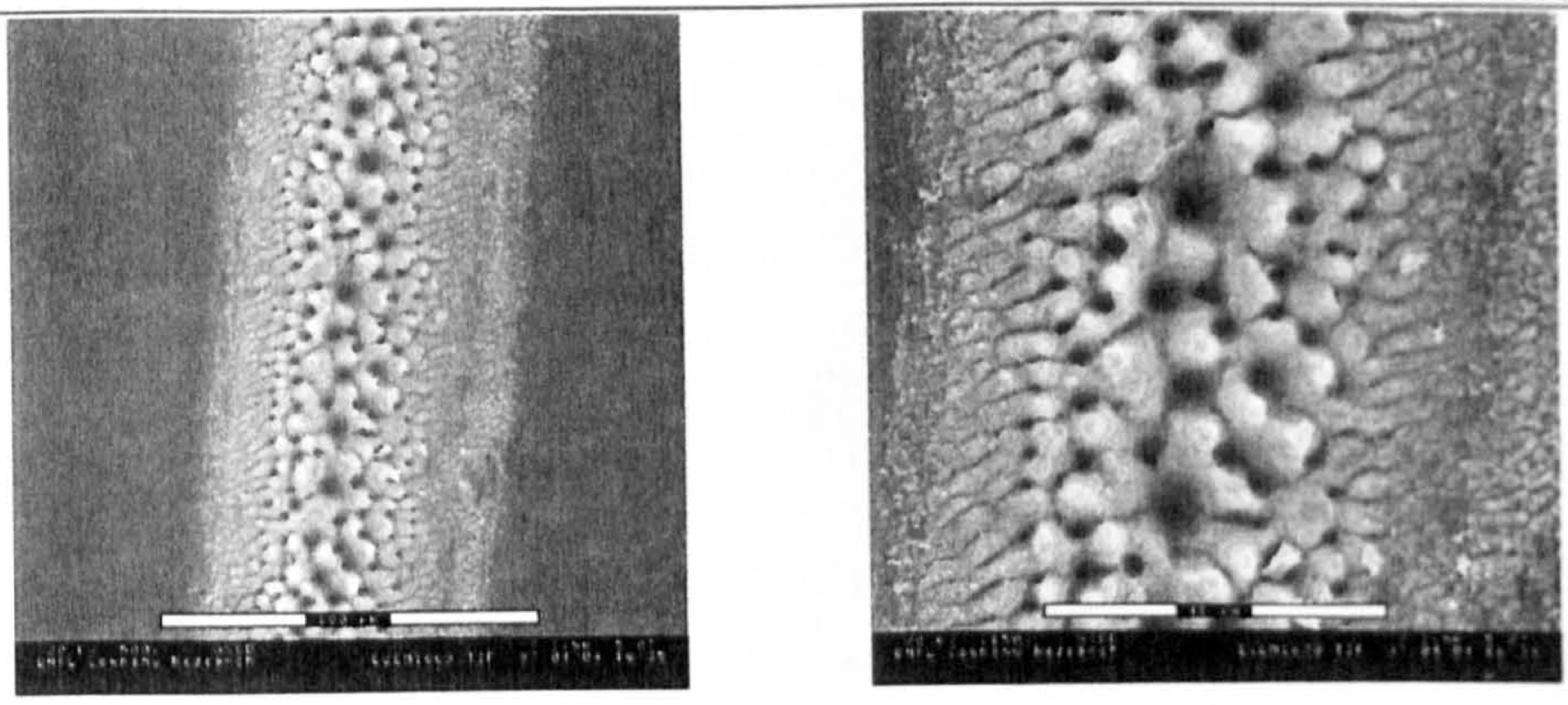

Fig. 4.1.16 ESEM images of silicon ablated at 50 μJ (F~ 0.6 Jcm^{-2}, λ= 790 nm) overscanned 50 times (~ 500 pulses).

In order to make direct comparisons with picosecond and nanosecond laser ablation, silicon was ablated using the uncompressed output from the regenerative amplifier at 300 ps and the 50 ns output of the regenerative amplifier without injection seeding. In both cases the laser beam mode is of better quality than observed for the femtosecond pulses and a spot size of ~ 20 μm is observed. Ablation at 50 ns and with an energy of 230 μJ/pulse (fluence ~ 73 Jcm^{-2}) is shown in Fig. 4.1.17. We clearly see the demarcation between each laser shot by a bar of expelled melt with a separation of approximately 7 μm corresponding to the scan speed (even though 10 overscans were used to make this track). We also observe an area to each side of the track extending the track width to ~ 40 μm, which is disrupted due to the interaction of a thick melt layer with the plasma and vapour phases. This corresponds to a heat affected zone of ~ 10 μm, which is compatible with that determined from the heat diffusion equation.

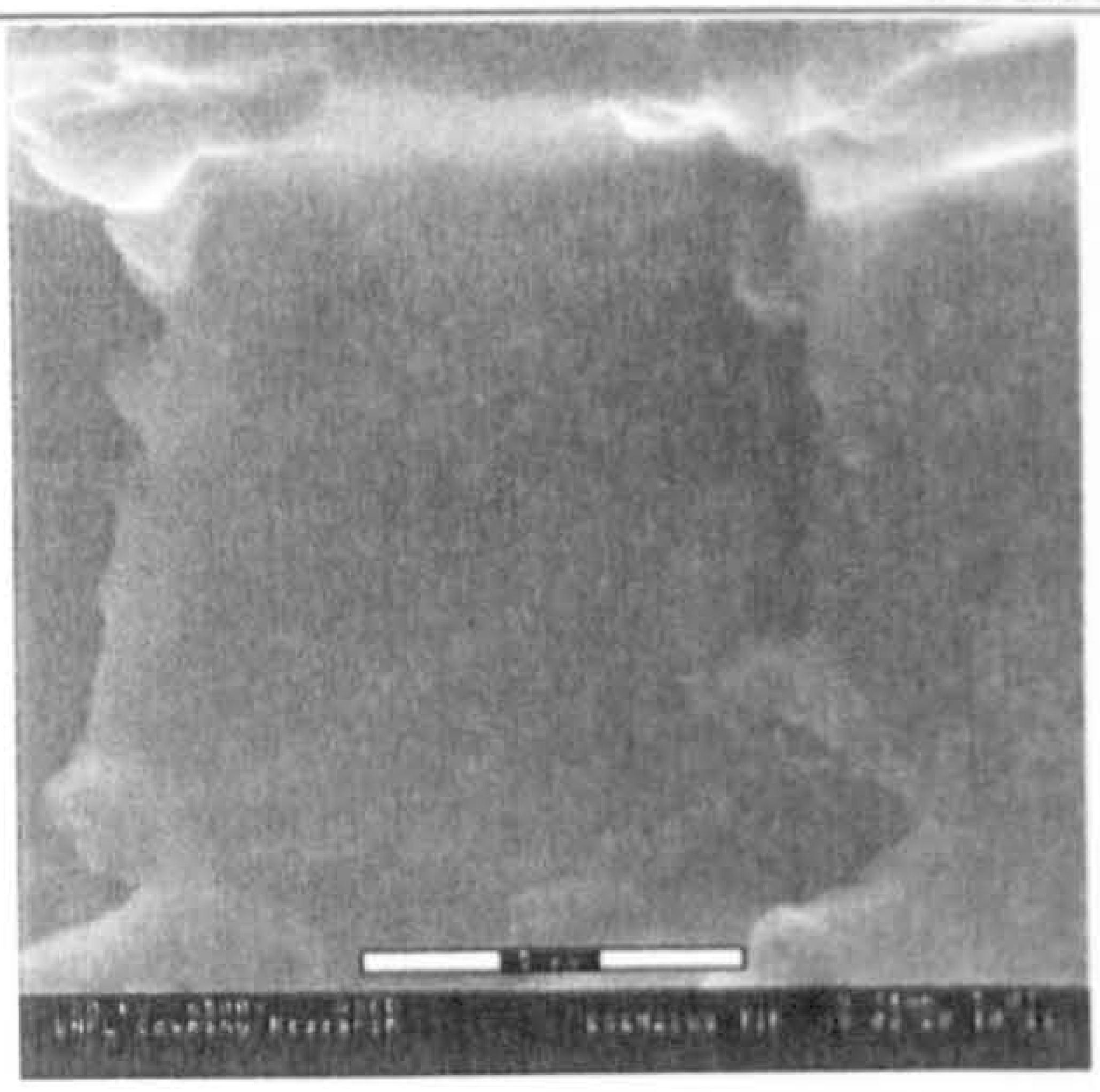

Fig. 4.1.17 ESEM image of silicon ablated with 50 ns pulses at ~ 73 Jcm^{-2} (800 nm).

Fig. 4.1.18 Shows 300 ps laser ablation of silicon at ~ 73 Jcm^{-2} overscanned 10 times. The residual surface features are similar to those shown for ablation with 50 ns pulses. However, the microstructure is more complex with melt ridges from previous scans observed suggesting a thinner melt depth and heat affected zone. Whilst the track appears broader (~ 46 μm), it is more well defined than the ns case and this might be attributed to a reduction in mode quality due to injection seeding. In any case, the disrupted surface observed for 50 ns pulses is not observed here and we attribute this to a reduction in both the heat affected zone [HAZ = $(k\tau)^{-0.5}$] and plasma shielding and therefore more efficient energy coupling into the silicon. The track produced from femtosecond pulses, in comparison, is broader due to the increased spot size (increased M^2) but we do not observe the large melt features and splashing associated with longer pulses. Calculated heat affected zones from equation 1.5.2 in Section 1.5 are given in Table 4.1.1.

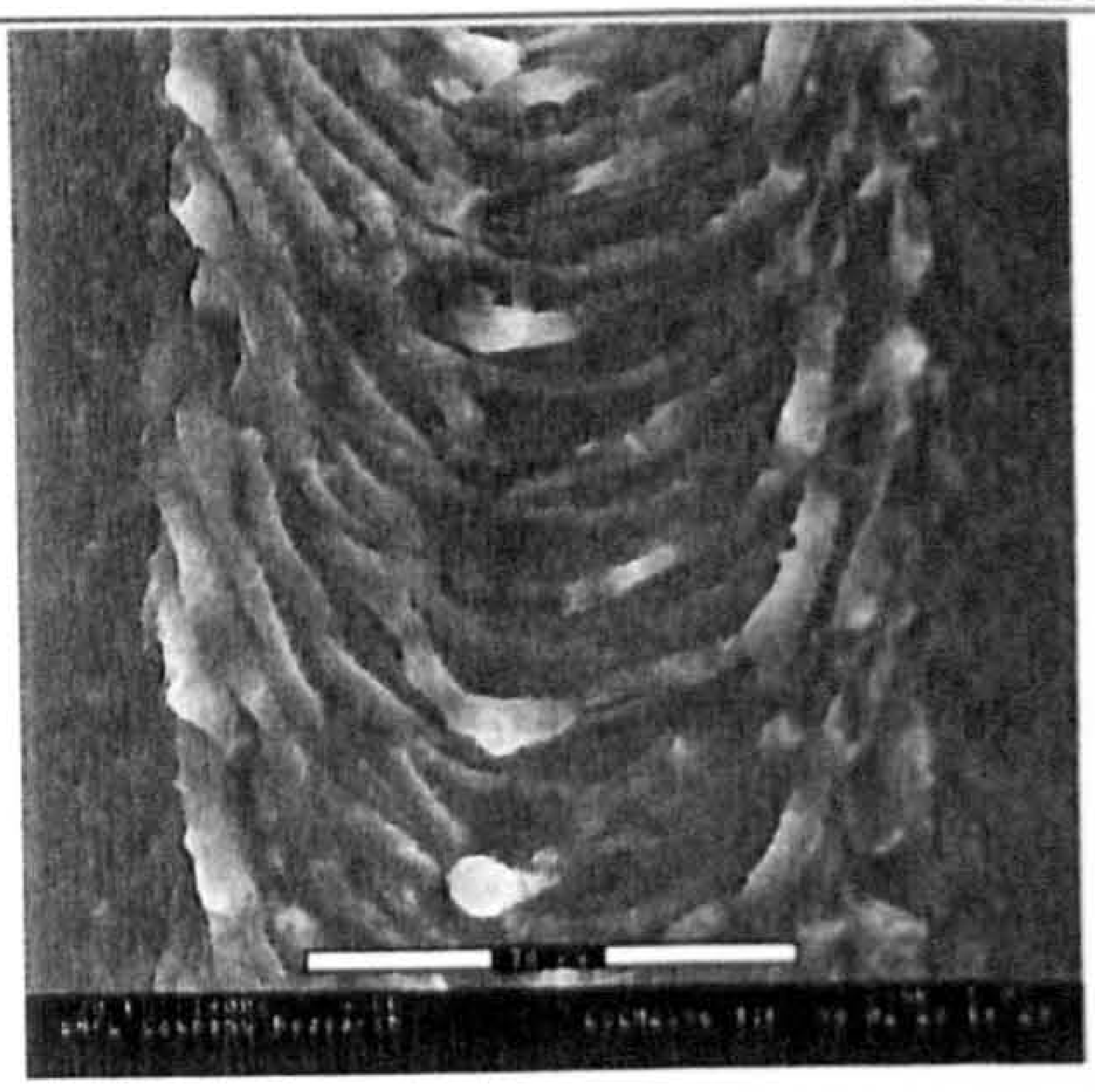

Fig. 4.1.18 ESEM image of silicon ablated with 300 ps pulses at ~73 Jcm^{-2}.

Table 4.1.1 Calculated heat affected zones for silicon and GaAs

Material	Thermal Diffusivity (cm^{2}s^{-1})	Absorption Depth (nm)		HAZ For Pulse Width (nm)		
		790 nm	395 nm	170 fs	300 ps	30 ns
Silicon	0.9	2500	12.5	4	164	1640
GaAs	0.24	250	20	2	85	850

The success of employing laser milling techniques to the ablation of fused silica led us to try the same process with silicon. This technique allows us to create a pseudo flat topped track profile, determined by the integral of the fluence impinging the surface. Ablation at low fluence ensured that large amplitude variations in the ablated surface were minimised throughout the ablation process, leading to uniform ablation across the track profile. An example of a track ablated using the milling technique is given in Fig. 4.1.19. Note that the microstructure is much reduced as compared to the case of a single track. Fig. 4.1.20 shows the ablated depth as a function of the number of overscanned milling patterns for laser ablation at 50 mW for a milled width of ~100 μm. The milled width did not vary significantly after the initial scans ± 5 μm. However, the roughness (plotted on the second y axis) rises dramatically after ~ 10 overscans and we see the appearance of relatively large (ϕ ~ 18.5 μm) regions which have undergone enhanced ablation. The positioning of these regions is random and does not seem to be due to the milling process. The peak to peak roughness (in the absence of the pitting) is reduced in comparison with the single scan case (no milling) but the target depths and overall roughness values could not be met at this wavelength.

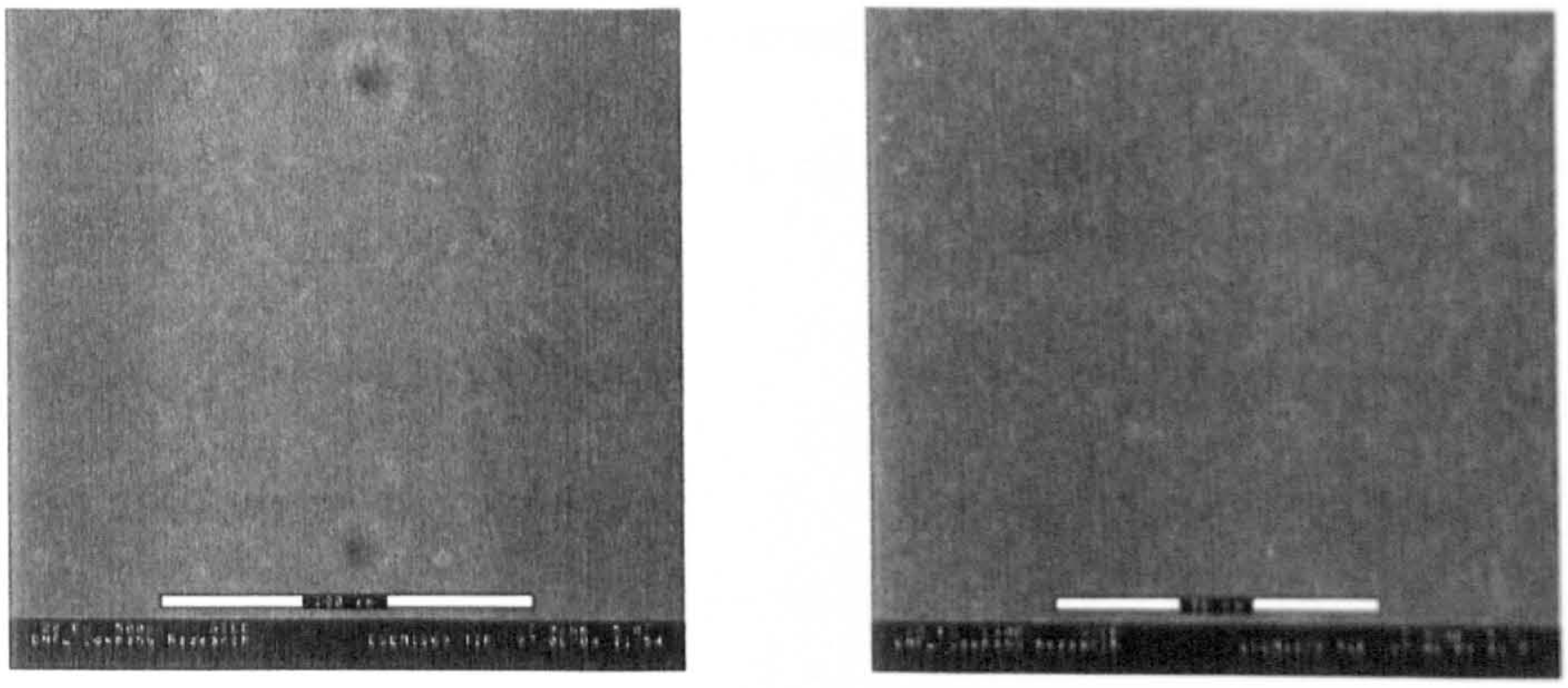

Fig. 4.1.19 ESEM image of laser milled silicon (790 nm, 50 μJ).

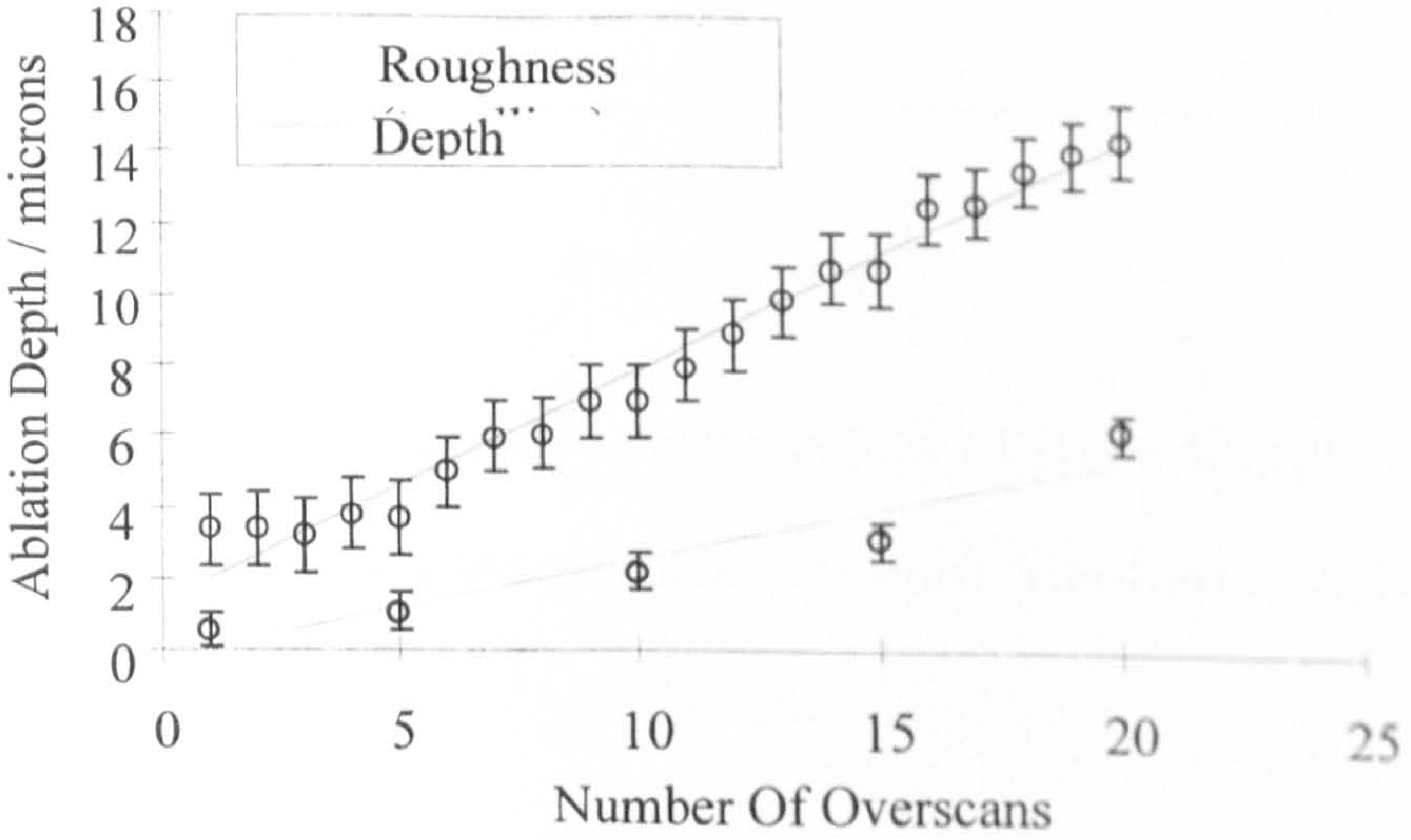

Fig.4.1.20 Ablated depth as a function of the number of laser milled layers for silicon with F ~ 1 Jcm^{-2}.

With these findings in mind we used the frequency doubled output of the Ti:Sapphire laser amplifier at 395 nm for a comparison with the near IR (790 nm) ablation. Due to the unavailability of an fθ lens (see Section 2.2) at the desired wavelength, a 150 mm focal length plano-convex lens with the plano face to the infinite conjugate was employed. Modelling[6] of the lens showed that orientation of the lens in this manner, whilst increasing spherical abberations, led to a flattening of the field curvature in comparison to the normal geometry. The ablation rate per pulse is given as a function of fluence in Fig. 4.1.21. with the data for ablation at 790 nm given for comparison.

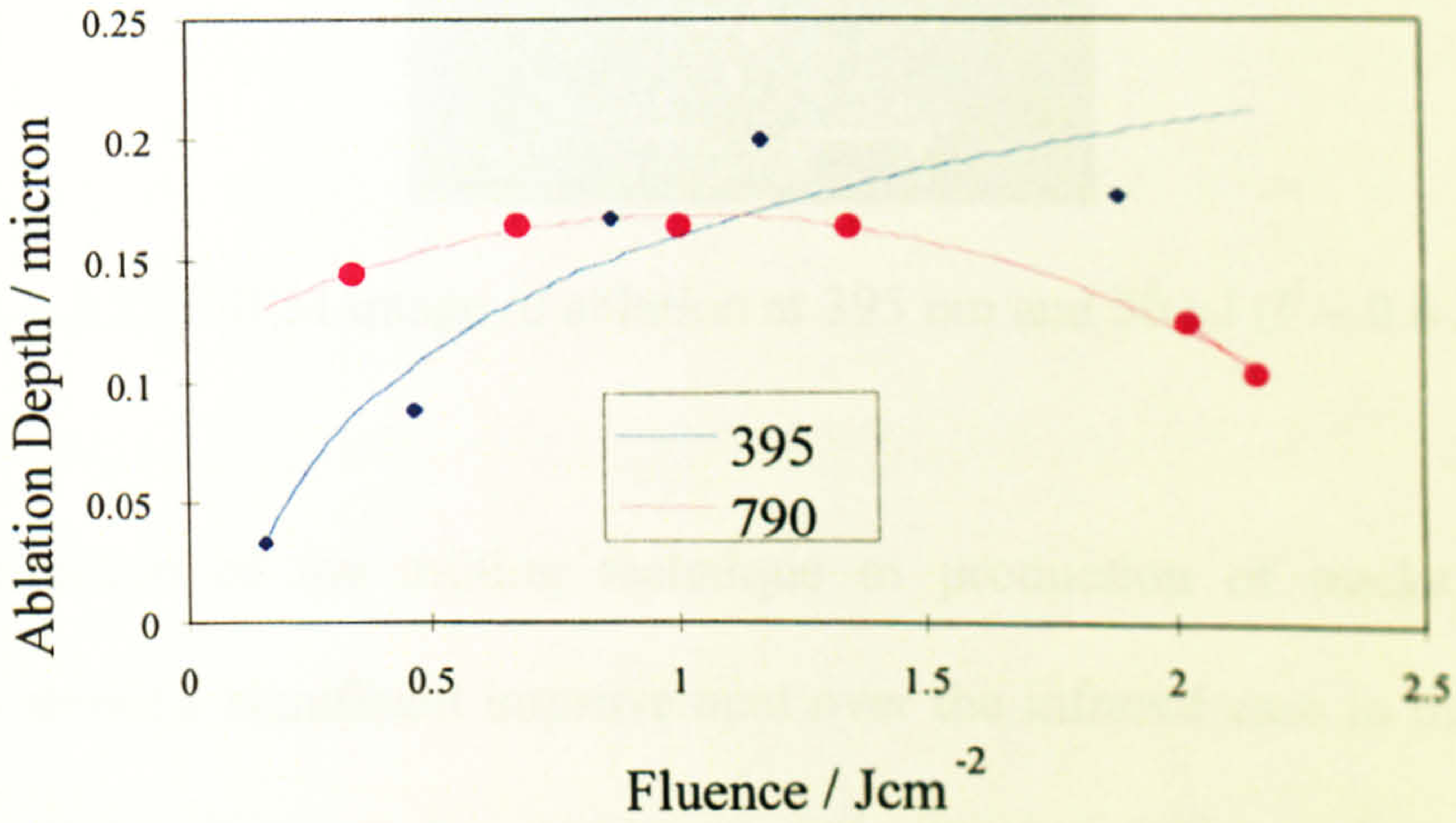

Fig. 4.1.21 Ablation rate per pulse as a function of laser fluence. Comparison between ablation at 790 (red circles) and 395 nm (blue diamonds). Trendlines are given as an aid to the eye.

A micrograph of a typical ablation track is given in Fig. 4.1.22. The residual surface morphology of the track is clearly different to that given in Fig. 4.1.14 (ablated with the same fluence and under the same experimental conditions), bearing more resemblance to that of Fig. 4.1.16 although the scale of the microstructure is reduced in the UV case. The observed asymmetry of the track is due to aberrations in the lens and reduced beam quality during the frequency conversion, with the right hand side of the track "seeing" more intensity than the left hand side. Certainly there is not the melting observed in the case of ablation at 790 nm. We believe that this is due to the reduction in linear absorption depth for 395 nm light.

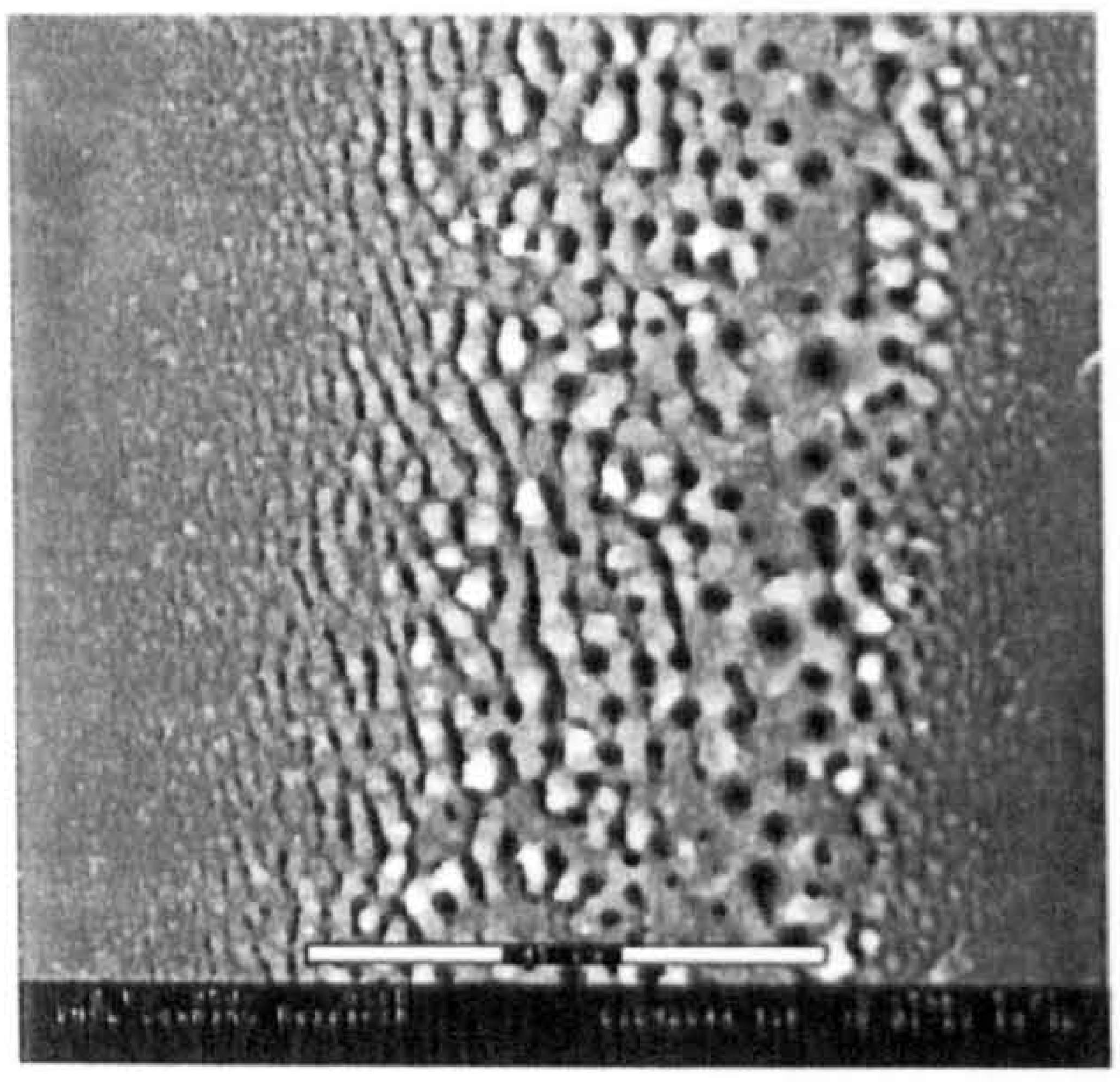

Fig. 4.1.22 ESEM image of ablation at 395 nm and 50 μJ (F ~ 0.6 Jcm^{-2})

Application of the milling technique to production of tracks with custom dimensions shows a significant improvement over the infrared case in that the residual surface roughness is more homogeneous and remains within tolerance limits for prototype production to a depth exceeding the target value. Fig. 4.1.23 shows ESEM images of features milled under the same experimental conditions (lens and pulse energy).

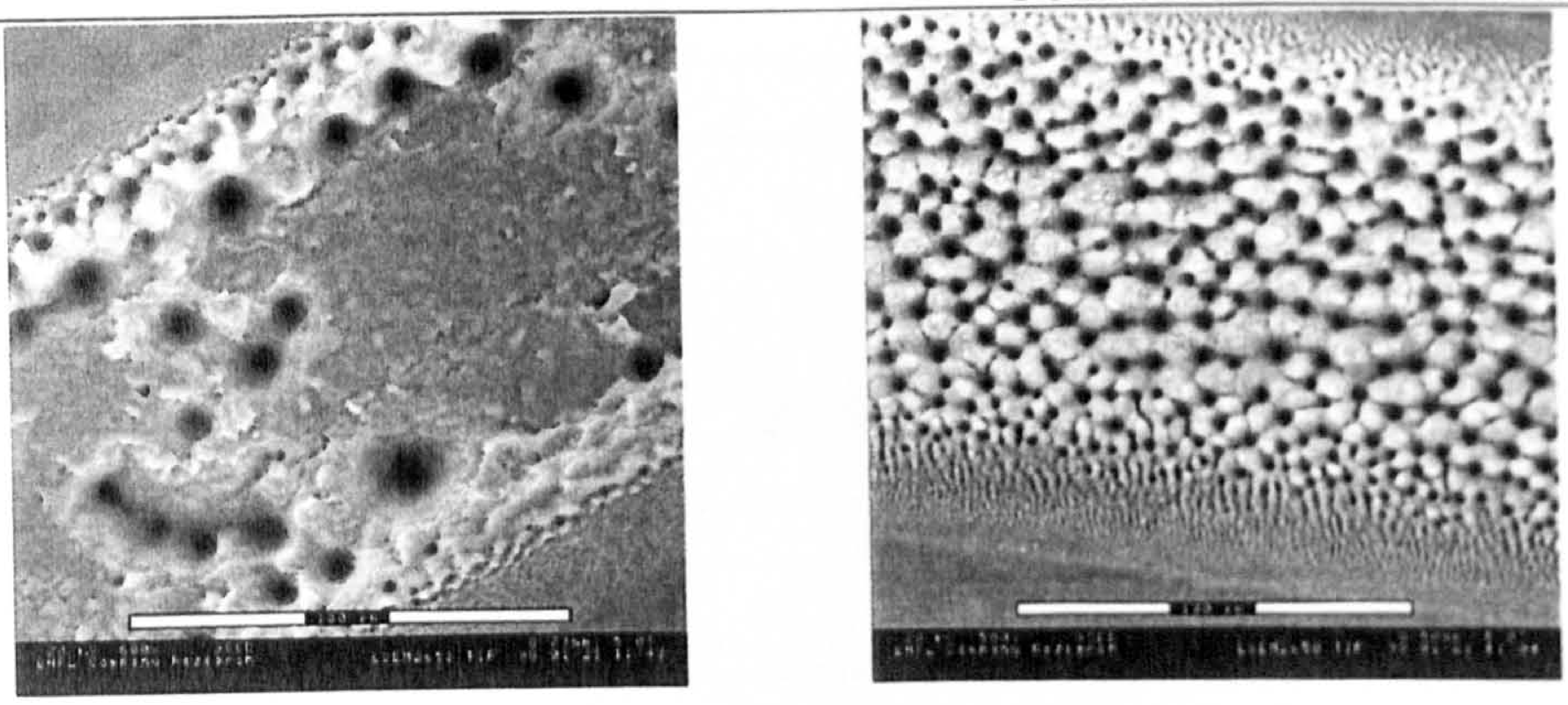

Fig. 4.1.23 ESEM images of laser milled tracks ablated with 790 (left) and 395 nm (right) under identical experimental conditions.

Fig. 4.1.24 shows a graph of ablation depth as a function of the number of overscanned layers of a raster pattern; a linear fit is given as an aid to the eye. Clearly target depths of 50 μm are achievable and correspond to approximately 90 overscans of the ablation pattern. Measurements of the average residual surface roughness using a Talysurf surface profiler are given in Table 4.1.2. These values are within tolerance for device fabrication. There is a clear discrepancy between the observed void features on the ESEM images of ablation tracks at 395 nm and the average roughness value. This cannot be explained by the size of the profiler tip which has adequate resolution to see these features. This is most likely due to the depth of field of the ESEM allowing excellent contrast in a relatively small depth region.

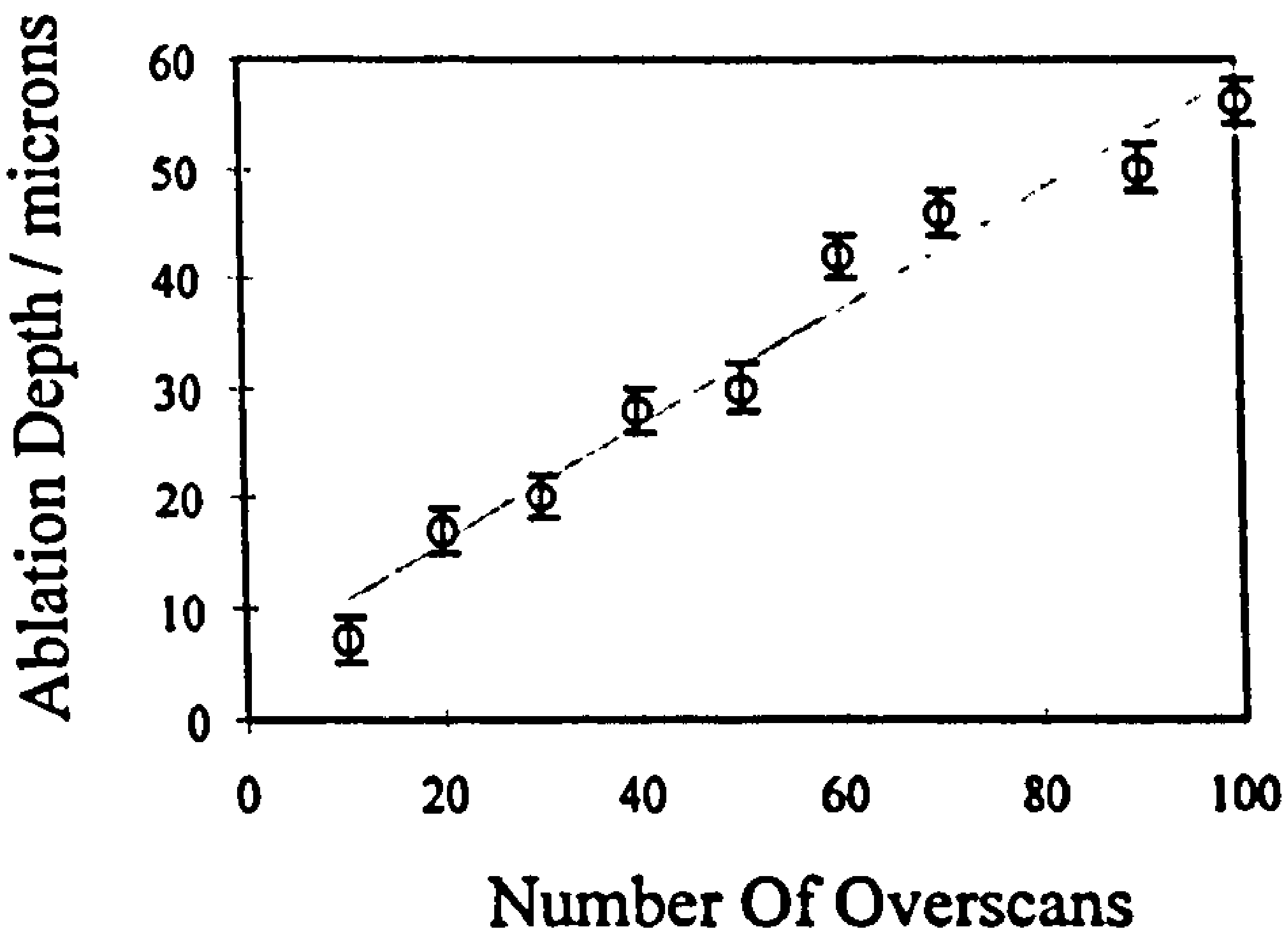

Fig. 4.1.24 Ablation Depth As A Function Of Overscanned Layers At 395 nm (~200fs laser pulses, F~ 0.6 J cm^{-2}).

Table 4.1.2 Roughness Measurements Using Talysurf Surface Profiler

Depth / μm	Roughness / μm
6.4	0.1
19.9	0.2
25.9	0.2
35.7	0.2
49.6	0.3
57.1	0.5

Gallium Arsenide

Gallium arsenide (GaAs) is a III-V semiconductor composite material with a direct bandgap of ~ 1.42 eV (at 300 K) which is used primarily for photonic applications (laser diodes) The absorption spectrum of GaAs was given in Fig. 4.1.12. GaAs was ablated at both 790 nm (close to the bandgap energy) and 395 nm with 170 fs laser pulses for direct comparison with the ablation of silicon. Fig. 4.1.25 shows ESEM images of the residual surface microstructure after laser ablation at 790 nm with a fluence of ~ 0.6 Jcm^{-2}. In the low magnification image, we clearly see a number of separate regions with similar characteristics to those seen for silicon. The low fluence region (in the wings of the laser intensity profile) show the familiar ripple structure (pitch ~ 700 nm) we observe in silicon and indeed in other metallic substrates (see below). We then see a region which shows both the ~ 700 nm ripple and some larger structural formations which are far less precisely defined with an axis perpendicular to that of the low fluence rippling and a pitch corresponding to approximately 2 μm (distance between pulses ablating track is ~ 10 μm). In the intersection between the ripple minima (dark contrast) we see areas which appear to have undergone preferential ablation to form sub-micron perforations, much as that observed in silicon. In the central region of the ablated track the surface has clearly undergone melting and subsequent solidification. Large material droplets are observed indicating a thicker melt depth than silicon, or at least a more pronounced interaction between the liquid and vapour phases. The asymmetry of the ablated track is due to a slight misalignment of the galvo system with respect to the lens.

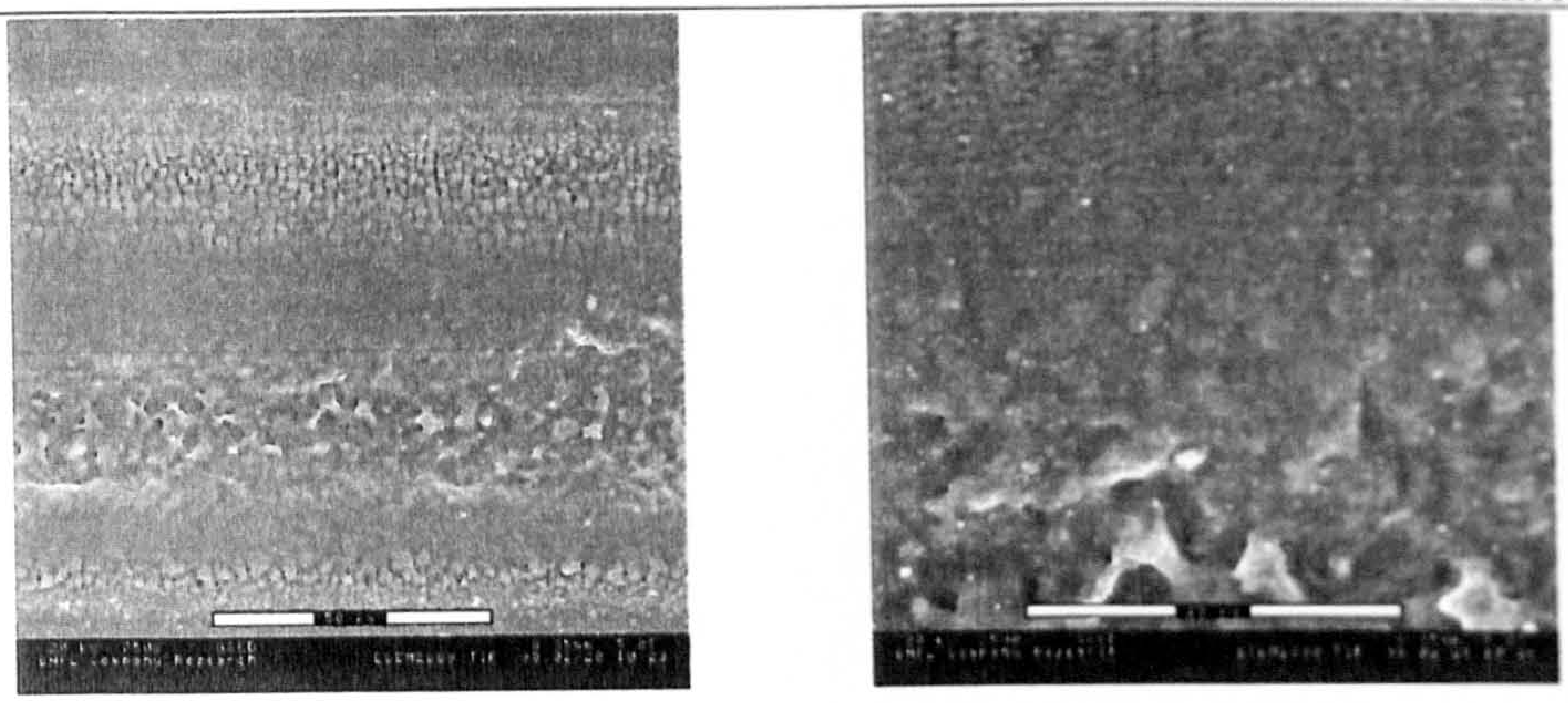

Fig. 4.1.25 ESEM images of GaAs ablated at ~ 0.6 Jcm^{-2} (λ = 790 nm, t_p~ 170 fs).

Fig. 4.1.26 Shows two ESEM images of GaAs ablated at 395 nm with ~ 0.6 Jcm^{-2}. The lower magnification image shows the large scale surface deformations observed for ablation at 790 nm, although the presence of a resolidification layer is less pronounced (if it is there at all) as we expect from the comparison of linear absorption coefficients. In this case, the appearance of regularity in the microstructure of the 790 nm ablated material is not observed, although at this magnification we see the sub-micron perforations seemingly at random along ablated features to the top and bottom of the image. We also observe the large scale ~ 2 μm, "random" hole drilling observed in silicon ablation at 790 nm. The higher magnification image shows the central region of the track and we see a ripple structure with a pitch of approximately 300 nm. This reduction in ripple pitch implies a connection between the observed microstructure and the wavelength.

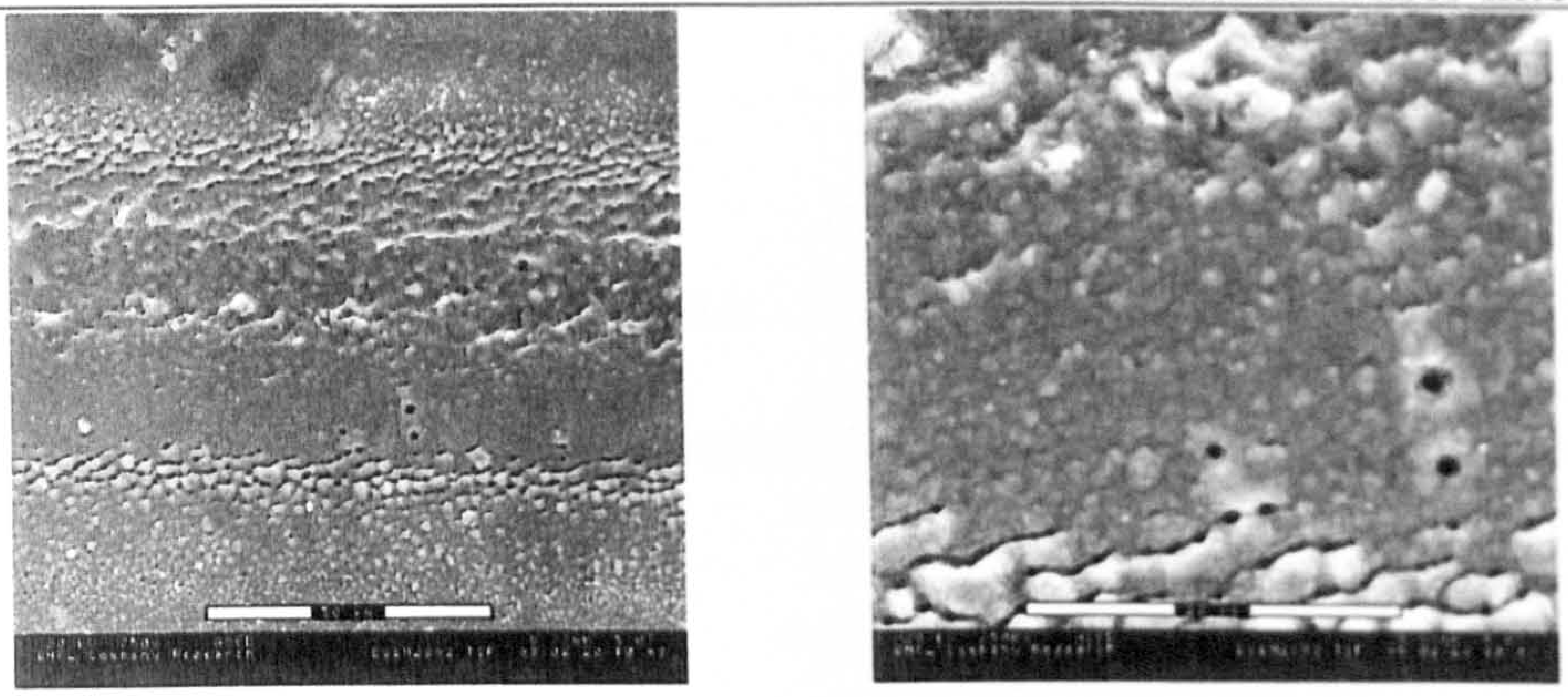

Fig. 4.1.26 ESEM images of GaAs ablated at ~ 0.6 Jcm^{-2} (λ = 395 nm).

Microstructures observed after ablation of silicon and GaAs show some similarities in terms of melting and micro-hole drilling. However, melting appears to be more pronounced on GaAs, which may be accounted for by a difference in the electron-phonon coupling rate in the two materials. Whilst on the evidence of previous experiments, an electron plasma (or melted surface) is formed within the pulse width (170 fs) in both cases, it is likely that the GaAs plasma forms more rapidly resulting in enhanced heating of the plasma and subsequent coupling back into the bulk.

4.1.3 Metals

We have undertaken some studies of stainless steel and aluminium, near the ablation threshold in various environments. The results for each material are taken in turn.

Stainless Steel

Ablation of stainless steel was undertaken near threshold fluence to investigate the residual microstructures formed by the process in air. In ambient atmosphere the ablated sites show signs of oxidation which obscure and degrade the structures. It was possible to reduce the formation of oxide deposits on the substrate by directing a nitrogen jet at the ablation site to both reduce the oxygen present and entrain the ejected ablation plume so that it was not redeposited at the ablation site. An ESEM image of two tracks ablated in stainless steel at approximately 10 μJ (F ~ 0.1 $\mathrm{Jcm^{-2}}$) is given in Fig. 4.1.27. Distinct periodic microstructure is observed parallel to the scan direction with a period of ~ 680 nm which is close to that observed on fused silica in vacuum.

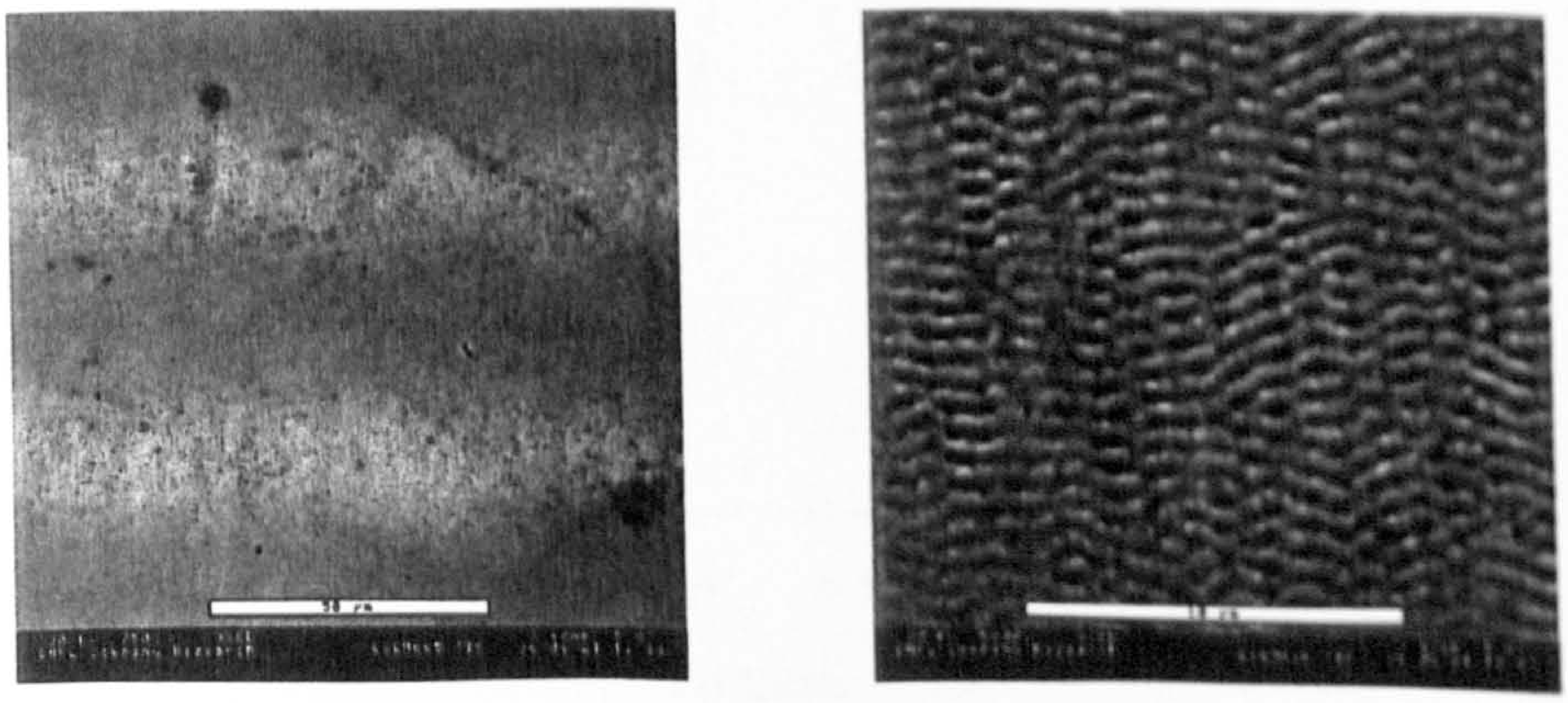

Fig. 4.1.27 ESEM image of stainless steel ablated near threshold fluence.

Studies of the ablation products ejected from the substrate under vacuum have also been undertaken on steel samples and formed part of a BNFL internal report[7]. 304 type stainless steel was ablated at near threshold fluences and the ablated ions probed using a quadrupole mass-spectrometer. The threshold fluence for laser ablation is characterised by the measurement of chromium ions (m/z = 52). The variation of ion count with laser fluence is given in Fig. 4.1.28. The result indicates a threshold for ionisation of ~ 0.3 Jcm^{-2} and the ion signal effectively saturates at a fluence of ~ 0.5 Jcm^{-2} although the signals are very noisy. Operating in RGA mode while ablating the metal sample did not reveal any neutral species, indicating that the ablation products are predominantly ionised. In comparison, ns laser pulses are relatively inefficient at producing ions[8]. The threshold ionisation fluence compares favourably with the ablation thresholds obtained by Preuss et al[9] for 500 fs pulses at 248 nm, summarised in section 1.6.2.1.

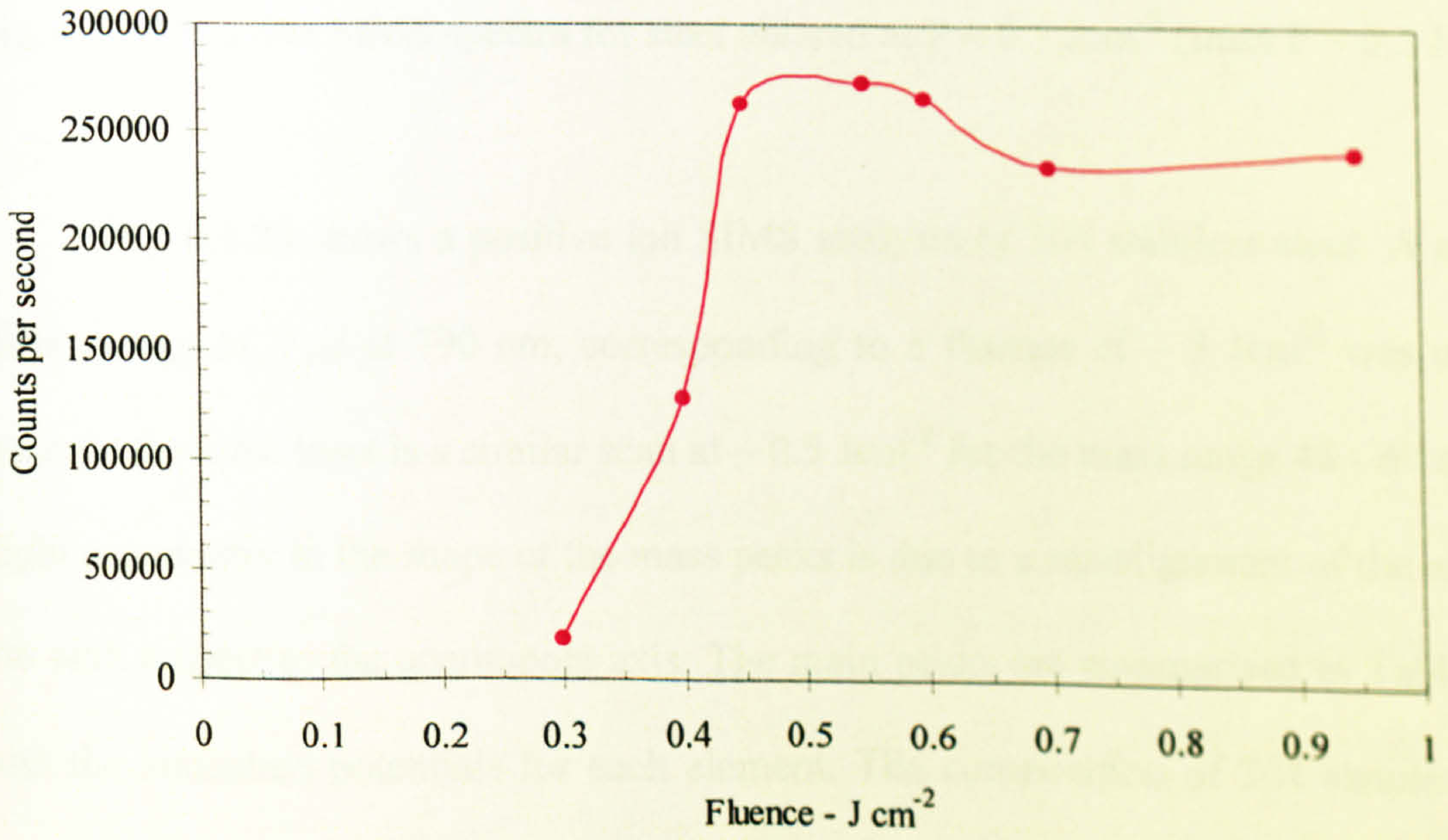

Fig. 4.1.28 Variation of ion count with laser fluence for m/z =52 (chromium)

The measurements in Fig 4.1.28 were undertaken with fixed extractor and ion lens voltages and the shape of the curve in the plateau region is probably an instrumental response due to increased ion energy with fixed extractor and lens voltages. Optimisation of the voltages for each laser fluence would allow a better acceptance ratio for higher ion energies. In such a case we would expect to see characteristic logarithmic dependence with laser fluence.

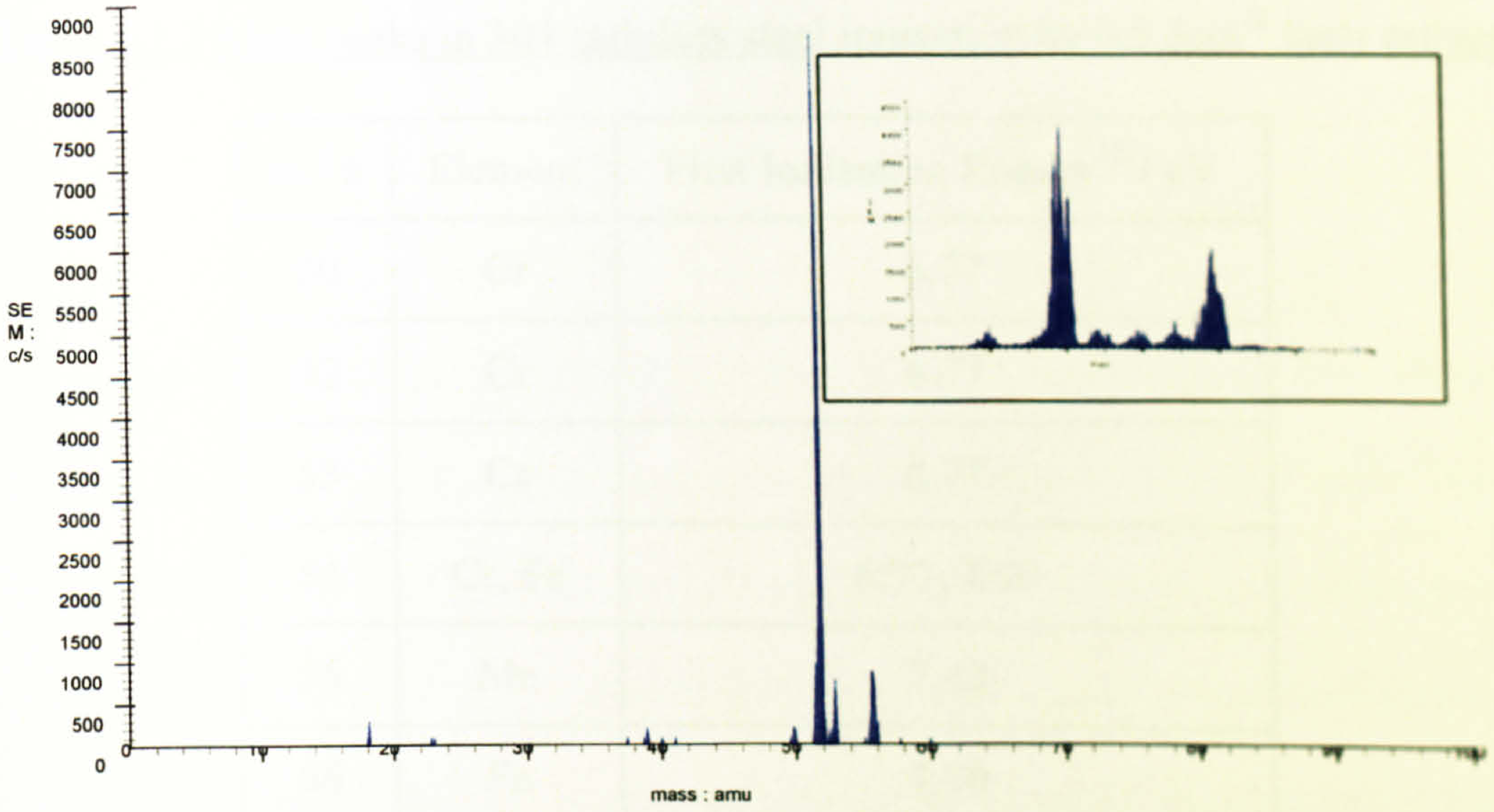

Fig. 4.1.29 Positive SIMS spectra for steel ablated at F ~ 0.3 Jcm^{-2} (Inset F ~ 0.5 Jcm^{-2}).

Fig. 4.1.29 shows a positive ion SIMS analysis of 304 stainless steel. A modest pulse energy of 7 μJ at 790 nm, corresponding to a fluence of ~ 3 Jcm^{-2} was used to generate the ions. Inset is a similar scan at ~ 0.5 Jcm^{-2} for the mass range 48 - 60 amu. A slight asymmetry in the shape of the mass peaks is due to a misalignment of the ablation site with respect to the quadrapole axis. The main peaks are summarised in Table 4.1.3 with the ionisation potentials for each element. The composition of 304 stainless steel (approx. 10% Ni, 18% chromium and 72% Fe) would suggest that the total of the Fe isotope peak heights should be the largest component of the mass spectra. Since this is clearly not the case, with the ^{52}Cr count in excess of the sum of the m/z values at 54, 56 and 57, it can be concluded that selective ionisation is occurring. The ionisation energies for the constituents seem to support this conclusion, with Cr being some 1.13 eV below Fe. Considering the photon energy is 1.57 eV (for 790 nm) we have what amounts to the difference between a four and five photon ionisation process.

Table 4.1.3 Main peaks in 304 stainless steel ionisation by 0.5 Jcm^{-2} laser pulses.

m / z	Element	First Ionisation Energy[10] / eV
50	Cr	6.77
52	Cr	6.77
53	Cr	6.77
54	Cr, Fe	6.77, 7.90
55	Mn	7.43
56	Fe	7.90
57	Fe	7.90
58	Ni	7.64
60	Ni	7.64

Fig. 4.1.30 shows steel ablated in vacuum at near threshold fluence ~ 0.3 Jcm^{-2} in vacuum (~ 10^{-7} mBar). We see what appears to be a roughening of the surface, with only small areas which appear to have under gone significant material removal (the scans are at approximately 0.1 mm s^{-1}). We also see ripple structures which appear to be at an acute angle to the scan direction. The ripple depth is clearly insignificant in comparison to the depth of the ablated voids.

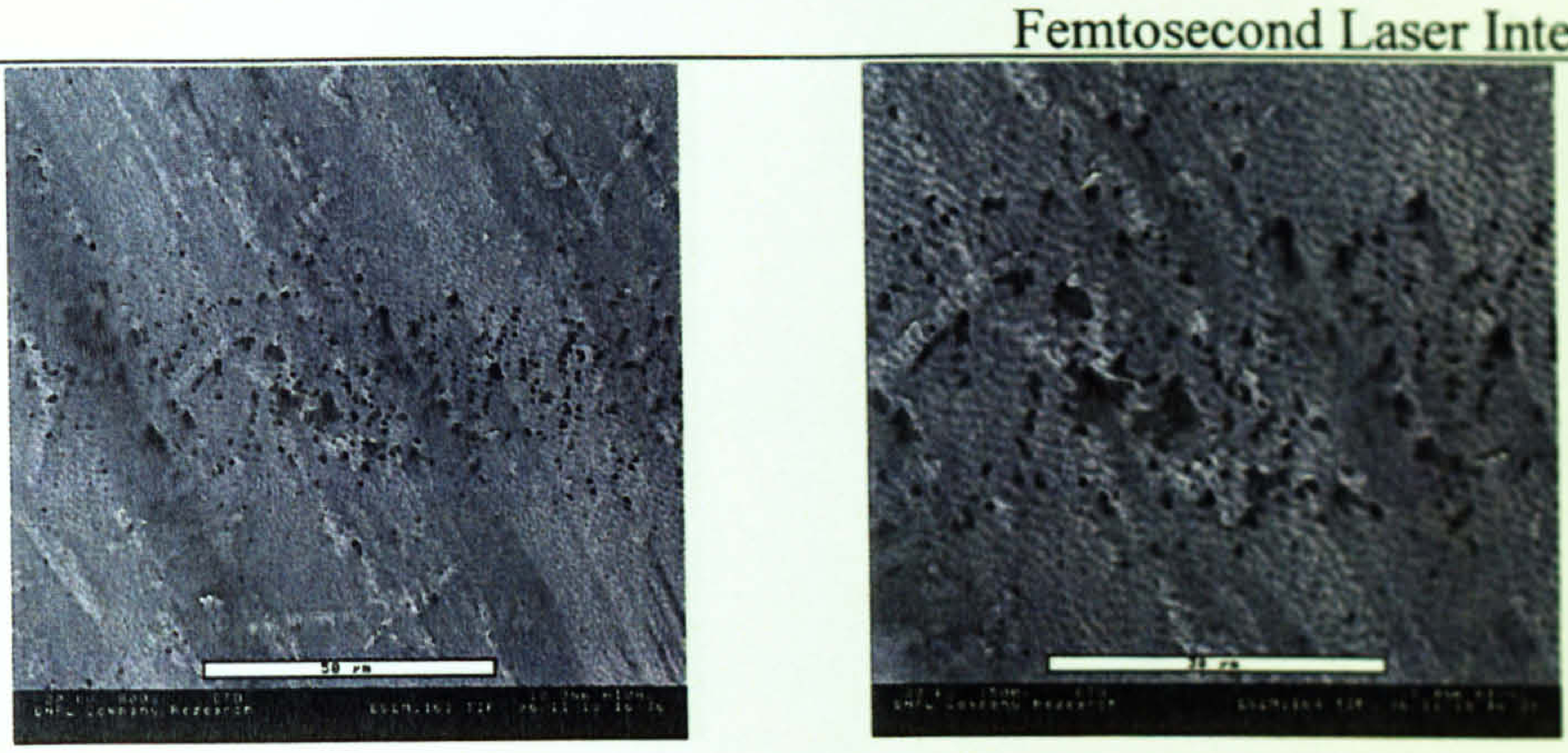

Fig. 4.1.30 ESEM images of stainless steel ablated at < 0.3 Jcm^{-1} At 10^{-7} mBar.

Aluminium

Surface modification of aluminium has proven problematical for ablation by nanosecond excimer laser due to its high reflectivity in the UV (Fig. 4.1.31)[11]. We have ablated aluminium using 170 fs laser pulses to compare residual microstructure with other ablated metals. Fig. 4.1.32 shows ESEM images of tracks ablated in Aluminium at near threshold fluence in air with a nitrogen jet present to entrain the ablation products.

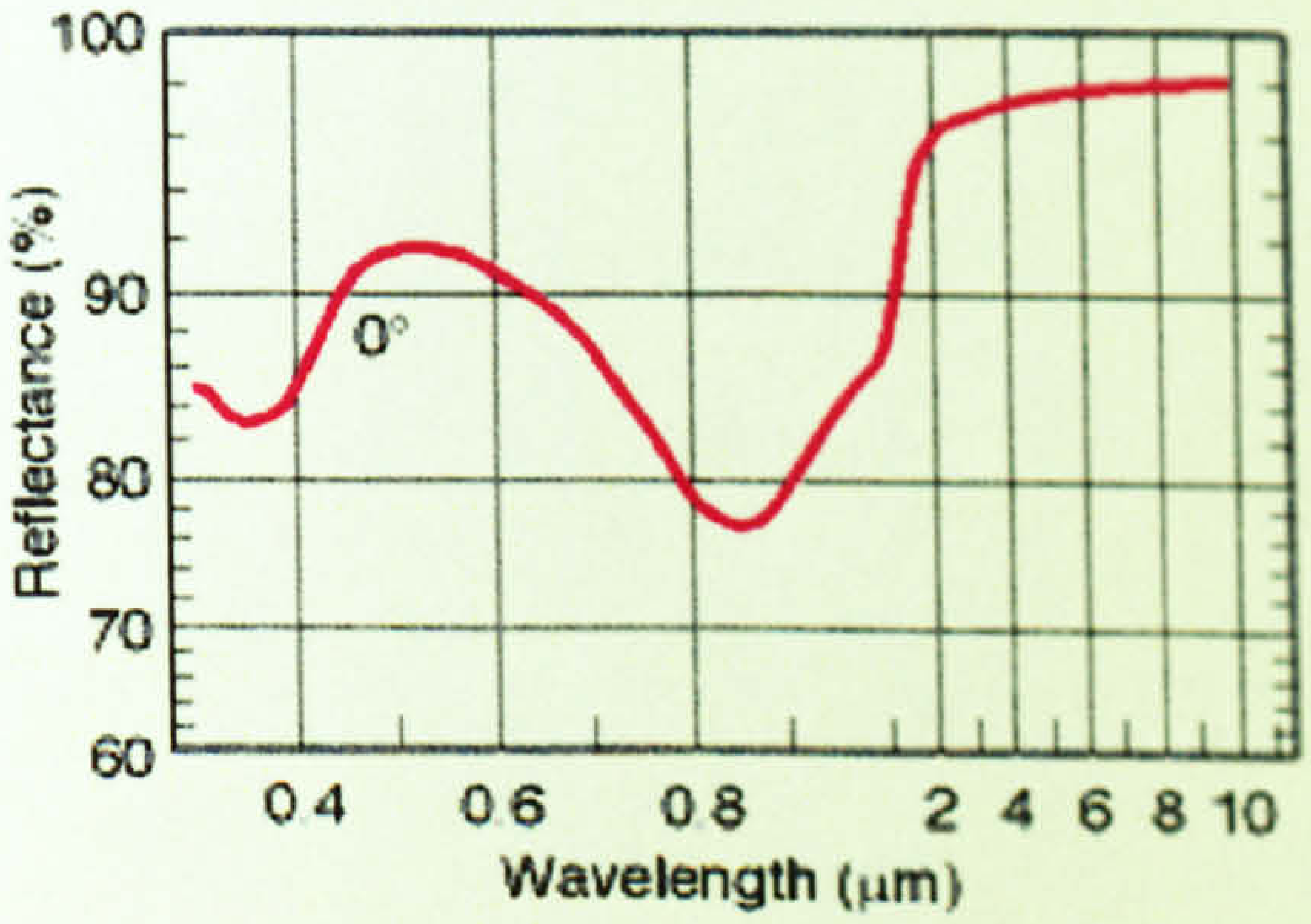

Fig. 4.1.31 Reflectivity spectrum for aluminium.

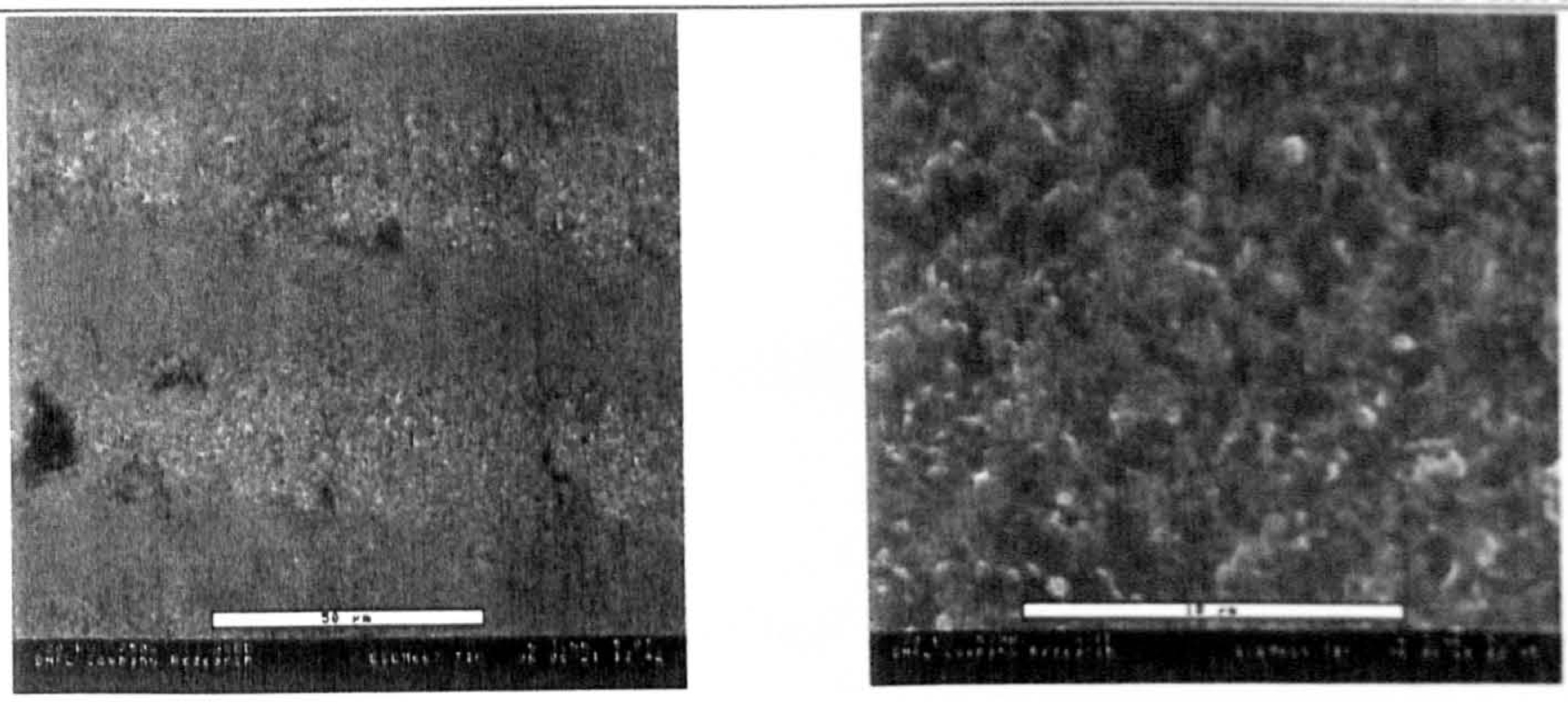

Fig. 4.1.32 ESEM image of aluminium ablated at near threshold fluence.

The difference in resulting surface structure compared to steel is clearly evident. Inspection under an optical microscope suggests that the aluminium surface has lost its high reflectivity. We see no evidence of the regular surface features that we observe on steel or silicon, indeed the residual microstructure appears chemically altered. The high reactivity of the aluminium surface in the liquid/vapour phase may play a significant role in the ablation process, however, more rigorous analysis of the process in controlled environments is required before conclusions may be draw. It is possible that effective micromachining of aluminium may be performed with femtosecond pulses in the presence of an inert gas or in vacuum.

4.2 Chemical Device Fabrication

4.2.1 Microchemical Contactor For Metal Ion Extraction

The application of microtechnology for chemical processing requires the creation of micron size channels of specific geometries in which reactants are brought together in a highly controlled fashion[12]. Solvent extraction (for metal separation) is important to the nuclear industry. Diffusion controlled solvent extraction of Fe^{3+} ions in 30 - 100 μm wide channels was recently demonstrated in microchemical "contactors" with immiscible liquids under laminar flow conditions, with subsequent complete separation of the phases[13]. Microchannels (and ports) have previously been produced in silicon and glass using standard lithographic and wet etching techniques, with the materials anodically bonded together to form devices. The timescales for prototype fabrication, however, range from weeks to months, limited by the time taken for mask fabrication. "Direct write" femtosecond laser microstructuring is an attractive alternative for short lead time prototype fabrication for devices with dimensional requirements limited by heat affected zones.

Fig. 4.2.1 shows a schematic diagram of a microcontactor in which fluid streams can be brought together, contacted at a stable interface over a controlled distance with subsequent complete separation of the streams. Requirements for the microchannels were to produce tracks with widths 80 - 100 μm and depths ~ 30 - 50 μm, residual surface roughness < 1 μm and with good edge definition.

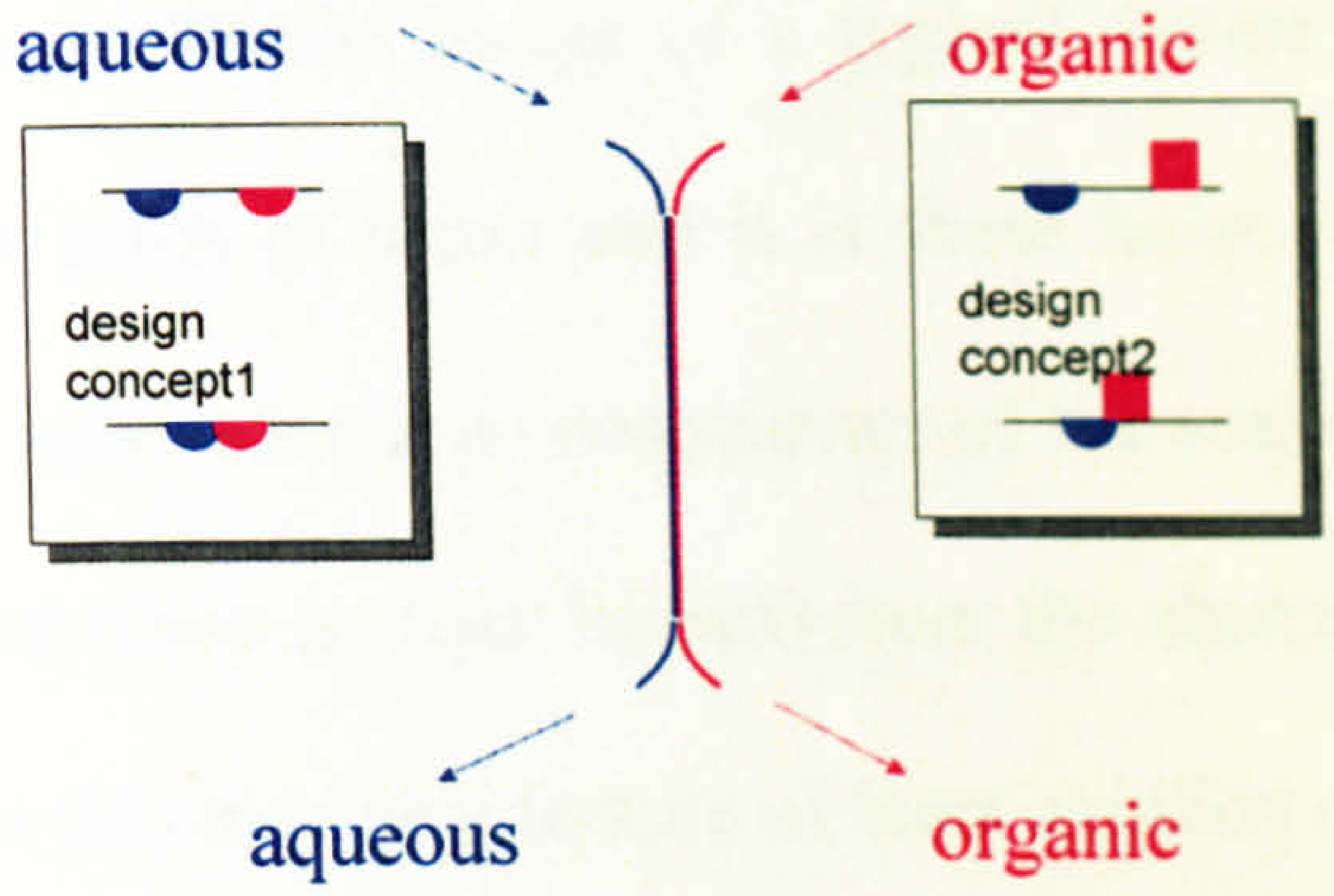

Fig. 4.2.1 Schematic of a microchemical contactor

Pyrex 7070 was laser milled (see section 4.1.1) with the second harmonic of the regenerative amplifier output at 395 nm with a fluence of 2.5 J cm^{-2} to produce a 40 mm long track consisting of a 10 mm straight with 180° bends at either end. The resulting edges were well defined and uncracked. The residual surface roughness is submicron as we have seen previously in Fig. 4.1.11. The width was 80 ± 3 μm and depth 35 ± 2 μm throughout the track length.

The second half of the device was to be made in p-type silicon and was to consist of a 40 mm track with width 150 μm and depth of 50 μm. Four 1 mm diameter ports for input/output of the two liquids were also to be provided. Drawing on our experience of ultrashort pulse ablation of silicon, we successfully carried out device fabrication at 395 nm to the required specifications.

Laser milling of the silicon devices was undertaken with pulse energy of ~ 25 μJ and a fluence of 0.6 J cm^{-2} and the required depth was achieved by overscanning a raster pattern consisting of 9 lines with 10 μm separation. One overscan of the pattern corresponds to an ablation depth of ~ 1 μm. Devices were produced with dimensions of width ~ 150 ± 5 μm and depth 50 ± 3 μm throughout the track length. Residual surface roughness is approximately 0.5 μm with peak to peak variations of < 2 μm.

Fig. 4.2.2 shows an ESEM image of a typical device in silicon. Micron size holes are present with a pitch of 6 μm and it is these holes which limit the ultimate resolution. Whilst these holes are not a consequence of the scanning pattern as discussed in section 4.1.2, they may result (at least in part) from the aberrations caused by the scan lens. But we suspect that this may be a feature of laser ablation of silicon in this regime.

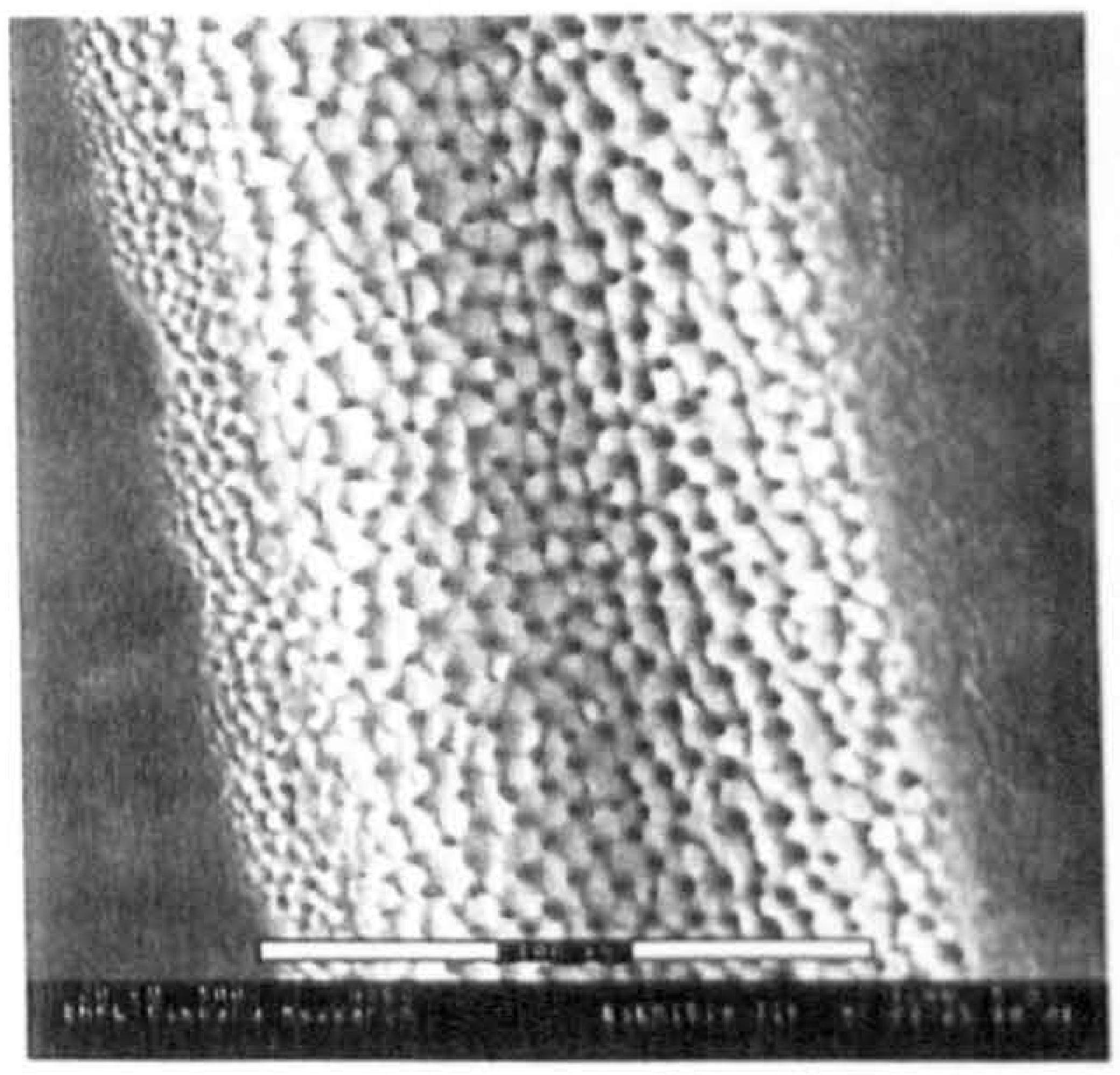

Fig. 4.2.2 ESEM image of laser milled device (silicon).

Circular ports with a diameter of 1 mm for liquid input and output were cut through 500 μm thick silicon wafer with a pulse energy 150 μJ per pulse (F~ 3.6 J cm^{-2}). As the amount of material to be removed was large, only the radius of the ports was marked until penetration through the wafer was achieved and the central region dropped through, typically taking approximately 10 minutes at 10 mm s^{-2} (corresponding to ~19100 laser pulses per spot diameter).

We have shown that microchemical contactors may be produced by direct laser writing using femtosecond laser milling techniques. The success of this project confirms that rapid prototyping using this technique is achievable at a significantly reduced cost to conventional techniques.

4.2.2 Microchemical Contactor For The Nitration Of Benzene

Fabrication of several micro-chemical contactor designs for the nitration of Benzene was undertaken for a BNFL collaborative project under the direction of Dr John R. Burns at the University Of Newcastle[14]. 260 mm diameter borosilicate glass disks were provided with pre-drilled ports for alignment and subsequent device operation. The devices were to be machined with rectangular track geometries to a depth of 50 ± 5 µm, according to Fig. 4.2.3

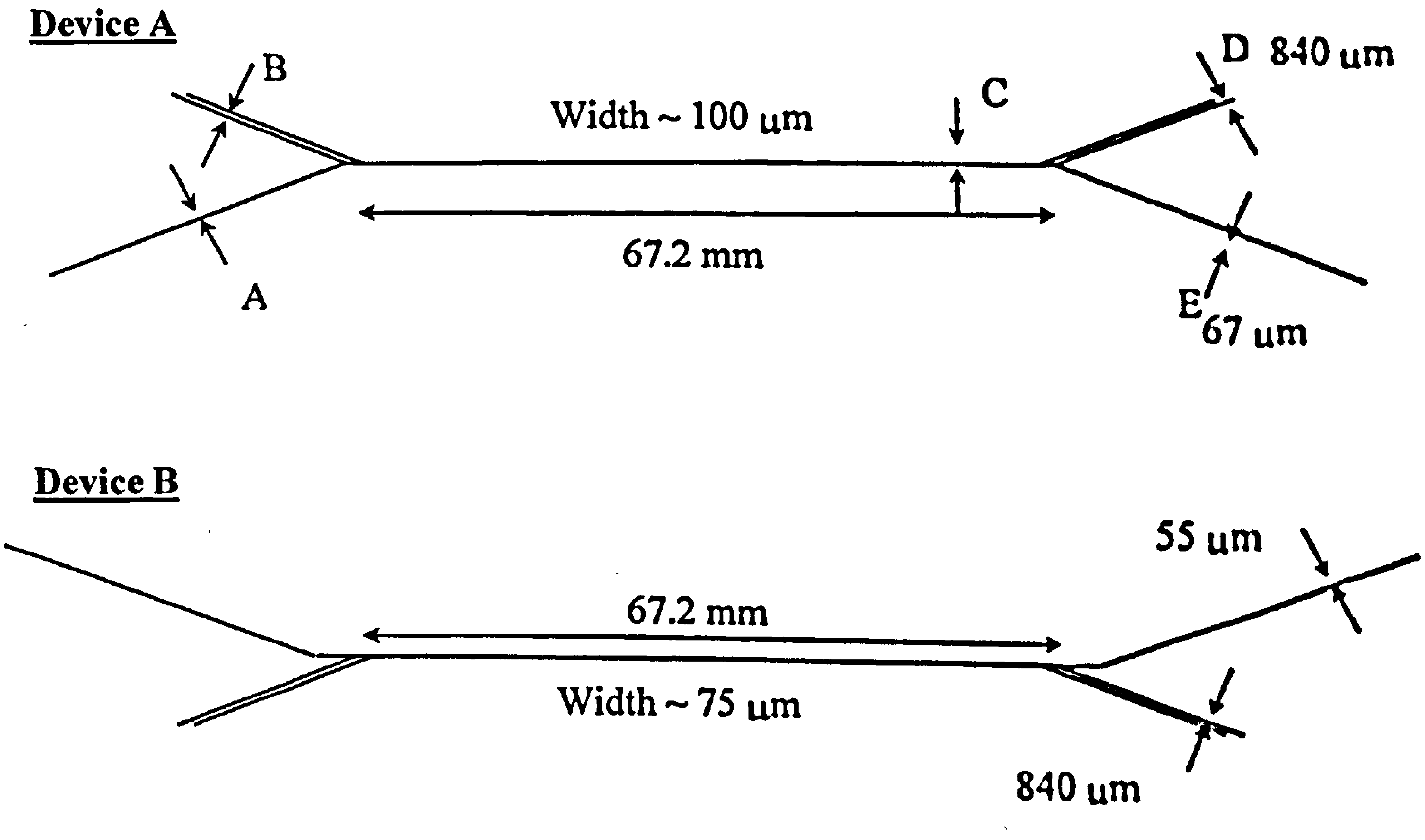

Fig. 4.2.3 Microchemical contactor for the nitration of benzene

This particular application required the production of a prototype device with uniform depth (50µm) over a field of 120 mm. This required the provision of a new scanning lens (previous maximum field was 110 mm) with a longer focal length (f = 350 mm) to give a field of 190 mm and the further development of laser milling techniques to maintain uniform depth throughout the device (discussion of scan lenses is presented in Chapter 2, Section 2.3).

The increase in effective focal length from 190 to 350 mm leads to a doubling of the $1/e^2$ spot diameter and a corresponding reduction in fluence at the focus. We accommodated this by increasing the diameter of the input beam from 8 mm to ~ 15 mm thereby maintaining the f-number of the lens system. Reflection losses due to poor anti-reflection coatings in the four element lens amount to a reduction in pulse energy of 50% at the substrate.

With a pulse energy of 120 μJ (measured prior to the lens system) the diameter of the pulse intensity profile above the ablation threshold was determined to be of the order 20 μm (single laser shot). However, taking into account incubation in the substrate we estimate the diameter of interaction to be ~ 35 μm (the width of a track after a sufficient number of pulses to eliminate incubation).

Prior work presented in section 4.2.1 showed that we could produce micro-channels of various widths by rastering the beam across the desired width. The required depth can then be reached by over-scanning the pattern. Depth resolution is determined by both the number of over-lapping rasters and the laser fluence. It is clear from a simple model of adding Gaussian intensity profiles that a critical point can be reached whereby adding additional rasters does not affect the overall depth, only the volume of material ablated. This has been shown to work experimentally for shallow tracks where the side walls are not too steep, however for deeper, narrower tracks the ablation rate can fall as a function of depth due to decreased laser fluence at the walls resulting in a triangular track profile.

Micro-cracking, due to the abrasive action of the high velocity ejecta (perpendicular to the substrate, regardless of the angle of incidence) is more serious for narrow, deeper tracks where the plasma is more confined. This can be avoided, as described previously (section 4.1.1), by slightly offsetting the over-scans at low fluence. However, for tracks <100 μm with a relatively large aspect ratio this is impractical and cracking can still occur. We have also observed that ablation at an angle of incidence other than normal to the surface may produce micro-cracking on only one edge of a track. This is due to the ejecta always being emitted perpendicular to the surface, abrading only the slightly undercut edge. Clearly, this phenomenon will lead, not only to micro-cracking, but track widening and asymmetry. This could be eliminated using a telecentric scanning lens for critical applications.

Calibration of the Job Editor software was achieved by measuring ablated track lengths and dividing by the expected length (calibrated for a 160 mm lens). The expected maximum field is of the order 230 mm (for f = 350 nm). Scan speed for the prototype device was set at 17.5 mm s^{-1}. This corresponds to approximately two overlapped pulses for a single scan (selection of this speed was arbitrary in that this was the slowest speed available with this lens), however the number of pulses per unit area is significantly increased as the number of rasters is increased up to the interaction diameter.

Alignment of the optical arrangement in the first instance was achieved by removing the flat field lens and overlapping a back reflection from the target with the incoming beam at a pinhole by manipulating the sample holder. After replacing the lens the various component back reflections were also aligned to the pin hole. The focal plane of the lens is always parallel to the plane of the final element (perpendicular to the optical axis of the lens) so a small tilt of the lens with respect to normal incidence of the laser beam will introduce a similar tilt of the focal plane. This is evident as a change in ablation rate (characterised by a loss of plasma at the surface) from one end of a long scan to the other. Fine adjustment of the target is achieved by monitoring the plasma and introducing small angular modifications until an even ablation rate can be observed throughout a long scan. Misalignment is indicated by the development of a self-focused filament, which can be seen to move towards the surface as the correct angular adjustment is applied. Gross misalignment may require an additional change in lens-target distance to re-acquire the focal plane after angular adjustment.

The scan pattern was aligned to the input ports by attenuating the laser energy to well below the ablation fluence and scanning the pattern continuously at high speed (3 m s^{-1}) onto the substrate. The pattern is seen as a series of points of generated white light continuum (observed by placing a piece of card beneath the substrate) which can be used to roughly align the ports. Fine adjustment of the start and end points of the scan can be achieved by observing the blue fluorescence on a piece of card placed at the input/output port. All alignment procedures can be followed without direct observation of the 790 nm laser light.

The prototype was produced by breaking the design into three parts corresponding to the three intersecting channels indicated in fig. 4.2.3. A raster pitch of 5 μm was chosen arbitrarily and the number of rasters required to reach the desired widths (taking into account the beam diameter) was calculated. It is important to maintain the raster width throughout the device or depth discrepancies may occur due to changes in the integrated intensity "seen" by the surface. The pattern was then marked onto the substrate to determine the ablation rate per pass which was of the order of 3.5 μm. The required depth corresponds to approximately 14 over-scans with a pulse energy of ~ 120 μJ. HPGL files written for the galvonometer Job Editor show a good correspondence to the experimental results. However, some fine tuning of individual vectors was required to produce the desired widths. Ablation of each of the two devices took approximately two hours due to the complicated nature and physical size of the scan pattern. A photograph of the ablated glass substrate is given in Fig. 4.2.4.

A summary of the dimensions of the various components (illustrated in Fig. 4.2.3) of the two devices is given in Tables 4.2.1 and 4.2.2. It is clear from the data that device A does not meet the design tolerance in terms of depth. However, the track widths and depths were calculated for channels with rectangular cross-section and the actual geometry is typically Gaussian (or even triangular) for relatively thin tracks. By increasing the depth we compensate for the reduced cross-sectional area of the ablated geometry. Similarly, the reduced width of the acid inlet will compensate for the slight increase in depth of this channel due to raster density.

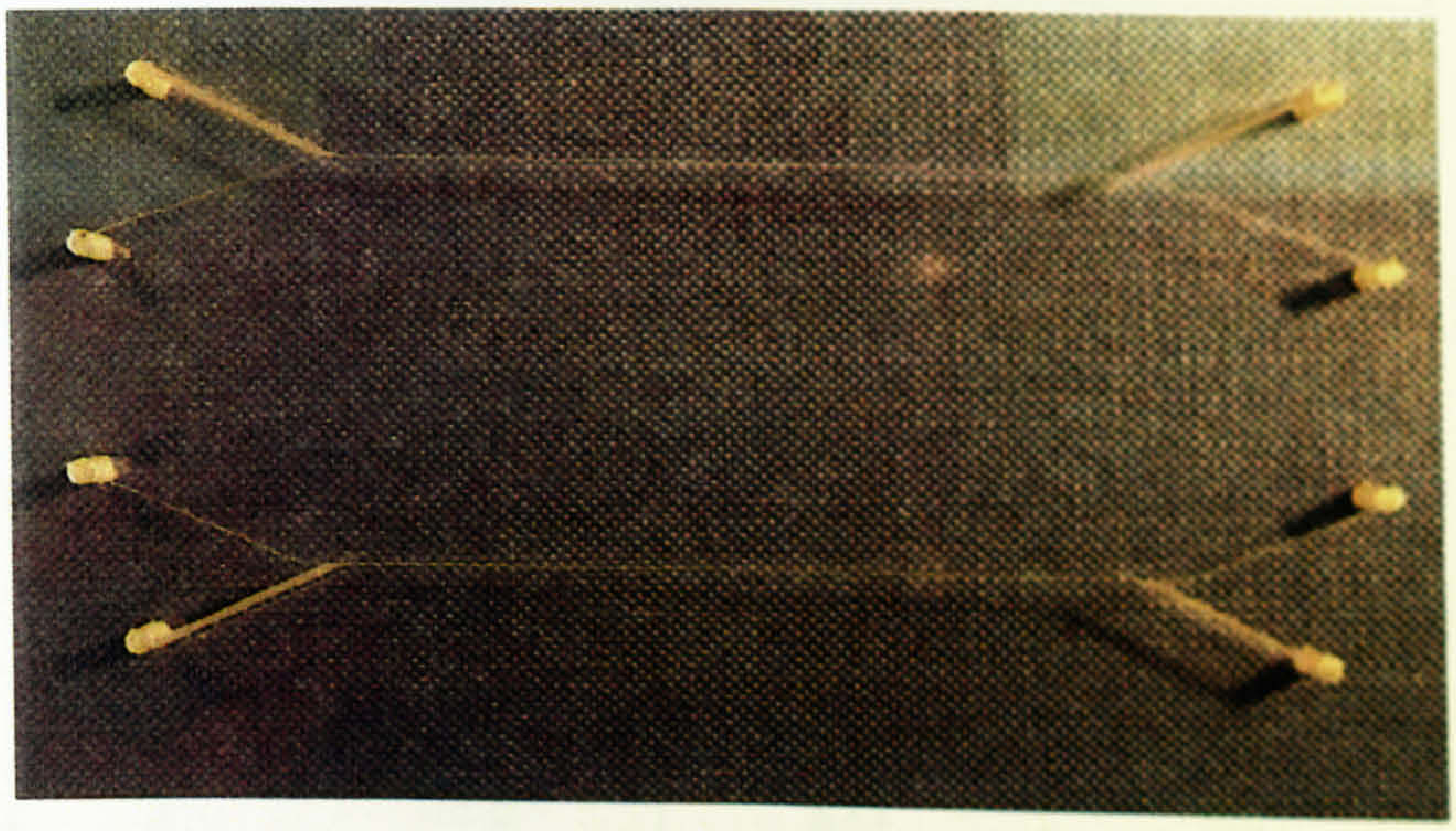

Fig. 4.2.4 Micro-chemical device for the nitration of benzene, machined by femtosecond laser ablation at 790 nm.

Table 4.2.1 Microchemical device A; dimensions

Position	Depth_{AV} (± 2 μm)	Width (± 1 μm)	Target Width (μm)
A_1	61.0	62.2	67
A_2	63.0	63.2	67
A_3	63.8	61.9	67
B_1	72.3	831	840
B_2	70.4	825	840
B_3	72.7	831	840
C_1	61.0	98.2	100
C_2	61.2	97.9	100
C_3	56.0	95.9	100
D_1	58.9	61.9	67
D_2	61.8	61.9	67
D_3	55.4	62.5	67
E_1	67.7	836	840
E_2	68.6	831	840
E_3	68.7	835	840

The subscript of the dimensions refers to the a separate group of measurements in a particular field of view for the confocal microscope.

Table 4.2.2 Micro-chemical device B; dimensions

Position	Depth_{AV} (± 2 μm)	Width (± 1 μm)	Target Width (μm)
A_1	47.8	60.9	55
A_2	48.4	59.6	55
A_3	49.9	60.9	55
B_1	59.0	824	840
B_2	60.1	837	840
B_3	56.5	828	840
C_1	48.2	76.6	75
C_2	50.0	78.6	75
C_3	52.1	77.3	75
D_1	51.4	60.1	55
D_2	51.4	62.2	55
D_3	50.1	60.2	55
E_1	63.5	829	840
E_2	57.1	831	840
E_3	60.6	827	840

A modulation of pitch ~70 μm can be seen in two directions (at 34° and 56° to the channel edge corresponding to the x and y planes of the scanning galvonometers respectively). Modelling a single pass of a raster pattern with speed 15 mm s^{-1} (pulse separation 15 μm) and raster separation 5 μm (assuming a Gaussian with FWHM 35 μm) we see no modulation of the relative intensity in the scan direction corresponding to the scan speed. However, the model neglects incubation effects which can lead to modulation corresponding to the pulse overlap. It is likely that the effect is due to incubation, with early overscans 'imprinting a memory' of modulation onto the substrate which is subsequently driven deeper into the material. The problem may be minimised by reducing the scan speed to maximise the pulse overlap and thereby reduce the ripple pitch, or indeed eliminate it altogether.

Rapid prototyping of microchemical devices by ultrashort pulse laser ablation holds significant advantages over existing photo-lithographic and LIGA techniques in terms of lead times and processing stages. No mask fabrication [the major time component in projection routes] or chemical etchants, are required leading to greater control of track dimensions within prescribed limits of resolution [clearly laser ablation at 790 nm will never achieve the resolution afforded by projection techniques]. Ablation of features below the diffraction limit is possible with careful control of laser energy with stability of ± 1%.

Two micro-chemical contactors have been produced with a lead time of three weeks. It is conceivable that this turn-around could be significantly reduced now that the problems regarding interfacing multiple channels of varying widths have been addressed. It is also possible that with more development, finer control of the residual structure may be achieved.

4.2.3 Auxetic Macro-filter

Auxetic materials exhibit a negative Poisson's ratio; that is they expand laterally when stretched and contract laterally when compressed[15]. This unusual, counterintuitive behaviour is very rare in naturally occurring materials although it has been an accepted consequence of classical elasticity theory for over 150 years. Recent interest in this property has resulted from a number of synthetic auxetic materials being produced. In nearly all these cases, the auxetic material has been formed by altering the internal microstructure of a conventional material, for example, foam[16] and microporous polymers[17], to produce auxetic behaviour.

The mechanism for producing a negative Poisson's ratio is not scale dependent so it is possible to envisage structures, rather than materials, exhibiting exactly the same phenomenon. In this situation, other benefits from having an effectively negative Poisson's ratio across the structure have been identified. One, which is the subject of this section, is the use of auxetic honeycombs and structures in filtration.

In order to use auxetic honeycombs in practical filtration systems it is necessary to construct honeycombs with cell sizes in the appropriate particulate size range. Microstructures of this type could be formed by conventional stereolithography. This has been identified as a method for producing auxetic microstructures for improved sensors and for micromachine manipulators. However, these applications require stiff materials that can only withstand very small strains before failure. In this instance we have fabricated polymeric and silicon structures having the geometry known to lead to auxetic behaviour, by femtosecond laser ablation. The polymeric membranes are capable of sufficient distortion for use in filtration.

UV laser ablation for micromachining and patterning of polymers using nanosecond excimer lasers (e.g. KrF, 248 nm) is a well established technique[18]. A strong UV absorption coefficient is desirable ($\alpha > 10^4$ cm^{-1}) and, in the case of weak absorption, significant thermal degradation effects may be observed[19]. Studies of femtosecond polymer ablation show that UV, visible and near IR femtosecond pulses may be used to microstructure transparent polymers at ultrahigh intensity since multi-photon absorption by chromophores dominates the ablation mechanism[20].

Micromachined re-entrant (auxetic) and conventional honeycomb polymeric membranes were formed by direct femtosecond laser ablation in air of a sheet of Hewlett Packard Colour Laser Jet Transparency film (part no. HP C2936A). Devices were successfully formed by ablation at both 790 and 395 nm. However, we observed significant darkening of the edges of the 395 nm ablated material due to linear absorption of photons and, possibly, thermal damage. Membranes ablated by 790 nm pulses show no such darkening of the unablated material, in addition to which, the scanning lens used for the 790 nm experiments produced a less aberated focal point over the whole field. Pulses with a fluence of ~ 1.3 J cm^{-2} were used to mark the cell perimeters at a scan speed of 5 mm s^{-1}. Penetration through the 128 μm thick polymer substrate was achieved after approximately 5 overscans per cell (~ 100 pulses / spot diameter) corresponding to an ablation rate of approximately 1.3 μm per pulse. In terms of the linear optical response, the membrane is essentially transparent at both wavelengths and absorbs strongly only below 350 nm. Examples of polymeric membranes with conventional and re-entrant honeycomb structures are given in Fig. 4.2.5 and 4.2.6 respectively.

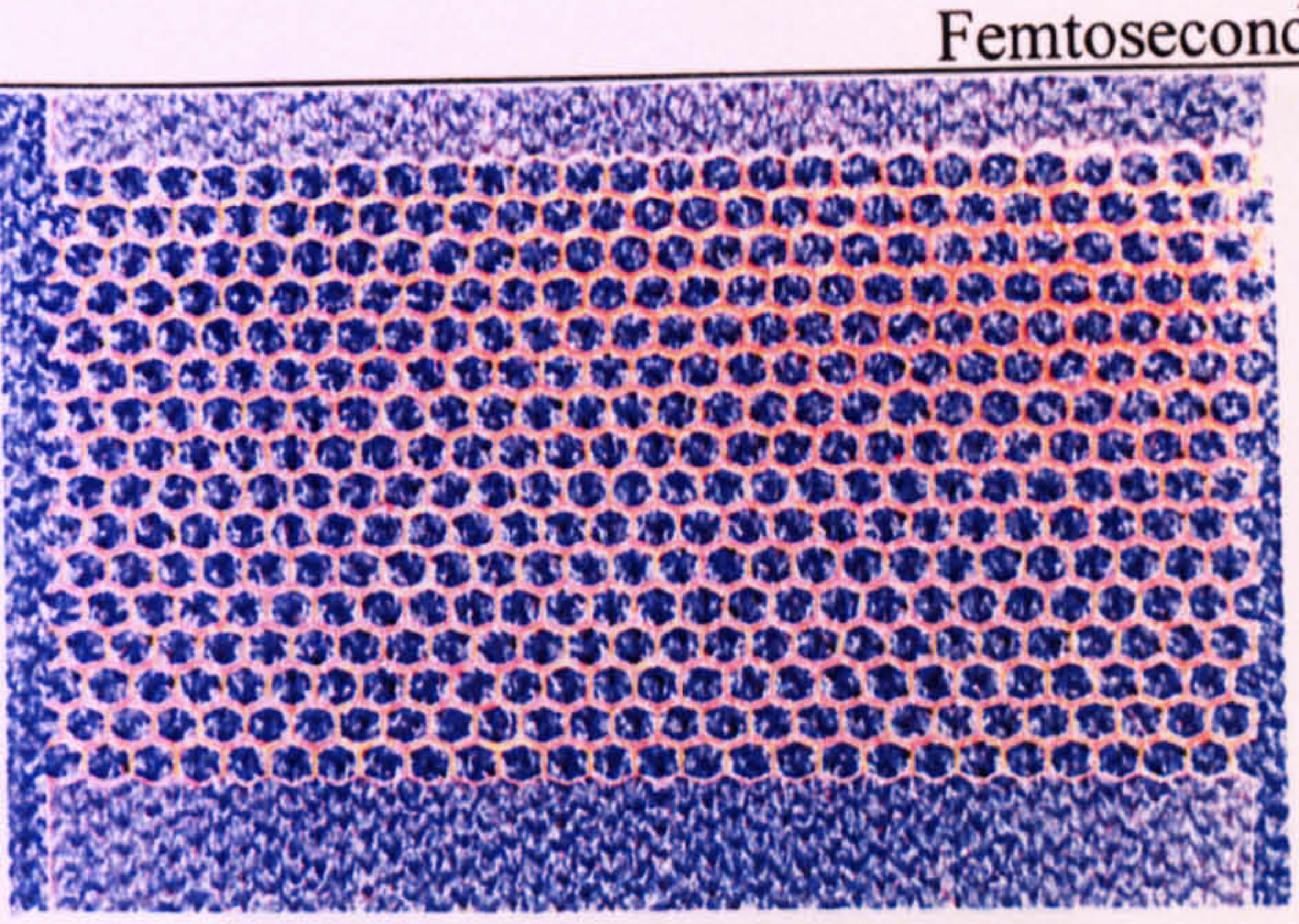

Fig. 4.2.5 Conventional polymeric membrane formed by femtosecond laser ablation.

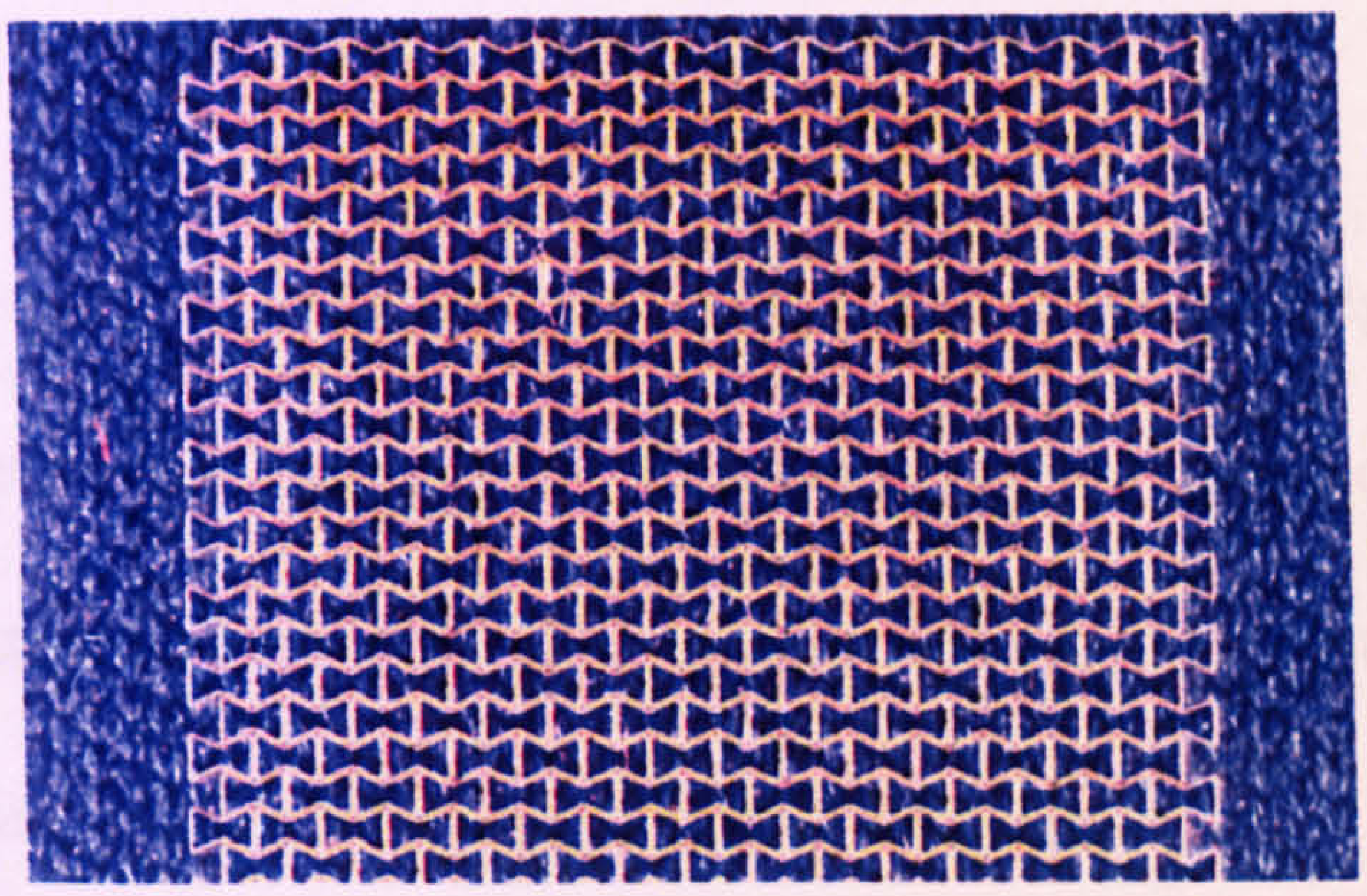

Fig. 4.2.6 Auxetic polymeric membrane formed by femtosecond laser ablation.

Similar structures were also formed in p-type silicon by ablation at 395 nm, although the ablation rate is significantly lower, as we found in previous work on microchemical contactors. An example of a cell ablated with a fluence of approximately 3.6 J cm^{-2} is given in Fig. 4.2.7. A small 5 × 5 cell auxetic structure was formed in the silicon due to the time taken for penetration in each cell (~ 10 mins) but the material is probably too brittle for use as a filter.

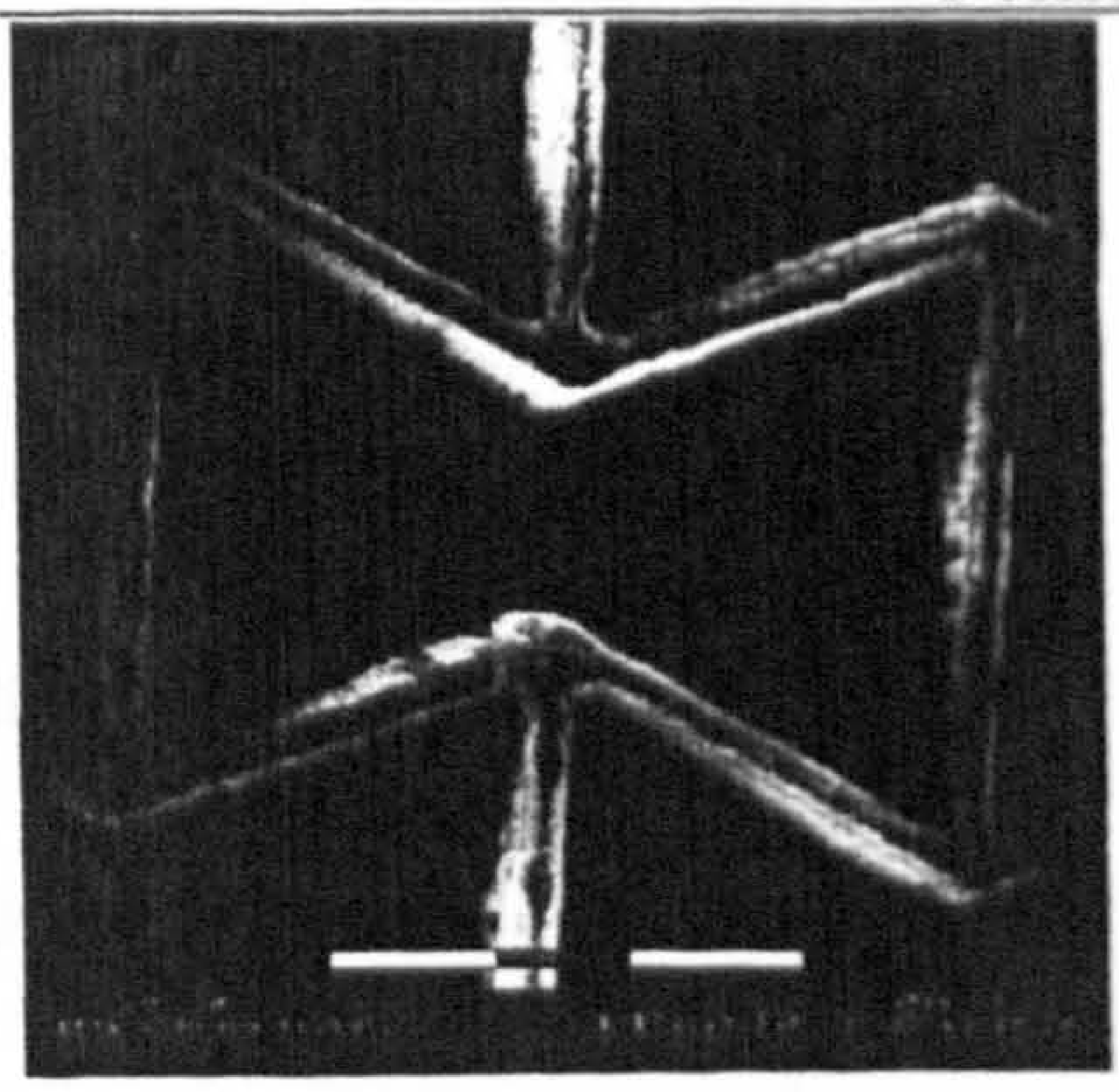

Fig. 4.2.8 ESEM image of auxetic honeycomb formed by laser ablation of silicon at 395 nm with F ~ 3.6 J cm^{-2}.

Both the polymeric membranes have been tested and a negative Poisson's ratio is observed for the re-entrant structure[21]. Furthermore, the auxetic membrane has been shown to offer benefits as a cleanable filter due to deformation of the membrane leading to the pores opening up in both in-plane principle directions.

4.3 Conclusions

Femtosecond laser ablation has been studied for a variety of dielectric, semiconducting and metallic substrates with emphasis on the development of the technique for rapid prototyping of micro-fluidic devices. Fundamental observations of the effect of ultrashort pulse laser ablation have been presented for fused silica, pyrex, silicon, GaAS, Steel and Aluminium for a variety of pulse energies and at both 790 and 395 nm. We find that residual surface microstructure is much reduced for all materials studied when compared to picosecond and nanosecond laser ablation. Micro-structuring of high quality micro-chemical devices has been achieved in fused silica, pyrex and silicon using a scanning galvanometer system. Pyrex and fused silica, can be micro-machined in the near infra-red (790 nm) and the UV (395 nm) to required tolerances, whilst silicon can only be accurately structured to 10 μm depth at 790 nm. For depths of ~ 50 μm, with sub-micron roughness, machining is accomplished at 395 nm where the linear absorption coefficient plays a greater role in the ablation process. Devices have been fabricated using a technique we describe as laser milling, which allows us to accurately control both the final dimensions of the devices and the residual surface roughness. We find that ultrashort pulse laser ablation is a practical method for rapid prototype production, given the degree of control over ablation depth and width, afforded by the technique.

We present a number of examples of components structured using the laser milling technique for chemical applications and also for a novel macro sized auxetic filter which has properties which allow it to be deformed for de-fouling purposes.

[1] J. Krüger and W. Kautek, *Appl. Surf. Science.* 96-98: p430 (1996).

[2] W. Kautek and J. Krüger, *Mat. Science. Forum.* 173-174: pp17 - 22 (1995).

[3] S. M. Sze, *Physic Of Semiconductor Devices (2^{nd} addition)*, John Wiley & Sons Inc., *(1981)*.

[4] J. Ilhemann, B. Wolff and P. Simon, Appl. Phys. A., 54: pp363 - 368 (1992).

[5] K. Sokolowski-Tinten, J. Bialkowski, A. Cavalleri and D. von der Linde, Appl. Surf. Sci., 127-129: pp 755-760 (1998)

[6] G. Mc Connell, *BNFL Report.* (1997).

[7] J.Wright, *BNFL Report* CRL / R 132 (1997).

[8] T. Hung and C. Su, *Rev. Sci. Instrum.*, 63: p5299 (1992).

[9] S. Preuss, A. Demchuk and M. Stuke, Appl. Phys. A. 61: p33 (1995).

[10] A. Beiser, *Concepts In Modern Physics*, McGraw Hill Book Co., (1987)

[11] D. A. Mc Neill, T. Morrow & P. Dawson, *Appl. Surf. Sc.*, 127-129: pp46-52 (1998).

[12] I. Simson & M. Harper, *IMechE Seminar: Micro & Nano Technol.: Thermofluids Dimension*, London, (Nov. 1995).

[13] I Robins, J. Shaw, B. Miller, C. Turner & M. Harper, *Proc. Int. Conf. Microreaction Technol.*: Frankfurt, (Feb. 1997).

[14] J. R. Burns & C. Ramshaw, Second International Conference on Microreactor Technology, New Orleans, U.S.A., (March 1998).

[15] K. E. Evans, *Chem. Ind.*, 20: pp 654 - 657 (1990).

[16] R. S. Lakes, *Science*, 235: pp 1038 - 1040 (1987).

[17] A. Alderson and K. E. Evans, *Polymer*, 33: pp 4435 - 4438 (1992).

[18] M. C. Gower, P. T. Rumsby and D. T. Thomas, *SPIE Excimer Lasers*, 1835: pp 133 - 142 (1992).

[19] S. Kuper and M. Stuke, *Mat. Res. Soc. Symp. Proc.*, 129: pp375 - 383 (1989).

[20] H. Kumagai, K. Midorikawa, K. Toyoda, S. Nakamura, T. Okamoto and M. Obara, Appl. Phys. Lett., 65: pp 1850 - 1852 (1994).

[21] A. Alderson, J. Rasburn, S. M. Ameer-Beg, P. G. Mullarkey, W. Perrie and K. E. Evans, *Submitted to Ind. Eng. Chem. Res.*, (1999).